Harmonic and interharmonic cross modulation in HVDC links

David James Hume

A thesis presented for the degree of
Doctor of Philosophy
in
Electrical and Computer Engineering
at the
University of Canterbury,
Christchurch, New Zealand.

July 2002

ABSTRACT

This thesis investigates techniques for modelling the steady state harmonic and interharmonic waveform distortion associated with HVDC links. Previous methods are reviewed and their associated problems discussed. A numerical frequency domain model of the single HVDC converter is presented. This is used to study the effects of applied waveform distortion, particularly on the commutation period, and leads to the development of a new linear small signal analytic model. The new model is extremely fast, accurate, and capable of directly predicting the returned harmonic and interharmonic spectra resulting from applied small signal waveform distortion.

Frequency coupling matrices, calculated directly with the new model, are used to represent the time variant frequency modulating nature of the converter. These sparse matrices relate the linearised transfers of distortion through and around the converter and are used in a linear matrix equation that relates the inherent coupling between the ac side phase sequences and dc. Nodal analysis is then used to connect the full HVDC system together including rectifier, inverter and the ac and dc systems to form a sparse linear system admittance matrix. Solution speed is directly dependent on the matrix size and sparsity. This results in simple calculations used to pre-determine the main frequencies involved in the modulating process of the link. Both synchronous and asynchronous back-to-back link case studies are developed and the steady state harmonic and interharmonic waveform distortion validated against PSCAD/EMTDC time domain simulation.

Finally, critical conditions for harmonic and interharmonic cross modulation are investigated. The effects of varying system impedance and operating point are examined, and worst-case scenarios demonstrated on a 50-50Hz back-to-back HVDC link with fundamental negative sequence unbalance on the rectifier terminals.

ACKNOWLEDGEMENTS

First, my sincere thanks must go to my supervisor, Dr Alan Wood for all his encouragement, support and friendship throughout this research. More often than not, a technical discussion on some aspect of this work would inevitably end in our latest outdoor plans or past adventures. Thanks Al.

I'd also like to thank both Emeritus Professor Jos Arrillaga and Dr Neville Watson. You were both directly responsible for my enthusiasm in electric power engineering during my undergraduate years and without your initial encouragement I'd not be here today. Thanks to you both.

I feel I've been very fortunate to study within the electric power engineering group here at Canterbury. The supportive (and often distracting...) environment in Room 310 has been essential for my sanity. Special mention must be made to Dr Bruce Smith, Dr Graeme Bathurst and Dr Alan Wood whos initial research on harmonic modelling of HVDC has been invaluable to my own research. Here, I must also mention my fellow friend and power systems researcher Chris Osauskas. Chris, your help has been invaluable, along with your 'fast right arm over', thanks mate. I'd also like to acknowledge the financial support from Transpower NZ and the support of the technical staff within the Electrical and Computer engineering department.

To all my various postgraduate colleges, friends and acquaintances who have helped provide various informative discussions, outdoor distractions or plan bad humour over the years; Dr Hamish Laird, that Irish chick (Karen Kennedy), Dr Jonathan Carr, Dr Simon Todd, Dr Thomas Kepler, Andrew Ward, Dr Jesus Contreras, Dr Timo Bretschneider, Christoph Saniter, Wojtek Piotrowicz, Dr Phil Talacek, Matt O'Neil, Dr Yong-Peel Wang, Yonghe Liu, Geoff Love, John Bryant, Dave Rentoul, Steve Pawson, Clare McLennan, Greig Hamilton, Chris Forne, Olivier Desvignes, Dr Elwyn Smith, Bridget de la Haye the many CCG members and the many others I've missed. A huge thanks to you all.

Finally I'd like to thank my family, Mum, Dad, my grand parents, Rachel, Alastair and my partner Katherine for their love, patience and support.

CONTENTS

GLOSSARY

Abbreviations

AC	Alternating Current
DC	Direct Current
CIGRE	Conference Internationale de Grandes Reseaux Electriques
EMTDC	Electromagnetic Transient Direct Current
FFT	Fast Fourier Transform
HVDC	High Voltage Direct Current
IEE	Institute of Electrical Engineers
IEEE	Institute of Electrical and Electronic Engineers
GIC	Geomagnetic Induced Current
pu	Per-unit
PI	Proportional-Integral controller
PSCAD	Power System Computer Aided Design - graphical interface for EMTDC
SCR	Short Circuit Ratio
ESCR	Effecive Short Ciruit Ratio
SIV	Switching Instant Variaition
FCM	Frequency Coupling Matrix
PSS	Partial Steady State
PT	Partial Transient
SPSS	Sampled Partial Steady State
SPT	Sampled Partial Transient
SSR	Subsynchronous Resonance
STATCOM	Static Compensator
TCR	Thyristor Controlled Reactor
LTI	Linear Time Invariant
LTP	Linear Time Periodic
GTO	Gate Turn Off
PAM	Pulse Amplitude Modulated
PDM	Pulse Duration Modulated
AMIT	Amplitude Modulated Impulse Train
PLO	Phase Locked Oscillaor
MATLAB	Matrix Laboratory - mathematical computer programming language
FACTS	Flexible AC Transmission Systems
PWM	Pulse Width Modulation
ABB	Asea Brown Boveri
CMF	Cross-modulation factor

Symbols

f_{fun}	Fundamental frequency
f_{base}	Base frequency
f_{dck}	Equivalent dc side distorting frequency
v_ψ	Instantaneous phase voltage on converter ac terminals
$v_{1\psi}$	Instantaneous fundamental phase voltage on converter ac terminals
Δv_ψ	Instantaneous distorted phase voltage on converter ac terminals
$V_1 \angle \varphi$	Fundamental ac voltage phasor at frequency f_{fun} on the ac side
$V_n \angle \delta_n$	Distorted ac voltage phasor at frequency n on the ac side
i_{dc}	Instantaneous dc current
I_{dc}	DC part of DC current
Δi_{dc}	Instantaneous distorted dc current
$I_k \angle \delta_k$	Distorted dc current phasor at frequency k on the dc side
α	Firing angle
α_o	Average firing angle
$\Delta\alpha$	Distorted firing angle
$\alpha_k \angle \delta_k$	Distorted firing angle phasor at frequency k on the dc side
μ	Commutation period
μ_o	Average commutation period
i_C^{PSS}	PSS ac current
i_C^{PT}	PT ac current
i_C	Commutating current during commutation period
v_{dc}^{PSS}	PSS dc voltage
ϕ_i	Commutation switching instants
θ_i	Firing angle switching instants
F_{ϕ_i}	Commutation switching instant mismatch
Ψ_i	Sampling functions, $i = 1 : 12n$
a_p	Start of sampling function
b_p	End of sampling function
I_A, I_B, I_C	Total ac currents
a	$e^{j\frac{2\pi}{3}}$
I_ψ	Base case ac current
V_{dc}	Base case dc voltage
$\Psi_\psi^{ac\leftarrow ac}$	Analytic sampling function sprectrum, ac current from ac voltage
$\Psi_\psi^{dc\leftarrow ac}$	Analytic sampling function sprectrum, dc voltage from ac voltage
$\Psi_\psi^{dc\leftarrow dc}$	Analytic sampling function sprectrum, dc voltage from dc current
$I_{\psi,SPSS}^{ac\leftarrow ac}$	Base case SPSS ac current spectrum
$I_{\psi,SPT}^{ac\leftarrow ac}$	Base case SPT ac current spectrum
$v_\psi^{dc\leftarrow ac}$	Sampled phase voltage spectrum
$\Delta I_\psi^{ac\leftarrow ac}$	AC current spectrum resulting from Δv_ψ
$\Delta I_{\psi,SPSS}^{ac\leftarrow ac}$	SPSS ac current spectrum resulting from Δv_ψ
$\Delta I_{\psi,SPT}^{ac\leftarrow ac}$	SPT ac current spectrum resulting from Δv_ψ
$\Delta I_\psi^{ac\leftarrow dc}$	AC current spectrum resulting from Δi_{dc}
$\Delta I_{\psi,SPSS}^{ac\leftarrow dc}$	SPSS ac current spectrum resulting from Δi_{dc}
$\Delta I_{\psi,SPT}^{ac\leftarrow dc}$	SPT ac current spectrum resulting from Δi_{dc}
$\Delta V_{SPSS}^{dc\leftarrow ac}$	SPSS dc voltage spectrum resulting from Δv_ψ
$\Delta V_{SPSS}^{dc\leftarrow dc}$	SPSS dc voltage spectrum resulting from Δi_{dc}
ΔV_{SIV}^{dc}	Change in dc voltage spectrum resulting from SIV
$\Delta V_{SIV}^{dc\leftarrow(dc,\alpha)}$	Change in dc voltage spectrum from SIV resulting from Δi_{dc} and $\Delta\alpha$

$\Delta V_{SIV}^{dc \leftarrow ac}$	Change in dc voltage spectrum from SIV resulting from Δv_ψ
$\Delta \Psi_{\psi}^{dc \leftarrow ac}$	Change in sampling function sprectrum resulting from SIV
$b \angle \delta$	Phasor describing the SIV
Y	Sparse admittance matrix
G	Control transfer function
f_{dc}	Resulting dc side frequencies on HVDC link
f_{acpr}	Resulting positive sequence ac side frequencies on HVDC link
f_{acnr}	Resulting negative sequence ac side frequencies on HVDC link
f_{acpi}	Resulting positive sequence ac side frequencies on HVDC link
f_{acni}	Resulting negative sequence ac side frequencies on HVDC link
f_{dck}	DC side distorting frequency
f_{baser}	Fundamental base frequency of rectifier
f_{basei}	Fundamental base frequency of inverter
n_b	Number of frequency bands required for reduced frequency set
f_{comm}	Common frequency between rectifier and inverter

Chapter 1

INTRODUCTION

1.1 GENERAL

Electric power is generated from both renewable and non-renewable resources. As non-renewable resources deplete, a greater emphasis must be placed not only on renewable generation, but also on the increased efficiency and reliability of the transfer of electric power. The current trend towards deregulation and recent technological advances have meant power electronic switching devices are becoming increasingly commonplace within the power system. Such devices increase the efficiency and power transfer capabilities of existing power networks and are becoming common in the conversion of power from small and large scale renewable generation and natural gas plant alike.

The gain in efficiency from using such devices is at times overshadowed by the associated Power Quality (PQ) problems they create. Power quality plays an important role in both the efficiency and reliability of the power system, encompassing a broad range of phenomena including transient stability, voltage stability and steady state waveform distortion [1]. Poor power quality can lead to a variety of different power system problems including the malfunction of system protection, increased electrical stresses on power system components, inaccurate power flow metering, light flicker and the tripping of ripple controlled relays.

HVDC links provide one of the largest sources of steady state waveform distortion on the power system. Though mature, advances in HVDC technology have meant HVDC systems have become increasingly economic and suitable for a wider range of power transfer situations. Since the first commercial link in Gotland, Sweden in 1954, HVDC technology has proliferated to all corners of the world both in developed and developing countries alike. There is now over 50GW of installed capacity with many more links in the planning stage[1]. Not only are HVDC links often more economical over long distance transmission, but they also provide reliable power flow control, added voltage and transient stability, and favourably are able to provide a power transfer between two ac systems of differing frequencies. This last advantage has led to back-to-back HVDC stations where the rectifier and inverter are enclosed within the same building, often without any dc impedance or smoothing inductor. Such schemes provide a strong coupling for the cross-modulation of waveform distortion between the connected ac systems and are similar in nature to the switching devices used in a lot of new renewable energy alternatives becoming available.

This thesis is concerned with the modelling of the steady state cross-modulation of voltage and current waveform distortion through and around HVDC schemes. This is perhaps the least understood of all the HVDC interactions. Although the work contained within this thesis models HVDC only, it is hoped that it may provide a sound basis for the future steady state harmonic and interharmonic modelling of power systems containing many power electronic devices.

[1] See appendix B[2]

1.2 RESEARCH OBJECTIVES

Previous research at the University of Canterbury has greatly influenced, enhanced and directed the work covered in this thesis[3][4][5]. This has allowed a higher base knowledge on the subject area, especially with respect to the modelling of the HVDC converter and link in the harmonic and frequency domains.

To date, the only models capable of accurately modelling the HVDC link harmonic and interharmonic cross-modulation have been time domain simulation models, such as the modular simulation package PSCAD/EMTDC and the harmonic domain model developed by Bathurst[5][6]. Though well established, time domain simulation is computationally slow having to simulate to the steady state, while Bathurst's model, though fast, is complicated, can model interharmonics if multiple cycles are modelled, and provides little insight into the frequency modulating nature of the HVDC link.

Frequency domain models are not new. In general two types of models have been developed; numerical harmonic domain models, such as developed by Smith[4] and Bathurst, which assume the converter is a nonlinear device, and analytic frequency domain models such as that developed by Wood[3] that linearise the converter about an operating point. Both types of model have their respective advantages and disadvantages and both are used within this thesis.

Two main advantages of linearised analytic techniques are: computational speed, especially when multiple perturbations and large systems are concerned, as well as insight acquired from analytic equations. Computational speed is often accompanied by a loss of accuracy. For linearised techniques, the accuracy is dependent on the linearity, or sensitivity of the device to be linearised. Historically, the problems associated with linearised modelling of such devices have not been due to the nonlinearity of the device, but due to various approximations made while trying to describe the complicated switching action of these devices. For the HVDC converter this relates to the complicated effects of waveform distortion on the commutation period and its associated effects on the switching instants. If a small signal analytic model can be defined, then insight provided by the model on the effects of certain variables will help in determining weather certain variables can be ignored or not, this to some extent is the idea behind the simplified modelling concept of chapter 8.

One key objective of this work is to define 'nonlinear' as applied to the HVDC converter while subjected to waveform distortion. Initial investigation using a nonlinear, numerical iterative frequency domain model of the converter has helped achieve this definition and paved the way for an accurate linearised analysis of the converter, and link, in the frequency domain.

The accurate analytic equations derived in this thesis can be solved directly and almost instantaneously for the frequencies of interest. Once a linearised equation set is developed, it can be used for many different studies of various HVDC links topologies. One example is to investigate worst-case scenarios for harmonic and interharmonic cross-modulation.

1.3 THESIS OUTLINE

Chapter 2 identifies the different types of cross-modulation, describes previous reported problem factors thought to influence cross-modulation before a review of previously related work in the field. Finally, a detailed outline of the research contained within this thesis is presented.

Chapter 3 describes an existing harmonic domain model first developed by Smith [7]. This modified version allows multi-cycle modelling, enabling interharmonic transfers to be calculated. At the same time it is a 'cut-down' version of the original model, offering investigation into the converter in isolation only, without ac or dc systems attached.

Chapter 4, investigates and describes the linearity associated with the HVDC converter while subjected to small signal waveform distortion using the iterative harmonic domain model. The results are influential in the further development and refinement of the linearised small signal model of the HVDC converter described in chapter 5.

Chapter 5 describes a new linearised small signal analytic model of the HVDC converter. The model uses a transfer function based approach similar to previous models for the wave shape outside the commutation period, but during the commutation period describes the transfers in terms of a Partial Steady State (PSS), and Partial Transient (PT) component that are added together. The model is the first to fully describe the effects of waveform distortion on the HVDC converter in analytic form. It is considered a true small signal linearisation and is very accurate when the distorting/perturbing source is small.

Chapter 6 describes the Frequency Coupling Matrices (FCMs). These matrices incorporate all frequency cross-coupling associated with the HVDC converter and preserve the inherent phase angle dependence using tensor relationships for the conjugated frequency terms. They are sparse and have a lattice like structure. Assuming linearity and superposition, a system equation describing the coupling between the positive and negative phase sequences and dc is used with the FCMs to describe the full frequency coupling of the converter as a whole. This linear equation set is then converted into nodal form, the time invariant ac and dc systems added and the system then solved. The results of fundamental negative sequence unbalance on the single HVDC converter are validated with the time domain simulation program, PSCAD/EMTDC, giving excellent agreement.

Chapter 7 extends the nodal analysis by writing the full HVDC link nodal equation and solving for various HVDC link case studies, including a modified CIGRE back-to-back scheme working in both synchronous and asynchronous operation. The effects of Switching Instant Variation (SIV) and the inclusion of the characteristic harmonic transfers are shown. Observation of the returned dc voltages around asynchronous links helps derive simple equations that describe a reduced frequency set. This is then used to reduce the memory requirement of the FCMs and is essential for the efficient modelling of the asynchronous HVDC link with small frequency differences in the rectifier and inverter ac systems. All results are validated with PSCAD/EMTDC time domain simulation showing the validity of the proposed method.

Chapter 8, looks at system scenarios that may cause worst-case harmonic and interharmonic cross-modulation. A simplified modelling approach is proposed to help give insight and formulate simple approximate 'rules of thumb' for identifying worst-case scenarios. The simplified approach is validated using multi-perturbation analysis of the full linearised solution method and approximate 'rules of thumb' presented.

Chapter 9 summarises the research described within the thesis and describes the proposed direction for future research and development.

Chapter 2

HARMONIC AND INTERHARMONIC CROSS-MODULATION IN HVDC LINKS

2.1 INTRODUCTION

In this thesis harmonic and interharmonic cross-modulation are terms used to loosely describe a variety of steady state waveform distortion and frequency interactions that occur around the two converters comprising an HVDC link. These interactions are complicated and dependent on many factors of each HVDC converter and their associated ac and dc systems.

It is easiest to first consider the single converter, which by its switching nature modulates a positive sequence three-phase fundamental ac voltage, ensuring a dc voltage is always present on the dc side. This same switching action takes the dc current on the dc side and switches it onto the ac side phases providing a positive sequence fundamental ac side current. The by-product of all this switching action is the generation of the well known characteristic harmonics, principally the ac side currents and dc side voltage [8][1]. The characteristic harmonics are always present and ac filter banks at the ac bus almost always filter these. However, if the HVDC link is operating in an asynchronous manner, then the characteristics on each side of the link are modulated by the same switching action, appearing as non-characteristic frequencies on the opposite side. To complicate things further, waveform distortion within the power system will also be modulated by the switching action, producing a set of different ac and dc system frequencies. The research within this thesis is concerned with the accurate and fast calculation and prediction of these non-characteristic harmonic and interharmonic frequencies. This chapter identifies the types of cross-modulation present in HVDC links, describing several reported cases and discusses modelling techniques. A review of previous models is given, their advantages and shortcomings described, before a brief research outline details the research contained within the thesis.

2.2 TYPES OF HARMONIC AND INTERHARMONIC CROSS-MODULATION

Non-characteristic cross-modulation from one ac system to another is classified into two types;

- Harmonic and interharmonic frequencies on both HVDC converters resulting from the presence of a distorting frequency on one or both ac systems, and,
- Harmonic and interharmonic frequencies on one HVDC converter, resulting from the characteristic frequencies of the other.

[1] Though the characteristic harmonics are well known, it is not well known that they have clearly defined phase sequences. For a 12-pulse converter the harmonics at $12n+1$ are of positive sequence and the harmonics at $12n-1$ are of negative sequence.

These have been designated as *distortion* sourced and *operating point* sourced cross-modulation respectively.

In synchronous HVDC links, distorting frequencies are usually found only at integer harmonics of the power frequency and the cross-modulation can be described as harmonic cross-modulation. This is not true for asynchronous HVDC links. These links have different ac system operating frequencies and cross-modulate with one another causing interharmonic frequencies.

Most HVDC systems operate in asynchronous mode connecting two ac systems of the approximate same operating frequency. Even small shifts in the ac system frequencies will result in some form of interharmonic *operating point* cross-modulation. Asynchronous links used to provide power links between two differing ac system operating frequencies, such as 50-60Hz HVDC links will always have *operating point* sourced cross-modulation.

Distortion sourced cross-modulation is the result of pre-existing distortion, usually on either one or both of the ac systems. This type of cross-modulation can be found on all types of links. The most common form of distortion is caused by asymmetries in the three phase ac transmission systems. This is usually caused by untransposed transmission lines and can be represented in phase sequence form as a fundamental negative sequence unbalance. This unbalance[2] cross modulates with the switching action of the converter resulting always in a positive sequence third harmonic and, for a 12 pulse link, results in the uncharacteristic negative sequence 9th and positive sequence 15th harmonics.

Operating point cross-modulation, is present only in asynchronous HVDC links such as 50-60Hz HVDC links or those links which appear in weak ac systems and experience large enough frequency shifts in one or both ac systems to warrant concern. The back-to-back link operating in Chandrapur, India is an example of such a link connecting two widely varying ac system frequencies [9]. In this scheme the filters have been designed for a fundamental frequency shift between 48.5Hz to 50.5Hz [10]. Interharmonic studies for such systems require a range of fundamental operating conditions and frequencies to be considered. Such schemes may excite subsynchronous oscillations in turbine generator rotor shafts, though there have been no documented cases of this.

2.3 REPORTED PROBLEMS

On occasions harmonic and interharmonic frequencies have been reported to have caused problems such as protection and hot water ripple relay circuits tripping, telephone interference, localised heating and consequent failure of various power system components. Several such cases include:

- Commissioning of the New Zealand HVDC link. Negative sequence unbalance, a result of untransposed transmission lines caused problems in the form of telephone interference and the tripping of various hot water ripple control relays. The problem was mainly associated with a 9th harmonic which was subsequently filtered [11].

- The Russia–Finland Vyborg back-to-back DC interconnection has experienced third harmonic, most likely due to negative sequence unbalance [12].

- The Kristiansand station of the Skagerrak HVDC transmission link between Denmark and Norway experienced low order harmonic distortion causing tripping of both transmission lines and transformers by overload protection. The causes have been identified as the result of a positive sequence third harmonic, and the result of transformer core saturation from

[2] Although strictly speaking, this is not a distortion, it is a deviation from ideal operating conditions, and can be treated in the same way as other waveform distortion.

a fundamental component on the dc line. The third harmonic was identified as the result of the switching action caused from negative sequence fundamental unbalance as well as a parallel ac network resonance tuned to the third harmonic. This situation was avoided by tripping a filter bank, detuning the ac system resonance, when required [13].

- Geomagnetically Induced Currents (GIC) on the Quebec-New England link caused an unexplained resonance due to transformer core saturation. This was later explained using a simplified and linearised transfer function analysis of the HVDC converter to calculate its impedance [14].

- As discussed in the introduction the back-to-back link operating in Chandrapur, India is an asynchronous HVDC link that is thought will consistently have nuisance operating point interharmonics [9] [10]. It is possible that such schemes may excite subsynchronous oscillations.

- Harmonic instability has been reported in the Swiss rail system and led to some very interesting research by the Department of Automatic control at the Lund Institute of Technology [15]. Though not an HVDC system, many of the techniques used in their research of the rail system are similar to that used for the time-variant modelling on the HVDC link in this thesis.

- Recently, turbine-generator rotor shaft vibrations have been reported on a Norwegian oil platform [16]. The cause has been detected as two 7MW variable speed drives (VSD) running compressors. The VSD drives are effectively 12-pulse back-to-back current sourced HVDC links attached to large synchronous motors. After extensive time domain analysis it was found that the cause was primarily due to interharmonic currents from the VSDs at certain motor operating frequencies. The problem was partially mitigated by increasing the rotor diameter of the VSD. This interesting case is a good example of the nuisance effects of interharmonics.

2.4 OTHER APPLICATIONS OF THIS ANALYSIS

As reported above, HVDC is not the only candidate for the analysis used within this thesis. The techniques can be used on a variety of power electronic devices for harmonic and interharmonic analysis. However, before embarking on this type of analysis it is wise to investigate weather the device in question is linearisable or not.

2.5 FACTORS INFLUENCING HARMONIC AND INTERHARMONIC CROSS-MODULATION

There are many factors that influence the magnitude of harmonic and interharmonic cross-modulation around HVDC links. Of these the most important have generally been thought to be the power system strength, or its short circuit capacity. The interaction between ac and dc systems is increased when the ac system is weak or has a low short circuit ratio (SCR). The SCR is derived at the fundamental frequency and hence many other interactions at other frequencies are ignored. However, if low SCRs are present then it is likely the ac systems will be of higher impedance and more likely susceptible to frequency shifts and harmonic and interharmonic problems associated with cross-modulation.

The impedance of the ac and dc systems is important at all frequencies of interest for any particular system distortion. Due to the time varying nature of the converter and link, many frequencies are involved and many impedances and hence frequency interactions must be considered.

Back-to-back links without dc side harmonic smoothing inductors represent the most significant case for harmonic and interharmonic cross-modulation to occur. It has been found that the effective dc side impedance of each converter can be estimated as a scaled sum of the positive and negative sequence impedance of the ac system and the converter transformers [3][17]. This impedance appears mainly inductive at most frequencies but is influenced by ac resonance conditions at lower frequencies[18]. This fact, and the fact that there is no dc line have led to the development of back-to-back schemes without the need for smoothing reactors to limit the dc side harmonics. In most cases this is fine, however resonant conditions in the ac systems are a cause for concern and it is possible that harmonic and interharmonic cross-modulation can be exacerbated under certain ac system conditions.

Many other factors such as the total ac and dc side impedance (including filters), the operating point and pulse number of the link are also of importance. The effects of these are not well known and chapter 8 of this thesis helps address and identify some of the likely problem scenarios.

2.6 MODELLING HARMONIC AND INTERHARMONICS IN HVDC CONVERTERS AND LINKS

To model harmonic and interharmonic interaction, fast and accurate solution methods that provide insight and understanding to the likely problems are required. Time domain simulation, though widely used, is generally too slow and requires many case studies to be looked at. However, the use of time domain simulation, though limited in the field of harmonic and interharmonic analysis, provides an accurate validated benchmark [19][20] which has been used in this thesis to not only provide operating point conditions, but also for comparisons with the frequency domain techniques developed.

Frequency domain methods on the other hand offer a much broader range of investigative techniques and are many orders of magnitude faster than equivalent time domain simulations. Many frequency domain models of the HVDC converter have been presented in the literature. It is not intended to describe all of them but to reference those that are important to the models, techniques and procedures used within this thesis. In the short history of frequency domain modelling of HVDC converters and links, two different approaches have been taken: *iterative frequency domain modelling*, which assumes the HVDC converter and link are non linear, and *direct frequency domain modelling*, which assumes the converter and link can be linearised about a base operating point. Both techniques have been used with success, and both have their respective advantages and disadvantages. To understand the difference in these techniques one must first understand the operating principle of the device being modelled, in this case the HVDC converter.

The HVDC converter is *nonlinear time-variant*, exhibiting characteristics such as frequency coupling and phase angle dependence. Non-linearity is caused by the dependence of the switching instants, and hence transfer of distortion on the magnitude of the applied distortion[3]. Time-variance is caused by the switching action or modulation process and means that any applied distorting frequency (perturbation) will result in a returned frequency spectrum. If a device has fixed switching instants, such as a STATCOM with a fixed firing angle, then the device can be described as *linear time-variant*.

Accurate linear steady state solutions of networks including power electronic circuits must incorporate frequency coupling and phase angle dependence. Frequency coupling means that a single frequency will generate a multitude of other frequencies while phase angle dependence is a result of time-variance and can be best understood by considering the modulation of a distortion by the device switching action, or in simple mathematical terms the multiplication of two sinusoids.

[3]See chapter 4.

The result of this modulation is the generation of sum and difference frequencies where the relative phase angles are subjected to the same sum and difference process. The summed frequencies have a phase angle that is directly related to the phase angle of the applied distortion, and the relationship can be described with a complex number. However, the difference frequencies have an angle related to the negative of the phase angle of the applied distortion, or its complex conjugate.

Frequency coupling can be modelled in a linear manner using time variant matrix transfers where the position of each element within the matrix relates the frequency conversion (transfer) from one frequency to another. This technique is relatively new but has recently been used by various researchers using various terminologies over the last few years. Several common terms include the Harmonic or Frequency Transfer Matrix and the Frequency Coupling Matrix (HTM,FTM,FCM). In this thesis they are termed Frequency Coupling Matrices (FCMs). A noteworthy paper describing these frequency coupling transfers is that by Fauri [21] who used them to describe the frequency coupling inherent in fluorescent lighting. Carbone [22] used them to present a paper for modelling harmonic and interharmonic distortion in multistage conversion systems. This paper demonstrated the fundamentals well but failed to present the actual models used, and no results were given. Recently, Mollerstedt and Bernhardsson used periodic linear time varying theory, developed by Wereley [23], in an excellent article on the harmonic instability caused by diode rectifiers in the electric trains used on the Swiss rail system [15].

The phase angle dependence of the conjugated (difference frequency) terms within the time variant matrix transfers can be either dealt with by allowing frequencies to be negative, or the relationships between the real and imaginary parts of each transfer can be described separately. Usaola [24] did this, and Smith [25] formally described it as a tensor relationship. Complex phasors are written as 2 element column vectors, and they are related by a tensor, a 2×2 matrix. This is easy to implement in linear algebra using real numbers, does not require the use of negative frequencies, correctly describes the phase angle conjugation that is inherent within the modulation process and means the transfer matrices will be square as opposed to rectangular.

As well as being time variant, the HVDC converter is a nonlinear device. This nonlinearity means that the returned spectrum will vary in a nonlinear manner as the magnitude of the applied perturbation changes. It is hence easy to conclude that, as the converter is nonlinear, iterative methods must be used. However, how nonlinear is the converter? This question must be answered before a decision is made on modelling the converter in an iterative or direct manner. In fact, this question must be answered before modelling all power electronic switching devices.

Another important aspect when modelling the power system is system data uncertainty. For example, the exact ac system impedance in a real system can be very hard to model being determined by the physical properties of the transmission lines and transformers etc. Often system databases are incomplete and system data may not be obtainable. It must be remembered that any model can only be as accurate as the data that is used.

Many authors simply state that the device is either linearisable in the small signal sense, or nonlinear and therefore modelled in an iterative manner. This is unfortunate as it is these types of basic initial assumptions that can either lead to vastly over complicated but accurate models, or vastly over simplified inaccurate ones. The fact remains that the converter is a *nonlinear time variant* switching device and should be treated as such. However, for the purpose of which the model is to be used, how nonlinear is the device?

Harmonic and interharmonics tend to be much smaller than the fundamental quantities and it is reasonable to assume that linearised models should give good results. Average results have been reported using direct linearised models, though due to the modelling of the complex commutation process, approximations are always made and no "true" small signal model has yet been developed. On the other hand excellent results have been seen with various iterative models, for example that developed by Smith [7] for the single converter and extended by Bathurst [26]

for the HVDC link. Hence, there are several unknowns that must be answered before a full assault on modelling the HVDC link is attempted. How linear (or nonlinear) is the time-variant HVDC converter for the purpose of the intended model? If linearised, how accurate will the model be?

The following section reviews previous HVDC converter and link models related to the work contained within this thesis, both direct linearised and iterative models are discussed, and their advantages and disadvantages described. Following this is an outline of the research contained within this thesis.

2.6.1 Iterative frequency domain HVDC converter models

A lot of research has been conducted on the iterative modelling of the HVDC converter in the harmonic domain. The harmonic domain is a subset of the frequency domain using iterative methods, like Newton's method, to solve the harmonic interaction around the converter and link. In general these methods solve an effective harmonic load flow using system mismatch equations. Perhaps the most detailed model was that developed by Smith [7][27][28][4] solving system mismatch equations using an iterative multi-variable Newton solution. The solution is very accurate, achieving excellent validation with time domain simulation. A good reference to the work on iterative harmonic analysis is the review paper written by Smith [29]. The work of Smith was later extended by Bathurst who modelled a full array of HVDC link configurations in the harmonic domain [26][5][30][31][32]. Bathurst's model was capable of multi-cycle steady state modelling with base frequencies as low as 1Hz.

Both Bathurst and Smith found that solution was often obtained using only one (sometimes two) Jacobian updates throughout the iterative procedure. The initial Jacobian is a linearisation of the system mismatch equations and if this does not need updating this may prove a good indication that the system may be quite linear. Bathurst did not show the effect of repetitive iterations on the solution variables, this would have been interesting, as it may have provided an early indication of linearity about the converter and link. Despite this, the work carried out by both Smith and Bathurst has influenced the work in this thesis. Chapter 3 presents a simplified version of Smiths original converter model that is used for linear analysis of the converter in the frequency domain in chapters 4 and 5.

2.6.2 Direct linearised HVDC converter models

Small signal linearised models fall into three categories;

- Analytically derived for harmonic and interharmonic analysis
- Analytically derived for control analysis
- Simulation derived for harmonic and interharmonic analysis

Analytically derived models generally use a transfer function based approach or can be obtained from multiple simulations of the device, although this can be a slow process unless a very fast simulation algorithm is available. Both simulation derived and analytically derived models for harmonic and interharmonic analysis are reviewed. Many authors have developed models specifically for control; some of these are applicable to the methods and work developed within this thesis. Notably, there is no single model that stands out and all models developed so far have used various approximations making them easier to derive but not exact in the small signal sense.

Simulation derived, for harmonic analysis

An approach that has seen some popularity is to model the converter in an accurate way, either in the time domain or by an iterative process in the harmonic domain, and then by a series of small signal perturbations gain the cross-coupling relationships between frequencies around the converter. A limited set of these can be used for a specific analysis, and a full set for harmonic analysis. The key to this process is to have a relatively fast converter model, so that the perturbations can be completed in a reasonable time. In the early stages of this research, multi-perturbation runs in PSCAD/EMTDC[4] were used to model the harmonic cross-modulation in HVDC links [33]. However, though an early basis for the work covered in this thesis the computational time required was excessive.

Larsen's HMAT program [34] was the first reported full solution by this process. He used an unspecified numerical converter simulation technique, and performed a large number of simulations to derive a harmonic cross-coupling matrix for a number of converter operating points. The control contribution was explicitly defined. The published verification unfortunately didn't include the full spectrum, with magnitude and phase angle, but did make an investigation into a control-induced instability, which verified the strongest harmonic transfers. Complex numbers were used to interrelate positive frequencies. Larsen also used a system equation, dependent on phase sequence to describe the HVDC converter. This equation is used throughout this thesis.

Analytically derived, for harmonic and interharmonic analysis

All the reported methods are based on a transfer function analysis. Transfer functions, defined in the frequency domain, are used to represent the action of the switches. In the case of an HVDC converter, +1 represents a connection of the ac voltage to the dc side (and the dc current to the ac side), 0 represents no connection, and -1 represents a negative or reversed connection. The operation of a three-phase device can be described by three transfer functions, one for each phase. Using phase shifting, higher pulse number converters can be built up easily. By multiplication of the transfer functions with the voltage on one side or the current on the other, a complete set of spectra around the device can be established.

In 1985 Sakui and Fujita [35] presented a switching function model of a controlled bridge rectifier, extended it to cover an uncontrolled rectifier [36] and then extended it further, by separate consideration of each commutation period to model operation under unbalanced conditions [37]. Although the effect of firing angle variation was not included, these models gave a good prediction for particularly the lower frequency harmonics, and the final paper was a clear recognition that the dynamic variation of the commutation period (and hence switching instants) does significantly affect harmonic transfers across a converter.

In 1992 Hu and Yacamini [38] presented a similar model of an HVDC converter, with a more accurate description of the current commutation process under undistorted conditions. Hu did not include the effect of firing angle variation, and commutation periods were assumed not to vary with the applied distortion. However, the approach was successfully used to predict steady state harmonic levels [39], and proved particularly good at predicting operating point interharmonics present in asynchronous HVDC links [40].

In 1995 Wood and Arrillaga [17] presented an analysis of an HVDC converter that reverted to Sakui's earlier approximation of a linear transfer of current from one phase to the next. However, it wrote equations that linearised the relationship between the applied distortion and the consequent variation of the commutation period. The spectrum associated with this variation, and firing angle variation, was included in the converter switching function. It was shown that

[4]See Appendix C.

dynamic commutation period variation, both from the switching instants and during the commutation periods affects the largest frequency couplings significantly. Although good for lower frequency harmonics, accuracy was quickly lost at higher frequencies due to approximations made in the commutation shape.

In 1998 Osauskas [41] reported a Thyristor Controlled Reactor (TCR) model based on a transfer function analysis. Although the TCR switches do not modulate between AC and DC, a similar approach to that used for HVDC converters was found to be appropriate. The model showed excellent accuracy up to quite high distortion levels and frequencies, and also described the effects of fast variation of the TCR firing angle.

More recently a similar model using the techniques developed in [17] and [41] as well as the work presented in this thesis is that developed by Laird [42] for the single-phase voltage sourced rectifier. Like the 6 pulse HVDC converter, the single-phase converter is *nonlinear time-variant*. The sensitivity or nonlinearity of the single-phase diode rectifier is unclear. The model developed was shown to be accurate for very small distortion magnitudes ($< 0.005pu$) and is good for approximate harmonic and interharmonic distortion analysis but possibly better for small signal transient control analysis. This is perhaps a case where perturbation analysis on either an iterative model or time domain simulation could have better determined the appropriateness of a linearised model.

Analytically derived, for control analysis

For control analyses, the strongest interactions that lead to closed feedback loops can be reduced to a set of three coupled frequencies around a converter that are referred to as the "3-port" transfers [34]. Thus it is important for the model to have the 3-port relationships represented correctly, while transfers to other frequencies are far less critical. Although most of these models were intended for control only, the techniques used are also applicable to the generalised modelling of the HVDC converter for harmonic and interharmonic studies.

In 1970 Persson [43] presented an early and thorough transfer function based analysis of an HVDC link. His model directly described the frequency transfers through a converter using individual phase firing, including an approximation of the effects on the commutation period. The effect of distortion on the firing angle control was modelled exactly in the small signal sense, though Persson and others most likely didn't realise this. The model was expanded to describe a full mono-polar 12-pulse HVDC link, and used to draw Nyquist diagrams for the link for a control analysis. This very noteworthy contribution has been largely overlooked.

In 1974 Sucena-Paiva and Freris [44] simplified the model by assuming equidistant firing, but still incorporated the effect of firing angle variation. This was also used from a control perspective, and considering only the main cross-coupling terms, Nyquist plots were generated, and stability predicted.

In 1995 Wood reduced his transfer function analysis to the strongest interactions, and used the model to describe the frequency dependent impedance of an HVDC converter [45], and composite resonance, a description of the coupling between impedances on both sides of a converter [46]. The model was subsequently used by Chen [47] to describe the mechanism of converter core saturation instability.

Recently Mohaddas [48] published an analysis of the AC side frequency dependent impedance of a STATCOM, based on transfer functions. Excellent agreement with time domain simulation was shown, and although higher frequency harmonics were not predicted, the model was capable of doing so accurately.

The frequency transformations implicit in a modulation process cannot be described using s-domain or state variable analysis directly, but if interactions at other frequencies are referred to

just one frequency, a model can be derived for that frequency. For an HVDC converter, the DC side suits, as a single dominant frequency is involved, associated with two on the AC side.

Todd [49] referred the frequency domain model presented by Wood [17] to the DC side, and fitted an s-domain rational function to the result. He was able to demonstrate a traditional but effective control design, based on the system model.

Simplified linearised converter models have been used to good effect in a number of practical situations. On the Quebec - New England link, an unexplained resonance excited by geomagnetically induced currents and transformer saturation was explained using a simplified and linearised transfer function analysis to calculate the HVDC converter impedance [14]. Stemmler also used a linearised model to design a control system to avoid core saturation instability on a back-to-back link [50].

Recently Mollerstedt and Bernhardsson presented a linearised harmonic transfer function model for a diode converter train. This linear time periodic model, though quite simple, used new LTP techniques, analogous with control techniques of LTI systems. This including a special Nyquist criterion used for LTP systems and was used to estimate the harmonic instability experienced in the Swiss rail system. Several papers have been published on this excellent modelling approach [15][51][52].

2.6.3 HVDC link models

Apart from time domain simulation there is a noticeable lack of published papers on full HVDC links in the frequency domain. The harmonic domain algorithm developed by Bathurst [5] is a full iterative frequency domain method capable of modelling the HVDC link with various control systems. The technique is modular and uses a multi-variable Newton method to solve the system mismatch equations. As the technique is iterative, it is not as fast as direct analytic techniques and also lacks the ability to model asynchronous links of close operating fundamental frequencies, though a 1 second steady state has been achieved. It is also complicated due to the assumption of nonlinearity and it is more of a "black box" description of the system, lacking insight into the mechanisms of waveform distortion interaction.

On the other hand, Hu developed direct frequency domain techniques using linearised transfer functions solving the main interactions about the link [38] [39]. Unfortunately, his model of the converter approximates the commutation period dynamics and the results are only approximate when modelling the distortion sourced interharmonics. Also no phase angle information is presented and it is assumed that phase information is ignored. However, a recent publication modelling the operating point interharmonics on an asynchronous HVDC link shows the resulting interharmonic magnitudes to be extremely good [40]. This indicates that linearised methods are capable of modelling operating point sourced harmonic and interharmonics accurately. Hu's success in modelling the operating point interharmonics is due to the frequencies involved, which are the direct result of the characteristic harmonic transfers. No switching instant variation is involved with these transfers as they are effectively part of the operating point of the link, modelled easily under the assumption that they stay constant. Once again Hu did not present any phase angle data in his results and it is unclear whether phase angles were used in his analysis. If improvements can be made to the existing linearised HVDC converter modelling techniques, and linear time variant frequency techniques used correctly, it is hoped that the accuracy of direct linearised calculation of the harmonic and interharmonic waveform distortion can be improved. The following section gives as brief outline of the research contained within this thesis.

2.7 RESEARCH OUTLINE

There exists little or no information on the nonlinearity of the HVDC converter in the literature. Even an explanation of the converter linearity/nonlinearity is lacking. Many authors assume time variance implies nonlinearity, however this is not necessarily the case. To decide whether iterative or direct linearisation is required a thorough investigation into the converter linearity must be undertaken. With this in mind chapter 3 presents a complete iterative frequency domain model of the HVDC converter, assuming the converter is nonlinear. The model derives mismatch equations that describe the switching instants. These equations are then solved using a single variable Newton iteration. The model is based on that developed by Smith, but is 'cut-down' representing the converter in isolation with no ac or dc systems. This model is then used in chapter 4 to investigate both the nonlinearity associated with the converter and the switching dynamics of the converter when various small signal waveform perturbations are applied to its terminals. The observation of the converter under small signal waveform distortion has lead to an enhanced understanding of the commutation period dynamics and switching instant variation. The promising results of chapter 4 lead to chapter 5 where a complete linearised small signal HVDC converter model is developed. This model is a small signal linearisation that is very accurate for small signal distortion. As analytic equations are used to derive the transfers, the calculation is direct and extremely fast.

Up until chapter 6, the research is concentrated on the modelling of the single HVDC converter in isolation from external ac and dc systems. Chapter 6 describes the methods used to model the converter embedded within a power system. The methods are relatively straightforward so long as linear time variant techniques are used correctly. First, time variant matrix transfers and tensor elements are used to describe the frequency coupling and phase angle dependence associated with the various HVDC converter transfers. These are then combined using system equations dependent on the sequence modulating nature of the HVDC link and can be rearranged accordingly so that the full system can be combined with the associated ac and dc systems. This is achieved using Larsen's equation and simple nodal solution methods forming the system time variant admittance matrix. This is then solved for the known and unknown distortions about the system.

Chapter 7 extends the time variant modelling to the HVDC link. Advances are made for the modelling of asynchronous links with the inclusion of the characteristic harmonics to model the operating point interharmonic cross-modulation. To avoid large matrices a reduced frequency set is proposed, reducing memory requirements and making matrix inversion much faster. The reduced technique allows any asynchronous HVDC link to be modelled with similar memory requirements of normal synchronous link operation. The techniques are demonstrated with excellent validation with PSCAD/EMTDC time domain simulation. Finally, chapter 8 reduces the complexity of the transfers down to the main transfers, investigating the conditions where harmonic and interharmonic cross-modulation may be exacerbated by both operating point conditions and different system impedances.

Chapter 3

ITERATIVE FREQUENCY DOMAIN MODELLING OF A 6 PULSE HVDC CONVERTER

3.1 INTRODUCTION

There have been two distinct approaches to the steady state modelling of the 6 pulse HVDC converter in the frequency domain. The first assumes the converter is nonlinear, solving the harmonic and interharmonic interaction using iterative methods. The second assumes the converter is linear, or at least linearisable, solving the interharmonic interaction directly by linearising about the base case operating point. Both methods have their individual advantages and disadvantages and these have been discussed in the previous chapter.

This chapter accepts that the current sourced 6 pulse HVDC converter is nonlinear, and hence a detailed description is given of an iterative frequency domain model. The model is based closely to that first developed by Smith [7] but is simplified, assuming strong ac and dc systems, and only a single distorting source. The model is validated against time domain simulation and used further in chapter 4 to assess the converter linearity as well as the commutation period dynamics for small signal distortion levels.

3.1.1 The HVDC converter in isolation

In the following three chapters the current sourced 6 pulse HVDC converter is considered in isolation, with only a fundamental ac voltage source on the ac side and a constant dc side current source on the dc side and any single arbitrary, ac side voltage or dc side current, distorting frequency source present. This isolates the nonlinear switching action of the converter from the associated effects of the ac and dc system impedances.

Under ideal conditions with no applied distorting source, the operating point of the converter is defined using the fundamental ac terminal voltage, the dc side current and the average firing angle. These quantities define the average commutation period which remains constant so long as no external distortion is applied to the converter terminals. However, under distorted operating conditions, the switching instants vary, affecting the average commutation period and hence operating point. This behaviour is inherently nonlinear as the distortion causes an operating point change and hence a change in the converter transfers. This chapter describes a full HVDC converter model using iterative methods which can model this non-linear behaviour. Chapter 4 proceeds to investigate the non-linearity using the model described in this chapter.

The current sourced 6 pulse HVDC converter can be thought of as a frequency modulator which transfers an ac voltage to dc voltage and a dc current to ac current via the characteristic switching transfers. The normal switching action of the converter switches the fundamental positive sequence ac voltage and dc side current, producing characteristic harmonics on the dc voltage and ac current respectively. The dc side voltage characteristic harmonics are produced

at frequencies $6n_g n f_{fun}$, where f_{fun} is the fundamental frequency, n_g the number of phase-shifted six pulse groups in series and n is any positive integer. The ac side current characteristic harmonics are sequence dependent and are at frequencies $6n_g n f_{fun} + f_{fun}$ and $6n_g n f_{fun} - f_{fun}$ in positive and negative sequence respectively. Interestingly, the power conversion process of the converter occurs when $n = 0$, here the dc voltage is at dc, the positive sequence current is at f_{fun} and the negative sequence is at $-f_{fun}$ or effectively at a positive sequence f_{fun} in positive sequence.

When a known arbitrary distorting frequency (perturbation) is applied to the ac side voltage, the converter modulates the perturbation to not only the dc side voltage but also to the ac side currents. As the ac and dc systems are assumed infinitely strong, the ac side voltages and dc side current are not affected by the returned frequencies of the converter, remaining at their fundamental values. When '*in situ*' within the power system the change in the fundamental ac side current and dc, dc side voltage will cause the operating point to change. This effect is ignored in this chapter. However, the following chapter investigates the effects of the likely operating point change by observing the change associated in the characteristic harmonic ac currents and dc voltage while the converter is under the effects of applied distortion.

The 6 pulse HVDC converter is a three-phase device (and is modelled this way in this chapter) it switches positive and negative sequence distortion in opposite ways. Both Larsen [34] and Wood [17] recognised this and used it to their advantage in their respective models. The converter is also insensitive to zero sequence components so these need not be considered.

The converter can be thought of as an input/output device. If no distortion is present, the input sources consist of the fundamental positive sequence ac voltage, the dc current and the firing angle, all of which define the converter operating point. If a distortion is present, in the form of a known perturbation of arbitrary frequency, then these are also included in the input. The outputs consist of the resulting ac current and dc voltage spectra. If no distortion is present, the output spectra of both the ac current and dc voltage consist of the characteristic (base case) harmonics. However, if some distortion, or perturbation, is present then the outputs consist of the characteristic harmonics plus other frequencies resulting from the modulation of the applied distortion with the characteristic frequencies. Figure 3.1 shows the input sources (ΔV_{acp},ΔV_{acn},ΔI_{dc} and $\Delta\alpha$) and the resulting outputs (ΔI_{acp},ΔI_{acn} and ΔV_{dc}).

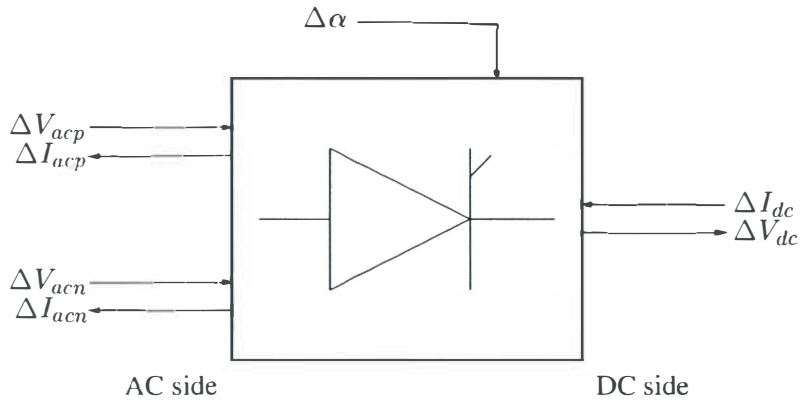

Figure 3.1 Inputs and outputs of the single HVDC converter in isolation.

The convolution of the characteristic harmonic spectrum with an applied distorting source results in what are termed the first order frequencies. These frequencies are described in row 1 of table 3.1[1] for any dc side frequency distortion f_{dck}. The term order is used here to describe the

[1] This table gives the returned frequencies for a frequency distortion f_{dck} on the DC side. To find the returned frequencies from an AC side distortion the equivalent DC side distorting frequency must be found. For a positive

number of frequency shifts associated with the returned spectrum resulting from the applied distorting frequency, f_{dck}.

Order	DC side	AC side	
		Positive Sequence	Negative Sequence
1^{st}	f_{dck} ⋮ $6n_g n f_{fun} \pm f_{dck}$	$f_{dck}+f_{fun}$ ⋮ $(6n_g n f_{fun}+f_{fun})\pm f_{dck}$	$f_{dck}-f_{fun}$ ⋮ $(6n_g n f_{fun}-f_{fun})\pm f_{dck}$
2^{nd}	f_{dck} ⋮ $(6n_g n f_{fun} \pm f_{dck})\pm f_{dck}$	$(f_{dck}+f_{fun})\pm f_{dck}$ ⋮ $((6n_g n f_{fun}+f_{fun})\pm f_{dck})\pm f_{dck}$	$(f_{dck}-f_{fun})\pm f_{dck}$ ⋮ $((6n_g n f_{fun}-f_{fun})\pm f_{dck})\pm f_{dck}$
3^{rd}	f_{dck} ⋮ $((6n_g n f_{fun} \pm f_{dck})\pm f_{dck})\pm f_{dck}$	$((f_{dck}+f_{fun})\pm f_{dck})\pm f_{dck}$ ⋮ $(((6n_g n f_{fun}+f_{fun})\pm f_{dck})\pm f_{dck})\pm f_{dck}$	$((f_{dck}-f_{fun})\pm f_{dck})\pm f_{dck}$ ⋮ $(((6n_g n f_{fun}-f_{fun})\pm f_{dck})\pm f_{dck})\pm f_{dck}$
⋮	⋮	⋮	⋮

Table 3.1 Returned frequencies for a single $n_g \times 6$ pulse HVDC converter in isolation, resulting from a distorting frequency f_{dck} on the dc side, where n=1,2,3 .... This table was developed from use of the iterative frequency domain model and the PDM spectrum derived in appendix E.

In the harmonic and frequency domains it is easiest to scale by the fundamental frequency f_{fun} of the converter. If the harmonic number of the returned frequencies is required, then the resulting frequencies in table 3.1 must be divided by f_{fun}.

There is a secondary effect of the applied distortion. This is the resulting effect of distortion on the variation of the switching angles. This variation affects the first order terms and produces higher order terms at frequencies that are shown in rows 2 and 3 of table 3.1. This effect contains non-linear terms altering the characteristic harmonics and hence operating point. Primitive models of the HVDC converter ignore the effects of the distortion on the switching instants, however Wood [3] showed that the effects of Switching Instant Variation (SIV) are important and for a full model this must be included. The model developed in this chapter is capable of determining the exact switching instants, and hence the higher order frequencies using an iterative solution method. Hence, using this model, the non-linearity of the converter is examined in more detail in chapter 4.

3.2 THE ITERATIVE FREQUENCY DOMAIN MODEL

The model described in this chapter has been developed specifically for harmonic and inter-harmonic perturbation studies and analysis of the converter nonlinearity and commutation period dynamics. It is a simplified version of Smiths [7] harmonic domain model, assuming nonlinearity when solving the switching instants, but considers the converter in isolation from ac and dc system impedances. This makes the model less complex, and computationally faster. In addition to the Smith model two main extensions are also employed, multi-cycle modelling for interharmonic studies and, predetermined frequency selection used for computational speed increases in the convolution process. Multi-cycle modelling refers to modelling the converter for longer than one fundamental period. This means interharmonic frequencies can be modelled, ie, at 10Hz intervals if five fundamental cycles are modelled. Hence the term 'iterative frequency domain' rather than harmonic domain is used.

sequence distortion it is the *AC distortion frequency* $- f_{fun}$, and for a negative sequence distortion it is the *AC distortion frequency* $+ f_{fun}$, where f_{fun} is the fundamental frequency. Note also, that if a returned frequency for an ac current is negative then it is positive in the reverse sequence.

When the 6 pulse HVDC converter, in isolation, is thought of as a frequency modulator, the returned frequencies and their order can be easily predicted using simple modulation theory. The returned frequencies from a single frequency perturbation are shown in table 3.1. Predetermined frequency selection can be used under the assumption that the converter terminal voltage and dc current are known in advance. Hence, for perturbation studies of the converter (in isolation) the perturbing frequency is known and hence the returned frequencies are also known in advance. This gives a major speed increase in the convolution algorithm, especially when multi-cycle modelling is used.

3.2.1 Definition of base and distorting Sources

The general specification of sources around the HVDC converter is important. The HVDC converter has both base and distorting/perturbing sources, and both must be defined clearly. The ac voltage, dc current, and firing angle of the converter are represented as a combination of a base component and a distorting component,

$$v_\psi = v_{1\psi} + \Delta v_\psi \tag{3.1}$$
$$i_{dc} = I_{dc} + \Delta i_{dc} \tag{3.2}$$
$$\alpha = \alpha_o + \Delta\alpha \tag{3.3}$$

The base components represent a positive sequence fundamental voltage $v_{1\psi}$, defined as,

$$v_{1\psi} = V_1 sin(\omega_o t + \varphi - \psi) \tag{3.4}$$

where φ is the voltage phase angle, and the ψ operator denotes the three phases, A, B, C with angles $0, 120$ and 240 respectively. Also included are the dc value of the dc current (I_{dc}) and average firing angle (α_o) that are both constants. These values define the base operating point of the HVDC converter.

The distorting sources are defined as sinusoids with arbitrary magnitude, frequency, and phase as follows,

$$\Delta v_\psi = V_n sin(n\omega_o t - s\psi + \delta_n) \tag{3.5}$$
$$\Delta i_{dc} = I_k sin(k\omega_o t + \delta_k) \tag{3.6}$$
$$\Delta\alpha = \alpha_k sin(k\omega_o t + \delta_k) \tag{3.7}$$

The ac side distortions are denoted with a frequency $n\omega_o t$, while dc side and firing angle distortions are assigned a frequency $k\omega_o t$, and are in general any real number, s represents the applied sequence of the distorting frequency source Δv_ψ, +1 for positive sequence, and -1 for negative sequence. This is very important as the converter modulates opposing sequences in different ways as previously mentioned and shown in table 3.1. The base and distorting components defined here are also used within the following chapters.

3.2.2 Piecewise linear representation of the HVDC converter

The single 6 pulse HVDC converter passes through 12 switching states each fundamental cycle. The circuit topology of each of these states depends on the switching characteristics of the converter. In the steady state, the order of the switching characteristics is periodic and known for a periodic steady state equal to the fundamental period.

The total number of states that must be modelled depends upon the lowest perturbing (or distorting) frequency. For example, the base frequency for a 50Hz converter with a 10Hz perturbing frequency is 10Hz. Hence, the periodic steady state is achieved every 0.1 seconds or every 12×5

converter states. Likewise, if a 1Hz perturbation is applied then 12×50 states must be modelled over the 1 second periodic steady state. The model described in this chapter is capable of modelling as many states as required to satisfy the lowest distorting frequency source. In general the required number of states is $12n$ where $n = \frac{f_{fun}}{f_{base}}$, f_{fun} and f_{base} being the fundamental and base frequencies respectively.

Of the $12n$ states per base frequency, $6n$ are direct conducting states and $6n$ are commutating states, the converter switching successively between the two different states. Each state can be described as the sum of a steady state response and a transient response of the appropriate linear circuit. As the converter is continually switching, the true steady state is never achieved, hence the steady state and transient responses can be described as the Partial Steady State (PSS) response and the Partial Transient (PT) response. Contreras described these terms as the transient and steady state terms in his fast steady state algorithm [53]. Figure 3.2 shows the direct and commutation states of the HVDC converter, corresponding to the switching table of the converter shown in table 3.2.

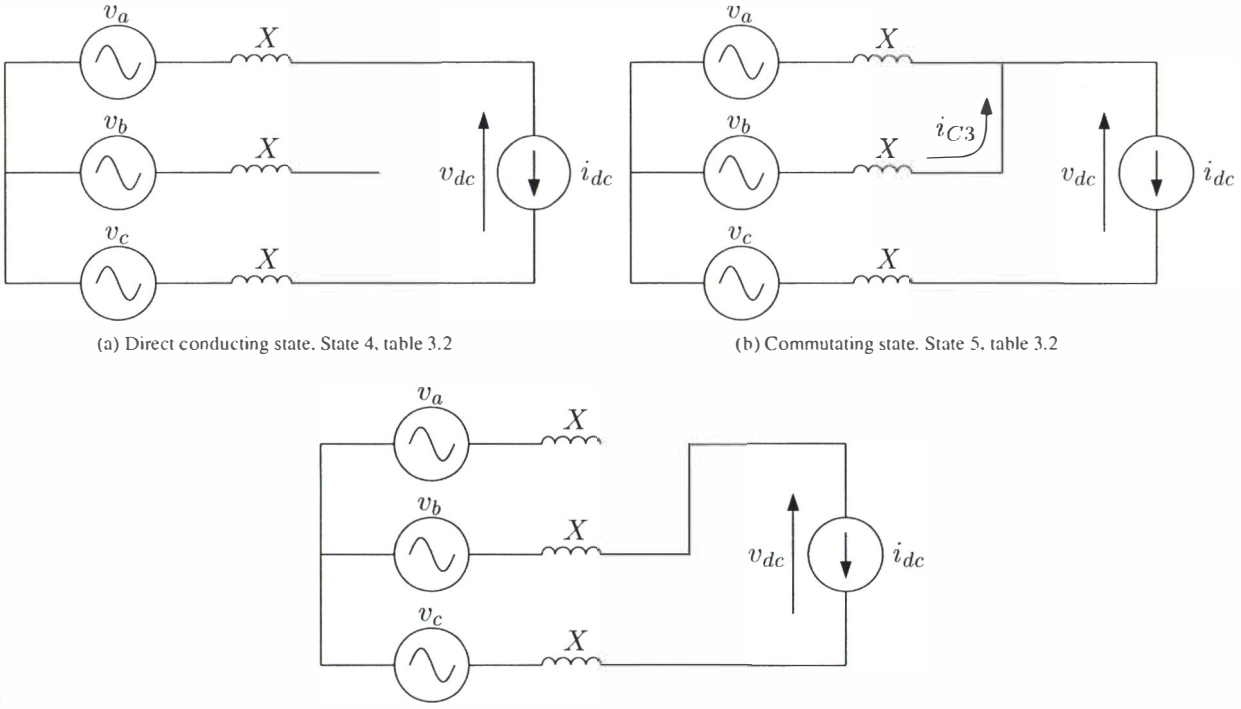

(a) Direct conducting state. State 4, table 3.2

(b) Commutating state. State 5, table 3.2

(c) Direct conducting state. State 6, table 3.2

Figure 3.2 Example circuit for commutation analysis, showing states 4-6.

During a direct conduction state (all even states in table 3.2), the steady and transient responses are achieved instantly and the resulting ac current and dc voltage wave shapes are simply the value of the directly connected source (plus any perturbing source present), figure 3.2(a)(c). During a commutation state (all odd states in table 3.2) the effects of the commutating impedance mean the wave shape has both a PSS response and a PT response, figure 3.2(b).

Each commutating state can be described as the addition of a PSS and PT response. The PSS response is found assuming piecewise linear circuit analysis of the commutating circuit for the particular switching state in question. However, the PT response depends upon the value of impedance being switched, and in particular for the HVDC converter, the resistance in the commutating circuit. The PT response per state is an exponential decay of the general form, $I_o e^{-\frac{R}{L}t}$ where R and L are the values of commutating resistance and inductance and I_o is the initial condition. When R is zero the decay becomes a constant offset dependent solely on

State	Phase Currents			DC Voltage					
	i_A	i_B	i_C	v_B	v_E	v_O	v_+	v_-	eqn.
1	i_{C1}	$-i_{dc}$	$i_{dc} - i_{C1}$	A	C	B	.	.	3.12
2	i_{dc}	$-i_{dc}$	0	.	.	.	A	B	3.13
3	i_{dc}	$-i_{C2} - i_{dc}$	i_{C2}	C	B	A	.	.	3.12
4	i_{dc}	0	$-i_{dc}$	.	.	.	A	C	3.13
5	$i_{dc} - i_{C3}$	$-i_{C3}$	$-i_{dc}$	B	A	C	.	.	3.12
6	0	i_{dc}	$-i_{dc}$	.	.	.	B	C	3.13
7	i_{C4}	i_{dc}	$-i_{C4} - i_{dc}$	A	C	B	.	.	3.12
8	$-i_{dc}$	i_{dc}	0	.	.	.	B	A	3.13
9	$-i_{dc}$	$i_{dc} - i_{C5}$	i_{C5}	C	B	A	.	.	3.12
10	$-i_{dc}$	0	i_{dc}	.	.	.	C	A	3.13
11	$-i_{C6} - i_{dc}$	i_{C6}	i_{dc}	B	A	C	.	.	3.12
12	0	$-i_{dc}$	i_{dc}	.	.	.	C	B	3.13

Table 3.2 Switching pattern for the ac current and dc voltage samples for one fundamental cycle.

the current flowing, I_o, at the firing instant. The model described in this chapter ignores the effects of commutating resistance (and snubbers), modelling the thyristors as ideal switches. This assumption means the PT response is simply some constant offset acting upon each commutating state, each of which is dependent on the initial switching conditions.

The partial steady state ac currents

The partial ac currents during a commutation are found from the summation of the PSS and PT responses for each of the $6n$ commutating states per base period. The PSS commutating currents are found from analysis of the star connected commutating circuit. They are derived as simple sinusoids describing the shape of the commutating current, while the partial transient response is added later to ensure they are offset accordingly. The value of each partial ac current is valid only during the commutation periods and each must be sampled with the appropriate sampling function.

Figure 3.2(b) gives an example of the commutating state. Here, phase a is commutating off while phase b is commutating on. In frequency domain phasor representation, summing the voltages around the commutation loop, including the commutating phases at harmonic multiple h, and solving for the commutating current with respect to figure 3.2 and table 3.2 gives the general PSS ac current magnitude,

$$i_{C_h}^{PSS} = \frac{v_{B_h} - v_{E_h}}{2jhX} \pm \frac{i_{dc_h}}{2} \tag{3.8}$$

where $\pm$ indicates the sign in the cases of positive or negative rail commutations. X is the commutating reactance. For a single perturbation the total PSS commutating current is the summation of the fundamental ($h = 1$) and distorting (h) components, ie,

$$i_C^{PSS} = i_{C_1}^{PSS} + i_{C_h}^{PSS} \tag{3.9}$$

The partial transient ac currents

The offset required to ensure that the PSS commutating current phasors are zero at the firing instant can be modelled as the addition of the PT response. As the commutating impedance is inductive only, the PT is a constant current acting over each of the commutating states. It

is achieved instantaneously when the appropriate thyristor is fired and is simply the negative value of the PSS response at the firing instant. Hence the PT response is a function of the PSS response and the firing instants.

$$i_C^{PT} = -i_{C_1}^{PSS} cos(\theta_i) - i_{C_h}^{PSS} cos(h\theta_i) \tag{3.10}$$

Where, θ_i are the firing instants. As shown, the PT response contains an offset resulting from the fundamental part of the PSS current response as well as an offset resulting from the distorted PSS current response. The total partial commutating current, is the summation of the PSS and PT responses and written as,

$$i_C = i_C^{PSS} + i_C^{PT} \tag{3.11}$$

The partial steady state DC voltages

As the PT response is a constant offset occurring during the commutating state no voltage is induced in the commutating impedance under the assumption of no commutating resistance. Hence, only the PSS response for each of the $12n$ states per base frequency cycle need to be modelled for the DC voltage samples.

The DC voltage during a commutation can be found by summing the voltages around the commutating loop including the DC current source. Analysis of figure 3.2(b) yields the general description of the DC voltage during a commutation,

$$v_{dc_h}^{PSS} = \pm \frac{v_{B_h} + v_{E_h}}{2} \mp v_{O_h} - \frac{3}{2} jhX i_{dc_h} \tag{3.12}$$

During the direct conduction the dc side is connected directly to the ac side via the transformer commutating reactance. From analysis of figure 3.2(a)(c) the dc voltage can be acquired for some dc side harmonic distortion, i_{dc_h}.

$$v_{dc_h}^{PSS} = v_{+_h} - v_{-_h} - 2jhX i_{dc_h} \tag{3.13}$$

Similarly to the AC current PSS, the total DC voltage is the summation of both the fundamental ($h = 1$) and distorting (h) components.

Table 3.2 shows the switching sequence of the phase voltages and how the dc side voltage is related to these through equations 3.12 and 3.13, where v_B and v_E are the phase voltages beginning and ending commutation and v_O the other phase voltage during a commutation state and v_+ and v_- the phase voltages which are connected directly during a direct connecting state.

3.2.3 The firing instants, θ_i

The valve firing depends on two aspects; the firing and converter controllers.

The firing controller consists of an ideal phase locked oscillator (PLO) tracking the fundamental positive sequence power frequency, generating equal-spaced timing references, β. The PLO is assumed unaffected by distortion, having a time constant of similar order as the fundamental. However, in practice lower order frequency distortion can affect the PLO timing references. This is not modelled, however the effect can be later incorporated using additional transfers. Figure 3.3 shows the effect of a large firing angle distortion, $\Delta\alpha_k$ on the firing instants, θ_i. The timing reference lines, degree per degree, are generated by the PLO and are assumed perfectly equidistant, spaced by 60^o. The instant when these intersect the modulated firing angle is the point when firing occurs. This is a nonlinear problem and the point of intersection can be found using an iterative Newton solution that is described in the following section. The nonlinear

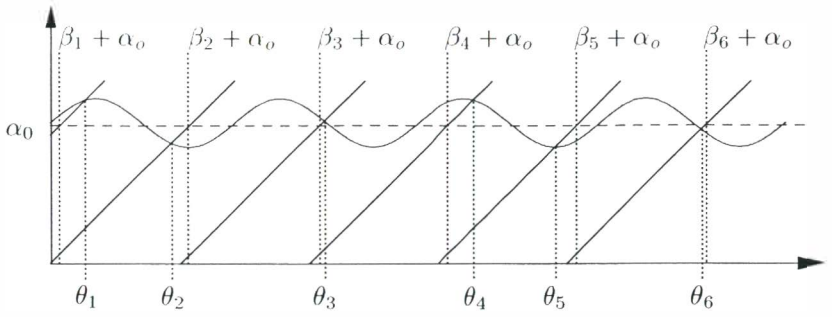

Figure 3.3 Calculation of device turn on's for a controlled converter.

mismatch, F_{θ_i}, is written as,

$$F_{\theta_i} = \beta_i + \alpha_o - \theta_i + \alpha_k sin(k\theta_i) \tag{3.14}$$

where $i = 1 \rightarrow 6n$ for one fundamental frequency cycle. The mismatch, F_{θ_i}, is then solved for zero using the iterative Newton method with some predetermined tolerance as described by equations 3.17 and 3.19 for the end of commutation instants.

This method must be used for the accurate solution of the firing instants. However, as the firing angle modulation tends towards zero ($\alpha_k \rightarrow 0$) the firing instants (θ_i) effectively become the product of a sampled sine wave. In this case a small signal linearisation can be made and the firing instant modulation described in a direct algebraic manner. This is discussed in more detail in chapter 5.

The converter controller can be any number of control transfers that are designed to reduce transient over voltages from either fault or sudden operating point change. These control transfers are dependent on the particular link and their design is often influenced by the strength and impedance of both the ac and dc systems. For the research covered in this thesis the controller is considered as a simple PI control transfer between the dc current and firing angle. Hence, any dc current distortion will affect the firing instants through the PI controller. The controller can be linearised about a base operating point and the effects of the controller added as additional transfer functions, as described further in chapter 6.

3.2.4 The end of commutation instants, ϕ_i

The end of commutation instants are found at the instant the partial ac commutating current, i_C equals the dc current, i_{dc}. This is the instant when the thyristor ceases conduction. The partial ac commutating current is the addition of the partial transient and partial steady state responses. Once the firing instants, θ_i are found the following equation can be written.

$$\begin{aligned} i_C^{PT} + i_C^{PSS} &= i_{dc} \\ \overbrace{-i_{C_1}^{PSS} cos(\theta_i) - i_{C_h}^{PSS} cos(h\theta_i)}^{PT\ response} + \overbrace{i_{C_1}^{PSS} cos(\phi_i) + i_{C_h}^{PSS} cos(h\phi_i)}^{PSS\ response} &= \underbrace{I_{dc} + I_k sin(k\phi_i)}_{DC\ current} \end{aligned} \tag{3.15}$$

Hence, a mismatch equation F_{ϕ_i} can be written, and solved for zero.

$$F_{\phi_i} = -i_{C_1}^{PSS} cos(\theta_i) - i_{C_h}^{PSS} cos(h\theta_i) + i_{C_1}^{PSS} cos(\phi_i) + i_{C_h} cos(h\phi_i) - I_{dc} - I_k sin(k\phi_i) \rightarrow 0 \tag{3.16}$$

where $i = 1 \rightarrow 6n$ for one fundamental frequency cycle. The mismatch, F_{ϕ_i}, is solved using the iterative Newton method, solving for the end of commutation angles, ϕ_i, ie.

$$\phi_{i(N+1)} = \phi_{iN} - \frac{F_{\phi_{iN}}}{\frac{\Delta F_{\phi_{iN}}}{\Delta \phi_{iN}}} \tag{3.17}$$

where, in this case,

$$\frac{\Delta F_{\phi_{iN}}}{\Delta \phi_{iN}} = -i_{C_1}^{PSS} sin(\phi_{iN}) - h\ i_{C_h}^{PSS} sin(h\phi_{iN}) + kI_k cos(k\phi_{iN}) \tag{3.18}$$

where during any solution only either the dc side distortion k is present or an ac side distortion h present. This solution is iterated for increasing $N = 1, 2, 3 \ldots$ until,

$$|\phi_{i(N+1)} - \phi_{iN}| < tol \tag{3.19}$$

Where *tol* is a predetermined switching tolerance and θ_{i1} and ϕ_{i1} are the initial guess at the firing and commutation angles found using the base case operating point conditions.

If the firing instants (θ_i) remain fixed, then the commutation instants (ϕ_i) are all that is required to construct the sampling functions, described in section 3.2.5. Figure 3.4 shows a distorted partial commutation current, i_C. The end of commutation instant (ϕ_i) is solved when this partial commutating current equals the undistorted DC current, I_{dc}.

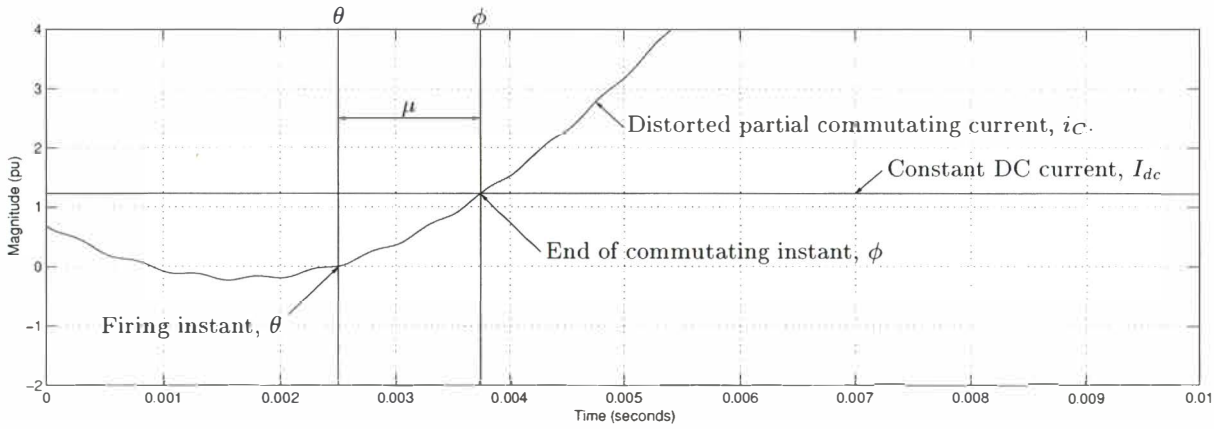

Figure 3.4 Solution of end of commutation.

3.2.5 The sampling functions

To generate a complete ac current and dc voltage spectrum the partial ac currents and dc voltages for each state must be sampled with the appropriate sampling function for that state. This is achieved under the assumption that the converter is piecewise linear. $12n$ sampling functions, of value 1 during their intended interval, are required. The total spectrum is built by adding each of the sampled partial wave shapes together. The bounds of each of the sampling functions are the calculated switching instants, as discussed in the previous sections. These are shown in table 3.3 below. Fourier analysis of each of the rectangular pulses Ψ_{p_k}, of height 1, gives the following complex Euler coefficients at harmonic k,

$$\Psi_{p_k} = \frac{1}{kn\pi}(cos(ka_p) - cos(kb_p)) + j\frac{1}{kn\pi}(sin(kb_p) - sin(ka_p)) \tag{3.20}$$

Sample	Ψ_1	Ψ_2	Ψ_3	Ψ_4	Ψ_5	Ψ_6	Ψ_7	Ψ_8	Ψ_9	Ψ_{10}	Ψ_{11}	...	$\Psi_{12\times n}$
a_p	θ_1	ϕ_1	θ_2	ϕ_2	θ_3	ϕ_3	θ_4	ϕ_4	θ_5	ϕ_5	θ_6	...	$\phi_{6\times n}$
b_p	ϕ_1	θ_2	ϕ_2	θ_3	ϕ_3	θ_4	ϕ_4	θ_5	ϕ_5	θ_6	ϕ_6	...	θ_1

Table 3.3 Limits of converter states.

where,

$$\Psi_{p_0} = \begin{cases} j\frac{b_p - a_p}{2n\pi} & \text{if } b_p > a_p \\ j\left[1 - \frac{a_p - b_p}{2n\pi}\right] & \text{otherwise} \end{cases} \tag{3.21}$$

p is the state and a_p and b_p are the start and end of conduction instants for the particular state, defined in table 3.3 and shown in figure 3.5.

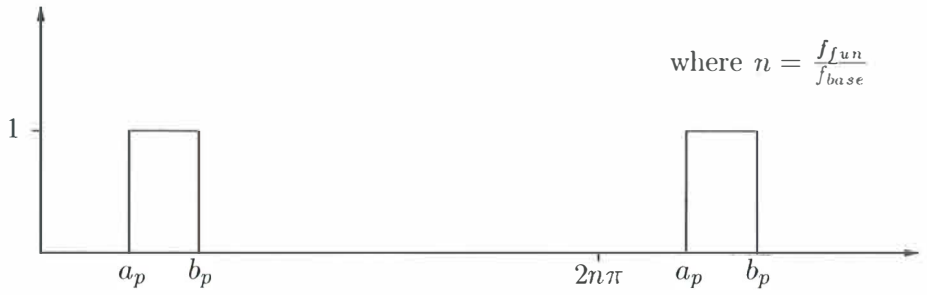

Figure 3.5 Square pulse sampling functions used for convolutions.

3.2.6 Construction of the ac current and dc voltage spectra

The convolution of the correct partial ac current or dc voltage with its required sampling function renders it correct for the required state. This is repeated over all switching instants for the base frequency, each convolved state summed to acquire the ac current and dc voltage wave shape/spectrum for one base frequency cycle.

When two different time domain waveforms of different operating frequencies are multiplied together the result is a set of sum and difference frequencies. Multiplying two sinusoids using the trigonometric identity for the product of sine waves can show this. Smith [7] did this and converted to phasor form to get,

$$A_k \otimes B_l = \begin{cases} \frac{1}{2}j(A_k B_l^*)_{(k-l)} - \frac{1}{2}j(A_k B_l)_{(k+l)} & \text{if } k \geq l \\ \frac{1}{2}j(A_k B_l^*)^*_{(k-l)} - \frac{1}{2}j(A_k B_l)_{(k+l)} & \text{otherwise} \end{cases} \tag{3.22}$$

To avoid negative harmonics the difference term (if k is less than l) is conjugated. This makes the convolution non-analytic, and hence not differentiable in complex number form. However, it avoids the need for negative harmonics. In general, the convolution of a partial wave shape (S) with its sampling function is given as,

$$S \otimes \Psi = \sum_{k=1}^{n_h} \sum_{l=1}^{2n_h} S_k \otimes \Psi_l. \tag{3.23}$$

Here, S may contain any number of known distorting harmonic frequencies from 1 to n_h. Also, as sum and difference harmonics are generated from the convolution, the sampling function spec-

trum (Ψ_l) must be evaluated up to twice the highest frequency (n_h). Substituting equation 3.22 into equation 3.23 and solving for the kth harmonic phasor component gives:

$$(S \otimes \Psi)_k = \begin{cases} \frac{1}{2}j\left[\sum_{l=0}^{n_h} S_l \Psi_l^* - 2S_0\Psi_0\right] & ,k = 0 \\ \frac{1}{2}j\left[\sum_{l=0}^{n_h}(S_l\Psi_{(l+k)}^*)^* - \sum_{l=0}^{k} S_l\Psi_{(k-l)} + \sum_{l=k}^{n_h} S_l\Psi_{(l-k)}^*\right] & ,k > 0 \end{cases} \tag{3.24}$$

This convolution requires all harmonic frequencies from $0 \rightarrow n_h$ to be convolved.

Fast selected frequency convolution

As only one distorting source is present at any one time, the returned frequencies can be easily predicted assuming the converter is operating in the steady state. This means the summation blocks of equation 3.24 need only sum those frequencies of interest.

Table 3.1 shows the returned frequencies around a single HVDC converter for some frequency distortion, f_{dck}, referred to the dc side. The table shows only the first, second and third order frequencies as these are the most significant. However, higher order frequencies exist as well. The algorithm developed generates lists of frequencies, based on table 3.1 which must be calculated for each known applied distortion. It has a built in option of calculating only the first order frequencies, the first and second order frequencies or all frequencies that are returned for a single frequency distortion. This provides a substantial increase in computational time for perturbation studies, particularly when modelling higher pulse number converters and many cycles.

Extension to multi-pulse models

For perturbation studies the extension of the 6 pulse model to higher pulse numbers (assuming series connected) is straightforward under the assumption the interconnecting transformers are balanced. If this is so, then the selected frequency convolution can be used to acquire the relevant harmonics for the pulse number required. Hence, for a 12 pulse series connected converter, table 3.1 with $n = 2$ would be used to generate the required frequencies for convolution.

Construction of the ac current spectrum

When modelling the converter over multiple cycles, reducing the total number of convolutions can create substantial computational time savings. For the construction of the ac current spectrum this can be achieved by using a compound sampling function for the dc current contribution during the direct conduction periods. This reduces the number of convolutions from $8 \times n$ to only n per phase required for the dc contribution to the ac current. These compound sampling functions are shown in equations 3.25 and 3.26 as parts i and vi. During the commutation periods the partial currents contain both the PSS and PT wave shapes. The presence of the PT term means each commutation current is unique, having a different dc offset, over the entire base frequency period.

Knowing the converter switching pattern, the following expressions can written for one fundamental cycle for the ac secondary side phase currents.

$$I_A = i_{dc} \otimes \overbrace{(\Psi_2 + \Psi_3 + \Psi_4 + \Psi_5 - \Psi_8 - \Psi_9 - \Psi_{10} - \Psi_{11})}^{i} + \underbrace{i_{c_1} \otimes \Psi_1}_{ii} - \underbrace{i_{c_3} \otimes \Psi_5}_{iii} - \underbrace{i_{c_4} \otimes \Psi_7}_{iv} + \underbrace{i_{c_6} \otimes \Psi_{11}}_{v} \quad (3.25)$$

Similarly the phase b and c currents can be written as.

$$I_B = i_{dc} \otimes \overbrace{(\Psi_6 + \Psi_7 + \Psi_8 + \Psi_9 - \Psi_{12} - \Psi_1 - \Psi_2 - \Psi_3)}^{vi} + \underbrace{i_{c_2} \otimes \Psi_3}_{vii} - \underbrace{i_{c_3} \otimes \Psi_5}_{iii} - \underbrace{i_{c_5} \otimes \Psi_9}_{viii} + \underbrace{i_{c_6} \otimes \Psi_{11}}_{v} \quad (3.26)$$

$$I_C = -I_A - I_B \quad (3.27)$$

The third phase, equation 3.27, is always the negative sum of the first two, as there is no path for zero sequence. As shown, eight convolutions, $i \rightarrow viii$, are all that is required to obtain all three phase currents when the base frequency equals the fundamental. Table 3.4 shows the number of states and required convolutions for the ac currents when the base frequency is less than the fundamental. The total required number of convolutions is half the total states plus 2.

$f_{base}(Hz)$	Total no. of states	Ph. A conv.	Ph. B conv.	Total convolutions
50	12	5	3	8
10	60	21	11	32
2	300	101	51	152
1	600	201	101	302
0.1	6000	2001	1001	3002

Table 3.4 Required number of states and convolutions for the ac current with different base frequencies, f_{base}.

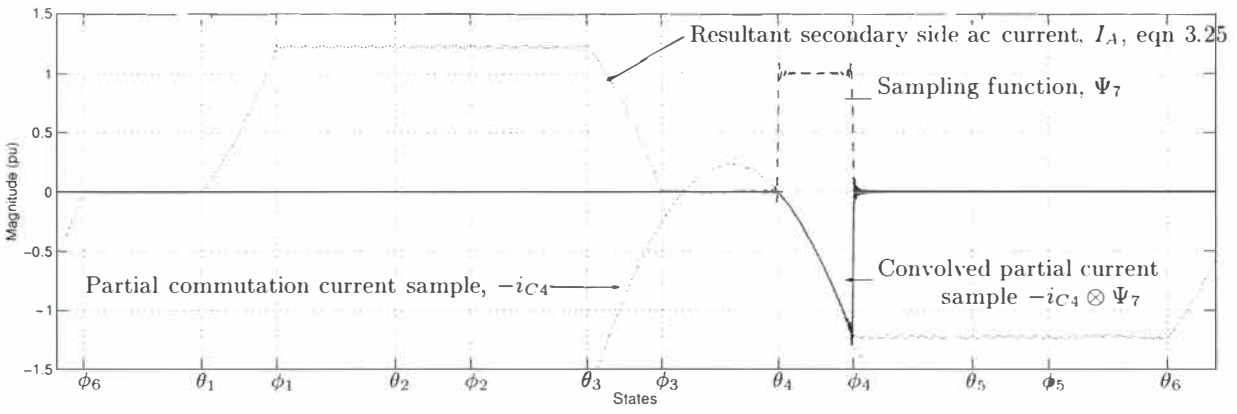

Figure 3.6 Convolution of one state for the ac current.

Figure 3.6 shows the time domain representation of the converter phase a current with the states of table 3.3 shown on the x-axis. The single convolution $-i_{c4} \otimes \Psi_7$ of equation 3.25 is shown.

Extension to phase sequence model

The three phase ac currents can be easily converted into sequence components using the following transformation matrix.

$$\begin{bmatrix} i_z \\ i_p \\ i_n \end{bmatrix} = \begin{bmatrix} 1 & 1 & 1 \\ 1 & a & a^2 \\ 1 & a^2 & a \end{bmatrix} \begin{bmatrix} i_a \\ i_b \\ i_c \end{bmatrix} \tag{3.28}$$

where, $a = e^{j\frac{2\pi}{3}}$.

Construction of the dc voltage spectrum

Equations 3.12 to 3.13 and table 3.2 are used to write the PSS dc voltage for each state. Figure 3.7 shows the convolution of a single partial voltage, v_{dc}^{PSS} with its appropriate sampling function, Ψ_1.

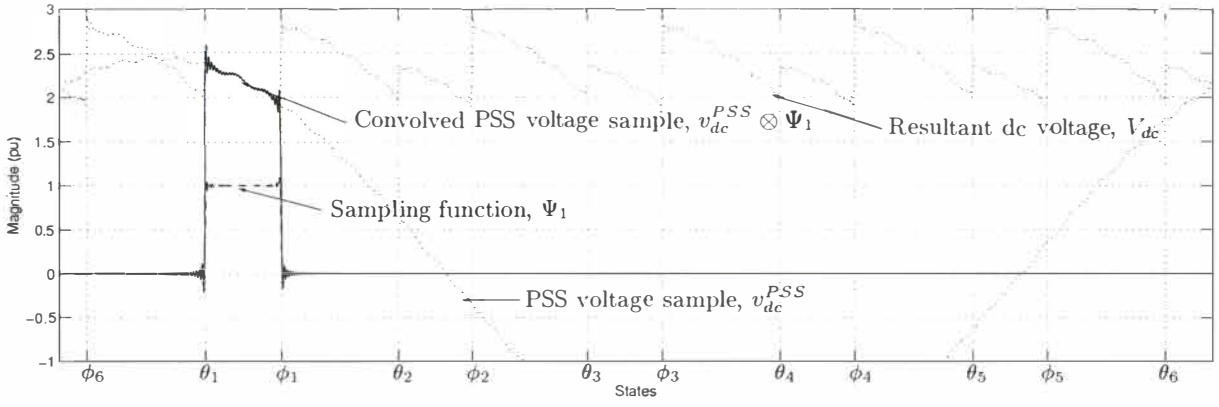

Figure 3.7 Convolution of one state for the dc voltage.

The partial transients have been described as a constant current, acting during the commutation period and satisfying the thyristor firing instants. Each of the $12n$ partial ac currents includes an additional PT response, making each of them unique over the $12n$ states. For the transfer to dc voltage, the PT response has no effect under the assumption that the commutating impedance is purely inductive. Hence, the partial dc voltages are described by only the PSS response of the commutating circuit, being the same for each of the n fundamental cycles modelled. Only 12 PSS responses are therefore required, independent of the number of cycles modelled.

Although only 12 PSS responses are required, each must be sampled n times. This is achieved by using 12 compounded sampling functions containing n single sampling functions per base frequency cycle. Though only 12 compound sampling functions are required they are unique in that each of the single sampling functions used to build the compound sampling function are of varying width dependent upon the switching instants, the switching instants being unique over the base frequency period. This is a very important observation as only 12 convolutions are ever required to construct the dc voltage spectrum, giving a significant computational speed increase.

3.2.7 Time domain comparison for a highly distorted system

To validate the iterative frequency domain model described in this chapter, a comparison is made with the PSCAD/EMTDC time domain simulation program. The standard 12 pulse CIGRE rectifier, described in appendix D, is used as a test case, with reduced snubbers. The rectifier is

in isolation from ac and dc system impedances, having a 345kV fundamental ac voltage source on the ac side and a 2kA (1.22pu) dc current source on the dc side with a constant firing angle of 15^o. In PSCAD the system is simulated with a time step of $10\mu S$ and allowed to settle for 2 seconds before a large 120Hz dc side current distortion (0.15pu) is applied. The system is then allowed to settle for a further second before the ac current and dc voltage time domain data are recorded for five fundamental cycles, or 0.1 seconds. The Fast Fourier Transform (FFT) is then applied to the time domain data and the results compared.

The non-harmonic frequency means the converter base frequency must be the lowest common denominator between $120Hz$ and $50Hz$. This is the lowest frequency which gives the periodic steady state and means a base frequency of $f_{base} = 10Hz$ must be used. Hence the iterative frequency domain model must model five fundamental cycles, or 60 states for a six pulse converter. As the CIGRE converter is a 12 pulse converter only those frequencies associated with the 12 pulse series connected converter are calculated. As the pulse number and distorting frequency are known, the returned interharmonic frequencies, and their order can be predetermined using table 3.1 and are given in table 3.5. Figures 3.8 and 3.9 show the excellent agreement obtained

	Returned frequencies (Hz)		
Order	DC side	AC side positive sequence	AC side negative sequence
Characteristics	0,600,1200,1800 ...	50,650,1250,1850 ...	550,1150,1750,2350 ...
1st Order	120,480,720,1080 ...	170,530,770,1130 ...	70,430,670,1030,1270 ...
2nd Order	0,240,360,600,840,960,1200 ...	50,290,410,650,890,1010,1250 ...	190,310,550,790,910,1150 ...

Table 3.5 Returned frequencies from a 120Hz dc side current distortion on a 12 pulse rectifier.

with time domain simulation.

3.3 CONCLUSIONS

An iterative frequency domain model, based on that developed by Smith has been described. The model is a simplified version of Smith's full iterative model assuming known ac side voltage and dc side current. The state representation of the switching process is described in terms of the Partial Steady State (PSS) response and Partial Transient (PT) response. This is a generalised description that can also be used for other power electronic switching devices and is used further in the development of an analytic model of the converter in chapter 5. The assumption of negligible commutating resistance and no snubbers is assumed adequate and it is acknowledged that this simplifies the commutation process. Several extensions have also been included to the basic Smith model, including multi-cycle modelling, so interharmonics can be modelled, and selected frequency convolution to help speed solution time. The model can be extended to higher pulse numbers very easily under the assumption that the connecting transformers are balanced.

Comparison of a large 0.15pu dc current distortion at an arbitrary frequency of 120Hz gives excellent agreement with the time domain simulation.

The model described here is used in the following chapter to help determine the linearity of the converter and investigate the commutation process for small signal distortions. This analysis leads to the development of the full analytic converter model described in chapter 5.

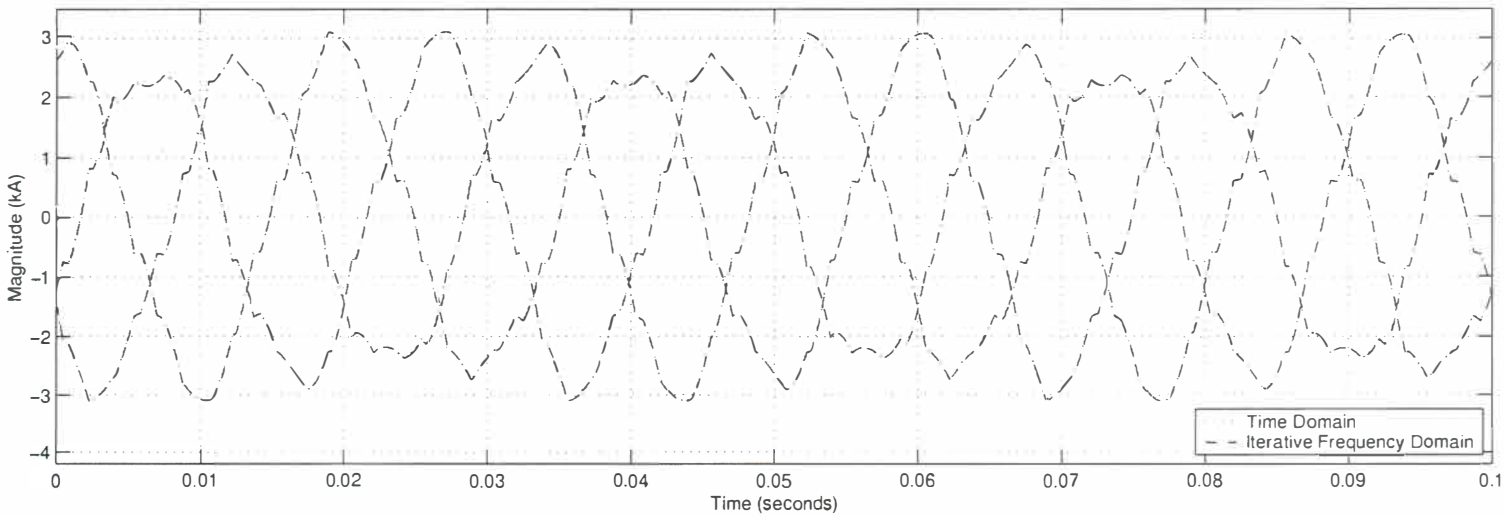

(a) AC current time domain comparison.

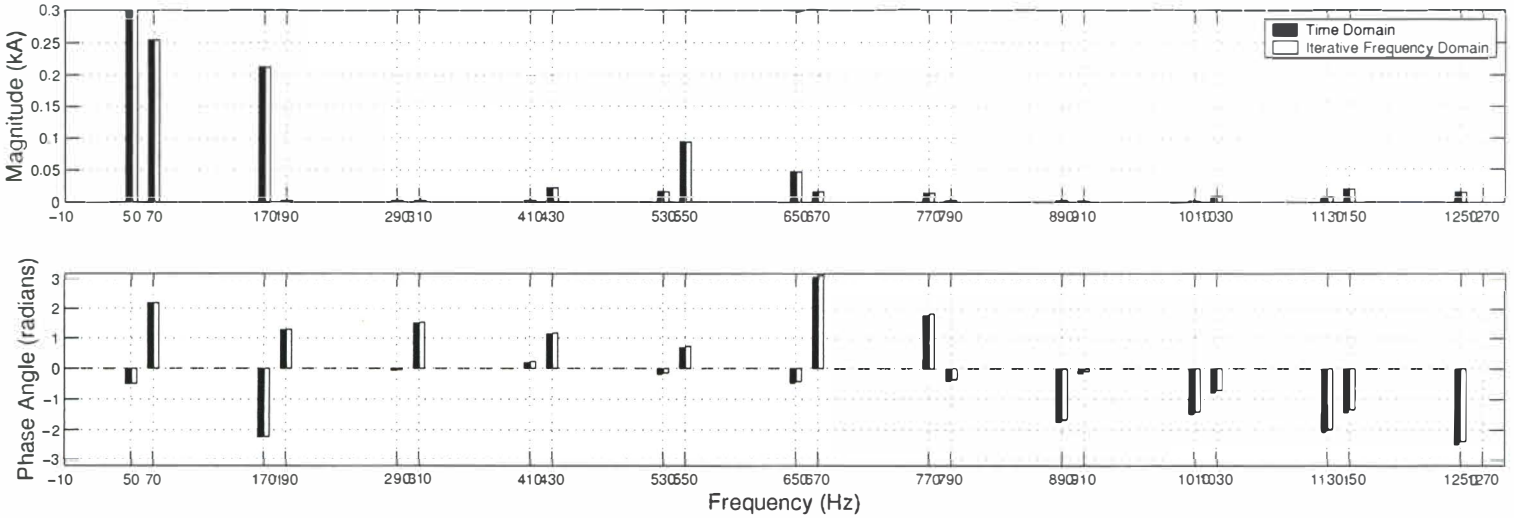

(b) AC current, positive and negative sequence frequency domain comparison.

Figure 3.8 AC current time and frequency domain comparisons for a 50Hz 12 pulse HVDC converter with a 0.15pu 120Hz dc side distortion.

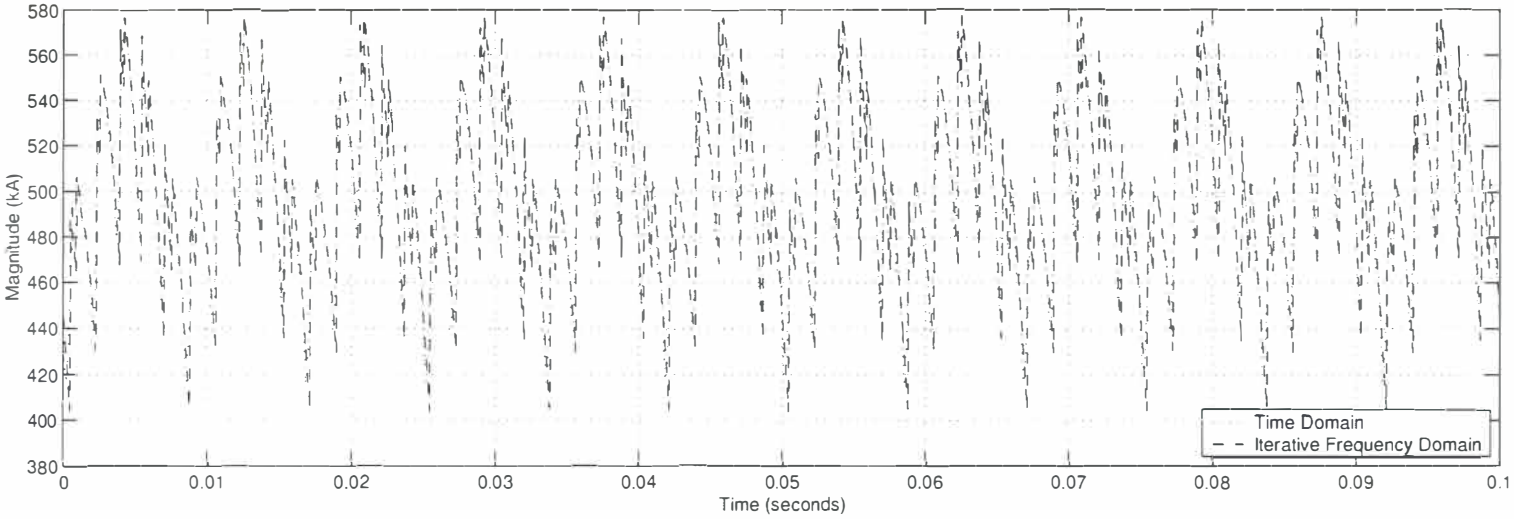

(a) DC voltage time domain comparison.

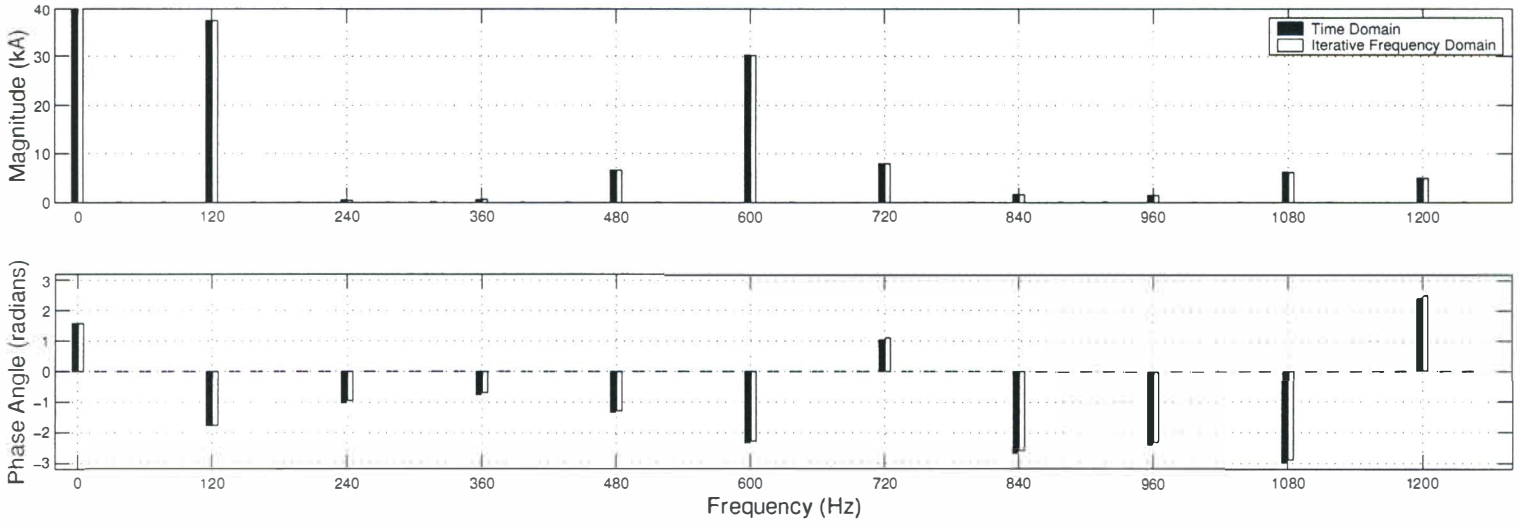

(b) DC voltage frequency domain comparison.

Figure 3.9 DC voltage time and frequency domain comparisons for a 50Hz 12 pulse HVDC converter with a 0.15pu 120Hz dc side distortion.

Chapter 4

HVDC CONVERTER LINEARITY

4.1 INTRODUCTION

This chapter investigates the nonlinearity associated with the 6 pulse HVDC converter, hence preparing the way for linear analysis of the converter and HVDC link for harmonic and interharmonic studies in the frequency domain. Linearity is a complex issue with regard to the HVDC converter. It might be assumed that the frequency modulating nature, or time variance of the converter implies nonlinearity. This is not necessary the case as time variant devices can often look linear when viewed in the frequency domain.

There is no doubt that the HVDC converter is a nonlinear power electronic device. The steady state operating point conditions of the converter or link, and the effect of these conditions are the result of various complex interactions dependent upon the power system and HVDC link requirements. While modelling such nonlinear devices, an iterative AC/DC load flow, dependent on the control scheme being used, is required. Iterative power flow methods of varying degrees of complexity have been used to accommodate this nonlinear control action [54][55][56]. Most methods ignore the effects of the higher frequency characteristic harmonics, assuming these are much smaller than the fundamental parts. However, the characteristic harmonics of each converter alter the average commutating period, and hence operating point, and their omission is a source of error. This is particularly so for single phase or low pulse converters whose characteristic harmonics are of a high magnitude proportional to their fundamental, or HVDC links of the same operating frequency where the characteristic harmonics of both the rectifier and inverter may interact with one another.

All small signal models of the HVDC converter linearise the relationships of small signal waveform distortion about a base operating point. The operating point must be known in advance, either from an iterative power flow of the system being modelled or possibly from real power system data. Linearisation around an operating point is valid as long as the operating point of the HVDC converter stays constant, or varies little, when subjected to power system waveform distortion.

This chapter formally describes a definition of operating point with respect to an HVDC converter and investigates the change in this operating point, resulting from system distortion. If the operating point changes little when subjected to distortion then the device in question can be accurately modelled using linearised techniques. However, if the sensitivity is high, then iterative nonlinear solution techniques will be required.

The commutation period plays a fundamental part in the distortion transfer mechanism of the converter. If accurate linearised small signal models are to be used then the dynamics associated with the commutation period, due to applied small signal distortion must be fully understood. Wood [17] successfully modelled the converter transfers, including the effects of small signal distortion, using linearised relationships. However, a few of the linearised assumptions were

only approximate, leading to inaccuracy in the small signal transfers.

Section 4.2 describes the key concepts behind linearised modelling of non-linear power electronic devices such as the HVDC converter. Section 4.3 describes the base case operating point of the HVDC converter in isolation. This is considered as the operating point that is linearised around and its definition is important. Section 4.4 investigates the effect that applied system distortion has on the base case operating point. Importantly, the effect of the applied distortion on the commutation period, switching instant variation, and the resulting effects on the ac current and dc voltage wave shapes are investigated. The results prove influential in the further development of an exact small signal model of the HVDC converter that is described in chapter 5.

4.2 LINEARISED MODELLING OF NON-LINEAR POWER ELECTRONIC DEVICES

Power electronic switching devices such as the HVDC converter exhibit time variance. In power electronics time variant devices generally consist of switching circuits, switching from one linear time invariant system to another. This makes the circuit a time variant circuit, in this case non-linear and time variant. Devices which use fixed or controlled switching instants (using GTOs etc), can be described as linear and time variant. Whether linear or not, the time variance must be modelled. This is discussed further in chapter 6 using time variant Frequency Coupling Matrices (FCMs).

The object of linearised modelling is to linearise the device around a base operating point. It is essential that the operating point stays reasonably constant for the linearisation is to be accurate. The true operating point of the HVDC converter is known if all switching instants are known and all values, and derivatives for all the state variables are known at the exact switching instants. The object behind iterative harmonic domain models is to find this operating point, whether the converter is part of a large HVDC system [6] with many system distortions or whether it is in isolation, such as that described in chapter 3. This thesis linearises the HVDC converter around an initial base case operating point, gaining in effect, the linearised operating point.

In this work, the base case operating point is used to describe the operating point of the HVDC converter that is to be linearised about, or the initial operating point. To simplify the analysis the base case operating point is defined as the operating point of the single converter, while in infinitely strong systems, and without any external system distortion. Hence it is described with the fundamental quantities as described in section 4.3 and is an approximation to the 'actual' operating point.

In general, any non-linear function can be described with a Taylor's series expansion. This expansion is common in the single function, single variable form, as shown in equation 4.1

$$y_o + \Delta y = y_o + \frac{\delta y}{\delta x}\Delta x + \frac{1}{2!}\frac{\delta^2 y}{\delta x^2}(\Delta x)^2 + \frac{1}{3!}\frac{\delta^3 y}{\delta x^3}(\Delta x)^3 + \ldots \tag{4.1}$$

However the converter, by nature of its switching action can be described with n functions of n independent variables. In general form, Taylor's series expansion can be written for n functions of n variables as follows [57],

$$\begin{bmatrix} y_o^a \\ y_o^b \\ \vdots \end{bmatrix} + \begin{bmatrix} \Delta y^a \\ \Delta y^b \\ \vdots \end{bmatrix} = \begin{bmatrix} y_o^a \\ y_o^b \\ \vdots \end{bmatrix} + \begin{bmatrix} \frac{\delta y^a}{\delta x^a} & \frac{\delta y^a}{\delta x^b} & \cdots \\ \frac{\delta y^b}{\delta x^a} & \frac{\delta y^b}{\delta x^b} & \cdots \\ \vdots & \vdots & \ddots \end{bmatrix} \begin{bmatrix} \Delta x^a \\ \Delta x^b \\ \vdots \end{bmatrix}$$
$$+ \frac{1}{2} \begin{bmatrix} \left(\frac{\delta^2 y^a}{\delta x^a \delta x^a} + \frac{\delta^2 y^b}{\delta x^a \delta x^a} + \ldots\right)\Delta x^a & \left(\frac{\delta^2 y^a}{\delta x^a \delta x^b} + \frac{\delta^2 y^b}{\delta x^a \delta x^b} + \ldots\right)\Delta x^a & \cdots \\ \left(\frac{\delta^2 y^a}{\delta x^b \delta x^a} + \frac{\delta^2 y^b}{\delta x^b \delta x^a} + \ldots\right)\Delta x^b & \left(\frac{\delta^2 y^a}{\delta x^b \delta x^b} + \frac{\delta^2 y^b}{\delta x^b \delta x^b} + \ldots\right)\Delta x^b & \cdots \\ \vdots & \vdots & \ddots \end{bmatrix} \begin{bmatrix} \Delta x^a \\ \Delta x^b \\ \vdots \end{bmatrix} + \ldots \tag{4.2}$$

for $n = 1$ and 2 where the vector y_o is the base case operating point to be linearised about. The first matrix in equation 4.2 is a linearised matrix of first order derivatives. For the HVDC converter it is this matrix that has been used in harmonic domain models to iteratively solve the operating point of the whole system, including all harmonic frequencies [28][5]. For linearised modelling it is also this matrix that is to be analytically derived. However, there are several important steps that must first be considered. First, what is the effect of the non-linearities in the higher order terms of equation 4.2, and secondly when linearised, what is the best method of modelling the system as a whole?

The second term of equation 4.2 contains a matrix of coefficients containing second order partial derivatives. Each matrix coefficient contains terms dependent on all other variables and each term has a $\Delta x^m.\Delta x^n$ relationship. Hence, as the distortion magnitude Δx tends towards zero, this second term, and all other terms of equation 4.2 also tend towards zero. This clearly means that linearised models are capable of modelling the change in operating point accurately, so long as distortions external to the device, ie, Δx are very small, tending towards 0. However, it is the coefficients that determine the degree of linearity and it is these that are effectively investigated within this chapter with regard to the HVDC converter.

4.2.1 Linearised modelling of the HVDC converter

Kron was perhaps the first engineer to develop a method or theory for modelling large complicated systems using piecewise solutions of smaller subcomponents [58]. Kron called this theory Diakoptics which he had used previously in his generalised frequency domain modelling of rotating machinery [59].

Larsen [34] used a similar theory for the HVDC converter, relating the effects of small signal distortions on the HVDC converter through the use of his linear network equation using linearised transfers. His equation effectively describes a method of representing the matrix of first order partial derivatives shown in equation 4.2 for the HVDC converter. Hence, it is a linearisation around a base case operating point, assumes superposition in the transfers, and relates the effects of positive and negative sequence ac, dc and firing angle distortions to the ac current and dc voltage. It is a linear frequency cross-coupling matrix, and is written as follows,

$$\begin{bmatrix} \Delta I_{acp} \\ \Delta I_{acn} \\ \Delta V_{dc} \end{bmatrix} = \begin{bmatrix} a & b & c & d \\ e & f & g & h \\ i & j & k & l \end{bmatrix} \begin{bmatrix} \Delta V_{acp} \\ \Delta V_{acn} \\ \Delta I_{dc} \\ \Delta \alpha \end{bmatrix} \tag{4.3}$$

where the transfers a to l are matrices built from the returned frequency spectra of many applied perturbations. These matrices are linear and time variant, describing the frequency cross-coupling associated with the modulation process of the converter. They are further discussed in chapter 6.

The inputs of equation 4.3 are the known applied perturbations ΔV_{acp} and ΔV_{acn}, (the positive and negative sequence applied voltage distortions) and ΔI_{dc} and $\Delta \alpha$, (the DC current and firing angle applied distortions). These are small signal sinusoidal distortions. The outputs are the resulting ac side currents and dc side voltage. These are frequency spectra resulting from the effects the applied distortion has on the switching action and commutation period dynamics of the converter. For Larsen's equation to hold, the transfers must be of a true small signal nature, which in the case of transfer a means,

$$a = \lim_{\Delta V_{acp} \to 0} \frac{\Delta I_{acp}}{\Delta V_{acp}} \tag{4.4}$$

The modulation process is complicated by the fact that the commutation periods, and hence switching instants, are affected by the applied distortion. The effect of the commutation period dynamics is to contribute extra nonlinear and linear terms to the resulting ac current and dc voltage spectra.

If the transfers of distortion are linear, or linearisable, equation 4.3 is valid and can be extended into a nodal analysis to solve the effects of associated ac and dc system impedances[1]. If the transfers are nonlinear then equation 4.3 is invalid and a full multi-variable iterative model such as that developed by Smith [4] and Bathurst [5] must be used. The following sections examine the linearity of each of these individual transfers.

4.3 THE HVDC CONVERTER BASE CASE OPERATING POINT

Any power electronic switching device operating in the steady state has an operating point. This operating point will include the characteristic harmonics associated with the switching action of the device and any other non-characteristic frequency distortion present in the associated ac or dc systems. Non-characteristic distortion will modulate, by the switching action, to other frequencies. For the purposes of the work contained within this thesis the operating point of the current sourced HVDC converter is defined without any non-characteristic system distortion and is termed the *base case* operating point. It is this base case operating point that is linearised about and it is noted that this operating point is an approximation to the true operating point of an actual system. However, this is a good approximation as the fundamental base case quantities are by far the largest quantities. The main advantages of this it that the operating point can be acquired from a single phase ac/dc load flow, or likewise from real power system data and it also significantly simplifies the linearised modelling process of the converter[2].

The base case operating point can be defined in several ways. In the time domain it is defined as the ac current and dc voltage wave shapes resulting from the switching action of the converter on the constant dc side current source, I_{dc}, and the fundamental positive sequence voltage source, $v_{1\psi}$, respectively. Section 5.2 derives the frequency spectra of these wave shapes in algebraic form. Figure 4.1 shows the time domain representation of the base case characteristic ac current and dc voltage, for the 6 and 12 pulse current sourced HVDC CIGRE rectifier. In the frequency domain this base case operating point consists of the fundamental voltage on the ac side, a constant dc current source on the dc side, and the characteristic frequencies on both the ac and dc sides. The frequency domain representation of the characteristics shown in figure 4.1, are shown in figures 4.2 and 4.3 for the ac current and dc voltage respectively. For linearised models to remain effective it is important that this base case operating point remains constant, or changes little. The effects small signal distortions have on this operating point are very important if a small signal linearisation is to be used, and it is these effects which are the focus of this chapter.

The base case operating point of a current sourced HVDC converter, with no applied distortion, can be defined exactly, knowing only the fundamental positive sequence voltage magnitude and angle (equation 3.4)[3], the dc side current, I_{dc}, as well as the firing angle, α_o. Using these three quantities the commutation period can be found using equation 4.5.

$$\mu_o = cos^{-1}[cos\alpha_o - \frac{2X_cI_{dc}}{\sqrt{3}NV_1}] - \alpha_o \tag{4.5}$$

[1] This is described is detail and validated against time domain simulation in chapters 6 and 7.

[2] Chapter 5

[3] The angle of the fundamental voltage is only required if the firing instants are independent of the positive sequence voltage. Usually, the firing instants can be considered dependent on the positive sequence fundamental voltage through the use of a PLO.

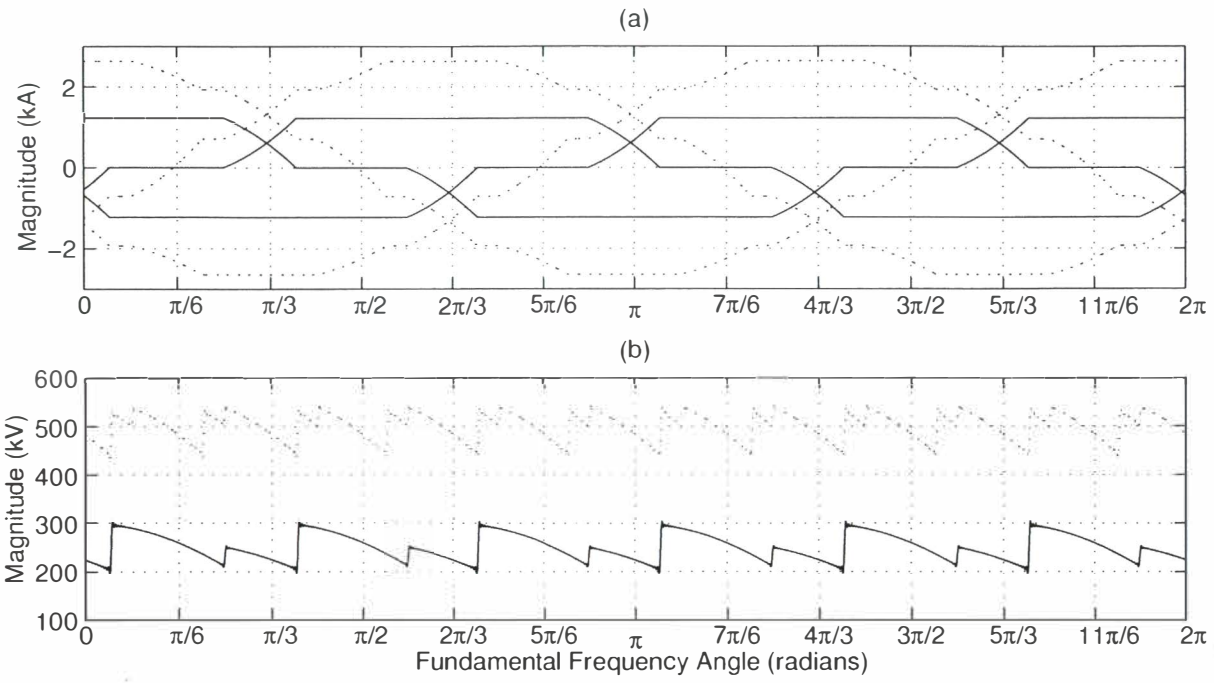

Figure 4.1 Base case characteristic time domain wave shapes for CIGRE rectifier operating point. 6 pulse - solid, 12 pulse - dotted. (a) AC current, (b) DC voltage.

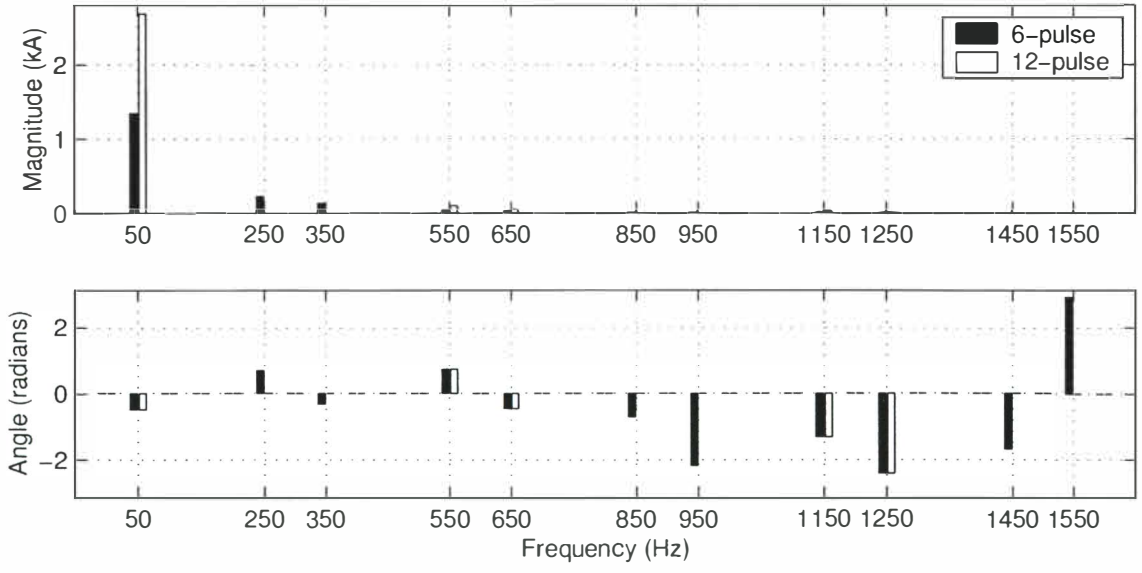

Figure 4.2 Base case characteristic AC current spectra for CIGRE rectifier operating point.

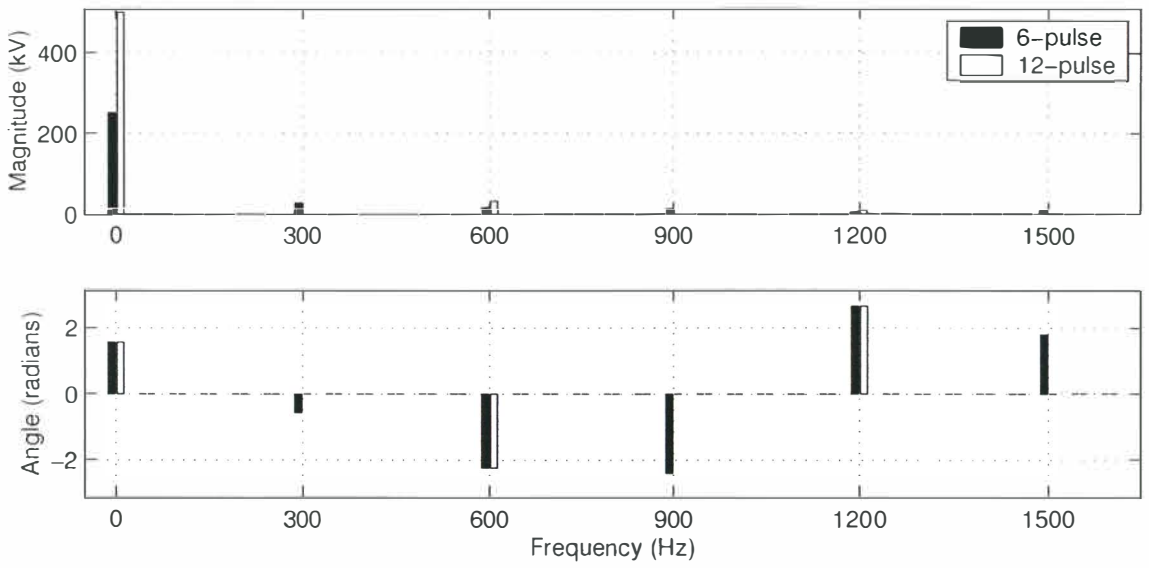

Figure 4.3 Base case characteristic DC voltage spectra for CIGRE rectifier operating point.

4.4 AN INVESTIGATION INTO THE LINEARITY OF THE HVDC CONVERTER

Although small signal techniques have been used quite extensively in the past there has been no rigorous investigation into the nonlinearity of the HVDC converter while subjected to waveform distortion. This section makes use of the iterative frequency domain model, described in chapter 3, to investigate both the linear and nonlinear behaviour associated with waveform distortion.

The base case operating point has been described in section 4.3 for the isolated HVDC converter. The effects of applied distortion on this operating point are important and must be described accurately. Figures 4.4 and 4.5 show the difference between the base case operating spectrum (no applied distortion) and the spectrum resulting from an arbitrary small positive sequence ac voltage distortion (180Hz in this case).

Figure 4.4 shows the change in the positive sequence ac current spectrum, while figure 4.5 shows the change in the dc voltage spectrum. Each of the figures show the resulting transfer, ie, the change in the base case ac current/dc voltage, divided by the applied distorting phasor. These are effectively transfers a and i in equation 4.3. Transfer a, from AC voltage to AC current, is due solely to the change in the commutating current during the commutation period.

The frequency domain spectra shown in both figures contain frequencies at the base case operating point frequencies, ie, at 50,350,650Hz, ... for the positive sequence[4], and at 0,300,600Hz for the dc voltage. This indicates that the applied positive sequence distortion has changed the base case operating point.

Both figures 4.4 and 4.5 show two different distorting magnitudes, 0.01pu (white) and a 0.10pu (black) positive sequence distortion. If the converter is a *linear* time variant device then the frequency transfers would be expected to remain constant as the transfer is divided by its distorting magnitude. If the converter is a *nonlinear* time variant device then the transfers would be expected to change as the distortion magnitude changes.

This provides a very interesting result as some of the transfers change little, while others change by a considerable amount. Hence, some parts of the resulting spectrum/transfer are more linear

[4]There are also changes at 250,550Hz, ... for the negative sequence, though this figure is not shown.

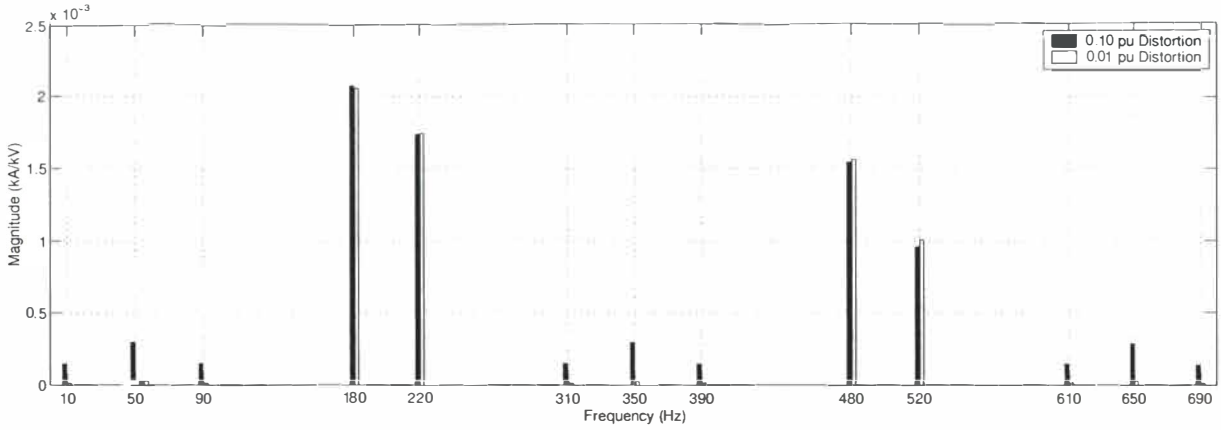

Figure 4.4 Difference in transfer a between 0.01 and 0.10pu distortions for a 180Hz positive sequence voltage distortion.

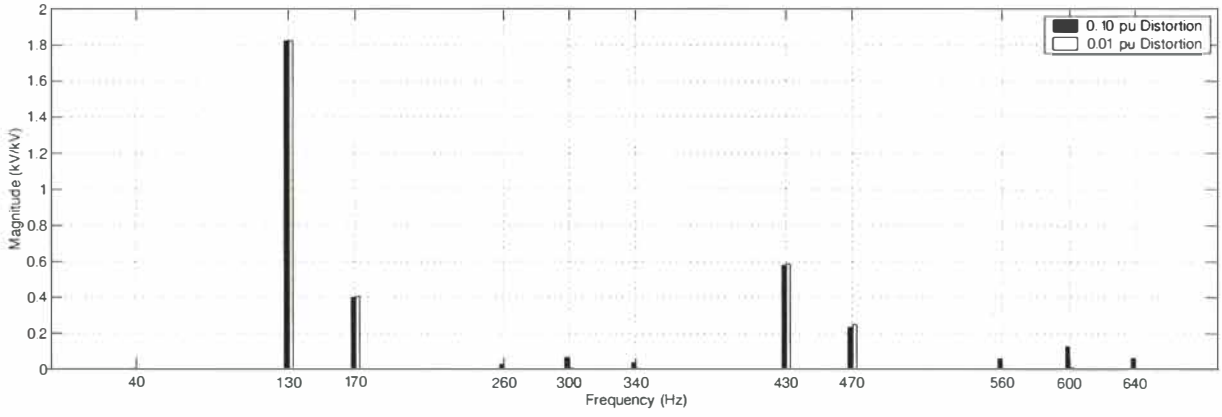

Figure 4.5 Difference in transfer i between 0.01 and 0.10pu distortions for a 180Hz positive sequence voltage distortion.

than others. In effect some parts of the transfer contain large linear terms described by the first part of the Taylors series expansion while others contain solely non-linear terms associated with the higher order terms of equation 4.2.

As the converter can be described as a simple modulator the first and higher order frequencies can be separated. Table 3.1 in chapter 3 shows the resulting frequencies generated from an applied dc side distortion f_{dck}.

The first row in table 3.1 shows the result of an applied distortion, modulating with the base case characteristic harmonics. These frequencies are termed the first order frequencies and are the larger terms in figures 4.4 and 4.5. The second row shows the second order terms, falling at frequencies $(6nf_{fun} \pm f_{dck}) \pm f_{dck}$. Two of these frequencies, $(6nf_{fun} + f_{dck}) - f_{dck}$ and $(6nf_{fun} - f_{dck}) + f_{dck}$ fall on the characteristic base case frequencies. Thus the ac side fundamental and characteristic harmonic currents change, as do the dc side voltage dc and characteristic voltages. These alter the operating point and are the key to the nonlinear behaviour of the converter under applied distortion. In fact, all resulting spectra of *even* orders affect the base case frequencies, however, the higher the order, the smaller the magnitude of the resulting spectra, and as shown in equation 4.2 a returned n^{th} order spectrum decays in an x^n fashion, from a small signal distorting phasor Δx.

The results of figures 4.4 and 4.5 show that the converter is a nonlinear device as the base case operating point changes with applied waveform distortion. Although only a positive sequence voltage distortion has been used, the same conclusions apply with negative sequence voltage distortion, dc current distortion and firing angle distortion.

Though the figures imply nonlinearity the change in the base case operating point is small and a second order effect. Also, the change exhibits a nonlinear relationship with the applied distortion, decaying to zero as the applied distortion tends towards zero. This relationship is mainly dependent on the returned second order spectra which have an x^2 dependence on the applied distortion, x. This is a promising result as it shows that the converter is linearisable for small signal distortions.

An alternative point of view is to look at the switching instants. The switching instants can be used to look at the effects of distortion on the operating point and can in fact be used to help describe the operating point. The following section defines a measure used to describe the change in the base case operating point, or in effect, the nonlinearity of the converter. This is done by measuring the variation of the switching instants, resulting from applied distortion, using the nonlinear model described in chapter 3.

4.4.1 A measure of converter nonlinearity

As shown in the previous section, when the converter is subjected to an arbitrary applied distorting frequency the operating point changes. The change in operating point has linear first order frequencies and non-linear second order frequencies that effect the base case operating point. This change in operating point, or the non-linearity of the converter is dependent not only on magnitude, but also on the applied frequency of the distortion and also on the base case operating point itself. Hence, a measure of the linearity of the converter is useful. In effect, it is the numerical determination of the coefficients of the second order partial derivatives in Taylors series expansion.

If a 6 pulse HVDC converter experiences a harmonic distortion from its associated ac or dc systems at a characteristic frequency, for example a negative sequence 250Hz ac side voltage, a positive sequence 350Hz ac side voltage or a 600Hz dc side current distortion[5], then the value

[5]It should be noted that the characteristic and modulated harmonics resulting from applied distortion are sequence dependent.

of the distortion will be the same during each individual commutation period and the switching instants will all move by the same amount and in the same direction. This causes the overall operating point to change as the average commutation period (μ_o) over the fundamental cycle will change and equation 4.5 will become inaccurate. This effect is linearisable if the characteristic distortion is applied to the converter.

However, if the distortion is at a non characteristic frequency then each of the commutation periods shift in different ways, depending on the value of the distorted commutating current at the switching instants. Unlike an applied characteristic distortion, the sum of all the changes in the commutating periods over the base frequency cycle averages to zero as the applied distortion tends towards zero. When the applied distortion is of some finite value, resulting second order terms are generated (as shown in table 3.1), some of which fall on the characteristic frequencies. These frequencies alter the average commutation period and hence operating point and the change can be described as a nonlinear second (or higher) order effect.

A single measure of this variation from the base case operating point is useful. As the average commutation period is dependent on the base case quantities, $v_{1\psi}$, I_{dc} and α_o, the change in the average commutation period $\Delta\mu$ seems a good indicator.

Figure 4.6 shows the change in the average commutation period for a set of applied perturbations of 0.04pu magnitude from 10Hz to 1250Hz in 10Hz increments for positive and negative sequence ac voltage, dc current and firing angle distortions.

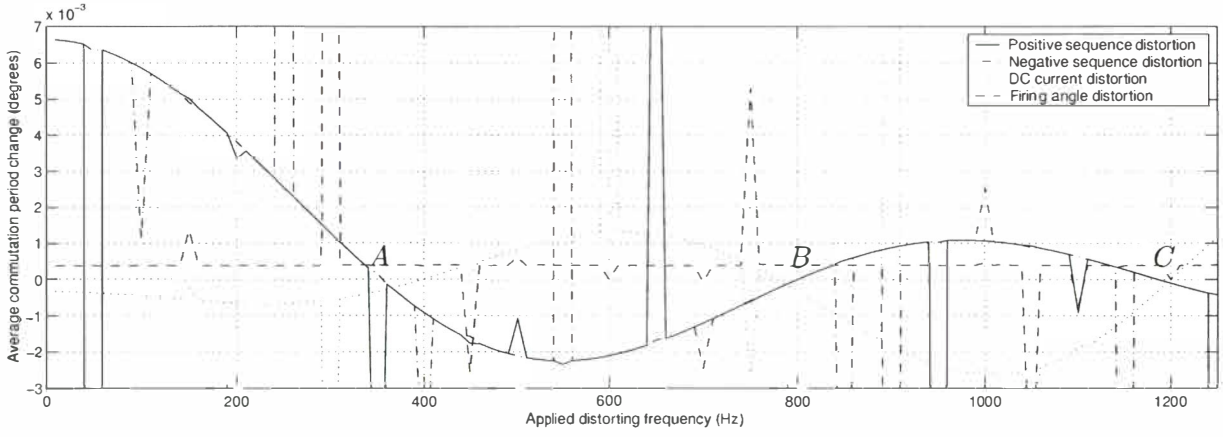

Figure 4.6 Change in average commutation period $\Delta\mu$ resulting from applied frequency perturbation.

For the operating point used in this study (see appendix D) the fundamental voltage is set to make the average commutation period 22.5^o.

As shown, the change in the average commutation period is very small, the maximum being about 0.007^o when a low frequency positive or negative sequence ac voltage distortion is applied.

The spikes, which are quite visible in both figures, are either the result of applied characteristic frequencies causing the operating point to shift more dramatically, or at a frequency such that the overall average switching variation is dependent on the phase angle of the applied distortion. Also, some of the smaller spikes are the result of second or higher order effects.

For positive and negative sequence distortion the minimum average commutation period change is shown by points A,B and C, at frequencies of approximately 350Hz, 800Hz and 1160Hz. At these points the average commutation period does not change.

However, although the average commutation period does not change at these points, it is possible that each commutating switching instant has a high variation, yet the overall average change is small or zero. If the actual commutation switching instants are recorded, it is seen that the minima at 350Hz and 1160Hz for the positive and negative sequence applied distortions have

in fact a large switching instant variation, the average being small over the whole converter switching base cycle[6].

The difference in the actual change of the commutation period instants is shown in figure 4.7 for points A and B for an applied positive sequence ac voltage distortion[7]. As shown, although the same applied magnitude of distortion is used, the switching instant variation is dramatically different, even though the average commutation period modulation is approximately zero for both cases.

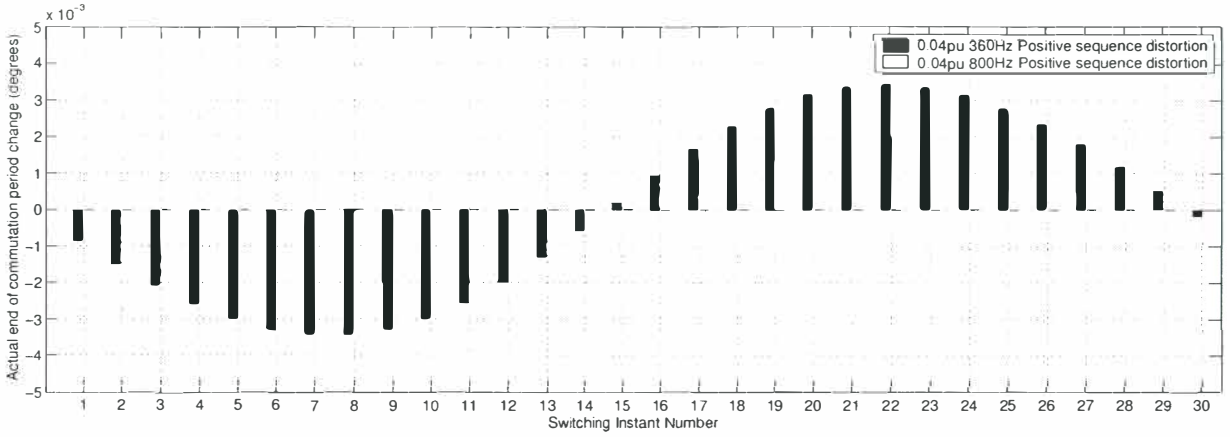

Figure 4.7 Difference in end of commutation switching instant for two applied frequency distortions of the same magnitude.

Although the switching instant variation produces both linear and nonlinear terms, it is assumed that its magnitude is a good indicator of the magnitude of the nonlinear terms. This is a reasonable assumption as when there is no switching instant variation there are no additional second order frequencies present and the converter can be described as in a completely linear manner, while when switching instant variation exists, nonlinear higher order frequencies are present.

The change in the average commutation period cannot be used as an indicator of converter linearity when subjected to applied distortion. To overcome this the mean absolute variation of the commutation period can be used instead. This is the absolute change in each individual commutation period, summed, and then divided by the total number of commutation periods. Figure 4.8 shows the absolute average commutation period change.

As shown in all figures in this section, the change in commutation period associated with the positive and negative sequence ac voltage distortion and dc current distortions is dependent on the applied frequency of distortion while the change associated with firing angle distortion appears independent of applied distorting frequency. This is due to the fact that both the beginning and end of the commutation period are modulated for firing angle distortions, the offset shown dependent on the operating point.

Figure 4.8 shows interesting cases when an ac voltage distortion of 800Hz, or a dc current distortion of 400Hz is applied to the terminals of the converter. Under these cases there is no switching instant variation, and the converter can be described as a linear and time variant device. This means that the converter still behaves as a modulator to the applied distortion, but the base case conditions do not change. Firing angle distortion on the other hand is a direct modulation of the switching instants, hence the converter under firing angle distortion

[6]In this case being 5 fundamental cycles to get a base frequency of 10Hz.

[7]Point A is at 350Hz, a positive sequence base case characteristic frequency. Hence, 360Hz is used as this is not affected by the base case.

always has nonlinear frequencies generated by the switching instant variation and can never be described as a complete linear time variant device.

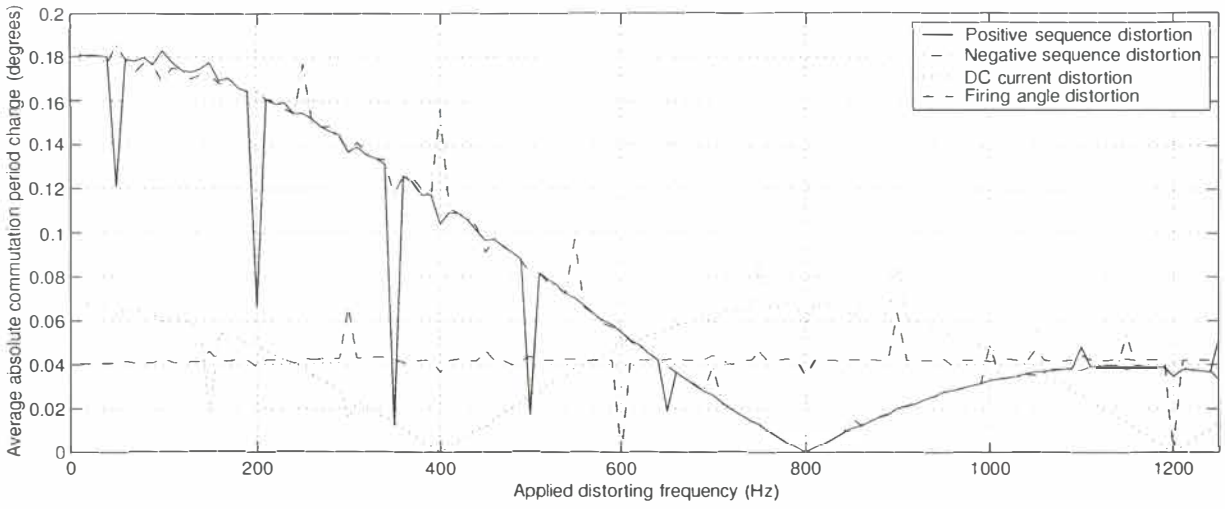

Figure 4.8 Change in absolute average commutation period $|\Delta\mu|$ resulting from frequency perturbations.

This section has proposed a single measure, capable of determining the linearity of the converter by measuring the switching instant variation. This is useful to the extent that it helps give a broader understanding of the converter linearity and switching instant variation due to applied small signal distortion. However, only a few models are capable of determining the exact switching instants. Hence, although this measure is a good single measure for determining switching instant variation (and nonlinearity) it is hard to measure without a model such as that described in chapter 3.

Further investigation is needed to determine the characteristics of the commutation period variation resulting from applied small signal distortion. The following section further analyses the commutation period using the iterative frequency domain model and in particular investigates the effect small signal distortions have on the associated ac current and dc voltage wave shapes during the commutation.

4.4.2 Further analysis of the commutation period variation

The effects of switching instant variation (SIV) on the ac current and dc voltage spectra are important. One advantage of the iterative frequency domain model described in chapter 3 is that effects associated with SIV can be easily observed.

By comparing two different solutions of the converter the effects of SIV can be isolated. The first solution method solves for the switching instants without any applied distorting source, using these switching instants in the distorted case, while the second solves for the actual switching instants. For the first case this means the switching instants are being forced, causing discontinuities in the AC current wave shapes. Comparing the two cases shows the difference between assuming fixed switching instants, and calculating their variation. This gives a measure of the importance of modelling switching instant variation.

Effects of using unchanged switching instants in perturbed system

To find the effect of calculating the transfers to AC current, with fixed or dependent switching instants, an example is given using the transfer from DC current to positive sequence AC current. Figure 4.9 shows the positive sequence AC current transfer spectrum resulting from the arbitrary

application of a 0.01pu, 90Hz distortion to the DC current, with and without the effects of the associated SIV. It can be seen that the transfer spectra are almost identical. Figure 4.10 shows

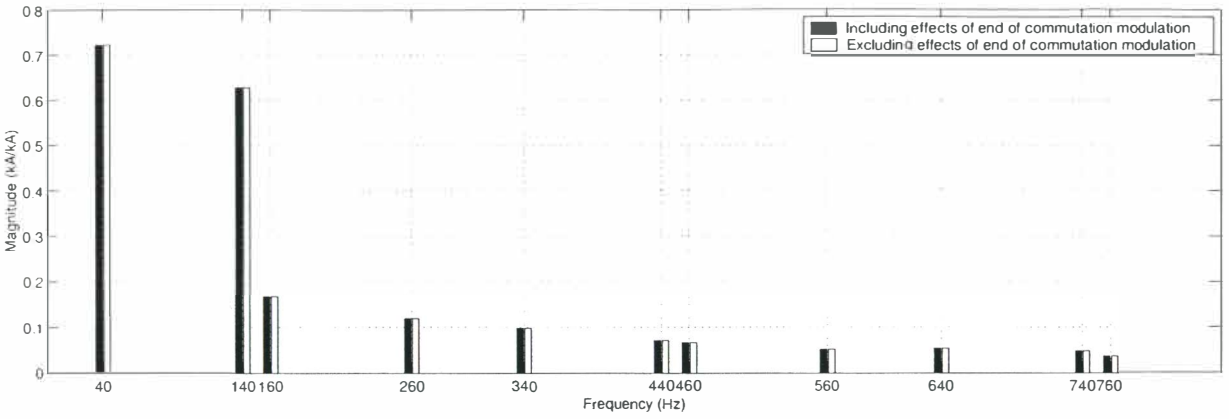

Figure 4.9 Effect of switching instant variation on transfer from 0.01pu DC current distortion to positive and negative sequence AC current.

the DC voltage transfer spectrum for the same applied dc current distortion, with and without the associated effects of SIV. In this case it can be seen that the transfer spectra are significantly different. The simulation results have been repeated for all types and many frequencies of

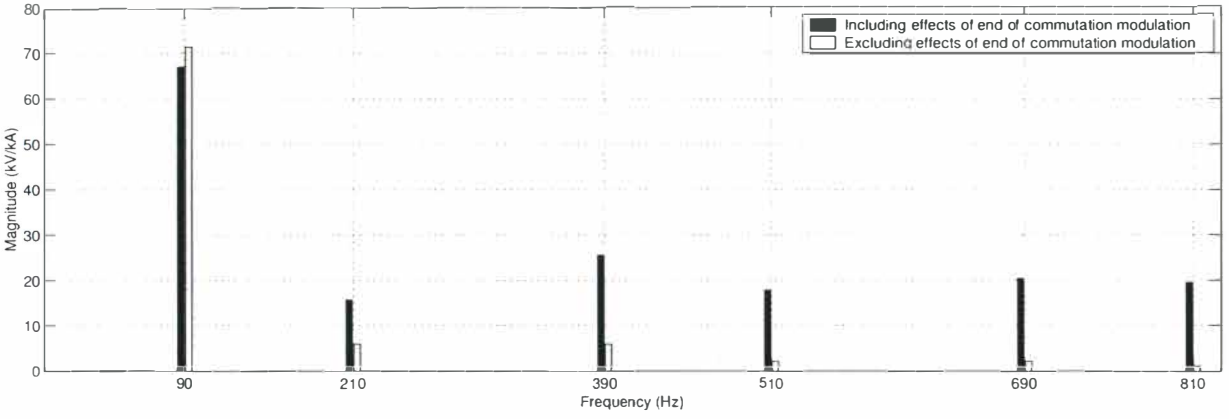

Figure 4.10 Effect of switching instant variation on transfer from 0.01pu DC current to DC voltage.

distortion around the converter. The findings are the same as those described, ie, for transfers to ac current the switching variation has little or no effect, while for transfers to dc voltage the effect is significant. This indicates that the effects of SIV are required only when modelling transfers to dc voltage for linearised small signal 6 pulse HVDC converter models.

Graphical representation of the SIV on the commutation period ac current and dc voltage wave shapes

Figure 4.11 shows an exaggerated effect of an AC voltage distortion on the commutation period (μ) dc voltage and ac current waveforms. The dashed line represents the operating point or base case waveform (with no distortion), while the solid line represents the waveform with the distortion present.

The change in the DC voltage and AC current spectra are dependent on the change on the voltage and current time areas. This change is indicated by the shaded areas and divided into two parts, which have been described as the direct and indirect areas [60]. The direct area is the

area which is not a result of SIV, it is the combination of the base case switching action with the distortion, and is indicated by the lighter shaded areas. The indirect area is the area that results directly from SIV, and is indicated by the darker shaded areas. In order to determine

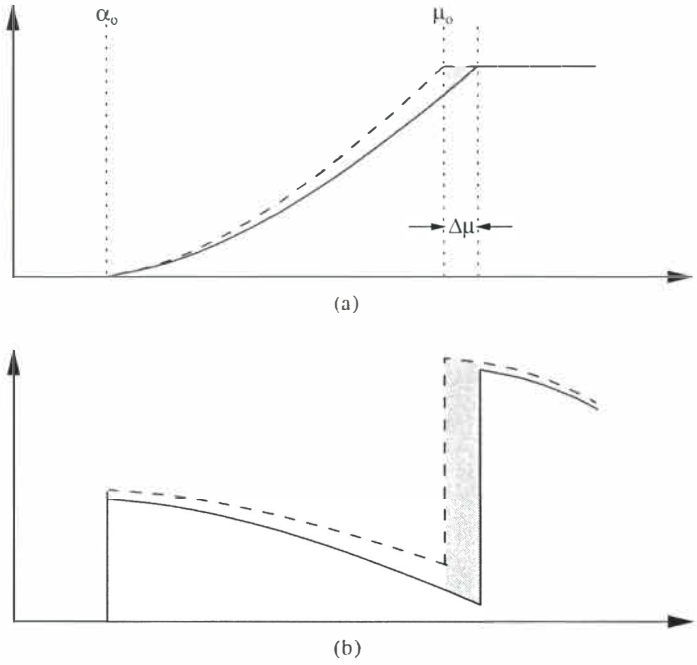

Figure 4.11 Exaggerated effect of applied AC voltage distortion on the commutation period current and voltage wave shapes.

if a voltage or current time area will contribute to the linear transfer, the ratio of the voltage or current time area to the distortion, as the distortion tends to zero must be determined. If the ratio tends towards zero then the area will not contribute to the linear transfer, whereas if the ratio tends towards a constant, the area will contribute to the linear transfer. In effect, this graphically determines whether the effect of the SIV contains linear first order terms, or is nonlinear, containing higher order terms associated with Taylor's series expansion. The area is of primary importance as the Fourier series expansion of the waveform depends directly on its time-magnitude integral, ie its area.

Figure 4.11 (a) shows the effect an AC voltage distortion has on the AC current. In this case the direct area has a fixed width, the base case commutation period, and a vertical dimension proportional to the applied distortion. As a result the ratio of direct area to distortion tends towards a constant, and it will contribute to the linear transfer. Examination of the indirect difference indicates that both the horizontal and vertical dimensions are dependent on the applied distortion, and it will not contribute to the linear transfer. The area represents a nonlinear higher order dependence.

Figure 4.11 (b) shows the effect an AC voltage distortion has on the DC voltage. In this case the direct difference has the same characteristics as those described in the previous paragraph. The indirect area however has a horizontal dimension proportion to the distortion and a fixed vertical dimension. As a result both the direct and indirect areas will contribute to the linear transfer.

Similar diagrams to those shown in figure 4.11 can be drawn to show the effect of DC current and firing angle distortion on the voltage and current waveforms. Examination of the direct and indirect areas in these cases will indicate that the same observations made in relation to AC voltage distortion are valid. In summary it is expected that a direct area will always contribute to the linear transfer, whereas whether or not a indirect area will contribute is dependent on the

individual case in question.

Effects of solving the switching instances using only one iteration

The previous section has shown that the SIV linearly affects the dc voltage spectrum of the 6 pulse HVDC converter. Hence, a linear model of the HVDC converter must include the effects of switching instant variation.

The iterative frequency domain model described in chapter 3 solves the switching instants using a Newton iterative solution method. This section examines the difference in the solved end of commutation switching instants using one iteration, in effect a linear solution, with the full solution using as many iterations required to satisfy the convergence tolerance. Figure 4.12 shows how the iterative method is used to find the exact switching instants. In this figure μ_o is the base case end of commutation instant without applied perturbation. $\Delta\mu$ is the actual end of commutation instant while $\Delta\mu_1$ and $\Delta\mu_2$ are the resulting end of commutation instants after one and two iterations respectively. The reason for examining the difference in the two switching

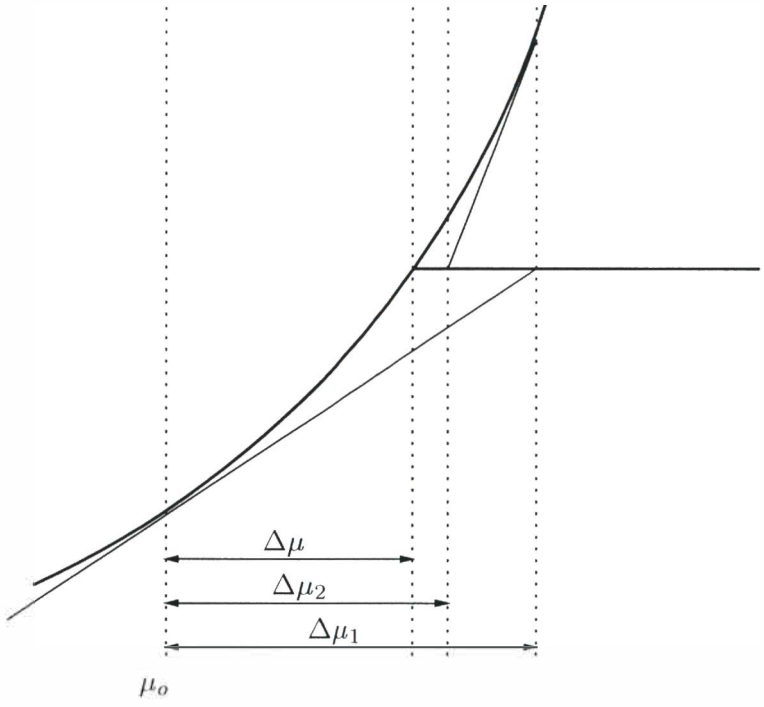

Figure 4.12 Newton method of solving end of commutation period. $\Delta\mu_1$ can be found using direct linearised equations.

angles $\Delta\mu$ and $\Delta\mu_1$ is important to determine whether accurate switching instant variation can be determined using linear analytic equations.

The iterative frequency domain model is run as per normal for 0.10pu distortions on the dc current and positive and negative ac voltage perturbations. The preset tolerance of the mismatch equation 3.19 is set to approximately 3×10^{-7} degrees. The end of commutation period function is then altered enabling only 1 iteration to be completed, ie $\Delta\mu_1$ in figure 4.12.

Figure 4.13 shows the percentage difference ($\frac{\Delta\mu_1 - \Delta\mu}{\Delta\mu} \times 100$) in the two solution methods for the three different distortions (V_{acp}, V_{acn} and I_{dc}). The figure shows a very small percentage difference between the actual solution of $\Delta\mu$ and the solution after one iteration, $\Delta\mu_1$. This result has very important implications for frequency domain modelling of the HVDC converter, indicating that the switching instants can be solved very accurately using direct linearised analytic equations.

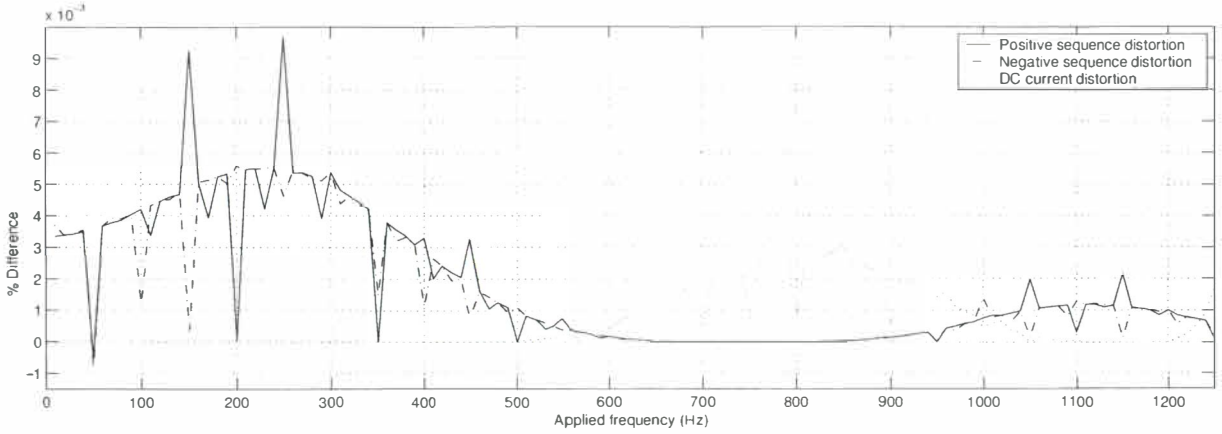

Figure 4.13 Resulting difference in $\Delta\mu_1$ which can be found using a direct linearisation and $\Delta\mu$ which is the actual switching instant.

4.4.3 Change in HVDC converter transfers

The change in the converter operating point and the effects of distortion on the commutation period has been shown in the previous sections. This section investigates the change in the small signal matrix transfers of Larsen's equation 4.3 for applied perturbations from 0.0008pu to 0.10pu. The matrix transfers are described in more detail in chapter 6.

As a high number of perturbations are required, time domain simulation is impractical due to the long computational times needed. Computational efficiency is achieved using the iterative frequency domain model described in chapter 3, which assumes known ac side voltage and dc currents.

The data acquired in this section perturbs for each transfer 125 times from 0.0008pu $\rightarrow$ 0.10pu distortion magnitude. For firing angle modulation the perturbations were applied up to half a degree modulation. The 0.0008pu case is taken to be the small signal case.

Each magnitude perturbation includes 125 frequency perturbations from 10Hz$\rightarrow$1250Hz, therefore 125 different magnitudes at 125 different frequencies are required to investigate the magnitude and frequency dependence of each of the 12 transfer matrices. A typical matrix transfer is described in chapter 6, figure 6.1 which shows the general sparse structure of the matrix transfers. With the following analysis, problems occur at the "cross over" points when the direct and conjugated frequencies lie on top of one another. Hence, twin perturbations, at quadrature phase angles, are required to separate the direct and conjugate parts and the analysis is done on both these parts separately, the results then combined. The transfers are acquired by dividing each perturbation matrix by the actual perturbation phasor and the nonlinear effects are easily shown as divergence from the reference or small signal case, ie the 0.0008pu case.

To gain a better insight into the nonlinear behaviour of the transfers, the small signal transfer can be subtracted and an absolute error gained. To show the percentage divergence, the absolute error is divided by the small signal transfer and multiplied by 100 to get the percentage divergence from linearity, ie,

$$Percentage\ Divergence\ Transfer(x) = \frac{|Transfer(x) - Transfer(ss)|}{|Transfer(ss)|} \times 100 \qquad (4.6)$$

The output of this equation is a set of matrices whose elements converge to zero for a diminishing level of applied distortion. This method shows the linearity of all the first order elements in a sparse matrix transfer.

Some of the smaller terms in the lattice matrix are less linear than some of the larger terms. This can be misleading as all elements in the lattice matrix transfer are given the same weight. This causes the converter transfers to look less linear as very small terms can behave in a highly nonlinear fashion. Weighting each small signal transfer element by its magnitude overcomes this. Equation 4.7 shows this, where $max|Transfer(ss)|$ is the maximum element in the "true" small signal matrix transfer.

$$Scaled\ Percentage\ Divergence\ Transfer(x) = \frac{|Transfer(x) - Transfer(ss)|}{max|Transfer(ss)|} \times 100 \quad (4.7)$$

Figures 4.14 and 4.15 show the average divergence from linearity for all elements in each of the 12 transfers. Figure 4.15 shows the effect of scaling on the nonlinear elements by their magnitude.

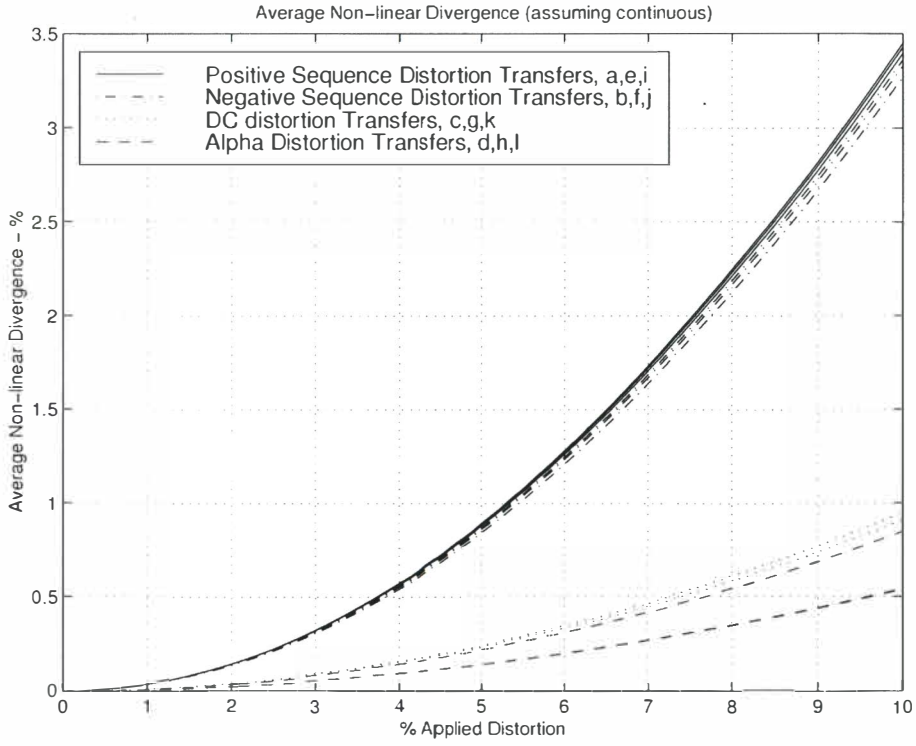

Figure 4.14 Average nonlinear divergence for all transfers.

To get the worst case information for all the transfers, table 4.1 shows the approximate maximum single element divergence from linearity of all the transfers, a through to l for a 0.10pu applied distortion. As shown, although the maximum divergence is sometimes quite high, the average of the elements in the transfers is always around 1%-3% and is at least 1% or less when scaled. The results show that, although some elements in the matrix transfers are highly nonlinear, in general the first order matrices are very linear even for distortions of up to 0.10pu. This result suggests the 6 pulse HVDC converter should be able to be accurately modelled using Larsen's equation and linear matrix algebra to combine linear ac and dc systems.

4.5 CONCLUSIONS

This chapter has described the base case operating point of the HVDC converter and investigated the non-linear change associated with this base case operating point when subjected to system waveform distortion. The first and higher order frequencies have been identified with respect to Taylor's series expansion, and a through numerical investigation conducted on the effect of

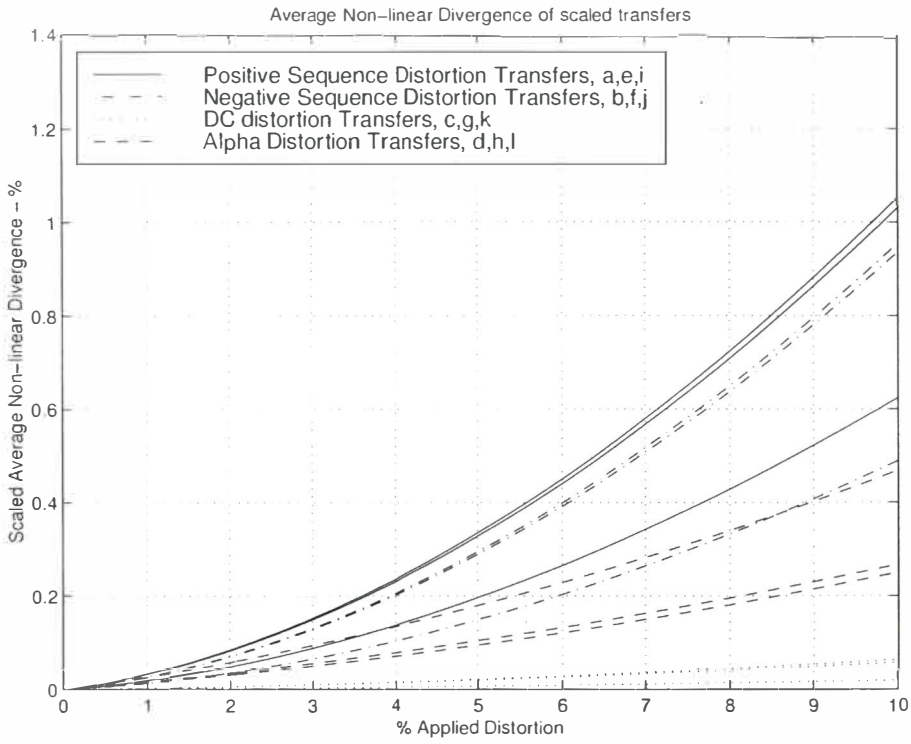

Figure 4.15 Scaled average nonlinear divergence for all transfers.

these non-linear terms using the model developed in chapter3. Essentially, the change in the base case operating point is an effective way of describing the nonlinearity of the converter. If it changes a lot, then the converter can be described as a nonlinear and time variant device, if it changes little, or in some cases not at all then the converter can be described as linear and time variant. It is shown that the change in the base case operating point is small, sometimes zero, depending on the applied distorting frequency and how this affects the switching instant variation. Hence the converter can be described as a linearised and time-variant device for small signal distortion.

The effects of switching instant variation are further investigated on the ac current and dc voltage wave shapes. It is found that the effect, for small signal distortion, is restricted to the dc voltage wave shape only. This is due to the vertical step in the dc voltage at the switching instants. The effect on the ac current wave shape is a nonlinear higher order effect and decays to zero for small signal distortion.

The switching instant variation is therefore considered very important when modelling the dc voltage. An extra study determining whether the switching instant variation is linearisable was conducted using the iterative frequency domain model. A single Newton iteration is a simple linearisation around the base case operating point. Hence, section 4.4.2 compared the full Newton solution with a partial solution using one iteration of the switching instants. It was found that the difference in the full and partial solution was nonlinear, being exact (ie, identical) when the distortion magnitude reduces to zero. This ensures that a full linearised model can be developed, being accurate for small distortion levels. Chapter 5 describes such a model.

Transfer	Maximum 2nd Order		Maximum 3rd Order		Maximum Average	
	Actual	Scaled	Actual	Scaled	Actual	Scaled
a	55%	12%	28%	6%	3%	1%
b	48%	9%	24%	6%	3%	1%
c	19%	0.6%	3%	0.2%	1%	$< 1\%$
d	11%	6%	2%	0.5%	1%	$< 1\%$
e	55%	12%	26%	6%	3%	1%
f	49%	9%	28%	6%	3%	1%
g	11%	0.6%	4%	0.2%	1%	$< 1\%$
h	10%	7%	2%	0.5%	1%	$< 1\%$
i	56%	12%	28%	6%	3%	$< 1\%$
j	42%	8 %	18%	4%	3%	$< 1\%$
k	11%	0.3%	4%	0.1%	1%	$< 1\%$
l	22%	8%	2%	0.5%	1%	$< 1\%$

Table 4.1 Maximum divergence from linearity of 2nd and 3rd orders as well as maximum divergence of averaged elements for 0.10pu distortion.

Chapter 5

ANALYTIC FREQUENCY DOMAIN MODEL OF THE HVDC CONVERTER

5.1 INTRODUCTION

The conclusions following the linear and commutation period analysis for small signal distortions in chapter 4 have given an understanding of the commutation period dynamics and led to the realisation of a complete small signal algebraic converter model. Such a model is described in this chapter [61], a joint development with Chris Osauskas and based closely on Woods [17] original small signal algebraic model.

As with similar small signal algebraic models [36][38][17], the model described uses a transfer function based analysis, building up the ac current and dc voltage spectra for both the base and distorting cases assuming piecewise linearity. Section 5.2 starts by describing a very simple case; the formulation of the base case ac current and dc voltage spectra, while sections 5.3 and 5.4 derive the linearised change in these spectra, resulting from small signal waveform distortion.

For the small signal transfers to ac current, the switching instant variation (SIV) caused by the applied distortion has a primary *nonlinear* effect. This is a higher order effect and means that for small signal distortions the effect of SIV on the ac current reduces to zero and can be ignored, as shown in chapter 4. However, during the commutation period the effect of distortion on ac current has two components, a partial steady state (PSS) component, and a partial transient (PT) component that is required to match the initial conditions at the thyristor firing instants. This has been described previously in chapter 3 as the partial transient (PT) and is presented here in linear analytical form using a Pulse Amplitude Modulated (PAM) spectra.

The small signal transfers to dc voltage exhibit linear and nonlinear voltage-time areas resulting from applied distortion. Both areas are dependent on the switching instant variation (SIV) and for a linearised model the linear area must be included. The linear and nonlinear parts of this voltage-time area can be separated mathematically using Schwarz's Pulse Duration Modulated (PDM) spectra [17]. Small signals result in the PDM spectrum becoming first order and it can then be described as an Area, or equivalently, an Amplitude Modulated Impulse Train, AMIT. As the dc voltage is linearly dependent upon the SIV, this must be modelled. The linearisation used to find the SIV are presented in graphical form, giving a thorough understanding of the processes involved.

The major advantages of such linearised small signal models are speed and the fact that any arbitrary frequencies can be used. If linearity is assumed, no iterative techniques are required and powerful systems of linearised nodal equations can be used to describe the interactions between the HVDC converter and the ac systems. This is further presented in chapters 6 and 7.

5.2 THE BASE CASE CHARACTERISTIC HARMONIC TRANSFERS

This section describes the formulation of the base case spectra, I_{ac} and V_{dc} around the converter. These can be derived using only the average commutation period, μ_o, the average firing angle, α_o, the fundamental voltage and angle, $v_{1\psi}\angle\varphi$, and the dc current, I_{dc}. The general formulation has similarities with that used in the small signal part of the model described in sections 5.3 and 5.4, without the extra complexity resulting from the effects of distortion on the commutation period dynamics.

5.2.1 Base case AC current spectrum

The base case ac current wave shape consists of the DC current during the direct conduction periods and an offset sampled sinusoidal wave shape during the commutation periods.

The direct conduction states, ignoring the commutation periods, require two rectangular current pulses per phase, one positive and one negative with the associated phase shifts. The Fourier series for a single pulse centred around $\omega_o t = 0$ and of width $\frac{2\pi}{3}$, and height 1, is given by,

$$E(\omega_o t) = \frac{1}{3} + \sum_{m=1}^{\infty} \frac{2}{m\pi} sin(\frac{m\pi}{3}) cos(m\omega_o t) \tag{5.1}$$

The required phase shifts are $-\frac{\pi}{2} - \alpha_o - \mu_o - \varphi$ for the positive going pulse and $-\frac{\pi}{2} - \alpha_o - \mu_o - \pi - \varphi$ for the negative going pulse. The $-\frac{\pi}{2}$ phase angle shift results from the addition of $-\frac{\pi}{3}$, half the width of the pulse, and $-\frac{\pi}{6}$, the difference between the line commutated voltage (hence the commutating current) and the positive sequence fundamental phase voltage. The addition of these two pulses gives the following spectrum,

$$\Psi_{\psi}^{ac \leftarrow ac,1} = \sum_{m} \frac{4}{m\pi} sin(\frac{m\pi}{3}) cos(m\omega_o t - m(\frac{\pi}{2} + \alpha_o + \mu_o + \psi - \varphi)) \tag{5.2}$$

where $m = 1, 3, 5 \ldots$ However at $m = 3, 6, 9 \ldots$ $sin(\frac{m\pi}{3}) = 0$. Therefore, $m = 1, 5, 7, 11 \ldots$ For the purposes of this chapter the base case operating conditions are those given in [62]. Hence, the dc side current for the CIGRE rectifier is 2kA, or 1.22 p.u. on the secondary side base, as shown in appendix D. The time domain wave shape for, $I_{dc}\Psi_{\psi}^{ac \leftarrow ac,1}$ is shown in figure 5.1(a).

During the six commutation states, the commutating current is effectively part of an offset sampled sinusoid. This has been described previously for the iterative frequency domain model developed in chapter 3, using the PSS and PT responses of a linear circuit.

The PSS response of the partial commutating current is a function of the line-commutated voltage magnitude and angle, $\sqrt{3}V_1\angle\varphi$ as well as the commutating reactance, X. For each of the six commutating states, six sinusoids, valid during each of the commutation periods can be written in analytical form as,

$$I_{i,PSS}^{ac \leftarrow ac} = -\frac{\sqrt{3}V_1}{2X} cos(\omega_o t - (i-1)\frac{\pi}{3} - \frac{\pi}{6} + \varphi) \tag{5.3}$$

where $i = 1, \ldots, 6$. Equivalently, these commutation currents can also be written in three phase form as,

$$I_{\psi,PSS}^{ac \leftarrow ac} = \pm\frac{\sqrt{3}V_1}{2X} cos(\omega_o t - \psi - \frac{\pi}{6} + \varphi) \tag{5.4}$$

The sampling functions for the commutating states can be easily derived analytically and are similar to that derived for the iterative frequency domain model in chapter 3, except each pulse

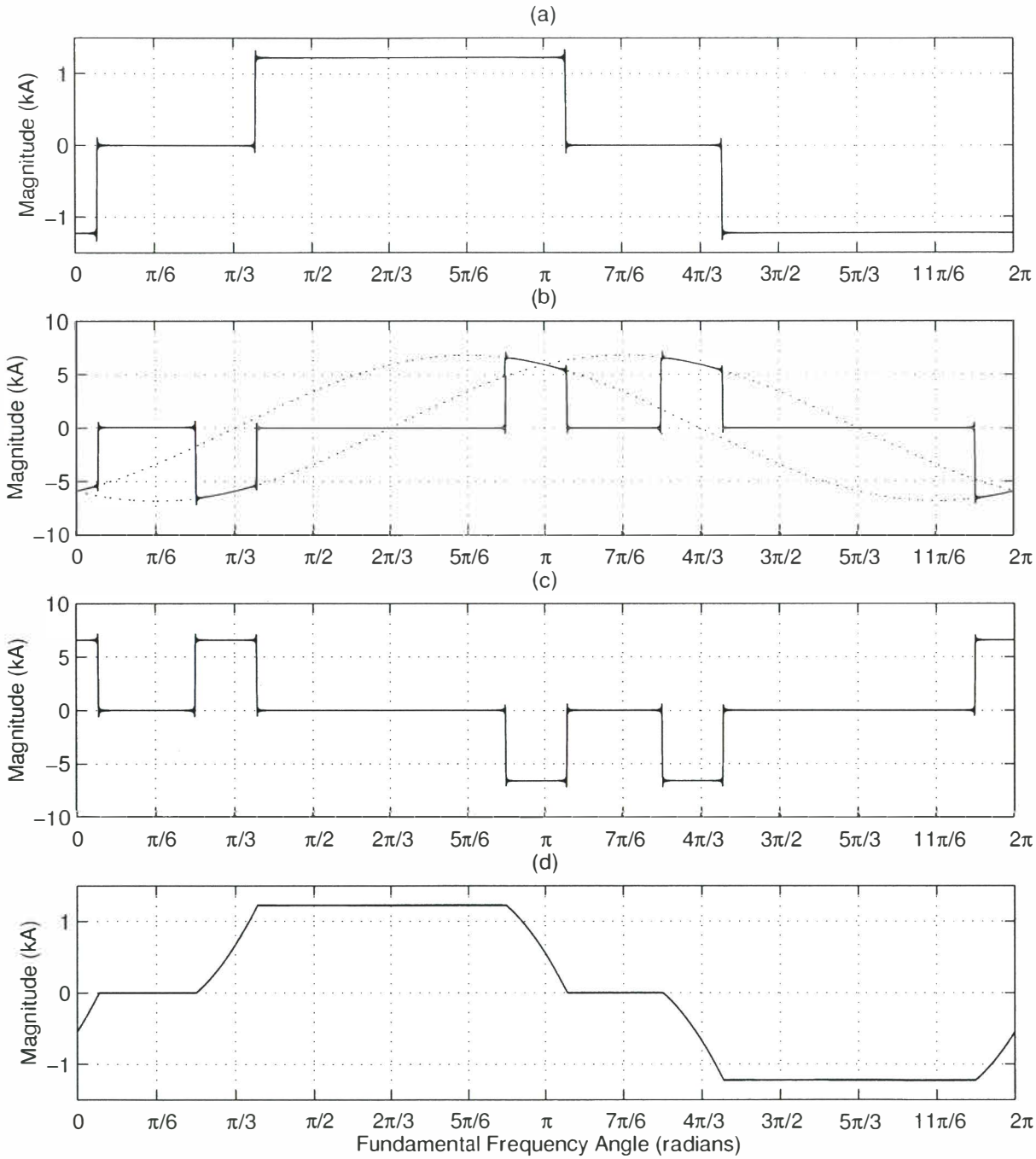

Figure 5.1 Phase a spectrum development of base case AC current wave shape. (a) Sampling function, $I_{dc}\Psi_a^{ac\leftarrow ac,1}$, (b) SPSS component during commutation periods, $I_{a,SPSS}^{ac\leftarrow ac}$, (c) SPT component during commutation periods, $I_{a,SPT}^{ac\leftarrow ac}$, (d) Total base case ac current, I_a^{ac}.

has the same width. A pulse of width μ_o centred at the origin ($\omega_o t = 0$) can be written as,

$$E(\omega_o t) = \frac{\mu_o}{2\pi} + \sum_{m=1}^{\infty} \frac{2}{m\pi} sin(\frac{m\mu_o}{2}) cos(m\omega_o t) \tag{5.5}$$

Each commutating current sample is valid twice during the fundamental period, once during the commutation to the positive rail, and once during the commutation to the negative rail. Hence, two of these pulses are required, phase shifted by π. The actual phase shifts are $(-\frac{\mu_o}{2} - \frac{\pi}{6} - \alpha_o + \varphi - \psi)$ and $(-\frac{\mu_o}{2} - \frac{\pi}{6} - \alpha_o - \pi + \varphi - \psi)$ giving the following sampling spectrum, $\Psi_{\psi}^{ac \leftarrow ac,2}$.

$$\Psi_{\psi}^{ac \leftarrow ac,2} = \frac{\mu_o}{\pi} + \sum_{m} \frac{4}{m\pi} sin(\frac{m\mu_o}{2}) cos(m\omega_o t - m(\frac{\mu_o}{2} + \frac{\pi}{6} + \alpha_o - \varphi - \psi)) \tag{5.6}$$

where $m = 2, 4, 6 \ldots$ To find the total sampled partial steady state (SPSS) commutating currents it is necessary to calculate the correct sampling functions convolved by the correct PSS commutation currents. The following expression can be derived for each commutating phase current.

$$I_{\psi,SPSS}^{ac \leftarrow ac} = I_{\psi,PSS}^{ac \leftarrow ac} \Psi_{\psi}^{ac \leftarrow ac,2} - I_{(\psi+2\pi/3),PSS}^{ac \leftarrow ac} \Psi_{(\psi+2\pi/3)}^{ac \leftarrow ac,2} \tag{5.7}$$

The first term in this equation represents the commutation on, and the second term the commutation off for phase ψ. The resulting sampled spectrum of equation 5.7 can be written as,

$$\begin{aligned} I_{\psi,SPSS}^{ac \leftarrow ac} = &+ \frac{3V_1\mu_o}{4\pi X} cos(\omega_o t - \psi + \varphi) \\ &+ \frac{\sqrt{3}V_1}{\pi X} \sum_{m}^{\infty} \frac{1}{m} sin(\frac{m\mu_o}{2}) sin((m+1)\frac{\pi}{3}) \\ &\qquad sin((m+1)\omega_o t - (m+1)(\psi + \frac{\pi}{2} - \varphi) - m(\frac{\mu_o}{2} + \alpha_o)) \\ &+ \frac{\sqrt{3}V_1}{\pi X} \sum_{m}^{\infty} \frac{1}{m} sin(\frac{m\mu_o}{2}) sin((m-1)\frac{\pi}{3}) \\ &\qquad sin((m-1)\omega_o t - (m-1)(\psi + \frac{\pi}{2} - \varphi) - m(\frac{\mu_o}{2} + \alpha_o)) \end{aligned} \tag{5.8}$$

The time domain wave shape resulting from this spectrum is shown in figure 5.1(b) with the dotted lines representing the commutating current samples for phase a. This is the analytical derivation of the sampled partial steady state (SPSS) part of the characteristic ac current. However, to satisfy the zero current initial conditions at the thyristor firing instants, the SPT spectrum must be added to acquire the total commutating current. The magnitude of the SPT spectrum can simply be described as the negative of the PSS response at the firing instants.

The required offset, or PT response, needed for the commutation current is easily included as an additional rectangular pulse current waveform of correct height and width. The value of the commutation current samples at the instant of thyristor firing is given simply as,

$$I_{\psi,PT}^{ac \leftarrow ac} = \frac{\sqrt{3}V_1}{2X} cos(\omega_o t_i) \tag{5.9}$$

where $\omega_o t_i$ are the base case firing angles, $\omega_o t_i = (i-1)\frac{\pi}{3} + \frac{\pi}{6} + \alpha - \varphi$, for $i = 1:6$. The sampled spectrum is the same as that described in equation 5.6 except that m is now odd, not even. This means the sampled spectrum contains one positive going and one negative going pulse, rather than two positive going pulses, per fundamental cycle. This spectrum is then multiplied by equation 5.9 to acquire the total sampled partial transient, which is shown in 5.1(c).

The addition of both the SPSS and SPT waveshapes shown in figure 5.1(b) and (c) with the direct conduction waveshapes $I_{dc}\Psi_{\psi}^{ac\leftarrow ac,1}$ shown in figure 5.1(a) gives the total ac side current shown in figure 5.1(d). This can be described as

$$I_{\psi} = I_{dc}\Psi_{\psi}^{ac\leftarrow ac,1} + I_{\psi,SPSS}^{ac\leftarrow ac} + I_{\psi,SPT}^{ac\leftarrow ac}. \tag{5.10}$$

5.2.2 Base case DC voltage spectrum

The base case dc voltage spectrum can be described as the addition of two sampling spectra convolved with the ac side fundamental voltage and summed over all three phases. The rectangular sampling functions required for each phase can be described with a direct conduction sampling function, $\Psi_{\psi}^{dc\leftarrow ac,1}$, and an additional commutation period sampling function, $\Psi_{\psi}^{dc\leftarrow ac,2}$. During the commutation, the ac voltage appearing on the dc side is half the magnitude of the voltage appearing during the direct conduction. Hence, the commutation period sampling function effectively accounts for the commutation period by making the direct conduction transfer a value of $\pm\frac{1}{2}$ during the commutation intervals. The direct conduction transfers can be written as,

$$\Psi_{\psi}^{dc\leftarrow ac,1} = \sum_{m} \frac{4}{m\pi} sin(\frac{m\pi}{3}) cos(m\omega_o t - m(\frac{\pi}{2} + \alpha_o - \varphi + \psi)) \tag{5.11}$$

and the commutation period transfer as,

$$\Psi_{\psi}^{dc\leftarrow ac,2} = \sum_{m} \frac{4}{m\pi} sin(\frac{m\mu_o}{2}) sin(\frac{m\pi}{3}) sin(m\omega_o t - m(\frac{\mu_o}{2} + \frac{\pi}{2} + \alpha_o - \varphi + \psi)) \tag{5.12}$$

where $m = 1, 5, 7, 11\ldots$ The addition of these two sampling functions gives the sampling wave shape shown in figure 5.2(a) and described as $\Psi_{\psi}^{dc\leftarrow ac}$. This is then convolved with the fundamental positive sequence ac voltage (equation 3.4),

$$v_{\psi}^{dc\leftarrow ac} = \Psi_{\psi}^{dc\leftarrow ac} v_{1\psi} \tag{5.13}$$

The resulting convolved spectrum can be written in full as,

$$\begin{aligned} v_{\psi}^{dc\leftarrow ac} = & -\sum_{m} \frac{\sqrt{3}V_1}{(m-1)\pi} sin(m\omega_o t - m\psi + m\varphi - (m-1)(\frac{\pi}{2} + \alpha_o)) \\ & 0 - \sum_{m} \frac{\sqrt{3}V_1}{(m+1)\pi} sin(m\omega_o t - m\psi + m\varphi - (m+1)(\frac{\pi}{2} + \alpha_o)) \\ & + \sum_{m} \frac{\sqrt{3}V_1}{(m-1)\pi} sin(\frac{m\mu_o}{2}) cos(m\omega_o t - m\psi + m\varphi - (m-1)(\frac{\mu_o}{2} + \frac{\pi}{2} + \alpha_o)) \\ & + \sum_{m} \frac{\sqrt{3}V_1}{(m+1)\pi} sin(\frac{m\mu_o}{2}) cos(m\omega_o t - m\psi + m\varphi - (m+1)(\frac{\mu_o}{2} + \frac{\pi}{2} + \alpha_o)) \end{aligned} \tag{5.14}$$

where, $m = 6, 12, 18\ldots$ This is shown in figure 5.2(b) for phase a. The dotted lines show phases b and c. To find the total base case dc voltage each of these three convolved phase voltage waveshapes must be summed over the fundamental cycle, ie,

$$V_{dc} = \sum_{\psi} v_{\psi}^{dc\leftarrow ac} \tag{5.15}$$

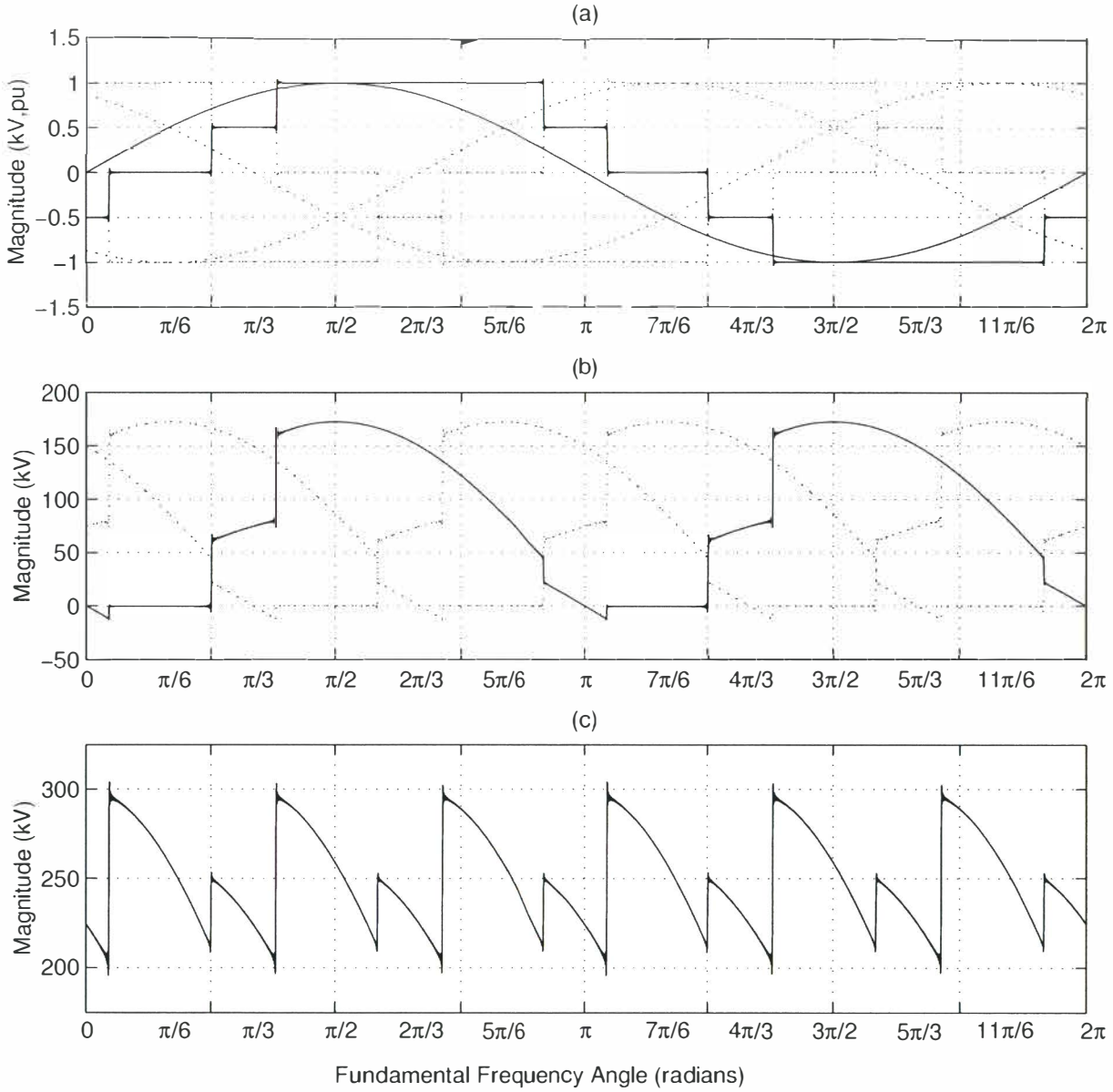

Figure 5.2 Spectrum development of base case DC voltage wave shape, Phase a - bold. (a) Sampling function, $\Psi_{\psi}^{dc \leftarrow ac}$, (b) Convolved result of positive sequence fundamental voltage $v_{1\psi}$ with sampling function $\Psi_{\psi}^{ac \leftarrow dc}$ giving $v_{\psi}^{ac \leftarrow dc}$, (c) Resulting dc voltage V_{dc}.

The summed spectra gives,

$$\begin{aligned} V_{dc} = &- \sum_m \frac{3\sqrt{3}V_1}{(m-1)\pi} cos(m\omega_o t + m\varphi - (m-1)(\frac{\pi}{2} + \alpha_o)) \\ &- \sum_m \frac{3\sqrt{3}V_1}{(m+1)\pi} cos(m\omega_o t + m\varphi - (m+1)(\frac{\pi}{2} + \alpha_o)) \\ &- \sum_m \frac{3\sqrt{3}V_1}{(m-1)\pi} sin(\frac{m\mu_o}{2}) sin(m\omega_o t + m\varphi - (m-1)(\frac{\mu_o}{2} + \frac{\pi}{2} + \alpha_o)) \\ &- \sum_m \frac{3\sqrt{3}V_1}{(m+1)\pi} sin(\frac{m\mu_o}{2}) sin(m\omega_o t + m\varphi - (m+1)(\frac{\mu_o}{2} + \frac{\pi}{2} + \alpha_o)) \end{aligned} \tag{5.16}$$

where as before, $m = 6, 12, 18 \ldots$ This analytically describes the base case dc voltage wave shape and is shown in figure 5.2(c).

5.3 THE SMALL SIGNAL TRANSFERS TO AC CURRENT

The small signal transfers to ac current describe the effects small signal distortions have on the base case ac current waveshapes.

The change in base case ac current spectrum, resulting from ac voltage, dc current, and firing angle distortions can be modelled using Partial Steady State (PSS) and Partial Transient (PT) responses. The PT response exists only during the commutating states while the PSS response can exist during both commutating and direct conducting states. Both responses are sampled for the period (state) they are valid and are called the Sampled Partial Steady State (SPSS) and the Sampled Partial Transient (SPT).

The SPSS is similar to that described previously in section 5.2.1, except that instead of convolving the sampling functions with the fundamental PSS quantities, the small signal PSS quantities are used. The SPSS currents are found for both the direct conduction and commutation periods. For the direct conduction periods the current is just a sampled dc quantity, while for the commutation periods the current is a sampled sinusoid.

During the commutation the initial commutating current must be zero, hence a SPT is required to add to the SPSS to validate these initial conditions. This offset is simply the negative of the SPSS sinusoid at the instant of firing. The SPT is modelled by sampling a sinusoidal signal (the partial transient, PT), which is linearly related through scaling, frequency shifting, and phase shifting, to the applied distorting source. Effectively, the SPT is a constant offset acting during the full duration of each commutation period, its magnitude dependent of the PT response at the firing instants. It is modelled using a Pulse Amplitude Modulated (PAM) spectrum.

In the case of DC current and firing angle distortion, at frequency $k\omega_o$ the PT responses are modulated at the distortion frequency $k\omega_o$, while in the case of an AC voltage distortion the modulation frequency is the distortion frequency, $n\omega_o$, less its sequence, or $(n-s)\omega_o$. Although the PAM spectrum was not used when describing the fundamental base case offset in section 5.2.1, it can be used, the end result being mathematically identical to that described in equation 5.6 with m odd.

This section is split into three subsections. Subsection 5.3.1 describes the SPSS spectrum for the transfers from ac voltage and dc current respectively while subsections 5.3.2 and 5.3.3 describe the PT response and then the SPT, modelled with the PAM spectrum, required to satisfy the initial conditions of each of the commutating currents. The transfer from firing angle distortion is an interesting case as it has no SPSS response, only a SPT response.

5.3.1 The sampled partial steady state (SPSS)

The SPSS ac current from AC voltage distortion, $\Delta I^{ac\leftarrow ac}_{\psi,SPSS}$

The effect on the transfers to ac current, from ac voltage distortion, result solely during the commutation period. During the direct conduction intervals the ac side is directly connected to the dc side, the ac side current the same as the dc current. During the commutating periods the distorted ac side voltage, and hence commutating currents are affected. The SPSS spectrum is derived here while the SPT spectrum is derived in section 5.3.3.

The 6 PSS responses for a given AC voltage distortion, (referenced in the direction the commutation current will flow due to the positive sequence fundamental voltage) are given by,

$$\Delta I^{ac\leftarrow ac}_{i,PSS} = -\frac{\sqrt{3}V_n}{2nX} cos(n\omega_o t - s((i-1)\frac{\pi}{3} + \frac{\pi}{6}) + \delta_n) \tag{5.17}$$

where $i = 1, \ldots, 6$. By recognition of the patterns associated with the six commutating currents a general expression can be written in 3 phase form, as

$$\Delta I^{ac\leftarrow ac}_{\psi,PSS} = -\frac{\sqrt{3}V_n}{2nX} cos(n\omega_o t - s\psi - \frac{s\pi}{6} + \delta_n) \tag{5.18}$$

The sequence of the applied distortion is important as the converter switches positive and negative sequence in different ways. As shown, the PSS response has phase angles which are dependent on the sequence of the applied distortion, ie, for positive sequence $s = 1$ while for negative sequence $s = -1$.

To render the PSS responses correct they must be sampled with the appropriate sampling function, the result being described as the SPSS.

The SPSS in the ψ phase during the commutating off periods is the negative of the SPSS in the phase which is commutating on. Hence, two sampling functions consisting of two pulses of duration μ_o (equation 5.6), are required to sample the PSS. The resulting SPSS spectrum is similar to equation 5.7 except now the distorting PSS responses $\Delta I_{\psi,PSS}$ are used.

$$\Delta I^{ac\leftarrow ac}_{\psi,SPSS} = \Delta I^{ac\leftarrow ac}_{\psi,PSS}\Psi^{ac\leftarrow ac}_{\psi} - \Delta I^{ac\leftarrow ac}_{(\psi+2\pi/3),PSS}\Psi^{ac\leftarrow ac}_{(\psi+2\pi/3)} \tag{5.19}$$

The resulting Fourier series can be written in full as,

$$\begin{aligned}
\Delta I^{ac\leftarrow ac}_{\psi,SPSS} = &+ \frac{\sqrt{3}\mu_o V_n}{n\pi X} sin(\frac{s\pi}{3}) sin(n\omega_o t - s\psi - \frac{s\pi}{2} + \delta_n) \\
&+ \frac{2\sqrt{3}V_n}{n\pi X} \sum_m^{\infty} \frac{1}{m} sin(\frac{m\mu_o}{2}) sin((m+s)\frac{\pi}{3}) \\
&\qquad sin((m+n)\omega_o t - (m+s)\psi - (m+s)\frac{\pi}{2} - m(\frac{\mu_o}{2} + \alpha_o - \varphi) + \delta_n) \\
&+ \frac{2\sqrt{3}V_n}{n\pi X} \sum_m^{\infty} \frac{1}{m} sin(\frac{m\mu_o}{2}) sin((m-s)\frac{\pi}{3}) \\
&\qquad sin((m-n)\omega_o t - (m-s)\psi - (m-s)\frac{\pi}{2} - m(\frac{\mu_o}{2} + \alpha_o - \varphi) - \delta_n)
\end{aligned} \tag{5.20}$$

where $m = 2, 4, 6 \ldots$ The process of building up the spectrum for the transfer to ac current is shown for phase a in figure 5.3(a) for a 0.01pu positive sequence third harmonic voltage. The two PSS responses are shown ($\Delta I^{ac\leftarrow ac}_{a,PSS}$ and $-\Delta I^{ac\leftarrow ac}_{(a+2\pi/3),PSS}$) as dotted lines for phase a, along with the convolved result of equation 5.20 shown in bold. This is the total SPSS response for

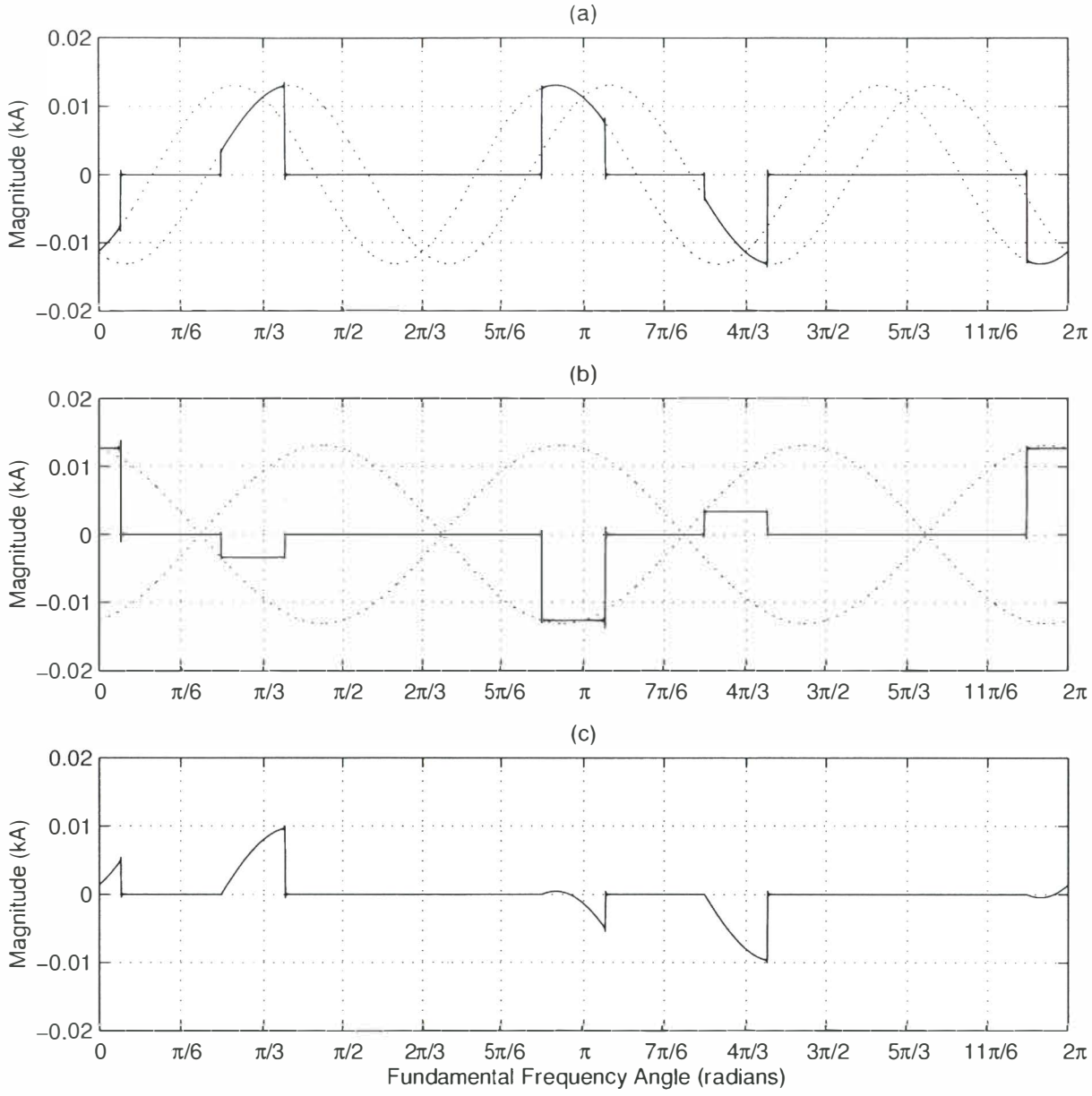

Figure 5.3 Phase a ac current resulting from a small signal 150Hz positive sequence AC voltage distortion. (a) SPSS component during commutation periods $\Delta I_{a,SPSS}^{ac \leftarrow ac}$, (b) SPT component during commutation periods $\Delta I_{a,SPT}^{ac \leftarrow ac}$, (c) Total change in base case ac current, $\Delta I_a^{ac \leftarrow ac}$.

the transfer of ac voltage to current for phase a.

Figure 5.3(b) shows the PT responses (dotted lines) and the resulting SPT spectrum acquired using the PAM spectrum. This is described later in section 5.3.3.

The total change in ac current resulting from ac voltage distortion is the addition of both the SPT and SPSS and can be written as,

$$\Delta I_{\psi}^{ac \leftarrow ac} = \Delta I_{\psi,SPSS}^{ac \leftarrow ac} + \Delta I_{\psi,SPT}^{ac \leftarrow ac} \tag{5.21}$$

and is shown for phase a in figure 5.3(c).

The transfer spectrum for this wave shape is compared with the time domain PSCAD/EMTDC program in figure 5.4. For this transfer the CIGRE benchmark rectifier was used with an applied small signal voltage distortion of 0.01pu at the positive sequence third harmonic.

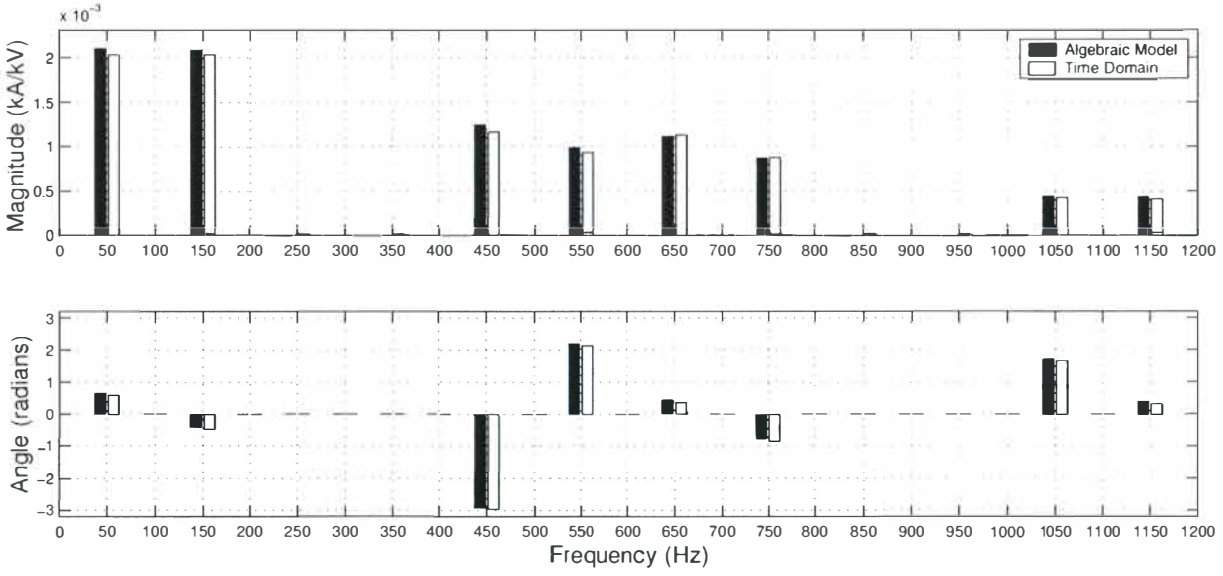

Figure 5.4 Time domain comparison of AC current spectrum resulting from 150Hz positive sequence AC voltage.

The results show the returned positive and negative sequence ac currents. The 50,450,650 and 1050Hz transfers are negative sequence while the 150,550,750 and 1150Hz transfers are positive sequence. These relate to the small signal transfers a and e in Larsen's equation 4.3.

The SPSS ac current from DC current distortion, $\Delta I_{\psi}^{ac \leftarrow dc}$

The transfer resulting from dc current distortion to ac current is similar to that for ac voltage distortion. However, the effect of distortion now occurs over the entire fundamental switching cycle rather than only during the commutation periods. Hence, the PSS component of the ac current is present during a direct conduction period as well as a commutation period, while the PT only affects the commutation periods. The SPSS response is described here while the additional SPT response is described in section 5.3.3.

The PSS response of the AC current due to a DC current distortion is simply either the positive or negative value of the dc current distortion during the direct conduction periods, or half the value of the distortion during the commutation periods.

Hence, the sampling spectra used for the SPSS can be described as the addition of two separate transfer functions. The first transfer function represents the direct conduction periods of the

converter (no commutation period) while the second modifies this to take into account the commutation periods. This sampling function has been described as the addition of equations 5.11 and 5.12 and is written as $\Psi_{\psi}^{dc\leftarrow ac}$ for the base case dc voltage. To save confusion with notation this sampling function is re-notated as $\Psi_{\psi}^{ac\leftarrow dc}$ for this small signal transfer to ac current.

The SPSS spectrum is found from convolution of the sampling function with the applied dc side distortion (equation 3.6), ie,

$$\Delta I_{\psi,SPSS}^{ac\leftarrow dc} = \Psi_{\psi}^{ac\leftarrow dc} \Delta i_{dc} \tag{5.22}$$

giving,

$$\begin{aligned}
\Delta I_{\psi,SPSS}^{dc\leftarrow ac} = &+ \sum_{m} \frac{2I_k}{m\pi} sin(\frac{m\pi}{3}) sin((m+k)\omega_o t - m(\frac{\pi}{2} + \alpha_o - \varphi + \psi) + \delta_k) \\
&- \sum_{m} \frac{2I_k}{m\pi} sin(\frac{m\pi}{3}) sin((m-k)\omega_o t - m(\frac{\pi}{2} + \alpha_o - \varphi + \psi) - \delta_k) \\
&- \sum_{m} \frac{2I_k}{m\pi} sin(\frac{m\mu_o}{2}) sin(\frac{m\pi}{3}) cos((m+k)\omega_o t - m(\frac{\mu_o}{2} + \frac{\pi}{2} + \alpha_o - \varphi + \psi) + \delta_k) \\
&+ \sum_{m} \frac{2I_k}{m\pi} sin(\frac{m\mu_o}{2}) sin(\frac{m\pi}{3}) cos((m-k)\omega_o t - m(\frac{\mu_o}{2} + \frac{\pi}{2} + \alpha_o - \varphi + \psi) - \delta_k)
\end{aligned} \tag{5.23}$$

where $m = 1, 5, 7, 11 \ldots$

Figure 5.5(a) shows the resulting SPSS ac current for phase a. The applied dc current distortion is shown as the dotted line and the resulting SPSS ac current, $\Delta I_{a,SPSS}^{dc\leftarrow ac}$, shown as the solid line after convolution with the sampling spectrum, $\Psi_{a}^{ac\leftarrow dc}$. The addition of this spectrum to the SPT spectrum shown in figure 5.5(b) and described in section 5.3.3 gives the total transfer resulting from dc current distortion shown in figure 5.5(c). The transfer spectrum for this wave shape is compared with the time domain PSCAD/EMTDC program in figure 5.6. For this transfer the CIGRE benchmark rectifier was used with an applied small signal dc current distortion of 0.01pu at the third harmonic. In this instance the frequencies of 100,400,700 and 1000Hz are of negative sequence while the frequencies of 200,500,800 and 1100Hz are of positive sequence, relating to transfers c and g in Larsen's equation 4.3.

The SPSS ac current from firing angle distortion, $\Delta I_{\psi}^{ac\leftarrow\alpha}$

A switching instant change, changes only the initial conditions, not the final steady state waveforms. Hence, the change in the base case ac current, resulting from an applied firing angle distortion can be described with the SPT response. There is no SPSS response and the SPT effect is described in the following sections.

5.3.2 The partial transient (PT) response

The sampled partial transients (SPT) are required to ensure that the zero current initial conditions at the thyristor firing instants are satisfied. To do this the partial transients (PT) must be defined at the instant of firing. These are defined by sinusoids of the correct modulating frequency, magnitude and phase which are used as modulating signals in the Pulse Amplitude Modulated (PAM) spectrum to derive the SPT.

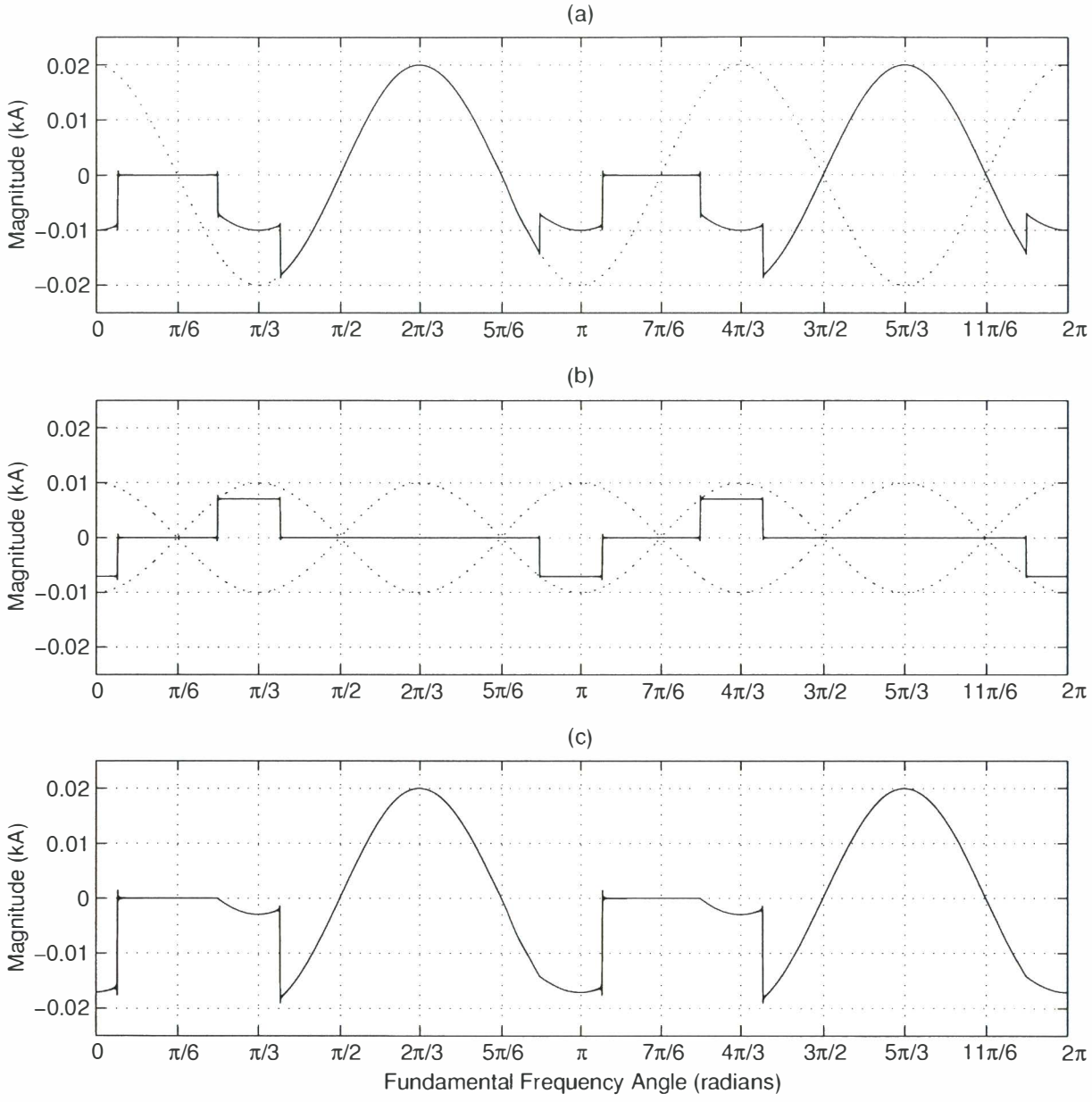

Figure 5.5 Phase a ac current resulting from a small signal 150Hz DC current distortion. (a) SPSS component $\Delta I_{a,SPSS}^{ac \leftarrow dc}$, (b) SPT component during commutation periods $\Delta I_{a,SPT}^{ac \leftarrow dc}$, (c) Total change in base case ac current, $\Delta I_a^{ac \leftarrow dc}$.

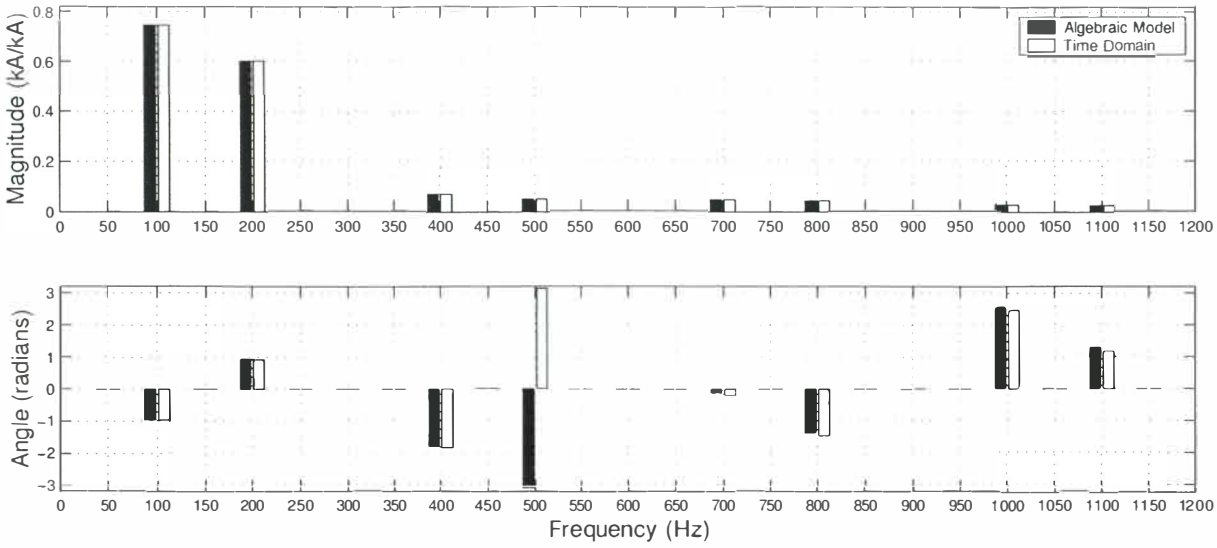

Figure 5.6 Time domain comparison of AC current spectrum resulting from 150Hz dc current distortion.

The unmodified firing instants, referenced to the fundamental phase a voltage, can be written as,

$$\omega_o t_i = (i-1)\pi/3 + \pi/6 + \alpha - \varphi \tag{5.24}$$

where $i = 1, \ldots, 6$. As the commutating current must be zero at the firing instant, the negative value of the PSS at the thyristor firing instant is the value of the required PT and hence SPT.

For an ac voltage distortion, substituting the firing instants, $\omega_o t_i$, into equation 5.17 for $\omega_o t$ results in the value of the distorted commutation current at the instant of thyristor firing, or,

$$\Delta I_{i,PT}^{ac \leftarrow ac} = -\frac{\sqrt{3}V_n}{2nX} cos((n-s)\omega_o t_i + s(\alpha_o - \varphi) + \delta_n) \tag{5.25}$$

where $i = 1, \ldots, 6$.

The PT associated with a DC current distorting source is simply the negative of its associated PSS at the start of the commutation period, ie,

$$\Delta I_{i,PT}^{ac \leftarrow dc} = -\frac{1}{2} I_k sin(k\omega_o t_i + \delta_k) \tag{5.26}$$

The effect of firing angle modulation is slightly different to the previous two cases and can be examined graphically using current-time areas, as shown in figure 5.7. The first effect on the current-time area is due directly to the switching instant variation, producing a nonlinear triangular area as discussed and shown in chapter 4 at the beginning (and end) of commutation. Assuming small signal distortions, these current-time areas can be ignored. Hence, the effect of firing angle modulation can be modelled as an offset acting over the commutation period. Interestingly, this was previously described by Persson [43] in 1970. The magnitude of this offset requires several small signal approximations.

The firing instant occurs when the instantaneous distorted firing angle control signal, and the PLO ramp reference, are equal. The first small signal approximation assumes that the firing instant can be accurately approximated by the value of the firing angle control signal at the unmodified firing instants.

The second approximation is a linearisation around the base case ac commutating current, as

shown in 5.7. The magnitude of the offset is directly proportional, through a small signal linearisation, to the magnitude of the firing angle distortion and the slope of the fundamental commutating current sinusoid at the instant of firing. This relationship is the partial transient associated with the firing angle modulation. The slope of the fundamental commutating current only is used, rather than the slope of the fundamental plus any small signal distortion(s). This is because when the converter is *in situ* within the power system the actual magnitude of the small signal distorting source is unknown. Iterative methods on the other hand iterate the system through mismatch equations finding the magnitude of the distorting source with ac and dc systems attached, then linearise the system after each iteration formulating the Jacobian. This is perhaps considered the 'true' linearisation but can not be calculated with a direct analytic method such as that described in this chapter.

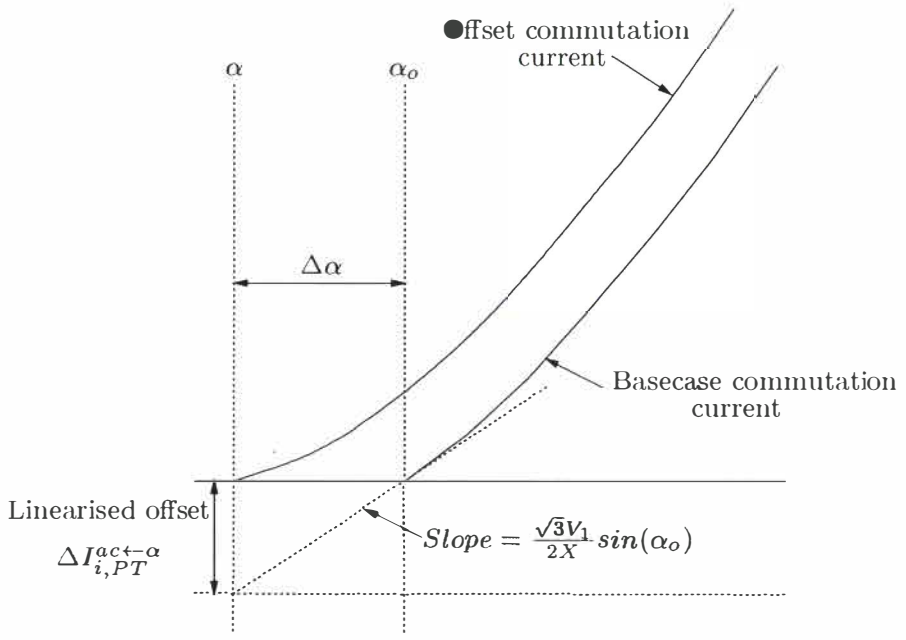

Figure 5.7 Linearisation process to find offset resulting from firing angle modulation.

Hence, the PT resulting from firing angle modulation can be described as,

$$\Delta I_{i,PT}^{ac-\alpha} = -\frac{\sqrt{3}V_1}{2X} sin(\alpha_o)\alpha_k sin(k\omega_o t_i + \delta_k) \tag{5.27}$$

Unlike the change in ac current resulting from AC voltage and DC current distortions, the change in AC current resulting from firing angle modulation is modelled with only a SPT. Comparison with the time domain is shown in figure 5.8 for a small signal, 100Hz, firing angle modulating frequency. Once again the frequencies 50,450,650 and 1050Hz are negative sequence and 150,550,750 and 1150Hz are positive sequence and these relate to the small signal transfers d and h in Larsen's equation 4.3.

The partial transients are described by sinusoids that are valid at the instant of firing, $\omega_o t_i$. These sinusoids are used to define the amplitudes of the PT at the beginning of each conduction period. They are simply linear scaled, phase and frequency shifted versions of the original distorting sources. For AC current distortions the sequence of the distortion is important, altering the frequency of the modulating signal which is either one fundamental frequency higher for negative sequence distortion, or one fundamental lower for positive sequence distortion, $(n - s)\omega_o$, where s is +1 for positive sequence and -1 for negative sequence. For DC current and firing angle distortions the partial transients are modulated at the distorting frequency. In summary the PT responses required for the SPT spectrum (described in section 5.3.3) are given in table 5.1.

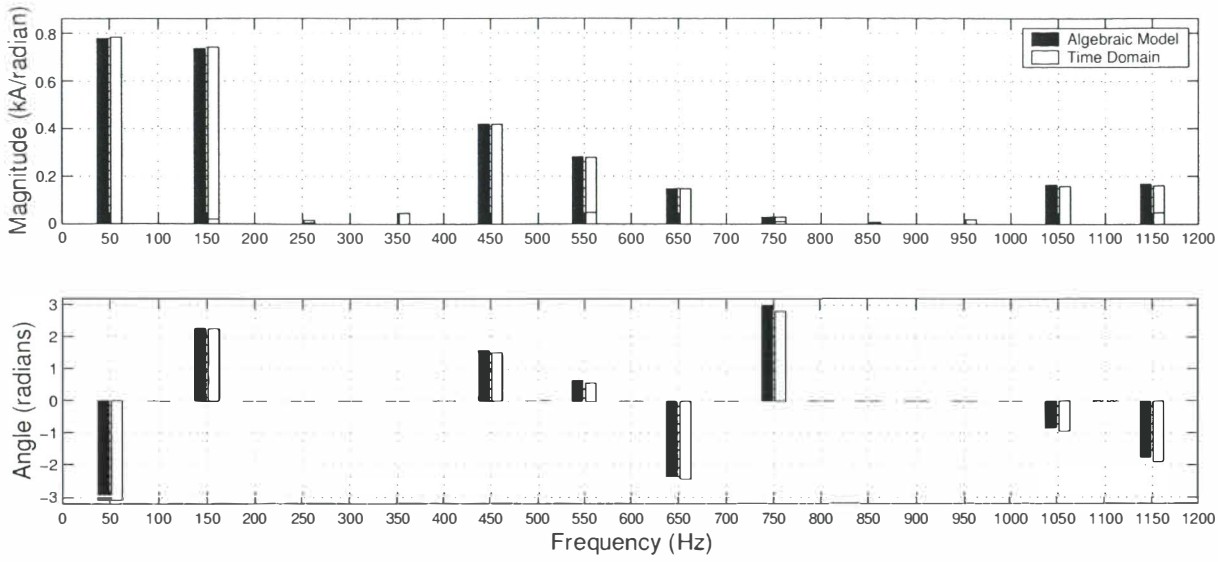

Figure 5.8 Time domain comparison of AC current spectrum resulting from 100Hz firing angle modulation.

Transfer	Applied distortion	PT modulation signal $bcos(k\omega_o t + \delta)$	Eqn. no.
$\Delta V_{ac} - \Delta I_{ac}$	$V_n sin(n\omega_o t - s\psi + \delta_n)$	$-\frac{\sqrt{3}}{2n\lambda} V_n cos((n-s)\omega_o t + s(\alpha_o - \varphi) + \delta_n)$	5.25
$\Delta I_{dc} - \Delta I_{ac}$	$I_k sin(k\omega_o t + \delta_k)$	$-\frac{1}{2} I_k cos(k\omega_o t - \frac{\pi}{2} + \delta_k)$	5.26
$\Delta\alpha - \Delta I_{ac}$	$\alpha_k sin(k\omega_o t + \delta_k)$	$-\frac{\sqrt{3}V_1}{2\lambda} sin(\alpha_o)\alpha_k sin(k\omega_o t + \delta_k)$	5.27

Table 5.1 Applied distortion and commutation current partial transient modulation signals.

5.3.3 The sampled partial transient (SPT)

The partial transient modulation signals in table 5.1 correctly describe the offset required during the commutation periods while modelling the AC currents. These modulation signals must be sampled at the start of the commutation periods, and hold the magnitude of the modulation constant during the commutation period. This is achieved by using a Pulse Amplitude Modulated (PAM) spectrum, modulated by the correct PT signals.

The general spectrum of a PAM wave shape with pulses occurring at $\omega_o t = 2n\pi$, of width μ_o, and having a modulation signal $bcos(k\omega_o t + \delta)$ is derived in appendix E and is given by,

$$\begin{aligned} PAM(\omega_o t) = &+ \frac{b\mu_o}{2\pi} sinc(\frac{k\mu_o}{2\pi}) cos(k\omega_o t - k\frac{\mu_o}{2} + \delta) \\ &+ \frac{b\mu_o}{2\pi} \sum_{m=1}^{\infty} sinc((m+k)\frac{\mu_o}{2\pi}) cos((m+k)\omega_o t - (m+k)\frac{\mu_o}{2} + \delta) \\ &+ \frac{b\mu_o}{2\pi} \sum_{m=1}^{\infty} sinc((m-k)\frac{\mu_o}{2\pi}) cos((m-k)\omega_o t - (m-k)\frac{\mu_o}{2} - \delta) \end{aligned} \tag{5.28}$$

Four PAM waveforms must be added together (one for each commutation period) to model each phase of the converter. Each of the four PAM waveforms are obtained by scaling and phase shifting the waveform described in equation 5.28 by the values given in table 5.2. The $\pm$ scalars are required as the partial transient modulation signal is referenced in the positive direction of the thyristors, alternating between the positive and negative directions of the AC current. The

general SPT can be described as,

$$\Delta I_{\psi,SPT} = \sum_{i=1}^{4} PAM_i(\omega_o t) \tag{5.29}$$

where the PAM spectra are modulated by the correct modulating signal b, depending on the applied distortion as described in table 5.1. The addition of the four spectra gives the fol-

Sign	Phase shift
$+1$	$-\pi/6 - \alpha_o + \varphi - \psi$
-1	$-5\pi/6 - \alpha_o + \varphi - \psi$
-1	$-7\pi/6 - \alpha_o + \varphi - \psi$
$+1$	$+\pi/6 - \alpha_o + \varphi - \psi$

Table 5.2 Phase shifts required for each PAM spectrum.

lowing general SPT spectrum, suitable for the SPT resulting from dc current and firing angle modulation,

$$\begin{aligned}\Delta I_{\psi,SPT}^{ac\leftarrow dc,\alpha} = &+ \frac{2b\mu_o}{\pi}\sum_m sin(\frac{m\pi}{2})cos(\frac{m\pi}{6})sinc((m+k)\frac{\mu_o}{2\pi}) \\ &\qquad sin((m+k)\omega_o t - (m+k)\frac{\mu_o}{2} - m(\frac{\pi}{2} + \alpha_o - \varphi + \psi) + \delta) \\ &+ \frac{2b\mu_o}{\pi}\sum_m sin(\frac{m\pi}{2})cos(\frac{m\pi}{6})sinc((m-k)\frac{\mu_o}{2\pi}) \\ &\qquad sin((m-k)\omega_o t - (m-k)\frac{\mu_o}{2} - m(\frac{\pi}{2} + \alpha_o - \varphi + \psi) - \delta)\end{aligned} \tag{5.30}$$

where $m = 1, 5, 7, 11 \ldots$.

For the transfers from ac voltage it is easiest to rewrite the spectrum frequency in terms of m and s instead of k. In order to do this, the following substitutions are made, $(m - s) \rightarrow m$, for the first summation and, $(m + s) \rightarrow m$, for the second summation. The values of m over which the summation is made now depend upon the sequence of the applied distortion. The resulting spectrum is,

$$\begin{aligned}\Delta I_{\psi,SPT}^{ac\leftarrow ac} = &+ \frac{2b\mu_o}{\pi}\sum_m sin((m+s)\frac{\pi}{2})cos((m+s)\frac{\pi}{6})sinc((m+n)\frac{\mu_o}{2\pi}) \\ &\qquad sin((m+n)\omega_o t - (m+n)\frac{\mu_o}{2} - (m+s)(\frac{\pi}{2} + \alpha_o - \varphi + \psi) + \delta) \\ &+ \frac{2b\mu_o}{\pi}\sum_m sin((m-s)\frac{\pi}{2})cos((m-s)\frac{\pi}{6})sinc((m-n)\frac{\mu_o}{2\pi}) \\ &\qquad sin((m-n)\omega_o t - (m-n)\frac{\mu_o}{2} - (m-s)(\frac{\pi}{2} + \alpha_o - \varphi + \psi) - \delta)\end{aligned} \tag{5.31}$$

Figures 5.3(b) and 5.5(b) show the SPT and their associated PT modulating signals resulting from both ac voltage and dc current distortion respectively.

5.4 THE SMALL SIGNAL TRANSFERS TO DC VOLTAGE

Unlike the transfers to AC current, switching instant variation directly affects the transfers to DC voltage. Therefore the linearised change in the base case dc voltage is calculated with the sum of two main effects: the transfer of the distorted waveshapes through the undistorted sampling functions, added to the effect of the base case waveshapes transferred through the distorted sampling functions. The effect of the distorted waveshapes on the distorted sampling functions is non-linear, of higher order and reduces to zero as distortion levels tend towards zero.

The PT responses associated with the transfers to ac current have no effect on the transfers to dc voltage. This is true under the assumption that the commutating impedance remains purely inductive.

To model SIV, first a linearised phasor describing the SIV must be found, then a correction term is required in the sampling function and convolved with the base ac voltage. The correction term required for the SIV is modelled with the use an Amplitude Modulated Impulse Train (AMIT) and generates extra nonlinear and linear terms in the dc voltage spectrum. The total transfers to dc voltage are hence made from a SPSS spectrum with an additional SIV spectrum.

This section is split into four subsections. The first describes the SPSS responses, denoted by $\Delta V_{SPSS}^{dc\leftarrow ac}$ and $\Delta V_{SPSS}^{dc\leftarrow dc}$ respectively. The second describes the linearisation around the base case commutating current, required to find the approximate SIV magnitude while the third uses the linearisation to derive the actual change in the DC voltage waveform resulting from the SIV. The final section shows the results verified against time domain PSCAD/EMTDC simulation.

5.4.1 The sampled partial steady state (SPSS)

The SPSS responses of the DC voltage due to an AC voltage distortion during the direct and commutation periods are described by the convolution of the sampling functions (equations 5.11 and 5.12) with the ac voltage distortion, Δv_ψ. The convolution of the sampling functions with the small signal ac voltage distortions are effectively the same as equations 5.13 and 5.14 except that the fundamental voltage, $v_1\angle\varphi$ (equation 3.4), is replaced by the distorting voltage $v_n\angle\delta_n$ (equation 3.5). In symbolic form, this can is represented as,

$$\Delta V_{SPSS}^{dc\leftarrow ac} = \sum_{\psi} \Psi_{\psi}^{dc\leftarrow ac} \Delta v_\psi \tag{5.32}$$

This gives a similar result to that shown in equation 5.16, except the fundamental parameters must be replaced by the distorting source parameters, this is not repeated here.

For the DC voltage SPSS response resulting from DC current, the commutation circuit must be analysed in a piece-wise linear manner for the direct conduction and commutation states. Figure 5.9 shows both states and the resulting PSS dc voltage generated from a dc current distortion, Δi_{dc}. These voltages are simply written as,

$$\Delta V_{PSS}^{dc\leftarrow dc,1} = -2kX\Delta i_{dc} \tag{5.33}$$

$$\Delta V_{PSS}^{dc\leftarrow dc,2} = -\tfrac{3}{2}kX\Delta i_{dc} \tag{5.34}$$

$$\tag{5.35}$$

where Δi_{dc} is as described in equation 3.6. As shown the difference between the PSS voltage, $\Delta V_{PSS}^{dc\leftarrow dc,1}$, during a direct conduction period and the PSS voltage, $V_{PSS}^{dc\leftarrow dc,2}$, during a commutation period is simply a scaling factor. This can be taken into account in the sampling transfer

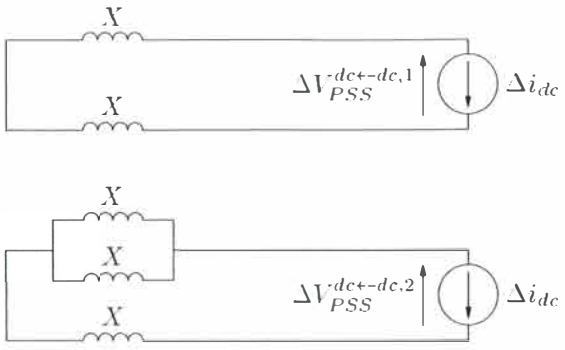

Figure 5.9 PSS dc voltage during the direct conduction and commutating states.

function, Ψ^{dc-dc}. Hence, the total DC voltage SPSS can be written simply as,

$$\Delta V_{SPSS}^{dc-dc} = -\Psi^{dc-dc} k X \Delta i_{dc} \tag{5.36}$$

The sampling function, Ψ^{dc-dc} is made from the addition of two Fourier series representing both the direct and commutation periods. The first Fourier Series representing the direct conduction periods is,

$$\Psi^{dc\leftarrow dc,1} = \frac{3\mu_o}{\pi} + \sum_m \frac{12}{m\pi} sin(\frac{m\mu_o}{2}) cos(m\omega_o t - m(\frac{\pi}{6} + \alpha_o - \varphi)) \tag{5.37}$$

The second Fourier series representing the commutation periods is,

$$\Psi^{dc\leftarrow dc,2} = (1 - \frac{3\mu_o}{\pi}) - \sum_m \frac{12}{m\pi} sin(\frac{m\mu_o}{2}) cos(m\omega_o t - m(\frac{\pi}{6} + \alpha_o - \varphi)) \tag{5.38}$$

Combining $\frac{3}{2}\Psi^{dc\leftarrow dc,1} + 2\Psi^{dc\leftarrow dc,2}$ gives the required sampling function,

$$\Psi^{dc-dc} = (2 - \frac{3\mu_o}{2\pi}) - \sum_m \frac{6}{m\pi} sin(\frac{m\mu_o}{2}) cos(m\omega_o t - m(\frac{\pi}{6} + \alpha_o - \varphi)) \tag{5.39}$$

This is shown in graphical form in figure 5.10(a). The SPSS dc current to dc voltage transfer then becomes,

$$\begin{aligned} \Delta V_{SPSS}^{dc-dc} = & -(2 - \frac{3\mu_o}{\pi}) k X I_k cos(k\omega_o t + \delta_k) \\ & + \sum_m \frac{3}{m\pi} sin(\frac{m\mu_o}{2}) cos((m+k)\omega_o t - m(\frac{\pi}{6} + \alpha_o - \varphi) + \delta_k) \\ & + \sum_m \frac{3}{m\pi} sin(\frac{m\mu_o}{2}) cos((m-k)\omega_o t - m(\frac{\pi}{6} + \alpha_o - \varphi) - \delta_k) \end{aligned} \tag{5.40}$$

and is shown in figure 5.10(b) where a 0.01 p.u. 150Hz dc current distortion is applied to the converter terminals.

Both $\Delta V_{SPSS}^{dc\leftarrow ac}$ and ΔV_{SPSS}^{dc-dc} show the partial steady state response assuming no switching instant variation. However, as shown in chapter 4, the SIV must be taken into account due to the step voltages occurring at the switching instants. The following section derives the required linearisations needed for finding the SIV.

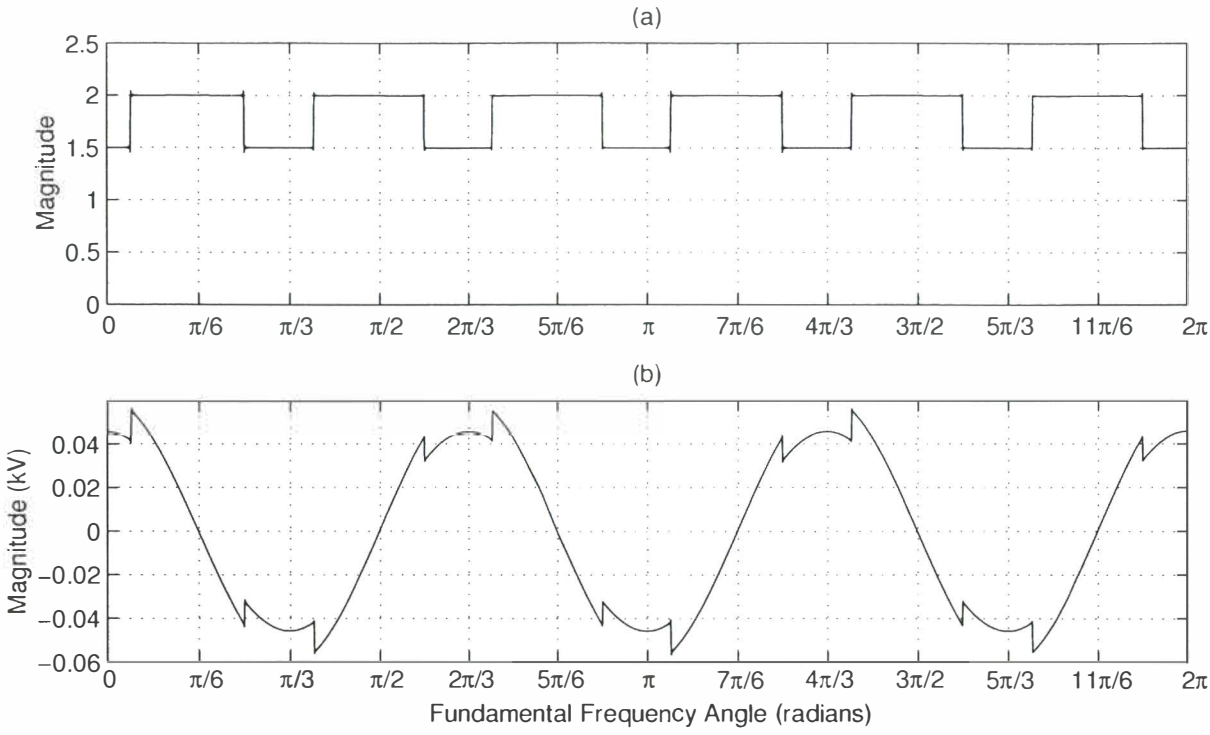

Figure 5.10 SPSS DC voltage resulting from a 150Hz dc current distortion. (a) Sampling function, Ψ^{dc-dc}, (b) Resulting SPSS DC voltage, V_{SPSS}^{dc-dc}.

5.4.2 The switching instant variation (SIV)

This section describes the linearisations required for predicting the resulting variation of the switching instants when the converter is subjected to applied waveform distortion. Although the exact SIV can only be found using an iterative model (such as that described in chapter 3), very good small signal linearisations can be made with careful observation of the commutation period dynamics resulting from the various applied distortions. SIV was first described by Wood [17] in his linearised converter model. His work is effectively repeated here, although described in a some what different manner.

It should be noted that this section derives phasors that describe the actual SIV resulting from small signal distortions, and not the effect of the SIV has on the dc voltage which is described in section 5.4.3.

This section is split into three subsections, each defining the phasor required to describe the SIV resulting from ac voltage, dc current and firing angle distortion separately. Linearised relationships are found using simple graphical analysis of the commutation period in all cases.

Switching instant variation resulting from ac voltage distortion

The SIV resulting from ac voltage distortion affects only the end of commutating instants, ϕ_i as the firing instants, θ_i remain fixed. The true end of commutation period occurs when the total commutating current equals the dc current and the thyristor stops conducting. When ac side voltage distortion is applied to the converter terminals the effects on the ac current are confined only to the commutation period as during the direct conducting periods the thyristors are directly connected to an undistorted dc current source.

The distorted commutation current causes the end of commutation instants to vary so that the conduction through the thyristor ends when the distorted commutating current equals the dc

current. A linearisation around the base case switching instants can be used to approximate this switching instant variation, and is described as follows. At the base case end of commutation switching instant, $\alpha_o + \mu_o$, (not the actual end of commutation switching instant, $\alpha_o + \mu$), there exists a small difference (mismatch, Y) in the current between the constant dc current on the dc side of the base case switching instant, and the distorted commutation current on the commutation side of the base case switching instant. This difference is easily found as both the distorted commutating current (a combination of the PT and PSS responses) and the constant dc current are known at the base case switching instant. Also, the slope, or gradient, of the fundamental commutating current is also known at the base case switching instant. Hence, to find the required SIV, simple trigonometry can be used as shown in figure 5.11. The mis-match,

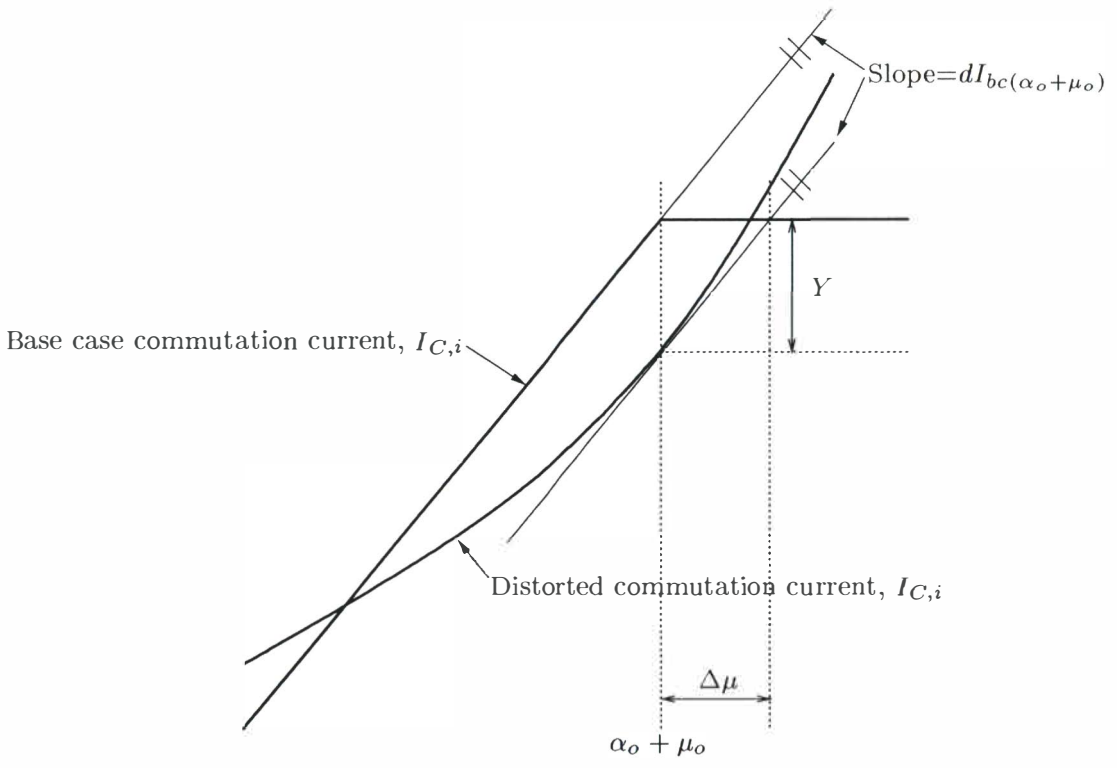

Figure 5.11 Linearisation process to find end of commutation period variation from ac voltage.

Y, can be written as,

$$Y = -\frac{\sqrt{3}V_n}{2nX}cos((n-s)\omega_o t_i + s\alpha_o + \delta_n) + \frac{\sqrt{3}V_n}{2nX}cos((n-s)\omega_o t_i + s(\alpha_o + \mu_o) + \delta_n) \quad (5.41)$$

where, $\omega_o t_i$ are the firing instants. The derivative of the base case commutating current at the average end of commutation is,

$$dI_{bc(\alpha_o+\mu_o)} = \frac{\sqrt{3}V_1}{2X}sin(\alpha_o + \mu_o) \quad (5.42)$$

Hence, the commutation period modulation can be found from,

$$\Delta\mu = \frac{Y}{dI_{bc(\alpha_o+\mu_o)}} \quad (5.43)$$

Table 5.3 gives the resulting SIV phasor for this transfer.

Switching instant variation resulting from dc current distortion

For the transfers from dc current distortion the firing instants, (θ_i), remain fixed and a similar relationship exists for the end of commutation SIV. In this case, the value of the dc current distortion at the end of commutation period $(\alpha_o + \mu_o)$ must be taken into account. Figure 5.12 shows this. Once again, the mis-match Y can be found knowing the value of the distortion

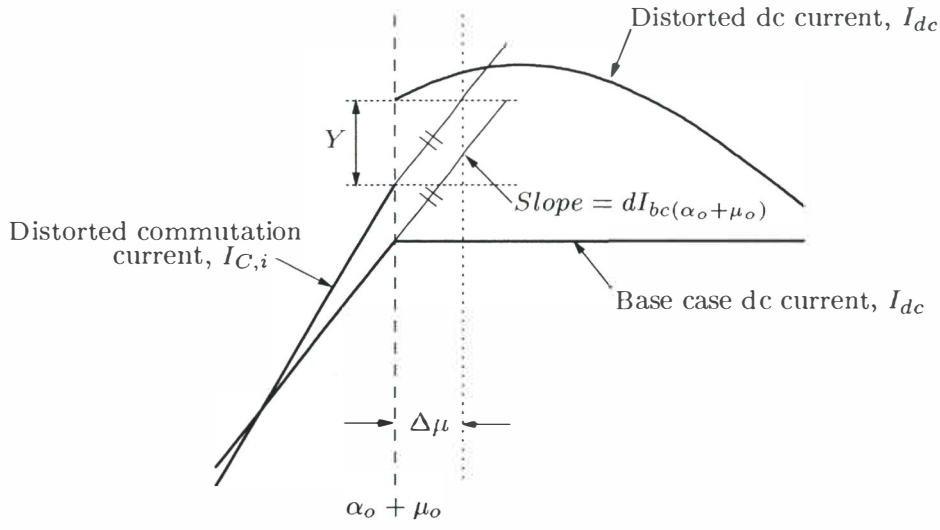

Figure 5.12 Linearisation process to find end of commutation period variation from dc current.

just after, and subtracting the value of the distorted commutation current, just before the base case end of commutation instant. The value just before the end of commutation comprises of the PSS (the dc current distortion divided by two), plus the required PT needed to ensure the commutating current is zero at the firing instant. The value just after the commutation period is simply the distortion itself at $\alpha_o + \mu_o$. Hence, in the order described above.

$$Y = I_k sin(k\omega_o t_i + k\mu_o + \delta_k) - (\frac{I_k}{2} sin(k\omega_o t_i + k\mu_o + \delta_k) - \frac{I_k}{2} sin(k\omega_o t_i + \delta_k)) \tag{5.44}$$

Which reduces to,

$$Y = I_k sin(k\omega_o t_i + \frac{k\mu_o}{2} + \delta_k) cos(\frac{k\mu_o}{2}) \tag{5.45}$$

Equation 5.43 can then be used to find $\Delta\mu$. The result is given in table 5.3.

Switching instant variation resulting from firing angle distortion

As discussed in chapter 3, the solution of the exact firing instants is nonlinear and must be solved using iterative means. For ac voltage and dc current distortions the firing instants remain fixed. For firing angle distortion however, the firing instants can be approximated by the value of the firing angle control signal at the unmodified switching instants, $\omega_o t_i$. This linearisation becomes exact as the distortion tends towards zero, equation 3.7.

To find the end of commutation period SIV resulting from applied firing angle distortion, two separate linearisations are required. The first is the linearisation needed to find the PT offset resulting from the applied firing angle distortion. This has been shown previously in figure 5.7 and described by equation 5.27 and is the value of Y in figure 5.13. The second is the linearisation required to find the end of commutation SIV and is similar to those described above. Figure 5.13 shows the effect of a firing angle distortion on the end of commutating period instant. The

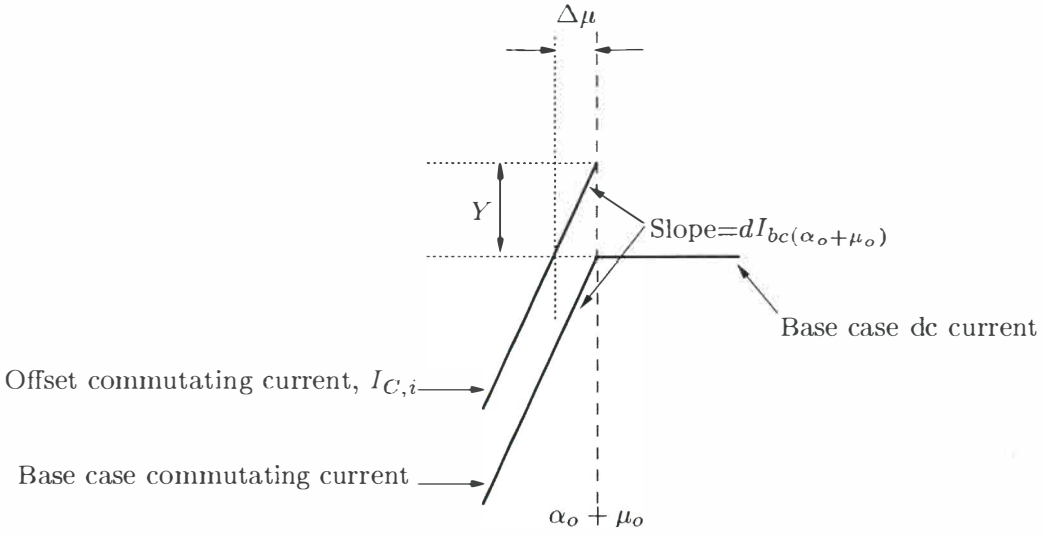

Figure 5.13 Linearisation process to find end of commutation period variation from fam.

commutation period variation, $\Delta\mu$, is then easily found using equation 5.43. The linearised SIV resulting form firing angle distortion, along with the resulting linearised variation from both ac voltage and dc current is given in table 5.3.

Transfer	SIV Beginning (θ_i)	SIV end (ϕ_i) in form $bcos(k\omega_o t + \delta)$
$\Delta V_{ac} - \Delta V_{dc}$		$-\frac{2sin(\frac{n\mu_o}{2})}{n\sqrt{1}sin(\alpha_o+\mu_o)} V_n sin((n-s)\omega_o t + s(\alpha_o - \varphi) + \frac{n\mu_o}{2} + \delta_n)$
$\Delta I_{dc} - \Delta V_{dc}$		$\frac{2\lambda cos(\frac{k\mu_o}{2})}{\sqrt{3}V_1 sin(\alpha_o+\mu_o)} I_k sin(k\omega_o t + \frac{k\mu_o}{2} + \delta_k)$
$\Delta\alpha - \Delta V_{dc}$	$\alpha_k sin(k\omega_o t + \delta_k)$	$\frac{sin(\alpha_o)}{sin(\alpha_o+\mu_o)} \alpha_k sin(k\omega_o t + \delta_k)$

Table 5.3 Linearised SIV phasors ($b\angle\delta$) resulting from ac voltage, dc current and firing angle distortions.

The SIV is given as a sinusoidal signal in general phasor form $bcos(k\omega_o t + \delta)$ describing the change in the unmodified, undistorted base case firing instants, $\omega_o t_i$. Each signal is a linearly scaled, frequency shifted and phase shifted version of the original distorting signal.

5.4.3 Effects of the SIV on the dc voltage

As shown in chapter 4, SIV has a linear effect on the transfers of distortion to dc voltage and must be modelled. Linearised phasors describing the SIV have been analytically derived in the previous section.

The base case dc voltage can be considered as being made from the piecewise combination of the partial steady state waveforms associated with only the base AC voltage $v_{1\psi}$, or,

$$V_{dc} = \sum_{\psi} \Psi_{\psi}^{dc \leftarrow ac} v_{1\psi} \tag{5.46}$$

The effect of SIV changes the sampling function $\Psi_{\psi}^{dc \leftarrow ac}$ and hence the change in dc voltage associated with this can be described as,

$$\Delta V_{SIV}^{dc} = \sum_{\psi} \Delta\Psi_{\psi}^{dc \leftarrow ac} v_{1\psi} \tag{5.47}$$

The SIV has been derived in the previous section using phasors referenced to the base case switching angles. These signals are required to make an additional modulating transfer, correcting the original sampling function. If the signal is negative at the original firing instant then the firing or commutation instant is advanced, while if the signal is positive the switching instant is delayed. As the signals are referenced to the base case firing instants ($\omega_o t_i$) the signals for the end of commutation period SIV must be delayed by the average commutation period, ie, phase shifted by μ_o.

The effects of SIV on the dc voltage, as described by equation 5.47, has been previously modelled by Wood [17] in his analysis of the commutation period dynamics using a Pulse Duration Modulated (PDM) spectra. This spectrum results in first and higher order frequency terms with nonlinear Bessel function multipliers. For the linear small signal model it can be shown that these higher order terms are insignificant for small signal distortion. Hence for a linear analysis, only the first order terms are required. Interestingly, the spectrum of the PDM wave shape for only first order terms is the same as an amplitude modulated delta function spectrum (*Dirac comb*) or equivalently an Area Modulated Impulse Train (AMIT). The spectrum for the AMIT is derived in appendix E. The Fourier series for a set of delta functions spaced at 2π intervals but modulated in their effective area by, $bcos(k\omega_o t + \delta)$, is given as,

$$AMIT(\omega_o t) = +\frac{b}{2\pi}cos(k\omega_o t + \delta) + \frac{b}{2\pi}\sum_{m=1}^{\infty} cos((m+k)\omega_o t + \delta) + \frac{b}{2\pi}\sum_{m=1}^{\infty} cos((m-k)\omega_o t - \delta) \tag{5.48}$$

For a single phase of the converter, the AMIT (or first order PDM spectra) is required at the end of the commutation period to correct the sampling function. Hence, four first order PDM spectra are required per phase and can be described as,

$$\Delta\Psi_{\psi}^{dc\leftarrow ac} = \sum_{i=1}^{4} AMIT_i(\omega_o t) \tag{5.49}$$

For firing angle distortion, another four AMIT spectra are required at the instant of firing hence requiring eight first order AMIT spectra per phase, this is shown graphically in figure 5.14. Table 5.4 gives the angles of the AMIT required for the beginning and end of each commutation period. Assuming the general case, four AMIT spectra can be added with the appropriate

i	Scaler	Angle shift beginning	Angle shift end
1	$-\frac{1}{2}$	$-\frac{\pi}{6} - \alpha_o + \varphi - \psi$	$-\frac{\pi}{6} - \alpha_o - \mu_o + \varphi - \psi$
2	$+\frac{1}{2}$	$-\frac{5\pi}{6} - \alpha_o + \varphi - \psi$	$-5\frac{\pi}{6} - \alpha_o - \mu_o + \varphi - \psi$
3	$+\frac{1}{2}$	$-\frac{7\pi}{6} - \alpha_o + \varphi - \psi$	$-7\frac{\pi}{6} - \alpha_o - \mu_o + \varphi - \psi$
4	$-\frac{1}{2}$	$+\frac{\pi}{6} - \alpha_o + \varphi - \psi$	$+\frac{\pi}{6} - \alpha_o - \mu_o + \varphi - \psi$

Table 5.4 Angle shifts required for AMIT spectra.

phase angles and written as,

$$\begin{aligned}\Delta\Psi_{\psi}^{dc\leftarrow ac} = &+\frac{b}{\pi}\sum_{m} sin(\frac{m\pi}{2})cos(\frac{m\pi}{6})sin((m+k)\omega_o t - m\psi - m(\frac{\pi}{2}+\varphi) - k\chi + \delta) \\ &+\frac{b}{\pi}\sum_{m} sin(\frac{m\pi}{2})cos(\frac{m\pi}{6})sin((m-k)\omega_o t - m\psi - m(\frac{\pi}{2}+\varphi) + k\chi - \delta)\end{aligned} \tag{5.50}$$

where $m = 1, 5, 7, 11\ldots$ and φ is the angle shift in the AMIT waveform and χ is the angle shift in the modulation signal. The relative values are given in table 5.5. This spectrum is then multiplied by the positive sequence fundamental frequency voltage and summed over the three

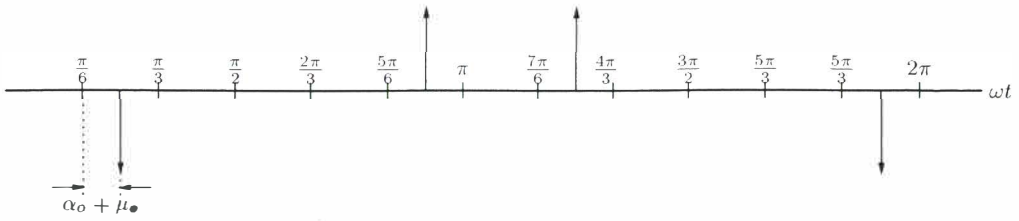

(a) Combined AMIT required for transfers from I_{dc} and V_{ac}, phase a.

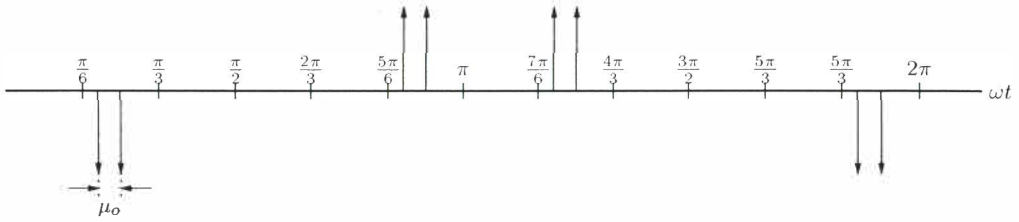

(b) Combined AMIT required for transfers from firing angle modulation, phase a.

Figure 5.14 Combined AMIT spectra for phase a

Variable	Angle beginning pulse	Angle ending Pulse
φ	$\alpha_o - \varphi$	$\alpha_o + \mu_o - \varphi$
χ		μ_o

Table 5.5 Required phase angles for AMIT spectrum and modulating signal.

phases to gain the full change in the dc voltage spectrum, equation 5.47.

Due to the sequence dependence on the AMIT spectra for transfers resulting from ac voltage distortion, two separate spectra are derived, one for the transfers associated with dc current and firing angle distortion and the second for transfers associated with ac voltage distortion.

The transfers resulting from dc current and firing angle distortion are written as,

$$\begin{aligned}
\Delta V_{SIV}^{dc \leftarrow dc,\alpha} = & + \frac{3\sqrt{3}V_1 b}{2\pi} cos(\frac{\pi}{2}+\varphi) cos(k\omega_o t - k\chi + \delta) \\
& + \frac{3V_1 b}{2\pi} \sum_m sin((m+1)\frac{\pi}{2}) cos((m+1)\frac{\pi}{6}) [cos((m+k)\omega_o t - (m+1)(\frac{\pi}{2}+\varphi) - k\chi - \varphi + \delta) \\
& + cos((m-k)\omega_o t - (m+1)(\frac{\pi}{2}+\varphi) + k\chi - \varphi - \delta)] \\
& - \frac{3V_1 b}{2\pi} \sum_m sin((m-1)\frac{\pi}{2}) cos((m-1)\frac{\pi}{6}) [cos((m+k)\omega_o t - (m-1)(\frac{\pi}{2}+\varphi) - k\chi + \varphi + \delta) \\
& + cos((m-k)\omega_o t - (m-1)(\frac{\pi}{2}+\varphi) + k\chi + \varphi - \delta)]
\end{aligned} \tag{5.51}$$

where $m = 6, 12 \ldots$ The SIV phasors derived in section 5.4.2 and given in table 5.3 must be substituted into this equation for $b\angle\delta$. The angles in table 5.5 must also be included. For firing angle distortion two spectra are required, one at the beginning and one at the end of the commutation period, both with the appropriate SIV phasor substitutions and angles of tables 5.3 and 5.5. The summation of both giving the total effect of SIV on the dc voltage from firing angle distortion.

For the transfer from ac voltage to dc voltage the first order AMIT spectrum must allow for the voltage sequence. Making the required frequency substitutions and summing over 3 phases

gives,

$$
\begin{aligned}
&V_{SIV}^{dc\leftarrow ac} = \\
&+\frac{3V_1 b}{2\pi}\sum_m sin((m+1+s)\frac{\pi}{2})cos((m+1+s)\frac{\pi}{6})cos((m+n)\omega_o t-(m+1+s)(\frac{\pi}{2}+\varphi)-(n-s)\chi-\varphi+\delta) \\
&-\frac{3V_1 b}{2\pi}\sum_m sin((m-1+s)\frac{\pi}{2})cos((m-1+s)\frac{\pi}{6})cos((m+n)\omega_o t-(m-1+s)(\frac{\pi}{2}+\varphi)-(n-s)\chi+\varphi+\delta) \\
&+\frac{3V_1 b}{2\pi}\sum_m sin((m+1-s)\frac{\pi}{2})cos((m+1-s)\frac{\pi}{6})cos((m-n)\omega_o t-(m+1-s)(\frac{\pi}{2}+\varphi)+(n-s)\chi-\varphi-\delta) \\
&-\frac{3V_1 b}{2\pi}\sum_m sin((m-1-s)\frac{\pi}{2})cos((m-1-s)\frac{\pi}{6})cos((m-n)\omega_o t-(m-1-s)(\frac{\pi}{2}+\varphi)+(n-s)\chi+\varphi-\delta)
\end{aligned}
\tag{5.52}
$$

where $m = 6, 12\ldots$ This describes the spectrum for the change in the dc voltage required for the transfers resulting from ac voltage distortion. As with equation 5.51 the SIV phasors in table 5.3 must be substituted for $b\angle\delta$ as well as the angle ending pulse data in table 5.5.

5.4.4 Validation of the transfers to dc voltage

To acquire the total transfers to dc voltage both the SPSS voltages and the change in dc voltage resulting from SIV are added together. The comparison between PSCAD/EMTDC and the algebraic model is given in figures 5.15,5.16 and 5.17 for the resulting change in the dc voltage due to ac voltage, dc current and firing angle distortions respectively. As shown, non-linear second order terms, not predicted by the linearised model, are seen in the time domain simulation results for all figures.

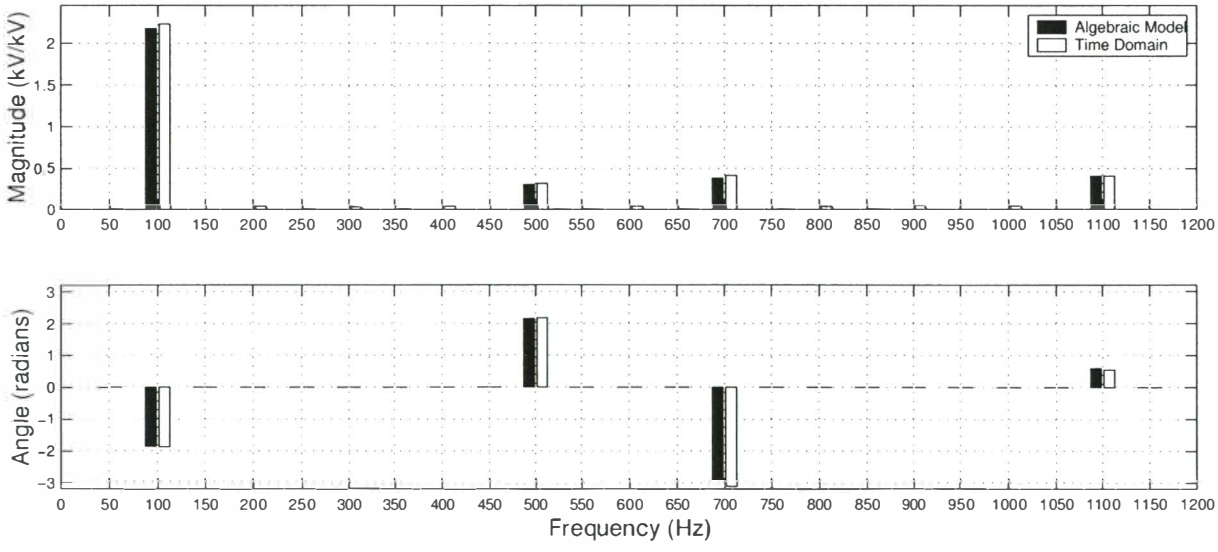

Figure 5.15 Time domain comparison of DC voltage spectrum resulting from 50Hz negative sequence distortion.

5.5 CONCLUSIONS

There are two parts of the resulting returned spectra when an arbitrary distortion is applied to the HVDC converter; there is a set of linear first order spectra and a set of nonlinear higher order

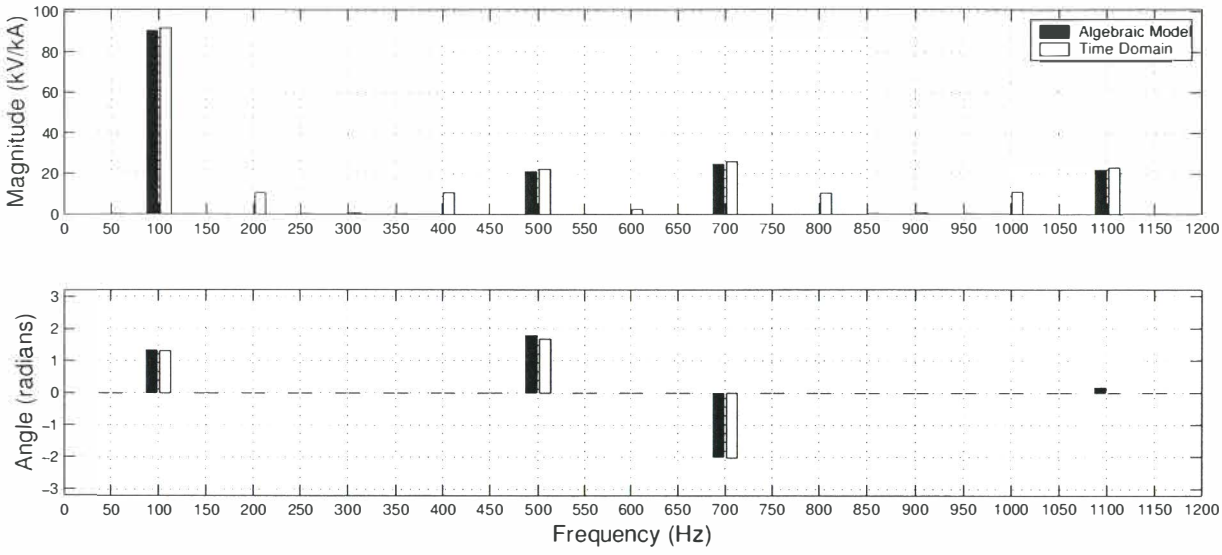

Figure 5.16 Time domain comparison of DC voltage spectrum resulting from 100Hz dc current distortion.

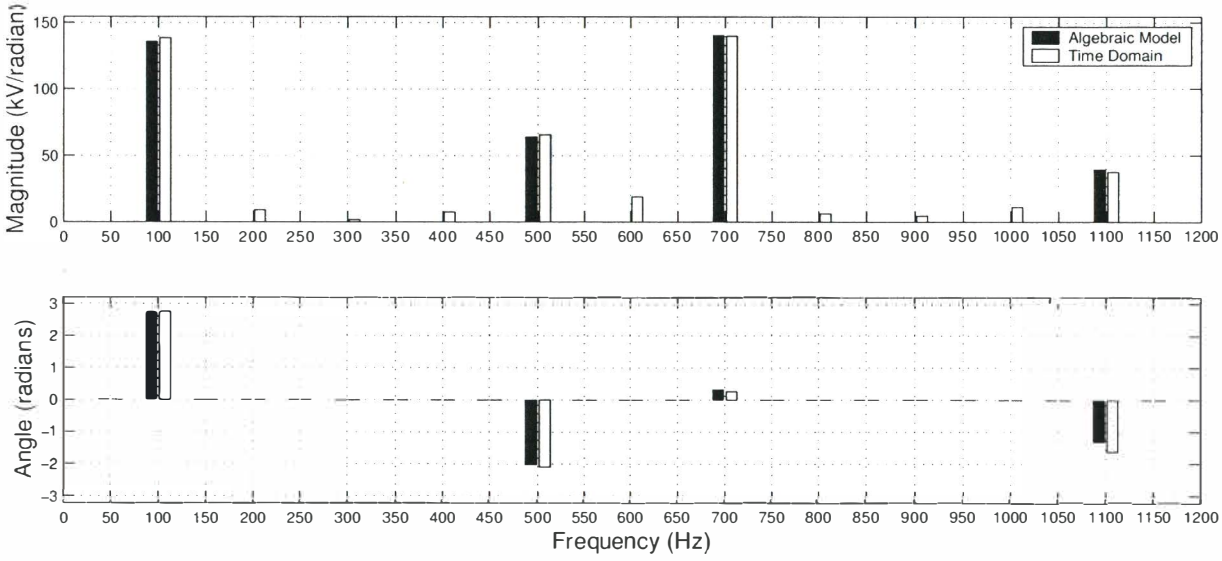

Figure 5.17 Time domain comparison of DC voltage spectrum resulting from 100Hz firing angle modulation.

spectra. The higher order spectra change the actual base case operating point at the base case frequencies, a nonlinear effect, while the first order parts change the base case spectra at other modulating frequencies, a linearisable effect. The second and higher order spectra diminish with decreasing distortion, whilst the first order spectra show a linear relationship with the applied distortion. Hence, it is the first order spectra which must be derived in a small signal analytic sense.

This chapter has described the formulation of both the base case and linearised small signal spectra around the HVDC converter in isolation. The derived small signal spectra are effectively the linearised transfers of waveform distortion through and around the converter. These transfers can be described as *linear* and *periodically time-variant* and describe the linearised change in the base case (large signal) transfers.

Owing to the fundamental differences caused by the complicated effects of the switching instant variation, the formulation of these resulting small signal transfers has been described in separate sections; the resulting ac current spectra, and the resulting dc voltage spectra. Both are made of a sampled partial steady state (SPSS) component (except when resulting from firing angle distortion) and either a sampled partial transient (SPT) for the resulting ac current, or a Switching Instant Variation (SIV) component, for the dc voltage. For ac current, the SPT component is derived with the use of a Pulse Amplitude Modulated (PAM) spectra, while for dc voltage the SIV component is derived with an Amplitude Modulated Impulse Train (AMIT). The resulting total small signal transfer being the addition of both the SPSS and SPT parts for ac current, and the SPSS and SIV parts for the dc voltage. The resulting spectra have been validated against PSCAD/EMTDC time domain simulation with excellent agreement.

What remains to be achieved is to use these linearised time-varying transfers in an actual HVDC system containing linear time-invariant ac and dc systems. This linearised time variant modelling of the HVDC converter is described in the following chapter for the single HVDC converter.

Chapter 6

LINEARISED TIME VARIANT MODELLING OF THE HVDC CONVERTER

6.1 INTRODUCTION

In general the HVDC converter can be described as *nonlinear* and *periodically time-variant*, exhibiting characteristics such as frequency coupling and phase angle dependence. Chapter 4, by way of numerical simulation has shown the converter to be linearisable and a complete small signal linearised model of the HVDC converter has been developed in chapter 5. The analytic model finds linearised transfers of distortion around the converter with infinite ac and dc systems, taking the effects of the commutation period into account. However, the model does not account for the effects of applied system distortion while the converter is '*in situ*' within the power system.

An assumption used within this thesis is based closely to that developed by Kron **??** for the modelling of large systems. By linearising each individual component within the system and then combining all linearised components, a full system can be built up easily in a piecewise linear manner. This is effectively what this chapter proves using the HVDC converter with its associated ac and dc systems as a case study.

The power system in which an HVDC link is connected can be represented using frequency dependent ac and dc systems. These systems are in general linear and time invariant, meaning the impedance magnitude and phase angle are dependent on the applied frequency of distortion, but not dependent on the applied magnitude or phase angle of distortion. The time invariant nature means that any applied distortion will cause only a single returned current or voltage at the same applied frequency. This is not so for power electronic switching devices as their effective impedance, admittance or transfer of distortion is dependent not only on frequency, but also on magnitude and phase angle of applied distortion[1]. The periodic time variant switching nature, as seen in the time domain, creates returned currents and voltages at more than one frequency in the frequency domain. If viewed from the frequency domain the resulting time variant transfers from system distortion are, in some cases completely linear (as shown in chapter 4) and in all other cases are linearisable under the assumption the system waveform distortion remains at small levels. If these conditions exist, power electronic switching devices such as the HVDC converter can be described accurately as linearised time variant devices and can be modelled analytically using models such as that described in chapter 5.

This chapter describes a novel approach to modelling the periodically time varying nature of the HVDC converter with associated linear frequency dependent ac and dc systems in the frequency domain. The method takes full advantage of the linearity of the HVDC converter and is applicable to other linearisable power electronic devices. To include the effect of the ac and

[1] Although PWM devices can appear time variant and frequency independent.

dc systems, a sparse linear equation set in the form $Ax = b$ is used. This linear equation set consists of a vector x, of n unknowns, and a vector b, of n knowns, as well as an $n \times n$ coefficient matrix A describing the linearised time variant and frequency cross coupling nature of the full system being modelled. This matrix relates different frequencies in a linearised manner and includes all associated effects of the converter control action and ac and dc systems. It is hence a matrix of partial derivatives, and is essentially similar to the Jacobian used in nonlinear Newton algorithms such as that developed by Smith [27] and Bathurst [5].

As linearity and hence superposition are assumed, a modular approach is used to 'build' the frequency cross coupling coefficient matrix. Each individual component of the system is modelled at the correct operating point, and then the whole system combined together using the fundamental laws of electrical networks (such as nodal analysis) resulting in the full system periodic time variant coefficient matrix. All elements must be represented in the same form, hence all elements of the system are represented as periodic time varying elements using frequency coupling matrix (FCM) transfers. These transfers are described in section 6.2 and are similar to those described by Fauri [21] for modelling florescent lamps. Larsen [34] recognised the importance of phase sequence in the modulating characteristics of the HVDC converter and consequently described the converter with a compound matrix equation allowing coupling between dc, positive and negative sequence[2]. Hence, the HVDC converter is represented using a compound matrix and the system coefficient matrix A will not only provide cross coupling between different frequencies, but will also provide coupling between different phase sequences.

The matrix transfers for any time variant device can be acquired either from the returned spectra of many sets of perturbed small signal frequency distortion, or directly from a linearised model such as that described in chapter 5 for the HVDC converter. The result in both cases is a sparse matrix whose structure represents the modulating nature of the switching device. If the time variant transfers are acquired by perturbation, many frequency perturbations over the frequency range of interest are required. Hume [33] did this while modelling the HVDC link by perturbing both converters using time domain PSCAD/EMTDC simulations. However, such simulations are very slow, requiring multiple runs, large data storage and post processing of the time domain waveshapes, including FFT to form the frequency domain time variant matrix transfers (see appendix C). Though slow, the method demonstrated the fundamental techniques described and used in this chapter and in chapter 7. A better solution is to use fast direct analytic models such as that described in chapter 5. This model has the advantage of being very accurate, is linear and able to calculate the FCM matrix transfers almost instantaneously. It calculates each diagonal and off diagonal using direct analytic expressions being only limited by memory requirements if the number of frequencies to be modelled is large.

The time variant compounded matrix transfers in A exhibit phase angle dependence, a result of the time variance. This phase angle dependence cannot be modelled with complex numbers alone. It can be dealt with by allowing negative frequencies [63] or the relationships between the real and imaginary parts of each phasor can be described separately. Usaola [24] did this, and Smith [25] formally described it as a tensor relationship. Tensors are used in this work and are described more fully in section 6.2.2.

Once the system coefficient matrix is known, solution of the linear equation set for the unknowns is easy. Solution speed is dependent on the sparsity of the network, the number of frequencies being modelled and the size of the system being modelled, these all directly relate to the size of the system coefficient matrix A.

This chapter describes the processes that are involved in modelling the single HVDC converter with ac and dc system impedances in a direct and linear time variant manner. The results of

[2]This equation is described and used throughout this thesis and is referred to as Larsen's equation.

fundamental frequency unbalance are compared to time domain simulation and the effects of time variance are demonstrated.

6.2 MODELLING THE TIME-VARIANT NATURE OF THE HVDC CONVERTER

Linear steady state harmonic solutions of networks including power electronic devices require that the definition of linear be extended to include time variant frequency coupling and phase angle dependence. As discussed in the introduction, frequency coupling implies that a single frequency will generate a multitude of other frequencies, a result of the time variant switching action of the converter. The frequency coupling nature can be modelled using frequency coupling matrix (FCM) transfers. Phase angle dependence is also the result of time-variance and can be modelled linearly using tensor elements.

These two associated effects of time variance must be taken into account when modelling linearised power electronic switching devices. The following sections describe how these time variant effects are modelled using FCM transfers and tensor elements.

6.2.1 The linearised FCM matrix transfers

The frequencies resulting from an applied small signal distortion on an HVDC converter, in isolation, can be linearly related. If the returned spectra are divided by the applied small signal distortion, the results are vectors of linearised transfers. These vectors are time variant and hence called linearised time variant transfers. They contain multiple linearised frequency transfers relating a single distorting frequency to a set of other frequencies. The converter models described in both chapters 3 and 5 are capable of producing these linearised time variant transfers.

A single linearised time variant transfer is sparse; the modulating frequency of each of the resulting frequency transfers (the individual elements within the vector) indicated by their relative position in the linearised vector. For small signal distortion, and hence linearised transfers, the returned frequencies are of first order and are predicted using table 3.1 in chapter 3. These transfers indicate the frequency cross coupling of the converter at a single applied frequency distortion. If they are to be used within a linear equation set such as that used by Larsen [34] they must include the frequency cross coupling information of the converter over the entire frequency range of interest. This is because there is multiple frequency cross coupling when the converter is placed into a system containing ac and dc systems. For example, a negative sequence distortion will be dependent of the ac system impedance at 150Hz (3rd), 450Hz(9th), 550Hz(11th), 650Hz(13th), 750Hz(15th) ... harmonics, hence the linearised time variant transfers at each of these frequencies must also be present.

To overcome this problem the frequency coupling matrix (FCM) transfers of distortion are used. These matrix transfers describe the linearised frequency cross-coupling transfer of distortion over the required frequency range of interest. Figure 6.1 shows a linearised time variant transfer matrix for the returned positive sequence voltage to current transfer. Perturbing positive sequence voltage distortion from 10Hz to 1250Hz in 10Hz perturbation steps, then recording the resulting currents before dividing them by the perturbed voltage effectively built this transfer. Any appropriate HVDC converter model can be used to acquire the FCM transfers in this manner, including time domain simulation. The analytic model described in chapter 5 assumes linearity, the output either in the form of a linearised time variant transfer at one particular frequency, or a full linearised FCM transfer, as shown in figure 6.1, depending on requirements.

For 125 frequencies between 10Hz and 1250Hz a 125×125 linearised FCM transfer results. If a 50Hz perturbation was used the resulting transfer would be a smaller, 25×25 matrix, however, only harmonic frequency distortions would be able to be investigated.

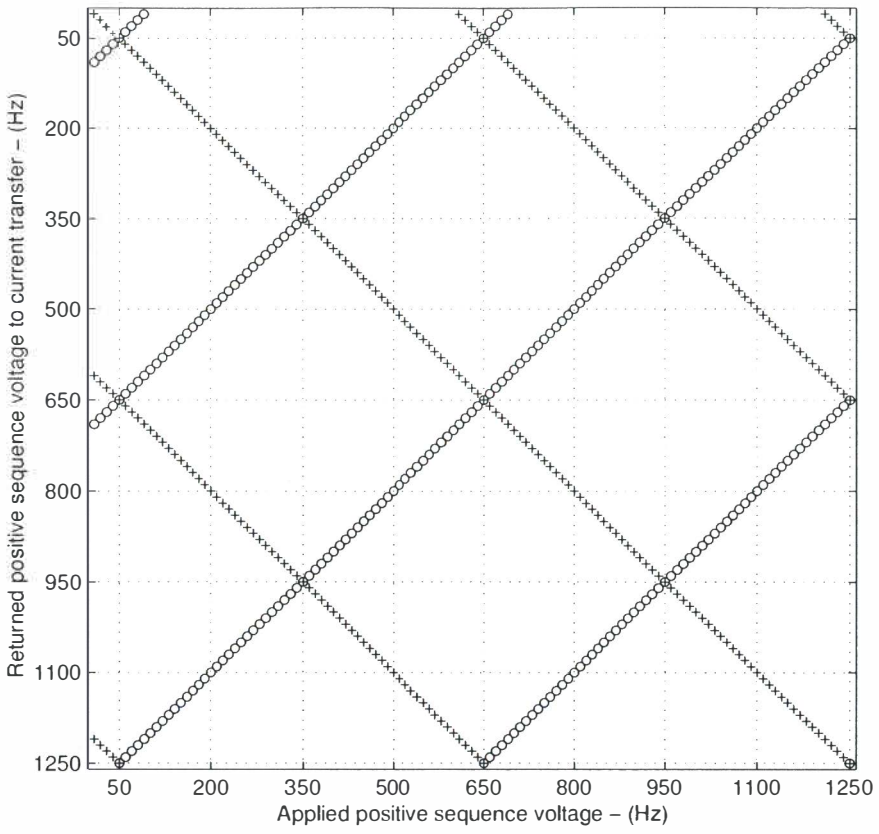

Figure 6.1 Linearised FCM matrix transfer a in Larsen's equation, for a 12 pulse HVDC converter.

This is also dependent on the system being modelled. For an HVDC link with the ac systems containing some distorting source, the base frequency (and hence incremental frequency step) must be the lowest common denominator between both ac system frequencies and the system distortion frequency. In some asynchronous HVDC link cases the ac system frequencies may be very close (<1Hz) and the matrix incremental perturbation step can be very small. In such cases sparsity routines must be used for efficient calculation and matrix inversion, or only relevant frequencies calculated, this is discussed further in section 7.4 when modelling asynchronous links. The sparsity of the transfer matrices increases with pulse number and a 12 pulse converter will have about half the non zero elements as a 6 pulse converter.

The full frequency cross coupling nature of the HVDC converter can be described by using all the transfers in Larsen's equation (6.15) in linearised time variant matrix form. These matrix transfers are gained by considering the four different distortions, ΔV_{acp},ΔV_{acn},ΔI_{dc} and $\Delta\alpha$ on the right side of the equation, separately, and recording the resulting positive and negative sequence voltage, and dc current spectra for each incremental perturbation. The matrices all have a sparse lattice like structure similar to that shown for transfer a in figure 6.1. Appendix F shows the structure of all the matrix transfers of Larsen's equation.

The phase angle dependence of the transfers must also be taken into account, this is achieved by relating the real and imaginary parts of the complex transfer using tensor elements and is discussed further in the follow section.

6.2.2 The phase angle dependence associated with the HVDC converter

Phase angle dependence occurs in all switching devices and is a result of time variance. It means the linearised time variant transfers of distortion are also dependent upon the phase angle of the

applied distortion at the converter terminals.

Phase dependence is best understood by considering the modulation of a distortion by the device switching action, or in simple mathematical terms, as the time domain multiplication of a sinusoid with a set of other sinusoids describing the switching action. The result is the generation of both sum and difference frequencies. The relative phase angles are subjected to the same sum and difference process, and the summed frequencies have a phase angle directly related to the phase angle of the applied distortion, while the difference frequencies have an angle related to the negative of the phase angle of the applied distortion, or its complex conjugate. The resulting transfer describing the difference frequencies cannot be described with a single complex number multiplier due to this phase angle dependence. However, they can be related using either negative frequencies or tensors. A tensor is a 2×2 matrix relating the real and imaginary components of an applied distortion to the real and imaginary components of the resulting voltage or current being found. Tensors are easy to implement in linear algebra using real numbers, they do not require the use of negative frequencies, and they correctly describe the phase conjugation inherent in the modulation process. Tensors are described in the following section.

Tensor representation

A tensor is a 2×2 real number matrix that can be used to describe the direct and phase angle dependent terms generated by the HVDC converter. As in all the linearised time variant transfers associated with the converter, the returned spectrum resulting from applied distortion consists of sum and difference frequencies. The difference frequencies are dependent on the applied phase angle of distortion, or the complex conjugate of the applied voltage distortion. Figure 6.1 in the previous section demonstrates this showing the linearised frequency dependent matrix transfer a. The terms marked '$\circ$' are the conjugated terms and have a phase angle related to the negative angle of the applied distortion, or the complex conjugate. The returned current in this case, can be related using the equation,

$$\Delta I = Y \Delta V^* \tag{6.1}$$

Likewise the direct part of the spectrum (marked '+') can be related with the equation,

$$\Delta I = Y \Delta V \tag{6.2}$$

To be fully general the converter transfers are described by Larsen's equation 6.15. This equation consists of applied perturbations, ΔV_{acp},ΔV_{acn}, ΔI_{dc} and $\Delta\alpha$ and returned frequencies, ΔI_{acp},ΔI_{acn} and ΔV_{dc}. Hence the transfers can be either *voltage→current*, *current→voltage*, *current→current* or *voltage→voltage* relationships. Or for firing angle distortion *radians→current* and *radians→voltage*. Hence, equations 6.1 and 6.2 can be described more generally as,

$$\Delta R = T \Delta P^* \tag{6.3}$$

and

$$\Delta R = T \Delta P \tag{6.4}$$

for the conjugated and direct terms respectively. For the generic HVDC converter, ΔP is the perturbing source, while ΔR is the returned spectrum.

Most values of applied distortion return a spectrum consisting of phase conjugated and direct frequencies all of which are at different returned frequencies. However, for some values of distortion the direct and conjugate parts fall on one another and the resulting impedance is the sum

of both 6.3 and 6.4, or,

$$\Delta R = T_1 \Delta P + T_2 \Delta P^* \tag{6.5}$$

These frequencies can be seen in the admittance matrix transfer (figure 6.1) from applied positive sequence voltage to positive sequence current at frequencies of 50,350,650Hz ... and are marked with an '⊕'.

Expanding equations 6.3 and 6.4 into their respective real and imaginary parts gives,

$$(R_{\Re} + jR_{\Im}) = (T_{\Re} + jT_{\Im})(P_{\Re} - jP_{\Im}) \tag{6.6}$$
$$R_{\Re} = T_{\Re}P_{\Re} + T_{\Im}P_{\Im} \tag{6.7}$$
$$R_{\Im} = T_{\Im}P_{\Re} - T_{\Re}P_{\Im} \tag{6.8}$$

for the conjugated terms, and,

$$(R_{\Re} + jR_{\Im}) = (T_{\Re} + jT_{\Im})(P_{\Re} + jP_{\Im}) \tag{6.9}$$
$$R_{\Re} = T_{\Re}P_{\Re} - T_{\Im}P_{\Im} \tag{6.10}$$
$$R_{\Im} = T_{\Im}P_{\Re} + T_{\Re}P_{\Im} \tag{6.11}$$

for the direct terms. Hence, in tensor form the conjugate terms can be written as,

$$\begin{bmatrix} \Delta R_{\Re} \\ \Delta R_{\Im} \end{bmatrix} = \begin{bmatrix} T_{\Re} & T_{\Im} \\ T_{\Im} & -T_{\Re} \end{bmatrix} \begin{bmatrix} \Delta P_{\Re} \\ \Delta P_{\Im} \end{bmatrix} \tag{6.12}$$

and the direct terms as,

$$\begin{bmatrix} \Delta R_{\Re} \\ \Delta R_{\Im} \end{bmatrix} = \begin{bmatrix} T_{\Re} & -T_{\Im} \\ T_{\Im} & T_{\Re} \end{bmatrix} \begin{bmatrix} \Delta P_{\Re} \\ \Delta P_{\Im} \end{bmatrix} \tag{6.13}$$

Equation 6.13 is identical to a complex number multiplication and must be used for all the direct frequency terms and also any linear time-variant impedance or admittance, while equation 6.12 incorporates the phase angle dependency and is required for modelling the phase conjugated transfers of the converter.

When represented in tensor form, the matrix transfers can be considered as linearised and time variant, meaning superposition can be used to combine the linearised frequency dependent matrix transfers into Larsen's equation. The analytic model described in chapter 5 calculates the linearised time variant matrix transfers in tensor form.

6.3 NODAL ANALYSIS OF THE SINGLE HVDC CONVERTER

The converter is best viewed as a harmonic (or interharmonic) current source on the ac side and as a harmonic (or interharmonic) dc voltage source on the dc side, as described by Larsen's equation.

A useful way to represent the converter is in nodal form. This is achieved simply by rearranging Larsen's equation. In this form, the linearised time variant matrix admittance transfers can be placed directly in a system that not only includes linear time invariant ac and dc systems, such as transmission lines, etc, but can also include other linearised time-variant devices such as other HVDC converters or linearised power electronic plant. This is required when modelling more complex power systems such as HVDC links or larger systems.

In nodal form the system can be built up easily, then solved for the particular distortion(s) of interest. For simplicity, this section describes only the single converter, demonstrating the

time-variant nature of the converter. Chapter 7 extends the analysis to the HVDC link solving the harmonic and interharmonic interaction around synchronous and asynchronous links.

The HVDC converter is a modulator and switches fundamental positive sequence ac voltage in such a way that ensures a dc voltage on the dc side of the converter. The same switching pattern takes the dc current on the dc side and switches it onto the ac side phases in such a way that a fundamental frequency positive sequence ac current exists on the ac side.

Hence, for a converter with or without applied distortion, it is the ac currents and dc voltage that are unknowns and a function of distortion around the converter.

The total ac side current and dc side voltage spectra around an HVDC converter can be described by the following equation,

$$\begin{bmatrix} I_{acp} \\ I_{acn} \\ V_{dc} \end{bmatrix} = \begin{bmatrix} I_{acp_{bc}} \\ I_{acn_{bc}} \\ V_{dc_{bc}} \end{bmatrix} + \begin{bmatrix} \Delta I_{acp} \\ \Delta I_{acn} \\ \Delta V_{dc} \end{bmatrix} \tag{6.14}$$

This equation splits the ac currents and dc voltage into the small signal and base case quantities. Here, I_{acp}, I_{acn} and V_{dc} are frequency domain vectors (phasors) giving the total harmonic distortion on the converter. The base case harmonics are, $I_{acp_{bc}}, I_{acn_{bc}}$ and $V_{dc_{bc}}$ and are a function of the converter operating point, while the harmonics and/or interharmonics resulting from an applied small signal distortion are $\Delta I_{acp}, \Delta I_{acn}$ and ΔV_{dc}. The small signal distortions can be

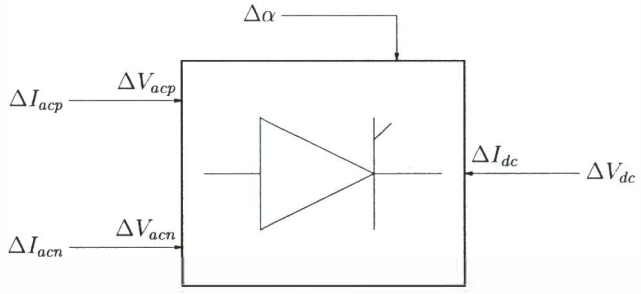

Figure 6.2 Single HVDC converter.

described, including the effects of firing angle distortion from constant current control (G), by Larsen's equation. The equation is repeated here,

$$\begin{bmatrix} \Delta I_{acp} \\ \Delta I_{acn} \\ \Delta V_{dc} \\ 0 \end{bmatrix} = \begin{bmatrix} a & b & c & d \\ e & f & g & h \\ i & j & k & l \\ 0 & 0 & G & -1 \end{bmatrix} \begin{bmatrix} \Delta V_{acp} \\ \Delta V_{acn} \\ \Delta I_{dc} \\ \Delta\alpha \end{bmatrix} \tag{6.15}$$

where $a \rightarrow l$ are the linearised time variant matrices described in section 6.2.1 and shown in appendix F. Care must be used with the sign of the transfers as this is dependent on how the model has been derived and whether the converter is in rectifier or inverter mode. As with general nodal convention, all currents are positive when flowing into the converter and negative when flowing out. The difference between the rectifier and inverter transfers in Larsen's equation is given in appendix G. Rearranging Larsen's equation in nodal form, consistent with the circuit layout of figure 6.3 gives,

$$\begin{bmatrix} \Delta I_{acp} \\ \Delta I_{acn} \\ \Delta I_{dc} \\ 0 \end{bmatrix} = \begin{bmatrix} Y_{11} & Y_{12} & Y_{13} & Y_{14} \\ Y_{21} & Y_{22} & Y_{23} & Y_{24} \\ Y_{31} & Y_{32} & Y_{33} & Y_{34} \\ Y_{41} & Y_{42} & Y_{43} & Y_{44} \end{bmatrix} \begin{bmatrix} \Delta V_{acp} \\ \Delta V_{acn} \\ \Delta V_{dc} \\ \Delta\alpha \end{bmatrix} \tag{6.16}$$

where ΔI_{acp}, ΔI_{acn} and ΔI_{dc} are the Norton equivalent currents representing independent

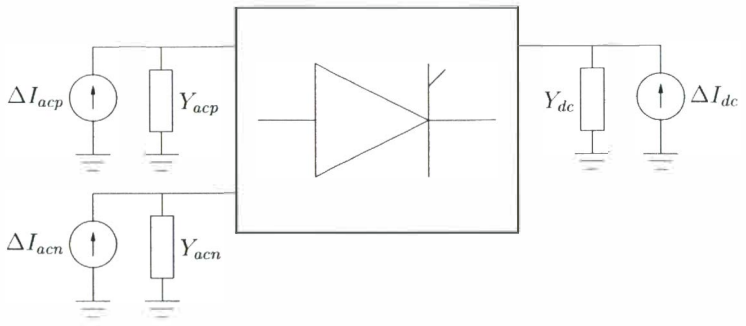

Figure 6.3 Nodal current injections of a single HVDC converter.

sources of distortion around the converter. The nodal terms $Y_{11} \rightarrow Y_{44}$ can be written by hand as,

$$Y_{11} = a - ck^{-1}i + [Y_{acp}] \qquad Y_{12} = b - ck^{-1}j \qquad Y_{13} = ck^{-1} \qquad Y_{14} = d - ck^{-1}l$$
$$Y_{21} = e - gk^{-1}i \qquad Y_{22} = f - gk^{-1}j + [Y_{acn}] \qquad Y_{23} = gk^{-1} \qquad Y_{24} = h - gk^{-1}l$$
$$Y_{31} = -k^{-1}i \qquad Y_{32} = -k^{-1}j \qquad Y_{33} = k^{-1} - [Y_{dc}] \qquad Y_{34} = -k^{-1}l$$
$$Y_{41} = -Gk^{-1}i \qquad Y_{42} = -Gk^{-1}j \qquad Y_{43} = -Gk^{-1} \qquad Y_{44} = -Gk^{-1}l - 1$$

This includes the ac and dc side admittances, Y_{acp}, Y_{acn} and Y_{dc}.

An alternative matrix manipulation method can be used by rearranging equation 6.15 into the form

$$\left[\begin{array}{ccccc|c} 1 & & c & -a & -b & -d \\ & 1 & g & -e & -f & -h \\ & & k & -i & -j \quad 1 & -l \\ \hline & & G & & & 1 \end{array}\right] \left[\begin{array}{c} \Delta I_{acp} \\ \Delta I_{acn} \\ \Delta I_{dc} \\ \Delta V_{acp} \\ \Delta V_{acn} \\ \Delta V_{dc} \\ \hline \Delta\alpha \end{array}\right] = 0 \tag{6.17}$$

The firing angle modulation terms (the bottom row and end column) can then be Kron reduced into the top left portion of the matrix, ie,

$$\left[\begin{array}{ccccc} 1 & & c^* & -a^* & -b^* \\ & 1 & g^* & -e^* & -f^* \\ & & k^* & -i^* & -j^* \quad 1 \end{array}\right] \left[\begin{array}{c} \Delta I_{acp} \\ \Delta I_{acn} \\ \Delta I_{dc} \\ \Delta V_{acp} \\ \Delta V_{acn} \\ \Delta V_{dc} \end{array}\right] = 0 \tag{6.18}$$

where the transfers x^* are the same transfers in equation 6.17 except they now include the effects of the control action on the firing angle variation.

This equation can then be solved in the following form, separating the ΔI and ΔV terms, ie,

$$\left[\begin{array}{cc} A & B \end{array}\right] \left[\begin{array}{c} \Delta I \\ \Delta V \end{array}\right] = 0 \tag{6.19}$$

where, $A = \left[\begin{array}{ccc} 1 & & c^* \\ & 1 & g^* \\ & & k^* \end{array}\right]$ and $B = \left[\begin{array}{ccc} -a^* & -b^* & \\ -e^* & -f^* & \\ -i^* & -j^* & 1 \end{array}\right]$

When solved for the ΔI terms gives,

$$\begin{bmatrix} \Delta I_{acp} \\ \Delta I_{acn} \\ \Delta I_{dc} \end{bmatrix} = -\begin{bmatrix} 1 & & c^* \\ & 1 & g^* \\ & & k^* \end{bmatrix}^{-1} \begin{bmatrix} -a^* & -b^* & \\ -e^* & -f^* & \\ -i^* & -j^* & 1 \end{bmatrix} \begin{bmatrix} \Delta V_{acp} \\ \Delta V_{acn} \\ \Delta V_{dc} \end{bmatrix} + \begin{bmatrix} Y_{acp} & & \\ & Y_{acn} & \\ & & Y_{dc} \end{bmatrix} \begin{bmatrix} \Delta V_{acp} \\ \Delta V_{acn} \\ \Delta V_{dc} \end{bmatrix}$$

$$\begin{bmatrix} \Delta I_{acp} \\ \Delta I_{acn} \\ \Delta I_{dc} \end{bmatrix} = \begin{bmatrix} Y_{11}^* & Y_{12}^* & Y_{13}^* \\ Y_{21}^* & Y_{22}^* & Y_{23}^* \\ Y_{31}^* & Y_{32}^* & Y_{33}^* \end{bmatrix} \begin{bmatrix} \Delta V_{acp} \\ \Delta V_{acn} \\ \Delta V_{dc} \end{bmatrix} \tag{6.20}$$

Both these methods can be used for converting Larsen's equation into the more general nodal form.

6.3.1 The KRON reduction

Kron matrix reduction is used for reducing the overall admittance/transfer matrix to the required variables. This form of reduction does not rid any information from the original transfers, but reduces the information down to the required variables. In most cases, it is used to reduce the control transfers into the main transfer equations as in equations 6.17 and 6.18. Other variables can be reduced as well. For example, if the effects on ac voltage are wanted from ac current distortion then, assuming the independent dc side current injection to be zero ($\Delta I_{dc} = 0$), equation 6.21 can be reduced, ie,

$$\begin{bmatrix} \Delta I_{ac} \\ \Delta I_{dc} \end{bmatrix} = \begin{bmatrix} A & B \\ C & D \end{bmatrix} \begin{bmatrix} \Delta V_{ac} \\ \Delta V_{dc} \end{bmatrix} \tag{6.21}$$

reduces to,

$$\Delta I_{ac} = [A - BD^{-1}C]\Delta V_{ac} \tag{6.22}$$

This admittance matrix now includes all associated effects of the dc and firing angle distortion transfers. A similar process can be followed for other transfers around the converter. For example, the dc impedance transfer used in the case study below and in appendix H will be of similar form, but written as,

$$\Delta I_{dc} = [D - CA^{-1}B]\Delta V_{dc} \tag{6.23}$$

The matrix inversion to solve for ΔV_{dc} can be slow unless a fast sparse matrix inversion routine is used.

6.3.2 Solution of the linear equation set

The nodal and Kron matrix reduction methods described in the previous sections have been used to form a time varying system admittance matrix of the single converter embedded within the power system. This system equation is able to describe the steady state harmonics and interharmonics resulting from some small signal system distortion or distortions. The characteristic harmonics are ignored under the assumption they are part of the system operating point and do not change. These can be modelled as transfers resulting from the fundamental positive sequence voltage, and are required to be modelled when the solution technique is expanded to model asynchronous HVDC links. This is demonstrated in the following chapter.

The solution of the system depends on what is known. The nodal form described in the previous section provides an easy way of connecting system components together, however a solution requires at least one or more variables to be known. This could be a known nodal current injection or a known terminal voltage. For the case of the single converter, the *known* variables

of the nodal equation will most likely be a terminal voltage and all current injections at all frequencies (except at the distorting frequency) which are set to zero.

Depending on what is known, the equation set must be ordered in the appropriate manner to solve for the unknowns. This is achieved by restructuring the nodal admittance matrix into the known and unknown variables and requires careful indexing of the matrix elements. This form is termed the linear equation set and is in the form $Ax = b$. Where A is the reordered admittance matrix (no longer a complete admittance matrix), x is a vector of n unknowns, and b a vector of n knowns.

As an example, the case of an HVDC converter with some known negative sequence unbalance on the rectifier terminals is chosen. The knowns in this case are the negative sequence fundamental voltage distortion and all current distortions around the link (set to zero) except the negative sequence fundamental. Those variables that are unknown are the negative sequence fundamental current injection and all other terminal voltages around the converter. Figure 6.4 shows the structure of the system admittance matrix for the 50Hz HVDC converter described by equation 6.20. For clarity the perturbation step is set to 50Hz and the maximum frequency is the 26th harmonic.

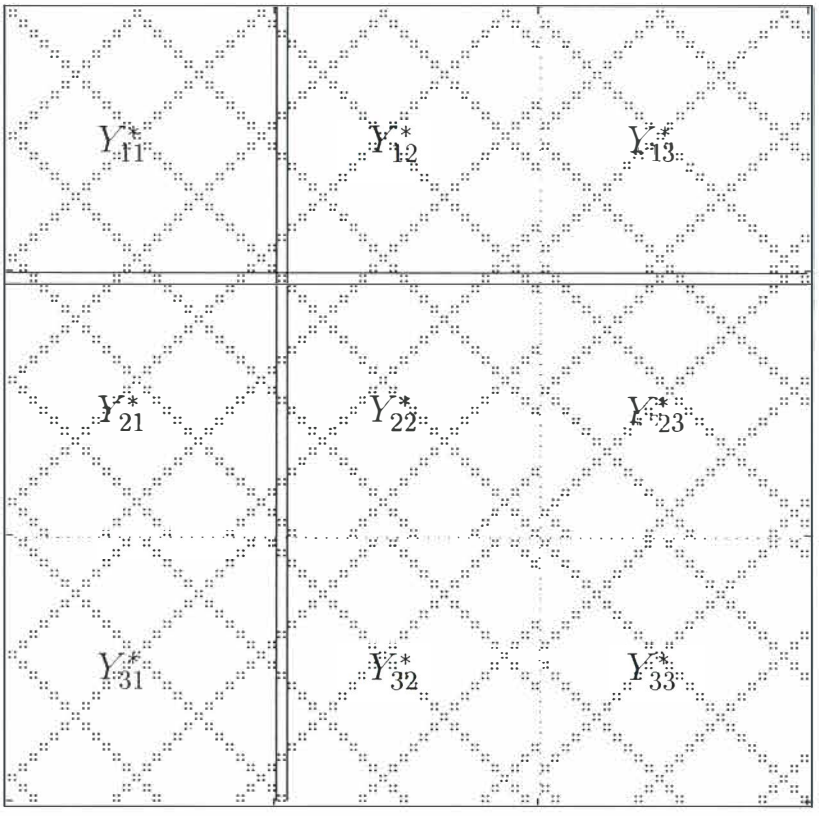

Figure 6.4 Sparse nodal admittance matrix of the HVDC rectifier.

Assuming that there is a known voltage distortion, say a 50Hz negative sequence fundamental distortion on the rectifier terminals, then the matrix must be re-ordered to group together the knowns and unknowns. In this case all nodal current injections will be known, except the negative sequence fundamental frequency, and all voltages around the link will be unknown, except the negative sequence fundamental frequency voltage distortion that is known. The highlighted row and column in figure 6.4 represent the individual frequency transfers associated with negative sequence fundamental unbalance. The linear equation set for the rearranged admittance matrix

can be written in the following form,

$$\begin{bmatrix} \Delta I_{known} \\ \Delta I_{unknown} \end{bmatrix} = \begin{bmatrix} A & B \\ C & D \end{bmatrix} \begin{bmatrix} \Delta V_{unknown} \\ \Delta V_{known} \end{bmatrix} \tag{6.24}$$

where $\Delta I_{known}, \Delta V_{known}, \Delta V_{unknown}, \Delta I_{unknown}$ are vectors of the known currents and voltages around the converter.

To solve for the unknowns, the rows and columns are shifted and grouped together as shown in figure 6.5.

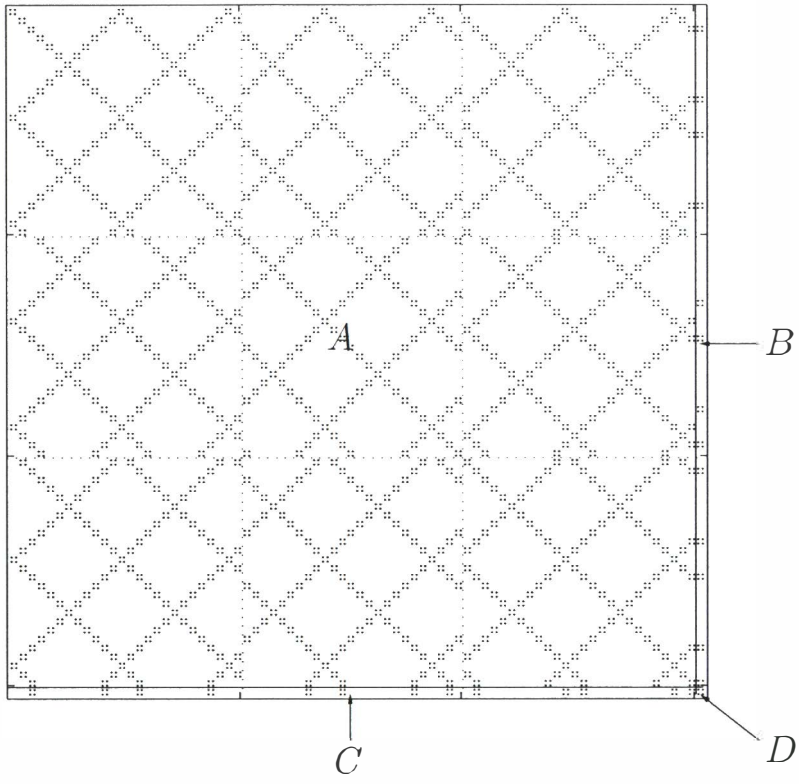

Figure 6.5 Rows and columns of known and unknown voltages and current injections around HVDC link.

Once the admittance matrix has been reordered into the known and unknown variables it can then be solved for the unknowns. For example,

$$\begin{bmatrix} \Delta I_{known} \\ \Delta V_{known} \end{bmatrix} = \begin{bmatrix} A - BD^{-1}C & BD^{-1} \\ -D^{-1}C & D^{-1} \end{bmatrix} \begin{bmatrix} \Delta V_{unknown} \\ \Delta I_{unknown} \end{bmatrix} \tag{6.25}$$

can be inverted to give,

$$\begin{bmatrix} \Delta I_{unknown} \\ \Delta V_{unknown} \end{bmatrix} = \begin{bmatrix} B - CA^{-1}B & CA^{-1} \\ -A^{-1}B & A^{-1} \end{bmatrix} \begin{bmatrix} \Delta V_{known} \\ \Delta I_{known} \end{bmatrix} \tag{6.26}$$

This is the general method adopted for rearranging the linear matrix equation set to solve for the unknowns.

6.4 THE SINGLE CONVERTER TEST SYSTEM

To test the methods described in the previous sections a single 12 pulse HVDC converter with weak ac and dc systems is used. The test system is based on the rectifier of the CIGRE benchmark model [62] and is described in appendix D. The rectifier is operating in constant current mode and the dc set point is 2kA. The ac system, filters and dc system impedance remain unaltered, and the fundamental positive sequence voltage is 1pu or 345kV. Figure 6.6 shows the base test system with the associated ac admittance Y_{ac} being the addition of the filter admittance Y_{filt} and the system admittance Y_{sys}. The dc side impedance is also included and a voltage source represents the inverter. The effect of the control transfer function and transducer frequency response, G, are also included on the transfers from dc current to firing angle distortion. The exact operating point conditions of the system are given in table 6.1.

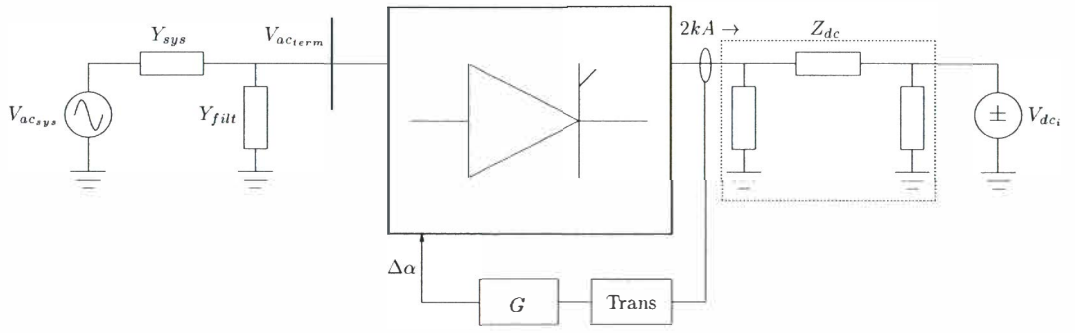

Figure 6.6 Case Study 1, CIGRE rectifier test circuit.

Parameter	Value
AC side voltage (kV, l-l rms)	$347.41\angle -0.10^o$
AC side terminal voltage unbalance (kV, l-l rms)	$5.92\angle -11.72^o$
Inverter DC source voltage (kV)	494.7
DC current (kA)	2.00
Firing angle (α_o)	14.99^o
Commutation period (μ_o)	23.03^o

Table 6.1 Operating conditions of the single HVDC converter case study.

6.4.1 The effects of negative sequence unbalance

Negative sequence unbalance is the most common form of power system distortion and is treated the same way as any other applied uncharacteristic frequency. It is used here as an example around the single HVDC converter with associated ac and dc system impedance.

When the converter is subjected to an uncharacteristic ac system distortion, the modulation process of the converter modulates this distortion around the base case characteristic harmonics. The largest components of the modulation are those that are modulated around the fundamental and dc quantities, however the applied distortion is also modulated around the other characteristic harmonics but in smaller magnitudes. These are the returned first order frequencies and have been described in previous chapters.

Of the larger first order modulations, a positive sequence distortion at frequency $f_{dck} + f_{fun}$, and negative sequence distortion at frequency $f_{dck} - f_{fun}$, are modulated to multiple f_{dck} on the dc side. Hence, negative sequence distortion ($f_{dck} = 100Hz$) causes a large 2nd harmonic on the dc side that in turn causes a large 3rd positive sequence harmonic distortion on the ac side. As

well as these, other significant first order uncharacteristic harmonic distortions are produced at frequencies of 450,550,650 and 750Hz and even higher frequencies of 1050.1150,1250Hz can be present in sufficient magnitudes to warrant concern, however in general it is the lower frequency components which tend to escape the effects of the filters and are of the main concern.

The frequencies on the dc side resulting from any applied distortion on the ac side for a converter, can be written as,

$$f_{dc} = 6nf_{fun} \pm f_{dck} \tag{6.27}$$

where $n = 2$ for a 12 pulse converter and f_{dck} is the equivalent dc side distorting frequency. Likewise the ac side frequencies resulting from the dc side distortion can be written as,

$$f_{acp} = (6nf_{fun} + f_{fun}) \pm f_{dck} \tag{6.28}$$

for the positive sequence, and,

$$f_{acn} = (6nf_{fun} - f_{fun}) \pm f_{dck} \tag{6.29}$$

for the negative sequence. These are the first order frequencies and can be solved in a linear algebraic manner using the methods outlined in chapter 5 and in this chapter. The full frequency spectrum generated by some applied distortion, which contains nonlinear higher order frequencies is shown in table 3.1 in chapter 3. The magnitude of the resulting frequency terms can be roughly estimated by simple hand calculations which use the knowledge of the converter switching phenomena, this has been described in [64]. The estimated values do not take into account the commutation period dynamics and lose accuracy quickly at higher frequencies.

In this test case the CIGRE test system has a 0.015pu negative sequence fundamental voltage unbalance at the converter terminals. Following the method outlined in section 6.3, Larsen's equation is converted into nodal form, rearranged for the known and unknown variables, and solved. In this case, the fundamental negative sequence voltage unbalance is known as well as all nodal current injections which are set to zero, except for the negative sequence fundamental distortion which is unknown and must be solved. The resulting ac side terminal voltage, the ac currents and the dc voltage are compared to PSCAD/EMTDC and shown in figures 6.7 and 6.8.

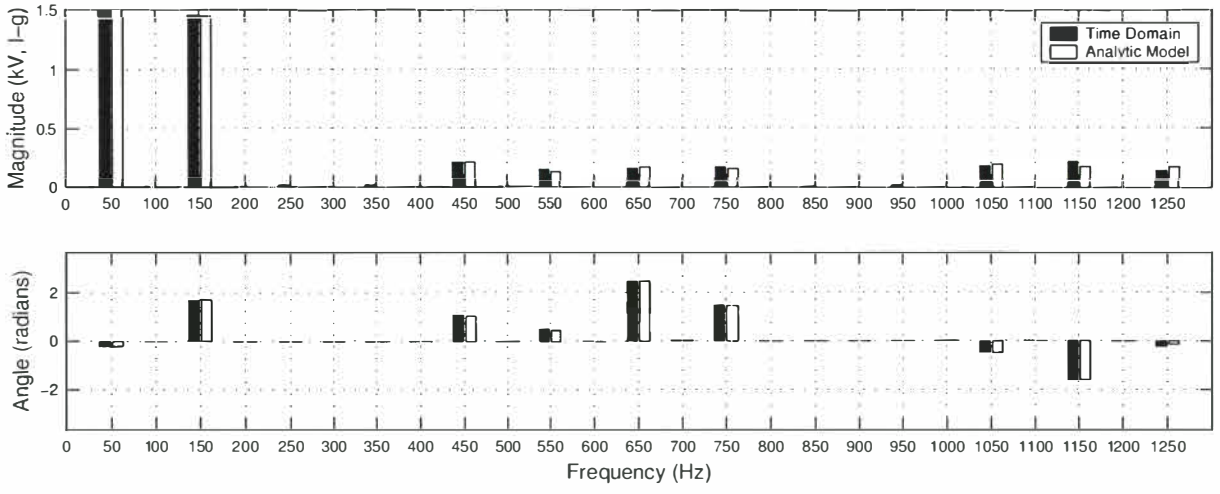

Figure 6.7 Rectifier ac terminal voltage spectra magnitude and angle resulting from a 0.017pu (5.92kV, l-l rms) negative sequence unbalance.

These figures compare the full direct solution using the linearised transfers to a full time domain

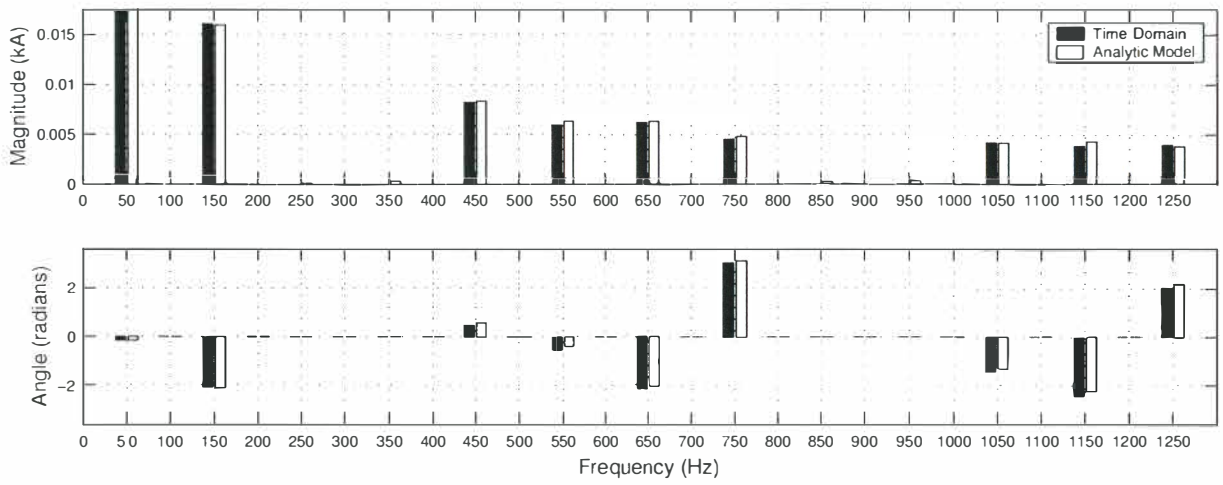

Figure 6.8 Rectifier ac terminal system current spectra magnitude and angle resulting from a 0.017pu (5.92kV, l-l rms) negative sequence unbalance.

simulation of the rectifier with ac and dc systems in PSCAD/EMTDC. In PSCAD/EMTDC the system was simulated with a $10\mu s$ time step and allowed to settle for 2.5 seconds before a 0.02pu fundamental negative sequence voltage unbalance was applied to the ac source voltage. This corresponds to a 0.017pu terminal voltage on the rectifier terminals. The system was then allowed to settle for a further 2.4 seconds before data was recorded and Fourier transformed in MATLAB. The change in the base case spectrum or the first order voltage spectrum that results from the applied small signal unbalance is shown. The negative sequence fundamental unbalance is 0.017pu (5.92kV, l-l rms), and the peak negative sequence ac phase current is 0.076kA. The analytic solution uses the negative sequence unbalance acquired from the time domain PSCAD/EMTDC simulation results.

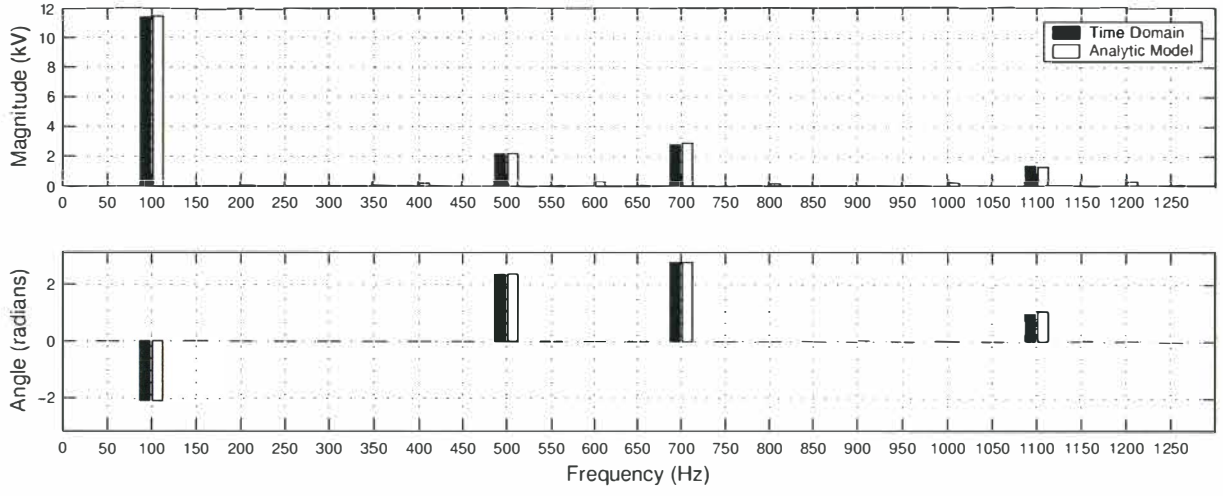

Figure 6.9 Rectifier dc terminal voltage spectra magnitude and angle resulting from a 0.017pu (5.92kV, l-l rms) negative sequence unbalance.

The results of figures 6.7,6.8 and 6.9 show very good agreement with time domain simulation. These results are significant as they prove that small signal waveform distortion within the power system can be modelled in a modular fashion using linearised, yet time variant transfers, combined with linear time invariant ac and dc systems.

Figure 6.10 shows the different current flows in the CIGRE ac system. Interestingly, the resulting negative sequence current flowing into the ac system is higher than that flowing from the

converter.

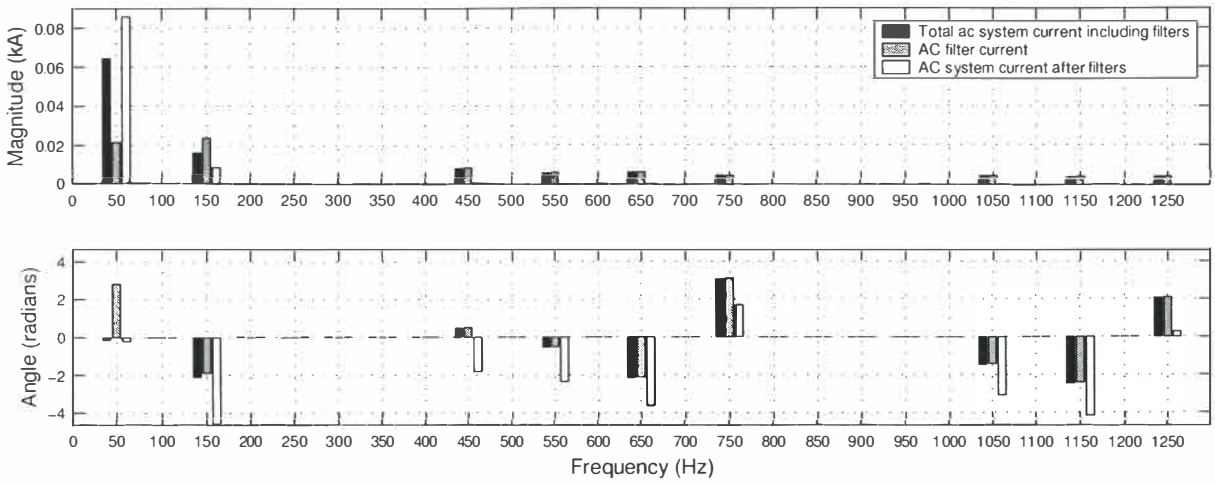

Figure 6.10 AC system currents, magnitude and angles resulting from a 0.015pu (4.1kV) negative sequence distortion.

The effect of the control on the transfer of distortion

The results shown in the previous section include the effects of the firing angle modulation resulting from the transfer of waveform distortion from the dc current through the PI control. Figures 6.11 and 6.12 show the difference in the resulting ac and dc voltage spectra around the single converter test system if the effects of control are ignored. This is equivalent as ignoring the transfer G in the equations shown in section 6.3.

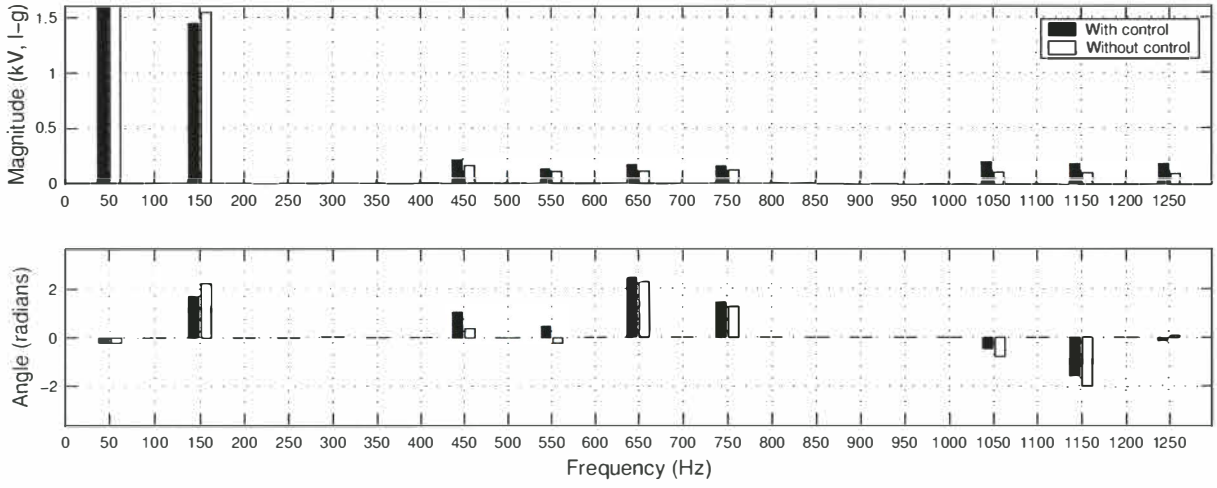

Figure 6.11 Effect of modelling the PI control transfer function G on the resulting ac side voltage spectrum.

As shown, a noticeable difference in the spectra occurs when the effects of the controller transfer function are ignored. Hence, for accurate harmonic and interharmonic prediction, the PI controller action must be modelled. In the steady state the inverter is assumed to be operating with a fixed firing angle as it would with minimum gamma control. This is a fair assumption so long as the harmonic and interharmonic distortion in the system remains at low enough levels so as to not interfere with the controller.

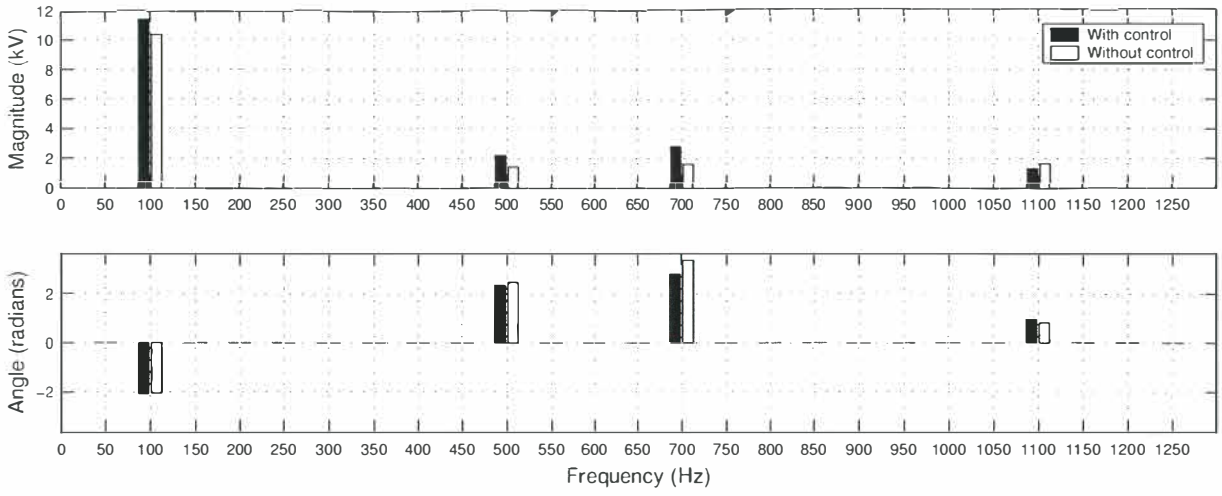

Figure 6.12 Effect of modelling the PI control transfer function G on the resulting dc side voltage spectrum.

6.4.2 The effect of time variance

This section demonstrates the effects of time variance on the returned spectra around an HVDC converter. The effects associated with the frequency cross-coupling and the phase angle dependent nature are investigated with reference to the single HVDC converter.

Frequency cross coupling

In the frequency domain the main observable effect of time variant devices is that of frequency cross coupling or modulation. This effect is shown in the lattice structure of the matrix transfers. Any applied waveform distortion on the converter is coupled to other frequencies through the converter switching action. The effect of the voltage and current distortion around the converter is not only dependent on the values of the ac and dc system impedances at the original distorting frequency, but also to a lesser extent on the impedances at the resulting modulated frequencies. As an example, the effects of a 50Hz negative sequence unbalance, as shown in the previous section, are dependent on the ac and dc system impedances at the frequencies described in equations 6.28 and 6.29 and shown in figures 6.7 to 6.9. The magnitude of the dependence is related to the magnitude of the transfer. Hence, for the HVDC converter the lower frequency transfers tend to have more effect than the higher frequencies, and a change in the 3rd harmonic ac system impedance will have a much larger effect on the resulting returned harmonic spectra than a change in the 1150Hz impedance. The effect of impedance on the harmonic and interharmonic cross-modulation around the HVDC link is investigated further in chapter 8. To demonstrate the frequency cross coupling, figure 6.13 shows the difference in the rectifier voltage spectra generated from a 4.1kV negative sequence unbalance with nominal CIGRE, zero, and infinite 3rd harmonic impedance values. The normal CIGRE third harmonic impedance is $39.5 - j65.2\Omega$. The largest change occurs when the third harmonic impedance is infinite in magnitude (zero admittance). This is equivalent to a sharp parallel resonance in the 3rd harmonic ac system impedance and gives rise to increased harmonic voltages around the converter. The third harmonic voltage rises from 0 to approximately 5.5kV or 0.02pu (not shown) and other frequencies increase by up to 100%.

This result demonstrates the dependence on impedance at the many different frequencies produced around an HVDC link while under system waveform distortion. In particular, the dependence between the lower frequencies is higher and if accurate harmonic and interharmonic

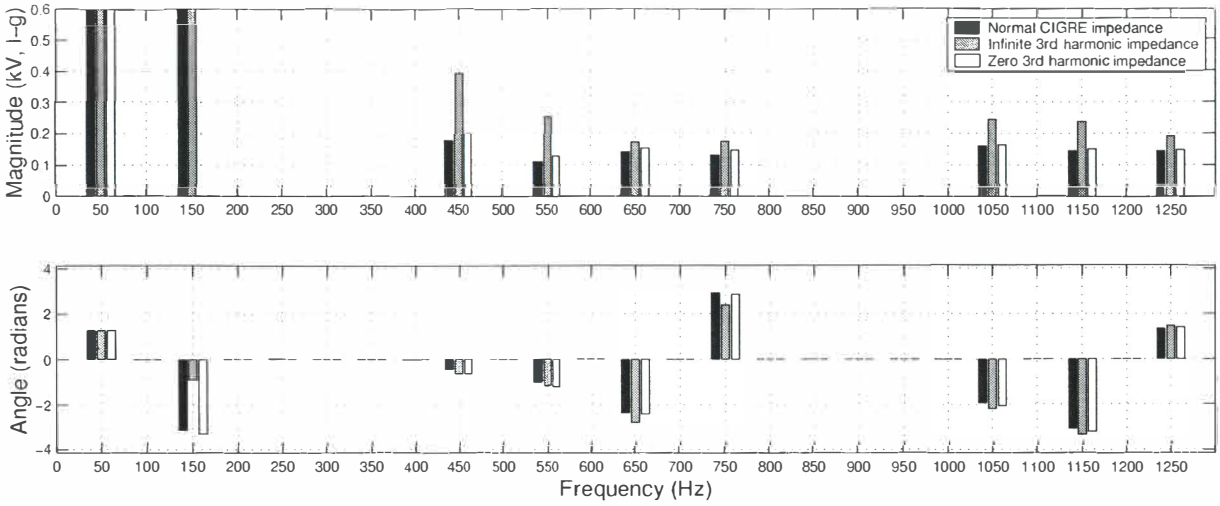

Figure 6.13 Difference in ac terminal voltage spectra magnitude and angle resulting from a 0.015pu (4.1kV) negative sequence distortion with altered 3rd harmonic impedance.

modelling is required then this frequency coupling dependence must be taken into account. This has been achieved in this chapter using the time variant FCM transfers.

Phase angle dependence

To demonstrate the phase angle dependence the same negative sequence unbalance case is used. However, the phase angle of the applied negative sequence distortion is increased from 0 to π radians. Figure 6.14 shows the change in the resulting phase angles of the increased spectra. The

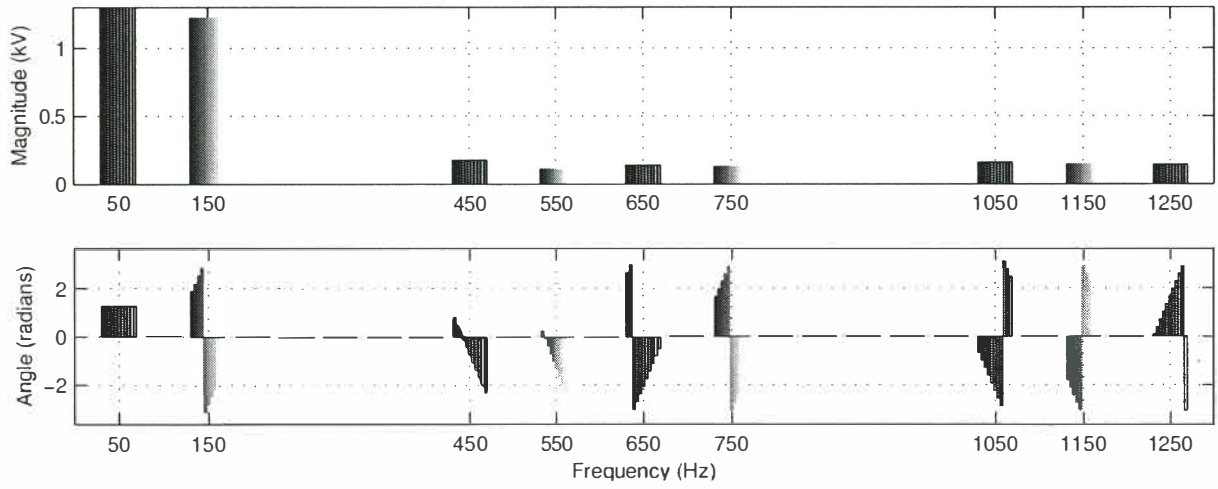

Figure 6.14 Rectifier ac terminal system current spectra magnitude and angle resulting from a 0.015pu (4.1kV) negative sequence distortion with varying phase angles from 0 to 180 degrees.

returned ac system frequencies that are conjugated fall at frequencies: 550Hz (11th), 1150Hz (23rd) in positive sequence and at frequencies: 450Hz (9th) and 1050Hz (21st) in negative sequence. These are the frequency transfers which require special attention and can not be modelled with complex numbers alone. As shown, the resulting change of phase angle on the returned spectrum is dependent on whether the returned frequency is at a direct or conjugated frequency. The conjugated frequencies show a negative change in phase angle while the direct frequencies change there phase angle in accordance with the applied distortion.

6.5 CONCLUSIONS

This chapter has discussed several important points regarding the modelling of linearised time variant devices, and in particular the HVDC converter in the frequency domain. Of particular interest has been the inclusion of the linear ac and dc systems with the linearised HVDC converter, forming a nodal linear equation set describing the system as a whole. Of importance in the equation set has been the associated effects of time variance and its linear analytic representation using FCMs and tensor elements.

The frequency cross coupling has been modelled under the assumption of superposition, using the sparse lattice structured FCMs. These matrices describe the frequency cross coupling characteristics of the converter, and are either generated using sets of perturbed frequency transfers to build up the main matrix transfers or directly using linearised analytic HVDC converter models such as that described in chapter 5. The resulting FCM transfers are linear and sparse, with a lattice like structure capable of describing the frequency modulating characteristics of each particular transfer of sequence distortion.

The phase angle dependence of the conjugated frequencies in the transfers is modelled using tensor elements. These 2×2 matrices have been used with good effect previously (Smith [27]) and have been discussed in detail and used within the linearised nodal analysis.

Of key importance to modelling the HVDC converter is its system equation (Larsen's equation) relating positive and negative sequence ac side distortion and dc side distortion through a cross-coupling matrix equation. This equation, forming the description of the converter, is well known and relates the ac side currents and dc side voltage to the ac side voltage and dc side current for the HVDC converter in isolation. Each of the elements in the equation comprises of a linearised time variant frequency cross coupling matrix. Hence, the equation is a compound matrix equation. The effects of the time invariant ac and dc systems are included into this equation by rearranging the equation into nodal form and including the ac and dc frequency dependent system admittances on the required transfer diagonals. In this form the whole system is a linear equation set capable of being easily solved for the required unknowns. PSCAD/EMTDC time domain simulations have proven validity of the proposed method for the single HVDC converter. Chapter 7 presents the same processes outlined in this chapter, but extends these to model the full HVDC link in both synchronous and asynchronous modes.

Chapter 7

MODELLING HARMONIC AND INTERHARMONIC CROSS-MODULATION IN HVDC LINKS

7.1 INTRODUCTION

This chapter investigates the harmonic and interharmonic cross-modulation associated with HVDC links. Both operating point and distortion sourced harmonics and interharmonics are considered and the effectiveness of small signal linearisation is demonstrated by validation with PSCAD/EMTDC time domain simulation.

The chapter is split into four main sections, the first demonstrating the basic techniques involved with modelling the time variant link in a direct linearised manner. This is similar to the techniques shown for a single rectifier in chapter 6. Included is the general nodal analysis of the link, the inclusion of the base case operating point time variant transfers (required when modelling the operating point harmonics and interharmonics), and the solution of the full linear equation set. The second section uses the linearised direct solution method to investigate the interharmonic interaction around two different links with three separate case studies. Both HVDC links are in back-to-back configuration with negligible dc side impedance ensuring maximum harmonic and interharmonic transfer.

The first case study details the nominal 50-50Hz synchronous back-to-back link with the associated distortion sourced harmonic cross-modulation associated with a small negative sequence unbalance on the rectifier terminals. The second study demonstrates the effectiveness of the linearised analytic method when modelling the operating point harmonics and interharmonics around the asynchronous link in a 50-60Hz configuration. Both cases are validated with the time domain PSCAD/EMTDC simulation package. The third case study uses both the 50-50Hz and 50-60Hz links to show the effect switching instant variation has on the transfer of waveform distortion through the link.

The third section describes the linearised modelling of asynchronous links with small frequency differences. To model such systems it is found that the linear equation set must be reduced as memory requirements become too large for modern day computers. To overcome this problem, reduced time variant matrices are proposed. Prior knowledge of the operating conditions, such as the exact ac system fundamental frequencies and any distorting frequencies present are used to derive the returned frequency set around the link. Once these frequencies are known, the time variant transfers can be reduced accordingly providing a much smaller, and hence faster, linear equation set to be solved. This method is then used to find the operating point interharmonics as well as the distortion-sourced interharmonics around the back-to-back 50-51Hz link.

Finally, a direct solution technique is discussed for general modelling of the HVDC link.

7.2 TIME VARIANT MODELLING OF HVDC LINKS

This section details the required methods, not previously discussed in chapter 6, which are involved when modelling the time variant HVDC link.

7.2.1 Nodal analysis of HVDC links

The nodal analysis of the HVDC link is similar to that described for the single converter in chapter 6. The nodal frequency cross-coupling transfers are calculated for each of the separate converters at the correct operating points, and then rearranged to link the two converters together via a dc system admittance. Like the single converter case, all admittance transfers are time-variant and use tensors to relate the phase angle conjugation inherent in the switching modulation of the converter. The nodal analysis of the standard HVDC link, as shown in figure 7.1 can be written as,

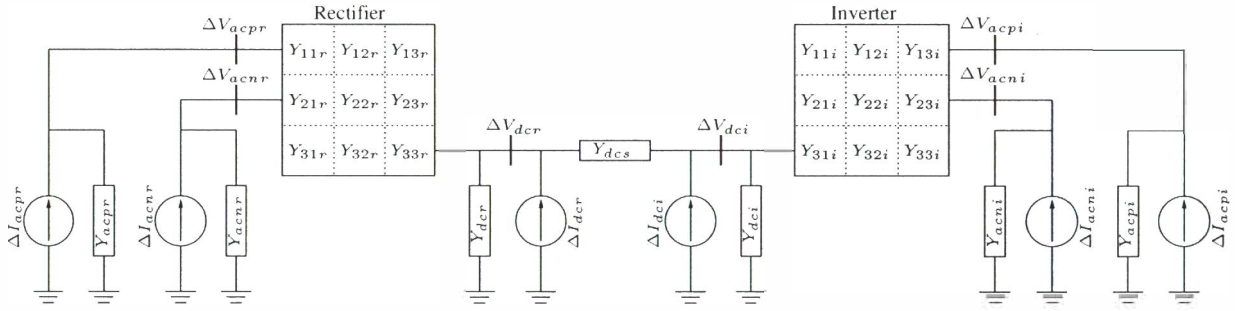

Figure 7.1 Nodal representation of the HVDC link.

$$\begin{bmatrix} \Delta I_{acpr} \\ \Delta I_{acnr} \\ \Delta I_{acpi} \\ \Delta I_{acni} \\ \Delta I_{dcr} \\ \Delta I_{dci} \end{bmatrix} = \left[\begin{array}{cccc|cc} Y_{11r}+Y_{acpr} & Y_{12r} & 0 & 0 & Y_{13r} & 0 \\ Y_{21r} & Y_{22r}+Y_{acnr} & 0 & 0 & Y_{23r} & 0 \\ 0 & 0 & Y_{11i}+Y_{acpi} & Y_{12i} & 0 & Y_{13i} \\ 0 & 0 & Y_{21i} & Y_{22i}+Y_{acni} & 0 & Y_{23i} \\ \hline Y_{31r} & Y_{32r} & 0 & 0 & Y_{Dr} & -Y_s \\ 0 & 0 & Y_{31i} & Y_{32i} & -Y_s & Y_{Di} \end{array}\right] \begin{bmatrix} \Delta V_{acpr} \\ \Delta V_{acnr} \\ \Delta V_{acpi} \\ \Delta V_{acni} \\ \Delta V_{dcr} \\ \Delta V_{dci} \end{bmatrix} \quad (7.1)$$

where,

$$\begin{aligned} Y_{Dr} &= Y_{33r} + Y_{dcr} + Y_{dcs} \\ Y_{Di} &= Y_{33i} + Y_{dci} + Y_{dcs} \end{aligned} \quad (7.2)$$

Y_{dcr} and Y_{dci} are the dc shunt admittances and Y_{dcs} the dc side series admittance which interconnects the two converters. For a back-to-back scheme this series admittance is usually very high (low impedance) and the two shunt admittances low.

The sparse tensor admittance matrix, relating all positive and negative sequence, and dc side distortion around the general HVDC link is shown in figure 7.2. This matrix equation is in the same form as shown in equation 7.1.

As with the single converter, the associated linearised effects of various HVDC link control schemes, PLO, etc, can be included into the equation set, prior to the nodal analysis, by simple matrix reduction.

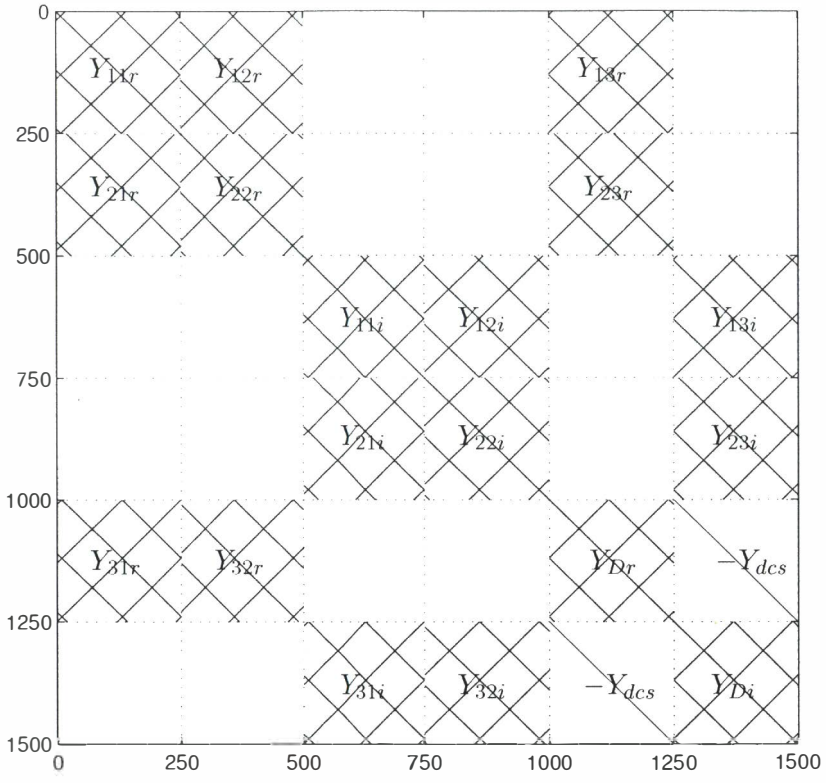

Figure 7.2 Sparse structure of HVDC link tensor admittance matrix.

7.2.2 Including the effects of the base case characteristic harmonics

Links of different operating frequencies, ie, 50-60Hz or links where both ac systems are weak and experience small frequency differences, such as 49-51Hz or 49.8-50.5Hz are of particular interest. In these cases the base case harmonics of each converter cross-modulate around the link to appear as *operating point* interharmonics.

The linearisation around the base case operating point assumes that a small signal distortion is small enough that the characteristic base case harmonics remain effectively unchanged. This has been shown in chapter 4 using the iterative frequency domain model described in chapter 3. These characteristic frequencies describe the operating point and are assumed not to change or change only by a small amount. They are considered linear, and are calculated analytically in section 5.2 of chapter 5. Two methods can be used to acquire the effects of the characteristics on the overall harmonic and interharmonic transfers. The first is to simply multiply the vector of base case quantities by the inverted admittance matrix, for example, the solution, $y = Ax + b$ is solved for x, ie, $x = A^{-1}y - A^{-1}b$ where b is the vector of characteristic harmonics. Alternatively, and a mathematically identical way is to convert the base case quantities to transfers by dividing by the fundamental quantities and including these transfers in the full admittance matrix before inverting. Though a little unorthodox this is the method used in this thesis.

To acquire the transfers, the base case ac current harmonics are simply divided by the fundamental ac voltage, and the base case dc voltage harmonics divided by the dc current. When solving the linear equation set, these transfers are effectively multiplied by the fundamental ac voltage (magnitude and angle) and the dc current to give the characteristic harmonics and, through the frequency cross coupling of the admittance matrix, the operating point interharmonics around the link.

Figure 7.3 shows the alteration of the linearised FCM transfer a for a 50Hz 12 pulse converter.

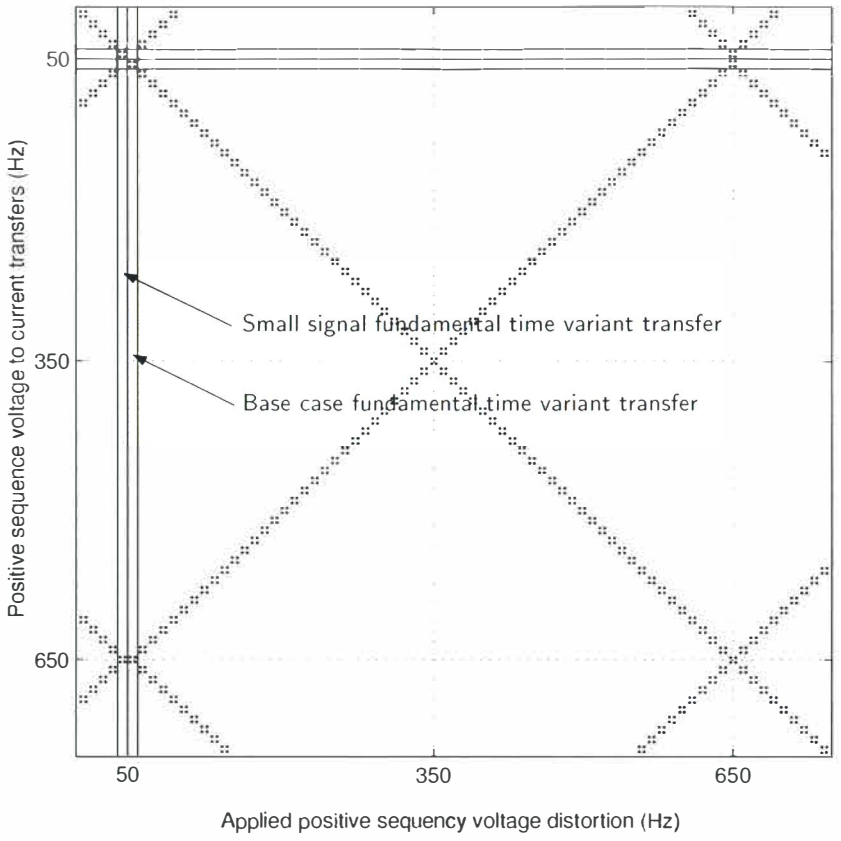

Figure 7.3 Inclusion of base case characteristic harmonic transfers for transfer a.

As shown, there now exists two 50Hz time variant transfers in the matrix, the first contains the linearised transfer while the second contains the base case transfer. Also, an extra row at 50Hz has been added, preserving the frequency cross coupling inherent in the time variant transfers. This row contains the same information as the original 50Hz row. Extra columns are required at 50Hz in both transfers e and i containing the base case transfers, ie, for transfer e, a column containing the negative sequence base case transfers at 550 Hz and 1150Hz ... and for transfer i a column containing the dc side base case transfers at 600Hz and 1200Hz ... Extra rows are also required in the transfers b, c and d to preserve the frequency cross-coupling. In general, these modifications are only required in the case of calculating the base case harmonics and operating point interharmonics around a converter or link.

7.3 TIME VARIANT MODELLING OF THE BACK-TO-BACK HVDC LINK

This section uses the methods described in section 7.2 to model the harmonic and interharmonic cross-modulation on two separate case studies; one a 50-50Hz link with negative sequence unbalance on the rectifier, the other is a 50-60Hz asynchronous link in normal operating mode. Both cases use a back-to-back configuration similar to that shown in figure 7.4, and based on the CIGRE benchmark test system described in section D.2. To allow maximum harmonic and interharmonic propagation through the link, the dc system impedance has been removed providing a direct coupling of the rectifier and inverter dc systems. It is noted that due to the negligible voltage drop on the dc side, the operating points are slightly different from those of the standard benchmark CIGRE HVDC link. However, for the purposes of the case studies this is not considered important. The ac side impedances and power factor capacitors remain unchanged in the 50-50Hz case, while in the 50-60Hz case the 60Hz inverter ac system is scaled

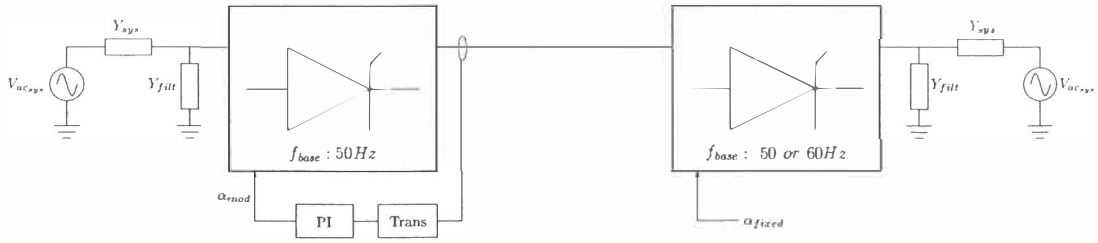

Figure 7.4 Case Study 1, Mono-polar Back-to-back HVDC test system.

accordingly.

In both case studies the time domain simulation program PSCAD/EMTDC is used to acquire the operating point and provide validation of the harmonic and interharmonics resulting from the proposed analytic linearised solution method. While simulating in the time domain the standard control systems are initially operational, however after a set time threshold the inverter firing angle is locked. The constant current PI control of the rectifier remains, and is included in the analytic linearised model, while the inverter firing angle control is assumed fixed[1]. The simulation is allowed to settle to the steady state and the operating point is recorded. This is used as the operating point to be linearised about. The linearised procedure is briefly outlined below.

- The operating point is acquired. This must be known to initialise the linearised model in order for the linearised model to linearise about. In these case studies time domain simulation is used.
- The small signal linearised time variant frequency cross-coupling matrices for both rectifier and inverter are calculated in tensor form. The frequency range of the transfers is up to 2500Hz. For the 50-50Hz case study 50Hz frequency steps are required and for the 50-60Hz case 10Hz frequency steps are required. This gives transfer matrix sizes of 100×100 and 500×500 in tensor form.
- The base case time variant transfers are calculated and included into the small signal linearised time variant transfers.
- The ac and dc system admittances are calculated and converted into diagonal tensor form for easy inclusion into the nodal equation set.
- Nodal equations are written and the matrix transfers concatenated into the full time variant linearised admittance matrix, Y.
- The linearised nodal equation set is split into the known and unknown quantities, then solved for the unknowns.

7.3.1 Case Study 1: The synchronous 50-50Hz back-to-back link with negative sequence unbalance

This case study is used to investigate the effects of negative sequence on the HVDC link, and to validate the linearised algorithm against PSCAD/EMTDC time domain simulation. Table 7.1 gives the operating point conditions for the 50-50Hz link. Figures 7.5 to 7.8 show the resulting characteristic and distortion sourced harmonics resulting from a 5.3kV (approximate 0.018pu)

[1] It should be noted that in both cases switching instant variation still exists at the end of commutation.

Parameter (Hz)	Sending end Rectifier (Hz)	Receiving end Inverter
AC side voltage (RMS)	$314.32\angle -1.14^o$	$230.38\angle -2.77^o$
AC side unbalance (RMS)	$6.53\angle 51^o$	-
Firing angle (α_o)	15.07^o	134.69^o
Commutation period (μ_o)	24.09^o	18.96^o

Table 7.1 Operating parameters of the 50-50Hz HVDC case study.

negative sequence unbalance. Two figures exist for both the rectifier and inverter, showing the positive and negative sequence harmonics respectively. This is because a negative sequence unbalance causes positive sequence 550Hz (11th), 1050Hz (23rd) ... harmonics and negative sequence 650Hz (13th) and 1250Hz (25th) .... These frequencies fall at the characteristic frequencies but are in opposite phase sequence. The main associated frequencies falling on both the rectifier and inverter ac terminals are: 150Hz (3rd), 550Hz (11th),750Hz (15th), 1150Hz (23rd) ... in positive sequence and 50Hz (1st), 450Hz (9th), 650Hz (13th), 1050Hz (21st) ... in negative sequence. These correspond to a 100Hz (2nd), 500Hz (10th), 700Hz (14th), 1300Hz (26th) ... on the dc side (not shown). Of the returned distortion sourced harmonics, both the positive sequence 150Hz (3rd) harmonic and the actual transfer of negative sequence unbalance through the link are the largest cause for concern. Problems have occurred in the past from other frequencies resulting from negative sequence unbalance. Of these, the 450Hz (9th) harmonic instability associated with the New Zealand HVDC bi-polar scheme [11] is of interest. This problem was cured with the addition of a extra ninth harmonic filter at the inverter terminal bus. For the test case the magnitude of the returned positive sequence 3rd harmonic on the

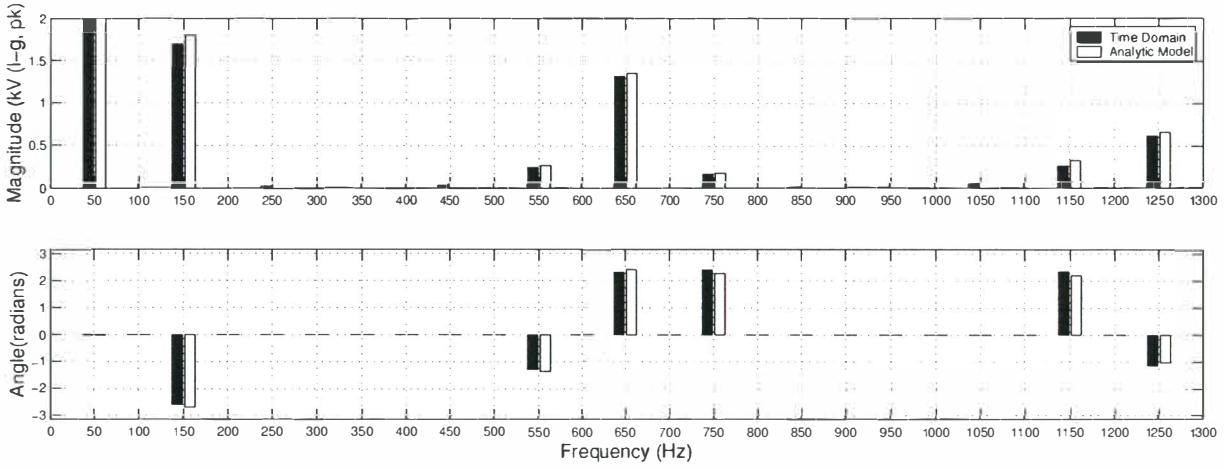

Figure 7.5 Returned rectifier positive sequence voltage spectrum resulting from 50Hz negative sequence distortion at rectifier - constant current control at rectifier.

inverter bus is higher than that at the rectifier bus. The rectifier has a 1.6kV (0.006pu) voltage magnitude while the inverter has a 2.4kV (0.013pu) 3rd harmonic voltage magnitude. Also, the 5.3kV (0.018pu) negative sequence unbalance has been transferred to a 2.2kV (0.0115pu) negative sequence unbalance at the inverter terminals.

7.3.2 Case Study 2: The asynchronous 50-60Hz back-to-back link

This case study shows the results of modelling the interharmonic cross-modulation present on the asynchronous back-to-back 50-60Hz HVDC link. The configuration of the link is identical to figure 7.4 except the inverter ac system is at 60Hz and all filters and the ac system are scaled

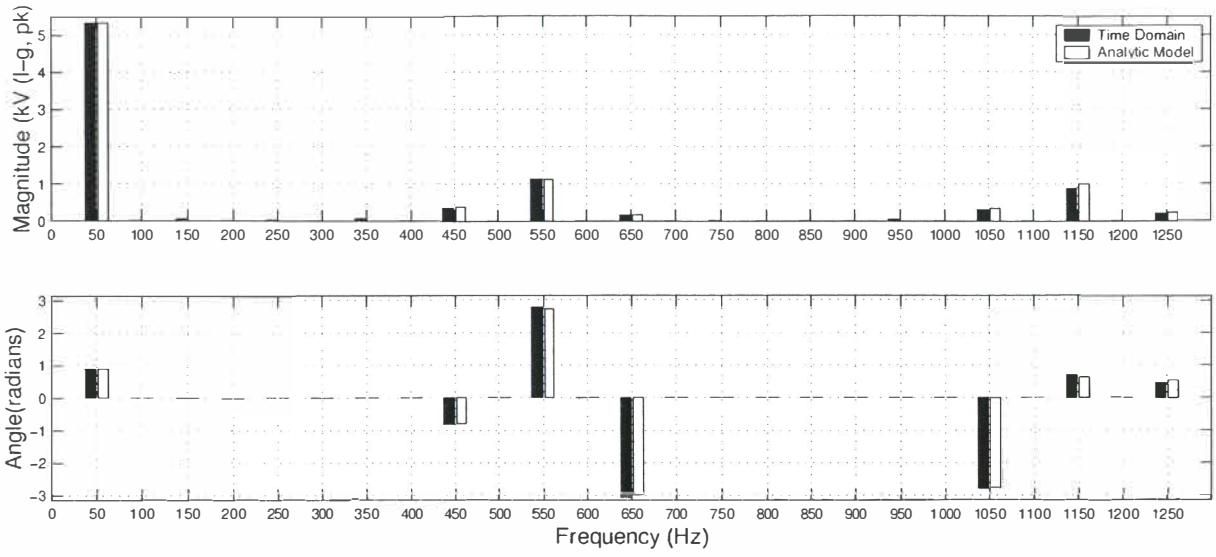

Figure 7.6 Returned rectifier negative sequence voltage spectrum resulting from 50Hz negative sequence distortion at rectifier - constant current control at rectifier.

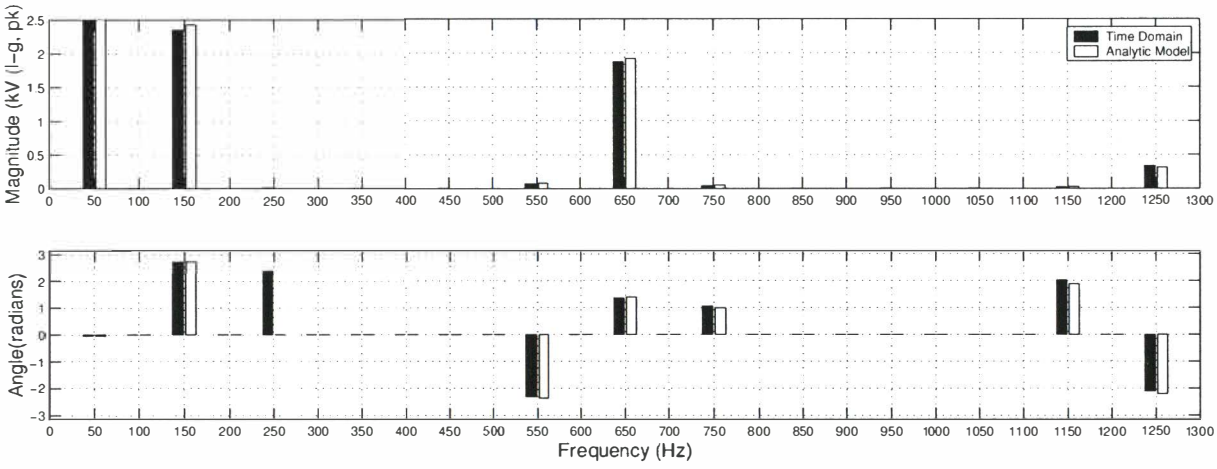

Figure 7.7 Returned inverter positive sequence voltage spectrum resulting from 50Hz negative sequence distortion at rectifier - constant current control at rectifier.

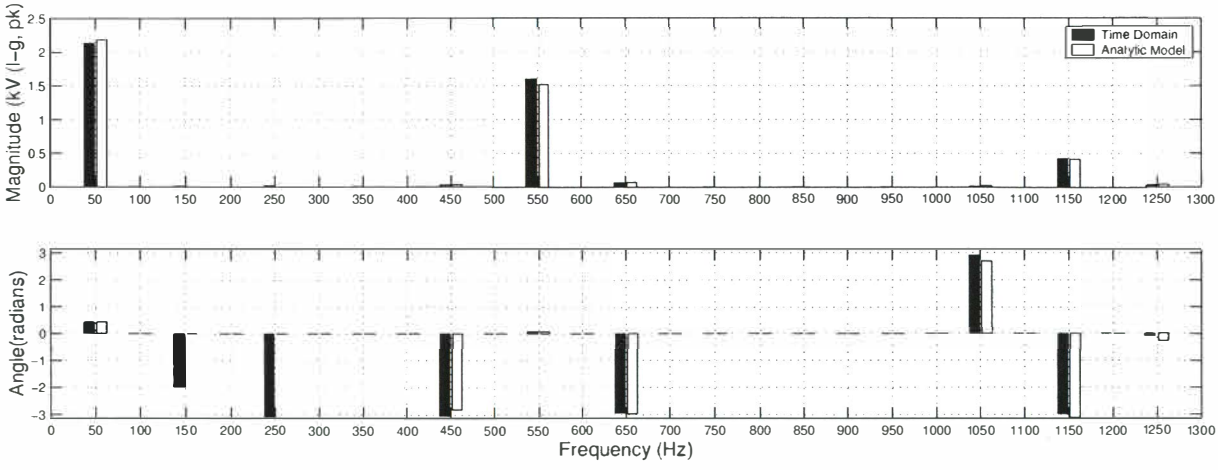

Figure 7.8 Returned inverter negative sequence voltage spectrum resulting from 50Hz negative sequence distortion at rectifier - constant current control at rectifier.

accordingly. As with the 50-50Hz case, the dc side impedance is assumed negligible allowing maximum interharmonic cross-modulation between both ac systems.

Both the operating point interharmonics, resulting from normal link operation, and the effects of negative sequence unbalance on both the rectifier and inverter ac systems are investigated. Table 7.2 gives the operating point conditions of the link.

Parameter (Hz)	Sending end Rectifier (Hz)	Receiving end Inverter
AC side voltage (RMS)	$307.68\angle 0.20^o$	$230.38\angle -0.43^o$
AC side unbalance (RMS)	$7.25\angle 30.07^o$	$3.94\angle 63.46^o$
Firing angle (α_o)	19.70^o	132.44^o
Commutation period (μ_o)	22.70^o	16.87^o

Table 7.2 Operating parameters of the 50-60Hz HVDC case study.

The *operating point* interharmonics on a 50-60Hz back-to-back link

Figure 7.9 shows the comparison between time domain simulation and the linearised analytic model for the dc side voltage of the 50-60Hz link in normal operation. Agreement is excellent. The main returned frequencies are at the 12 pulse characteristic dc side frequencies for both the 50Hz rectifier and 60Hz inverter. Other smaller components are present at 120Hz intervals and these are also matched well, as indicated by the excellent phase angle match.

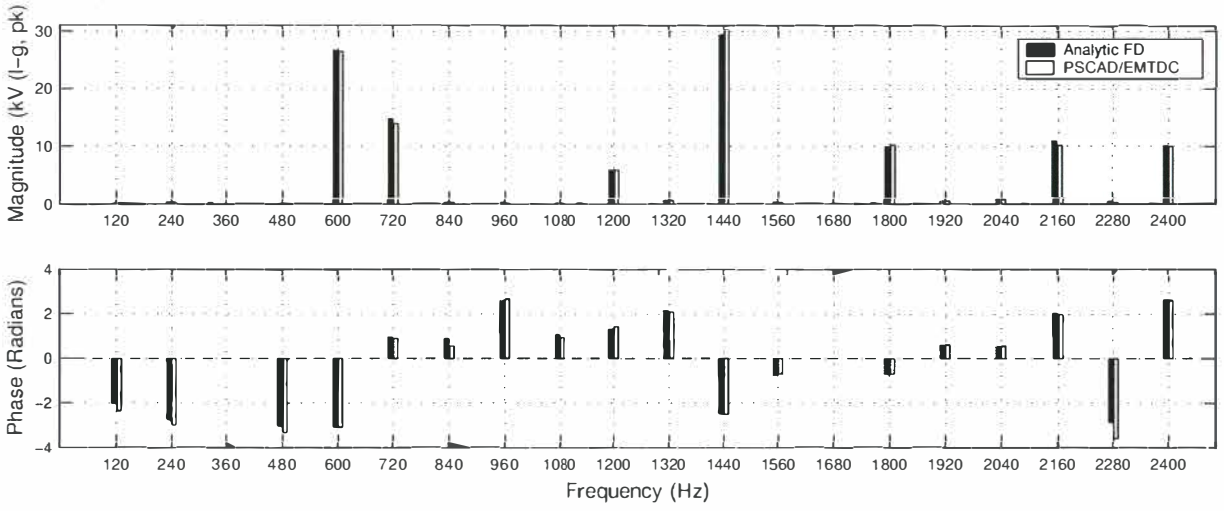

Figure 7.9 Returned dc side voltage spectrum on a 50-60Hz back-to-back HVDC link.

Figure 7.10 shows the returned voltages present on the rectifier side of the HVDC link. The characteristic harmonic voltages are present at about the same levels as those seen in figures 7.5-7.8 for the 50-50Hz link, however operating point interharmonics resulting from the cross-modulation with the inverter dc side characteristic harmonics are also present. Of these the major frequencies are: 170Hz, 290Hz, 770Hz in positive sequence and at 70Hz, 190Hz, 310Hz, 670Hz in negative sequence. The 670Hz and 770Hz distortions are the result of the inverter 12th (720Hz) harmonic on the dc side. Once again validation with time domain simulation is excellent.

Figures 7.11 and 7.12 show the inverter side terminal voltage in positive and negative sequence respectively. In this case the main extra returned frequencies, a result of the rectifier dc side characteristics, are a negative sequence 540Hz and 1140Hz and positive sequence 180Hz distortions.

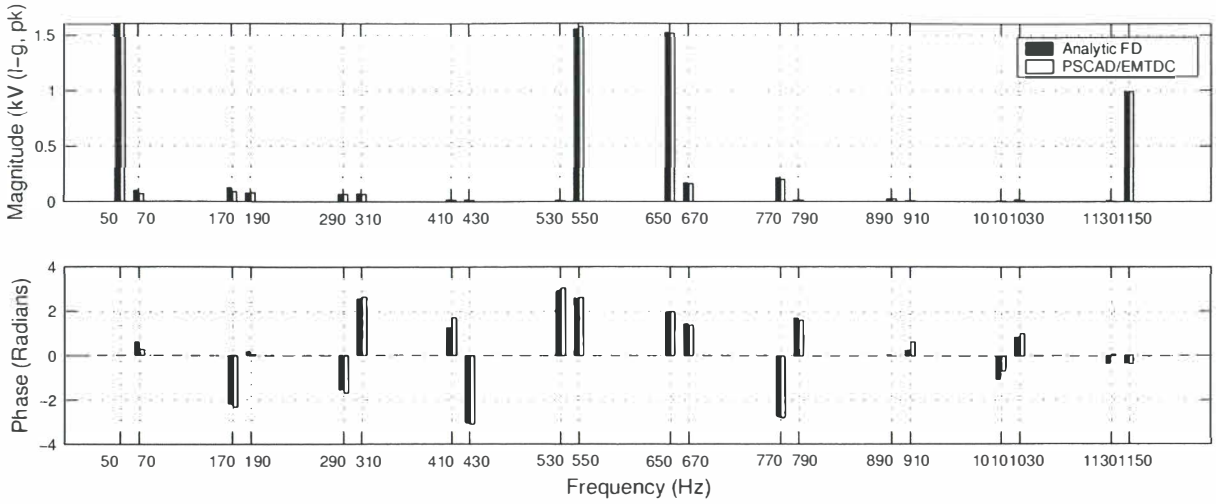

Figure 7.10 Returned rectifier voltage operating point interharmonics for 50-60Hz link - constant current control at rectifier.

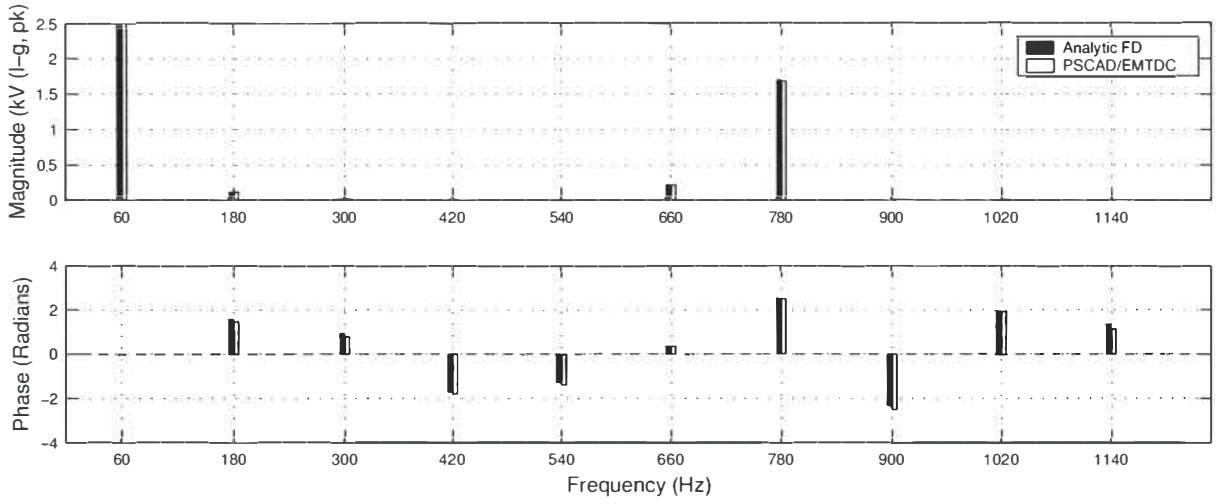

Figure 7.11 Returned positive sequence inverter operating point interharmonics for 50-60Hz link.

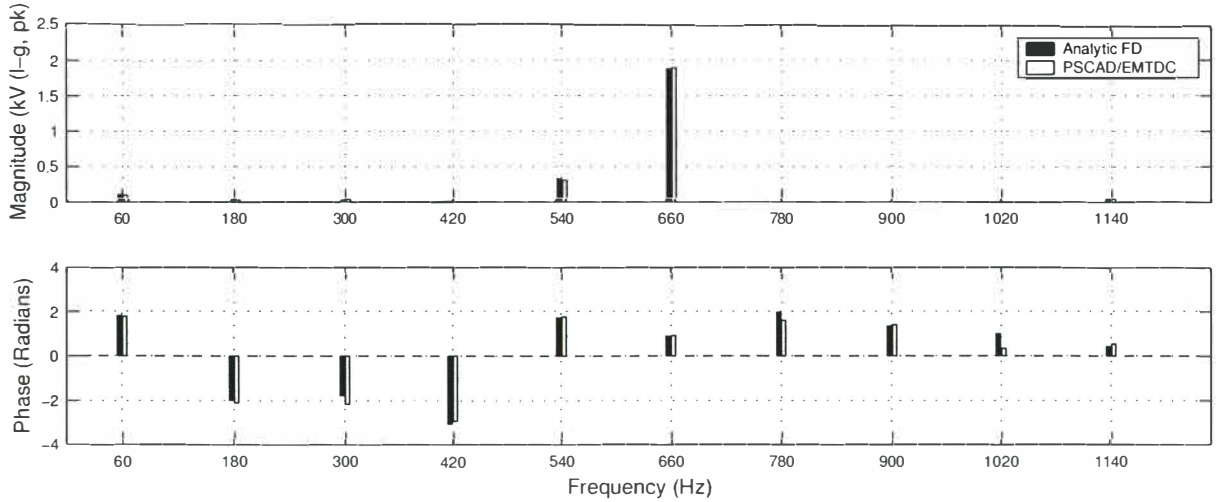

Figure 7.12 Returned negative sequence inverter operating point interharmonics for 50-60Hz link.

The following section looks at the effects associated with negative sequence unbalance on the 50-60Hz back-to-back HVDC link.

The negative sequence *distortion sourced* interharmonics on the 50-60Hz back-to-back link

The results of negative sequence unbalance at both the 50Hz rectifier and the 60Hz inverter are shown here. Figure 7.13 shows the dc side voltage spectrum resulting from negative sequence unbalance on the rectifier while figure 7.14 shows the dc side voltage spectrum resulting from negative sequence unbalance on the inverter.

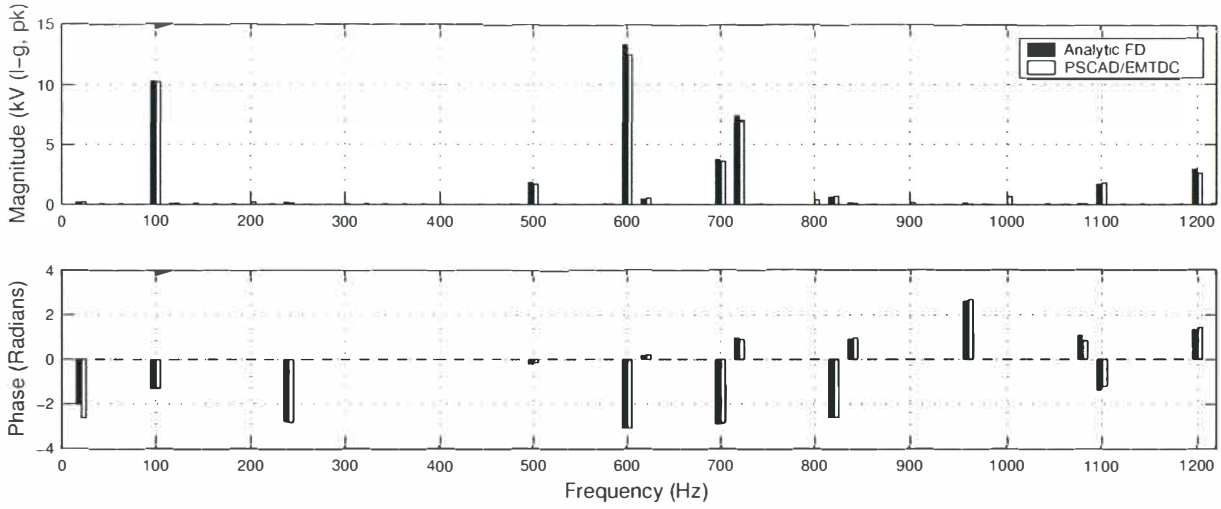

Figure 7.13 DC side voltage on 50-60Hz link with a 0.024pu negative sequence unbalance on the rectifier.

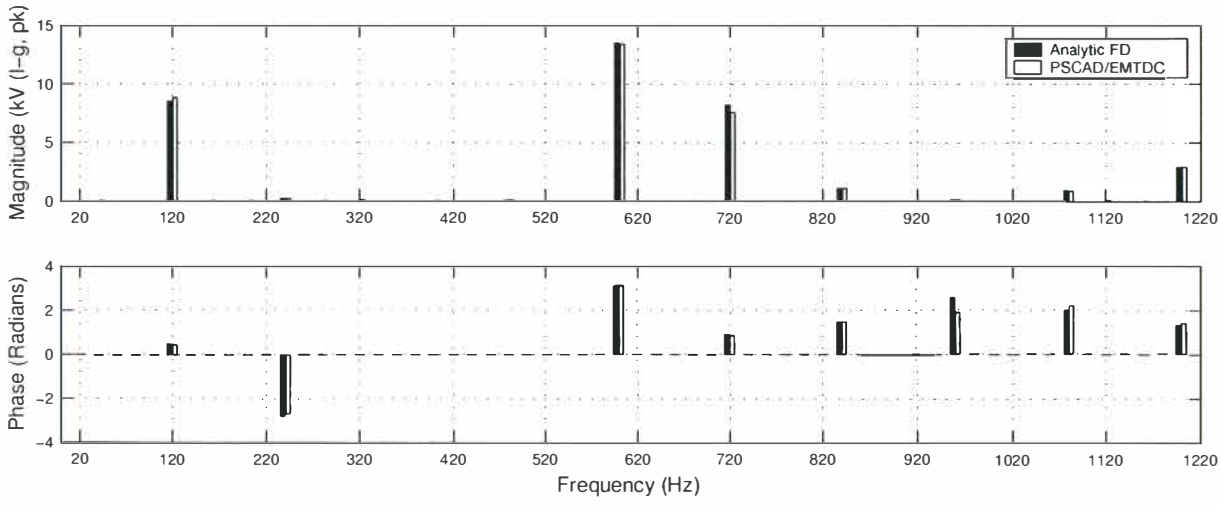

Figure 7.14 DC side voltage on 50-60Hz link with a 0.017pu negative sequence unbalance on the inverter.

As shown, addition harmonics are present at the 2nd, 10th, 14th, 22nd ... for both cases. Of these, the 2nd harmonics are the largest. Appendix I.1 shows the results of negative sequence unbalance at the rectifier and appendix I.2 for the inverter. The returned negative sequence spectrum on the opposite side of the link,(ie, the converter without applied distortion) is the most interesting as this represents the cross-modulation from one system to the other.

Figure 7.15 shows the negative sequence unbalance on the 60Hz inverter resulting from the rectifier 50Hz unbalance. As shown a major returned distortion is the negative sequence 40Hz. This

frequency is one that may modulate to subsynchronous frequencies on the rotor of a generator. However, in this instance it is not a cause for concern as the generator modulates in the same way as a converter, causing the negative sequence 40Hz to modulate to the dc side rotor at a frequency of 100Hz, well away from the subsynchronous torsional modes of generator shafts.

Figure 7.16 shows the negative sequence unbalance on the 50Hz rectifier resulting from an inverter 60Hz unbalance. As shown the major returned distortion is the negative sequence 70Hz. This will modulate onto any electrically close rotor shafts at a frequency of 120Hz, also well away from the subsynchronous torsional modes of generator shafts. The effects of the interharmonics on the SSR on turbine-generator rotor shafts are discussed in more detail in section 7.5.

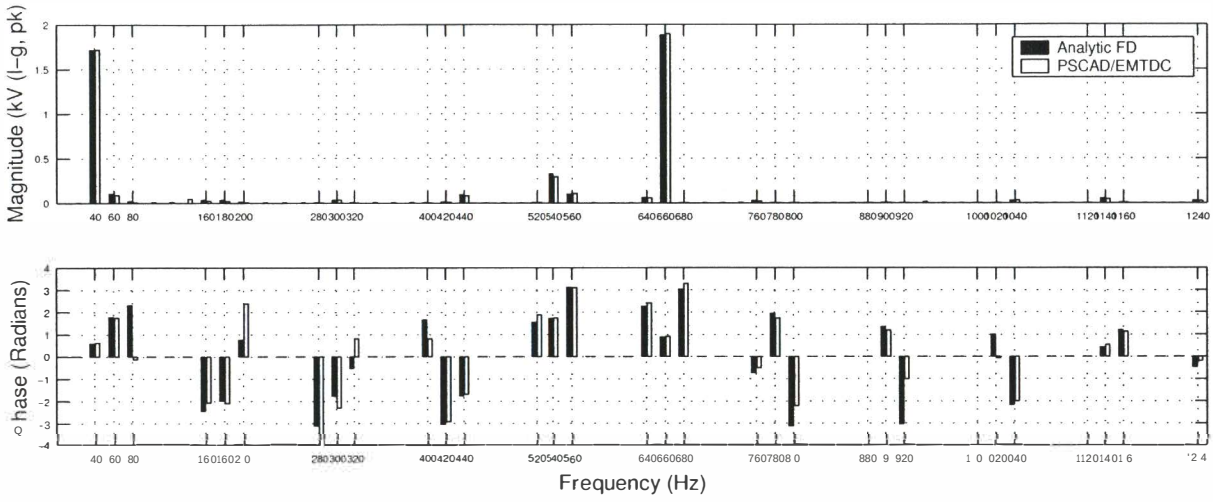

Figure 7.15 Resulting negative sequence spectrum on inverter due to 0.024pu negative sequence unbalance on rectifier.

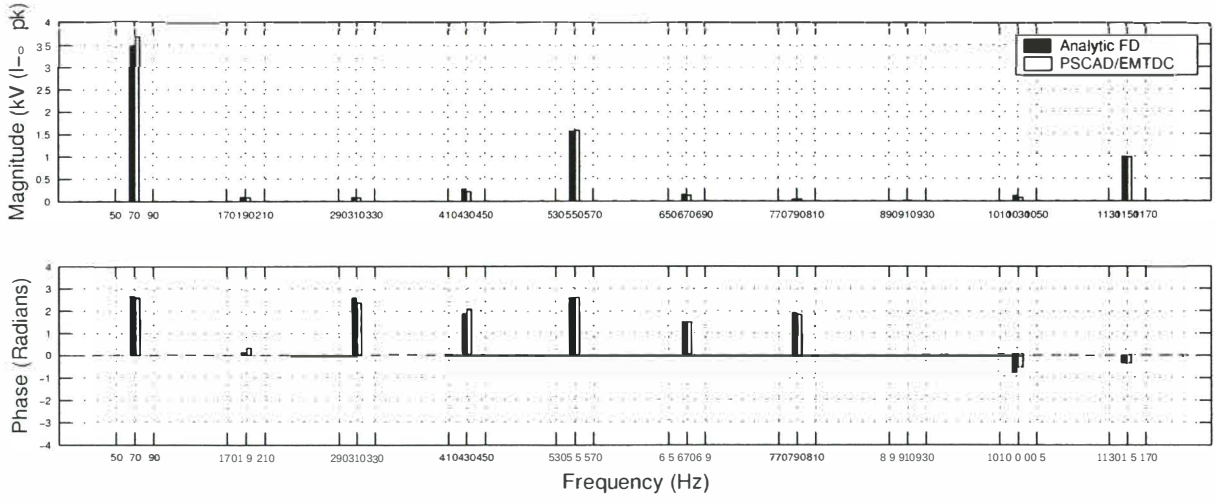

Figure 7.16 Resulting negative sequence spectrum on rectifier due to 0.017pu negative sequence unbalance on inverter.

The results so far have shown excellent agreement with PSCAD/EMTDC time domain simulation. The following section shows the effects associated with the switching instant variation and how, why and when it is important to model this phenomena while modelling the transfer of distortion through an HVDC link.

7.3.3 Case Study 3: The effects of SIV on the transfers on distortion through a link

This section discusses the effects of SIV on modelling the harmonic and interharmonic distortion around the HVDC link. In particular, the effects of SIV on the two previous case studies, described in sections 7.3.1 and 7.3.2 are discussed.

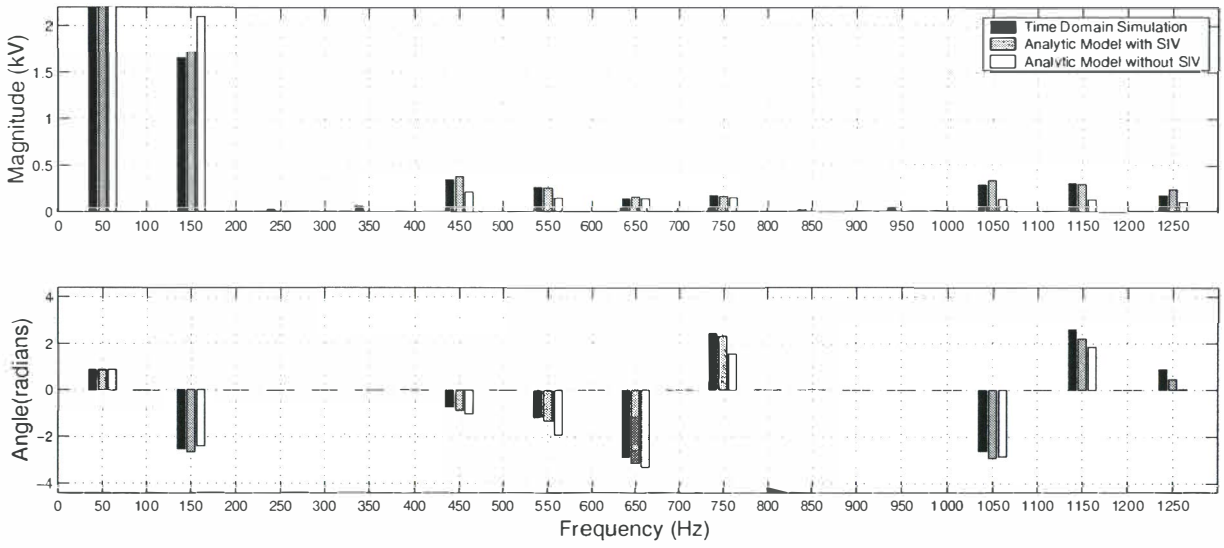

Figure 7.17 Effect of SIV on returned rectifier voltage spectrum resulting from 50Hz negative sequence distortion at rectifier, 50-50Hz back-to-back HVDC link.

Many models ignore the effects of switching instant variation (SIV) when modelling the HVDC converter or link. Chapter 4 showed how the effects of SIV are important when modelling the effects of distortion on the dc side voltage and chapter 5 has modelled this phenomenon using the area modulated impulse train (AMIT).

To demonstrate the effects of SIV, figures 7.17 and 7.18 show the returned harmonic voltages, resulting from negative sequence unbalance on the rectifier, around the 50-50Hz back-to-back link test system used in section 7.3.1. Both figures omit the characteristic harmonics which, assuming small signal distortion, are independent of SIV.

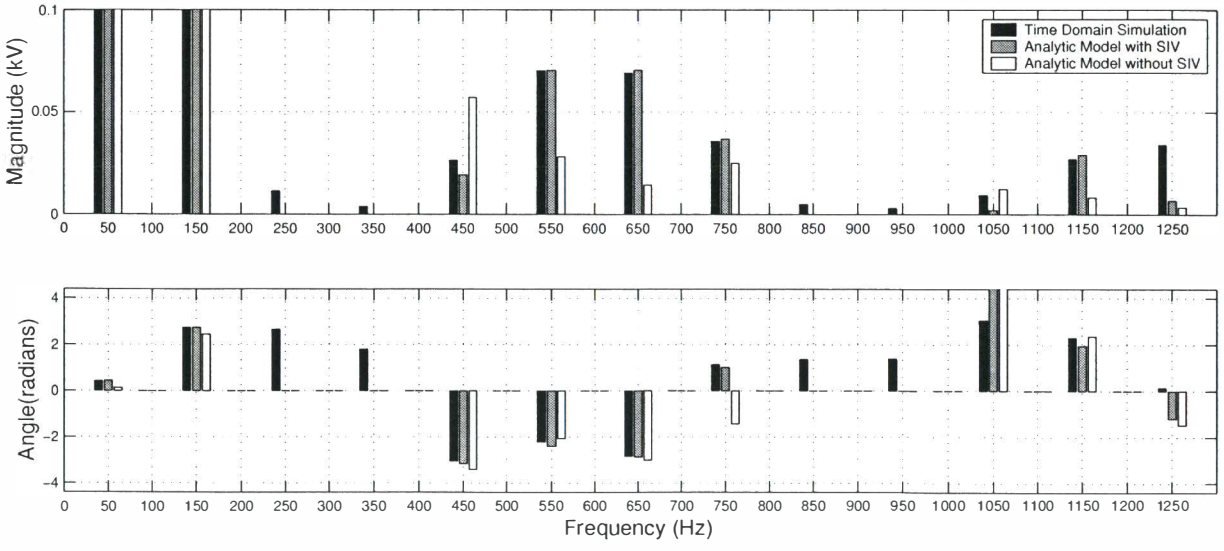

Figure 7.18 Effect of SIV on returned inverter voltage spectrum resulting from 50Hz negative sequence distortion at rectifier, 50-50Hz back-to-back HVDC link.

The effect of SIV on these distortion sourced voltages is noticeable, the difference between the actual time domain spectrum and the analytic spectrum is about 25% or worse in the case of the rectifier. The effect of the harmonic cross-modulation through the link on the returned inverter spectrum is even more noticeable.

Figure 7.19 shows the dc side voltage spectrum for the 50-60Hz HVDC link with an applied negative sequence unbalance. The dc side voltage spectrum consists of the characteristic dc side frequencies resulting from the rectifier and inverter (which cause the operating point interharmonics) and the distortion sourced harmonics associated with the negative sequence unbalance on the rectifier. The results show the effects of modelling with and without SIV. The effect SIV has on the operating point interharmonics (600Hz,720Hz) occurring in an asynchronous link is negligible, while in general a significant effect on the returned distortion sourced interharmonics (100,500,620,700,820Hz ...) caused by the negative sequence unbalance can be seen. The

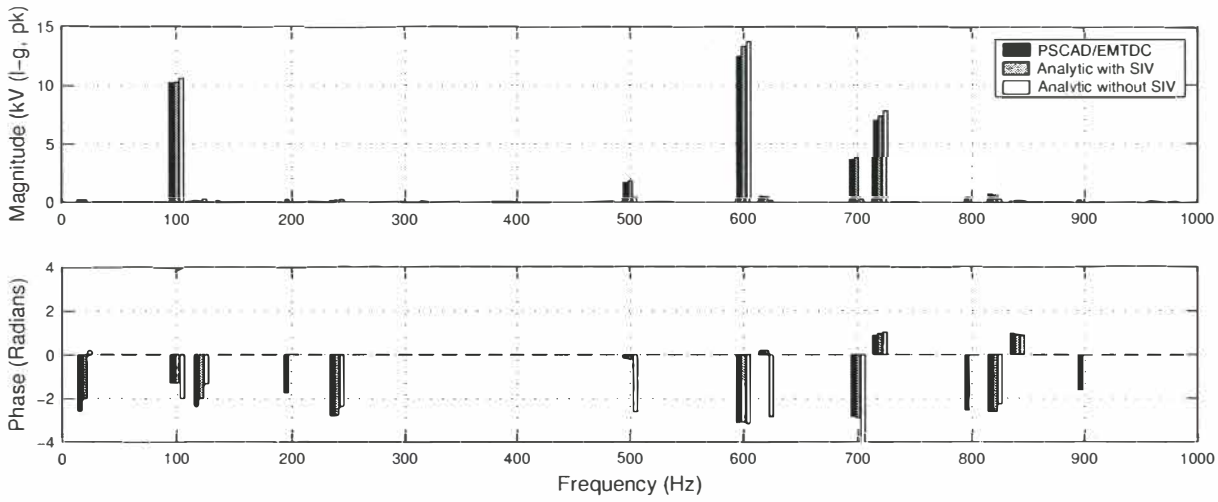

Figure 7.19 Effect of SIV on returned inverter voltage spectrum resulting from 50Hz negative sequence distortion at rectifier, 50-60Hz back-to-back HVDC link.

characteristic frequency transfers are independent of SIV, but require the accurate modelling of the commutation period (see chapter 5). There is no associated effect with the switching instant variation, and good results using the method depicted in section 7.2 can be achieved using accurate HVDC converter models which model the effect of the commutation period but do not model the effects of SIV. Hence, the operating point interharmonics around asynchronous links are generally not dependent on the SIV.

The distortion sourced interharmonics shown in figures 7.18 and 7.19 for both the 50-50Hz and 50-60Hz HVDC links with negative sequence unbalance are dependent on SIV. In both cases the cross-modulation effects of SIV are very noticeable. This is because of the switching instant dependence associated with the dc side transfers of distortion (see chapters 4 and 5). However, it should be noted that the effect of the SIV is generally more dominant at the higher frequency transfers. This can be seen in figure 7.19 for the 100Hz dc side distortion.

The results in various papers by Hu, notably [65][66] and [40] confirm these observations. Hu fails to model SIV but gets very good results for the returned operating point interharmonics around an asynchronous HVDC link [40]. In [65] and [66] the results of low order returned frequencies are good but progressively get worse at higher frequencies. This is due to lack of SIV modelling in Hu's HVDC converter model. If accurate predictions of harmonic and interharmonic currents and/or voltages are required, then these distortion sourced interharmonics must be modelled with HVDC converter models capable of modelling the effects of SIV, such as the models described in chapter 3 and 5.

The following section looks at modelling the asynchronous HVDC link with smaller frequency differences in both ac systems. These cases provide a challenge for the method described thus far as computational memory requirements for the time variant matrices become large due to the small frequency steps required in the FCM transfers.

7.4 MODELLING ASYNCHRONOUS LINKS WITH SMALL FREQUENCY DIFFERENCES

The previous methods have demonstrated the capabilities of a direct linearised approach for solving harmonic and interharmonic cross-modulation around HVDC links. The techniques presented so far have included all harmonic and interharmonic coupling via the FCM transfers. Often asynchronous HVDC links, operating in weak ac systems experience small frequency shifts in their associated ac systems. When modelling a link in these conditions using the approach described so far, the frequency steps required for the matrix transfers become very small and the memory requirements large (even though they are sparse). For example, if a 50-50.1Hz HVDC link is to be modelled then the frequency step required becomes 0.1Hz. If the frequency range of interest is 0-1250Hz, then the FCM size of each transfer is 12500×12500. In tensor form this is a matrix with 625 million elements. Even at 96% sparsity this represents a matrix containing 25 million elements. In this case the admittance matrix size would be 150000×150000 and contain approximately 450 million non-zero elements. Bathurst [6] recognised that this was prohibitive in his Newton solution of the HVDC link and developed an adaptive frequency selection method. Alternatively, if the HVDC link is of small enough frequency difference then it may be possible to model the link as a 50-50Hz or 50-60Hz with slowly varying phase shifts applied to one, or both terminals of the converters. This is the same as a small frequency difference. In terms of modelling, the returned harmonics will be at different frequencies and hence the effect of different ac system impedance at these frequencies will cause error in the returned results. This will be particularly pronounced if the ac systems have any high Q resonances. The point when this method may become feasible is unknown and would vary from case to case. Hence, this method is not covered in this thesis.

The following section concentrates of the former method, assuming that all frequencies are modelled correctly and further investigates methods for reducing the computational memory requirement of the matrix transfers. This is achieved by observing the main frequency couplings associated with an asynchronous HVDC link both with and without applied system distortion.

7.4.1 The reduction of the FCM transfers

A clear understanding of the frequency cross coupling occurring in asynchronous HVDC links can be gained by observing the returned frequency spectra around a link. For a single rectifier or inverter, frequencies are easily predicted using simple modulation theory. Table 3.1 in chapter 3 shows the modulating relationships of the single HVDC converter with a dc side distortion f_{dck}. This section shows the main frequencies involved in the frequency cross-modulation of the general asynchronous HVDC link leading to two forms of reduced time variant transfers. One effect that is unaccounted for is the effect of asymmetries causing sequence coupling at all higher frequencies. If sequence coupling magnitude is high then more harmonic and interharmonic frequencies will be involved and it may become difficult to predict those frequencies which are most important. However, in general the inter-sequence coupling at higher frequencies is likely to remain small, hence it is ignored in this work.

The reduced transfers

The common system in an HVDC link is the dc system. Hence, reducing the admittance transfer matrix of a full HVDC link to the dc side variables shows all possible frequencies that result from an arbitrary dc side distortion f_{dck}. Figure 7.20 (a) shows the reduced dc side time variant impedance transfer for a 50-51Hz HVDC link, while figure 7.20 (b) shows the inversion of this matrix, or the time variant admittance transfer matrix. Plotting a vertical line, corresponding to a dc side voltage distortion, f_{dck}, on the admittance matrix gives the returned dc side currents at frequencies where the line intersects the light grey grid. The dark grey grid shows the largest frequency transfers after a tolerance of $1e^{-6}$ is applied[2]. These results can be used to predict both distortion sourced interharmonic frequencies, by relating any applied distortion to its dc side equivalent f_{dck}, or operating point sourced interharmonic frequencies by simply looking at the retuned interharmonics resulting from both the rectifier and inverter dc side voltage characteristics.

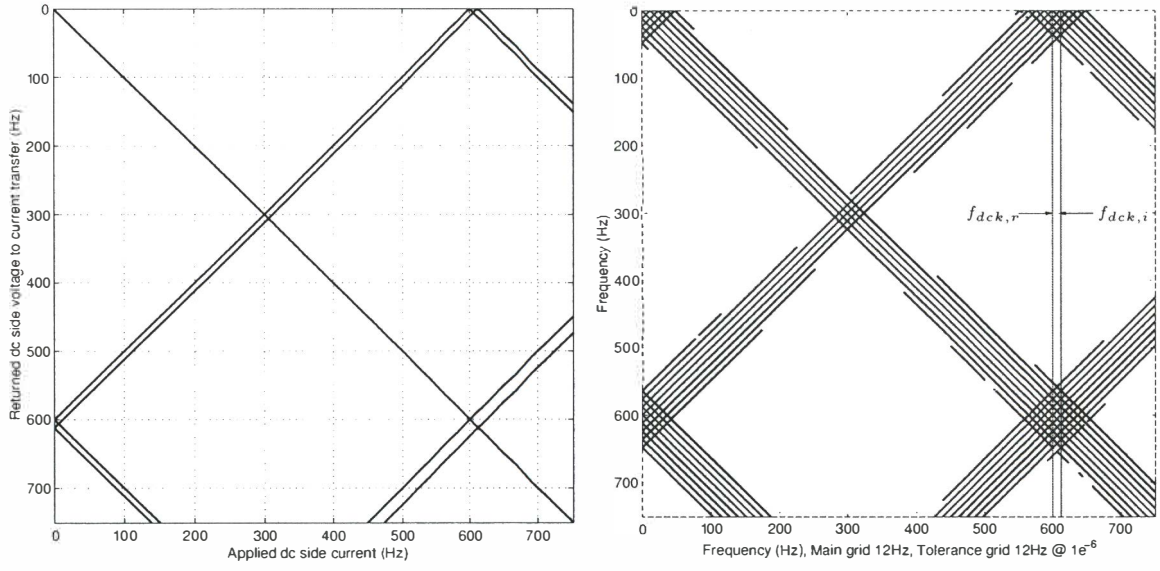

(a) Reduced dc side impedance transfer.

(b) Inverted dc side (admittance) transfer.

Figure 7.20 The reduced dc side transfers for a 50-51Hz HVDC link.

To show the returned operating point sourced interharmonic frequencies for the 50-51Hz asynchronous HVDC link, the vertical lines in figure 7.20 (b) are plotted at the characteristic 12th dc side voltage frequencies for the rectifier $f_{dck,r}$ (600Hz) and inverter $f_{dck,i}$ (612Hz)[3]. The returned dc side frequencies, resulting from both of the characteristic distortions fall at the same frequencies. The resulting operating point interharmonics are at frequencies where these lines intersect with the light grey grid and it is these frequencies and their equivalent ac side frequencies that are all that is needed in a full linearised solution of an asynchronous HVDC link. In all different instances the interharmonic frequencies resulting from the rectifier and inverter characteristics fall at the same frequencies. In this case, the operating point interharmonic frequencies fall at frequencies of: 12,24,36,48,60,72Hz ... or at 12Hz intervals. Once these dc side frequencies are

[2]Similar grid lattices are shown in appendix J, where one converter is always 50Hz and the other varies from 51Hz through to 60Hz in 1Hz intervals.

[3]If the matrix was extended to include the characteristic 24th dc side voltage harmonics then the returned currents would be at the same frequencies.

known, it is easy to find the equivalent positive and negative sequence ac side frequencies for each converter. Knowing the frequencies associated with the converter in asynchronous operation allows each admittance transfer to be reduced accordingly. Assuming no applied system distortion, all transfers will have a $(6n_g)^2$ reduction in their memory requirements, where n_g is the number of series connected six pulse groups.

A simple equation can be written for the returned first order frequencies on the dc side of the asynchronous HVDC link. This equation describes returned frequencies on the light grey grid of figure 7.20 (b), for some dc side distortion f_{dck},

$$f_{dc} = 6n_g n(f_{comm}) \pm f_{dck} \tag{7.3}$$

f_{comm} is the common frequency between the two operating frequencies of the 12 pulse HVDC link and is effectively the common multiple between both the rectifier and inverter fundamental frequencies. If both the rectifier and inverter fundamental frequency are divided by the common frequency, the result will be an integer multiplier in both cases. Table 7.3 shows the difference in the ac side frequencies (Δf), the common frequencies (f_{comm}) and the required grid lattice frequency (f_{grid}) for various asynchronous HVDC schemes.

Converter1	Converter 2	Δf	Common Frequency f_{comm}	Grid lattice frequency f_{grid}
50.0	50.0	0	50.0	600
50.0	51.0	1.0	1.0	12
50.0	52.0	2.0	2.0	24
50.0	53.0	3.0	1.0	12
50.0	54.0	4.0	2.0	24
50.0	55.0	5.0	5.0	60
50.0	56.0	6.0	2.0	24
50.0	57.0	7.0	1.0	12
50.0	58.0	8.0	2.0	24
50.0	59.0	9.0	1.0	12
50.0	60.0	10.0	10.0	120
50.0	50.1	0.1	0.1	1.2
50.1	60.0	9.9	0.1	1.2
50.5	60.6	10.1	10.1	121.2
49.9	50.1	0.2	0.1	1.2
48.0	52.0	4.0	4.0	48
48.0	56.0	8.0	8.0	96

Table 7.3 Common frequencies between different 12 pulse asynchronous HVDC links.

On the ac side similar equations can be written,

$$f_{acpr} = 6n_g n(f_{comm}) \pm f_{dck} + f_{baser} \tag{7.4}$$
$$f_{acnr} = 6n_g n(f_{comm}) \pm f_{dck} - f_{baser} \tag{7.5}$$
$$f_{acpi} = 6n_g n(f_{comm}) \pm f_{dck} + f_{basei} \tag{7.6}$$
$$f_{acni} = 6n_g n(f_{comm}) \pm f_{dck} - f_{basei} \tag{7.7}$$

where, f_{acpr} and f_{acnr} indicate the returned rectifier positive and negative sequence frequencies and likewise, f_{acpi} and f_{acni} indicate the returned inverter positive and negative sequence frequencies for a $6n_g$ pulse link. These sets of frequencies can be used to reduce all the FCM transfers of Larson's equation.

As an example, figures 7.21(a)(b)(d)(e) show the full and reduced transfers for transfer a in Larsen's equation that would be required for the 50-51Hz asynchronous link with and without negative sequence unbalance at the rectifier terminals, or $f_{dck} = 100Hz$. Figure 7.21(a) and (d)

show the full transfer originally required, while figures 7.21(b) and (e) show the reduced form of this transfer using the 12Hz grid depicted by the light grey grid in figure 7.20(b) and using equation 7.4.

Figures 7.21(g)(h) and (i) show the full admittance matrix transfers, first the full transfer, then the reduced and tolerance reduced transfers for normal asynchronous operation without any additional system distortion. The following section describes the tolerance reduced transfers shown in figures 7.21(c)(f) and (i).

The tolerance reduced transfers

The darker tolerance grid shown in figure 7.20(b) and in the figures in appendix J show the further redundancy in the full matrix transfers when some small tolerance is applied to the cross coupling transfers in each of the time variant dc side transfers.

Further observation of the tolerance grid in figure 7.20(b) and in appendix J provides evidence that the major returned frequencies in any asynchronous link are effectively "banded" around the dc side impedance lattice before it is inverted, as shown in figure 7.20(a). Also, the observed difference between the "banding" frequencies is simply the frequency difference in the two HVDC converters multiplied by the lowest pulse number of the link, ie ($f_{band} = 6n_g \times \Delta f$). Hence, the major resulting dc side frequencies resulting from the rectifier can be written as,

$$f_{dcr} = (6n_g n(f_{baser}) \pm n_b f_{band}) \pm f_{dck} \tag{7.8}$$

and from the inverter as,

$$f_{dci} = (6n_g n(f_{basei}) \pm n_b f_{band}) \pm f_{dck} \tag{7.9}$$

where, n_b is an integer from 0 to the number of bands required on either side of the main uninverted lattice. A larger value of n_b gives greater accuracy in the resultant spectrum. In the case shown in figure 7.20(b) for a tolerance of $1e^{-6}$, $n_b = [0, 1, 2, 3]$ has been used. A tolerance of $1e^{-3}$ gives about ± 1 to 2 bands while a tolerance of $1e^{-9}$ gives ± 4 to 5 bands which is more than adequate.

The resulting ac side frequencies can be written as,

$$f_{acpr} = (6n_g n(f_{baser}) \pm n_b f_{band}) \pm f_{dck} + f_{baser} \tag{7.10}$$

$$f_{acnr} = (6n_g n(f_{baser}) \pm n_b f_{band}) \pm f_{dck} - f_{baser} \tag{7.11}$$

$$f_{acpi} = (6n_g n(f_{basei}) \pm n_b f_{band}) \pm f_{dck} + f_{basei} \tag{7.12}$$

$$f_{acni} = (6n_g n(f_{basei}) \pm n_b f_{band}) \pm f_{dck} - f_{basei} \tag{7.13}$$

Figure 7.21(b) shows the reduced transfer a in Larsen's equation, required if there is no external ac or dc side distortion. This transfer will give the exact same results as the full transfer shown in figure 7.21(a) and the required frequencies are found in equation 7.4. Figure 7.21(c) on the other hand shows the same transfer with the required frequencies found using the reduced tolerance equation (equation 7.10) with $n_b = [0, 1, 2, 3]$. This transfer does not model all first order frequency cross coupling, however it models the main frequency couplings in the transfers and its size is dependent on n_b.

If there is some applied distortion in the one or both ac systems the reduction in memory requirements will still be significant, however in general each additional distortion will cause twice as many frequencies again as the normal undistorted asynchronous case. This assumes each additional distortion causes extra frequencies from those already present. This is illustrated in figures 7.21(c) where there is no applied distortion, compared with figure 7.21(f) where there exists a negative sequence unbalance on one of the ac systems.

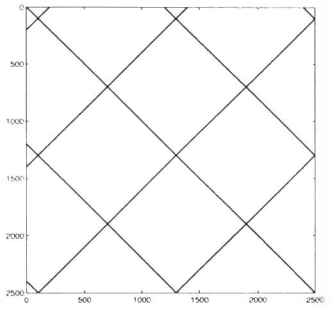

(a) Full 1 Hz grid, normal asynchronous operation.

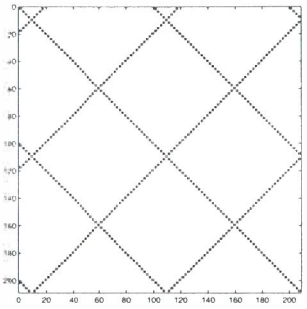

(b) Reduced 12Hz grid, normal asynchronous operation.

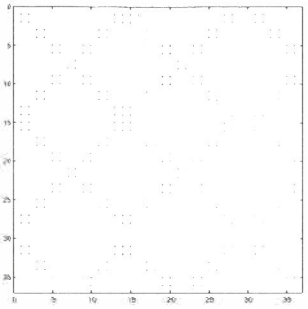

(c) Reduced tolerance grid ($n_b = 3$), normal asynchronous operation.

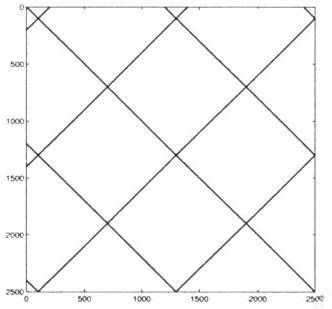

(d) Full 1 Hz grid, negative sequence distortion ($f_{dck} = 100Hz$).

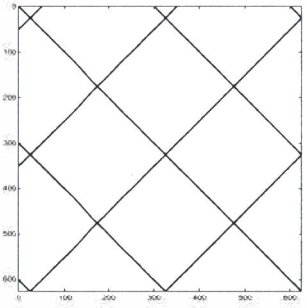

(e) Reduced 12Hz grid, negative sequence distortion ($f_{dck} = 100Hz$).

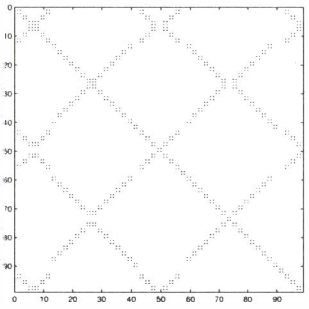

(f) Reduced tolerance grid ($n_b = 3$), negative sequence distortion ($f_{dck} = 100Hz$).

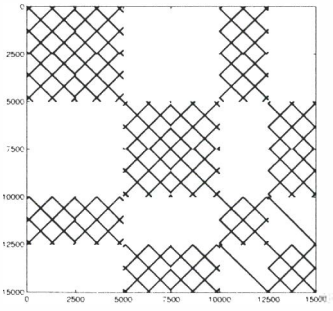

(g) Full admittance transfer.

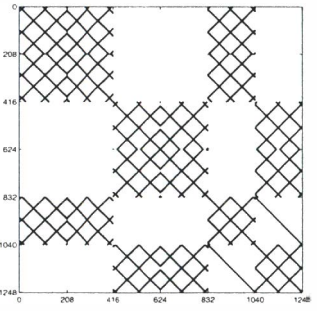

(h) Reduced admittance transfer.

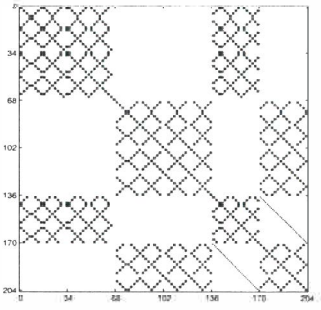

(i) Reduced admittance transfer ($n_b = 3$).

Figure 7.21 Effect of reducing transfers, in this case Transfer a and the full admittance transfer.

The memory reduction of the reduced transfers

Assuming no applied system distortion, and using the reduced frequency transfers, the memory requirements will be $(6n_g)^2$, or for the 12 pulse HVDC link, a 144-fold reduction in what was previous required for all the FCM transfers. If some arbitrary distortion is present in the HVDC system, and is not at a frequency falling at the equivalent dc side frequencies described by equations 7.3,7.8 or 7.9, then more frequencies are required. Table 7.4 gives an example of the memory reduction gained in the matrix transfers required for the 50-51Hz HVDC link, both with no applied distortion and with one and two applied distortions. It is assumed that the applied distortions cause extra frequencies, hence the assumption that these distortions are at non-multiples of 12Hz[4]. The size, number of non-zero elements and sparsity of the transfers are shown. as well as the reduced size of the full and sparse transfer matrices. The reduced sizes of the sparse matrices are calculated as the reduction in non-zero elements. Column 2 shows details for the full transfers, with a 1 Hz spacing while column 3 shows the reduced transfers and column 4 the tolerance reduced transfers with $n_b = [0, 1, 2, 3]$.

Normal asynchronous operating conditions, no applied distortion.			
	Full	Reduced	Reduced ($n_b = 3$)
Size	2500×2500	208 × 208	34×34
Number of non-zero elements	20952	1712	260
Sparsity	99.6%	96.0%	78%
Reduced size (full)	-	144	5400
Reduced size (non-zero elements)	-	12	79
With one applied distortion at non-multiple of 12Hz			
Size	2500×2500	624×624	100×100
Number of non-zero elements	20952	5200	780
Sparsity	99.6%	98.7%	92%
Reduced size (full)	-	16	625
Reduced size (non-zero elements)	-	4	27
With two applied distortions each at non-multiples of 12Hz			
Size	2500×2500	1040×1040	167×167
Number of non-zero elements	20952	8667	1240
Sparsity	99.6%	99.2%	96%
Reduced size (full)	-	5.7	226
Reduced size (non-zero elements)	-	2.4	16.9

Table 7.4 Size of transfers with reduced grids and with one or two applied distortions for the 50-51Hz HVDC link.

As shown the reduction in memory requirements is large when using the reduced transfers and even larger when using the tolerance reduced transfers. In general, the more distortions in the system, the bigger the reduced transfers must be and the reduction in the size of the transfers reduced. The reduction in memory for the reduced transfers does not lose any information in the cross-coupling time variant matrices but reduces the original matrices down to the required transfer frequencies, while a loss of information is present in the reduced tolerance transfers, dependent on the value of n_b.

7.4.2 Case study: The modified CIGRE 50-51Hz back-to-back HVDC link

This section uses the above-described methods to model a modified CIGRE benchmark HVDC link with the rectifier at 50Hz and the inverter at 51Hz. Such a case can arise in 50-50Hz systems

[4]A distortion that produces a multiple of 12Hz on the dc side will not add additional transfers to the reduced and tolerance reduced transfers for normal asynchronous operation. Likewise, if two distortions are applied to one of the ac systems at 12Hz multiples no additional transfers will be required.

where one or both ends of the link are weak. The link is modelled in a back-to-back configuration with negligible dc system impedance allowing maximum harmonic and interharmonic propagation through and around the link. Two cases are studied; the first shows the resulting operating point interharmonics around the HVDC link, while the second shows the resulting distortion sourced interharmonics resulting from negative sequence unbalance on both rectifier and inverter ac systems. The results are validated with PSCAD/EMTDC time domain simulation. Table 7.5 gives the operating point conditions of the link.

Parameter (Hz)	Sending end Rectifier (Hz)	Receiving end Inverter
AC side voltage (RMS)	$310.7\angle -0.2^o$	$229.0\angle -0.2^o$
AC side unbalance (RMS)	$5.2\angle 48.1^o$	$3.4\angle 58.0^o$
Firing angle (α_o)	17.4^o	132.6^o
Commutation period (μ_o)	23.5^o	17.1^o

Table 7.5 Operating parameters of the 50-51Hz HVDC case study.

Normal asynchronous operation

In PSCAD/EMTDC the HVDC link is simulated for 24 seconds allowing any transients associated with start up to decay. Data is then recorded for one second, including both ac system and dc system voltages and the firing angles of each of the converters. This time domain data is 11 columns by 50000 elements (with a $20\mu s$ print step) giving a total data file size of 9 Mbytes. A Fourier transform is applied to this data in MATLAB providing frequency domain data for comparison. To give the best results possible, the average firing angles, fundamental voltages and dc current on both the rectifier and inverter are recorded and then used as the operating point for the frequency domain analysis. Under normal asynchronous operation the main re-

V_{dc} (Hz)		V_{acpr} (Hz)		V_{acnr} (Hz)		V_{acpi} (Hz)		V_{acni} (Hz)	
12	1176	14	674	514	1162	15	675	513	1161
24	1188	26	686	526	1174	27	687	525	**1173**
36	**1200**	38	698	538	1186	39	699	537	1185
564	1212	**50**	1214	**550**	1198	**51**	1215	549	1197
576	**1224**	62	1226	562	1210	63	1227	**561**	1209
588	1236	74	1238	574		75	1239	573	
600	1248	86	**1250**	586		87	1251	585	
612	1260	614	1262	598		615	1263	197	
624		626	1274	1114		627	**1275**	1113	
636		638	1286	1126		639	1287	1125	
648		**650**	1298	1138		651	1299	1137	
1164		662	1310	**1150**		**663**	1311	1149	

Table 7.6 Returned frequencies from 12 pulse asynchronous 50-51Hz HVDC link.

sulting frequencies on the dc side of the HVDC link are described using equations 7.8 and 7.9 where in this case, $f_{band} = 12Hz$ and $n_b = [0, 1, 2, 3]$. Table 7.6 shows these main resulting frequencies where the frequencies in bold represent the individual characteristic harmonics of each converter.

Figure 7.22 shows the resulting dc side voltage on the HVDC link. The black bars are the result of frequency domain analysis while the white bars are the time domain comparison. As shown the agreement is excellent. Of importance are the low frequency distortions of 12Hz and 24Hz, these propagate around the fundamental onto the ac sides at: 26Hz,38Hz,62Hz and 74Hz on the

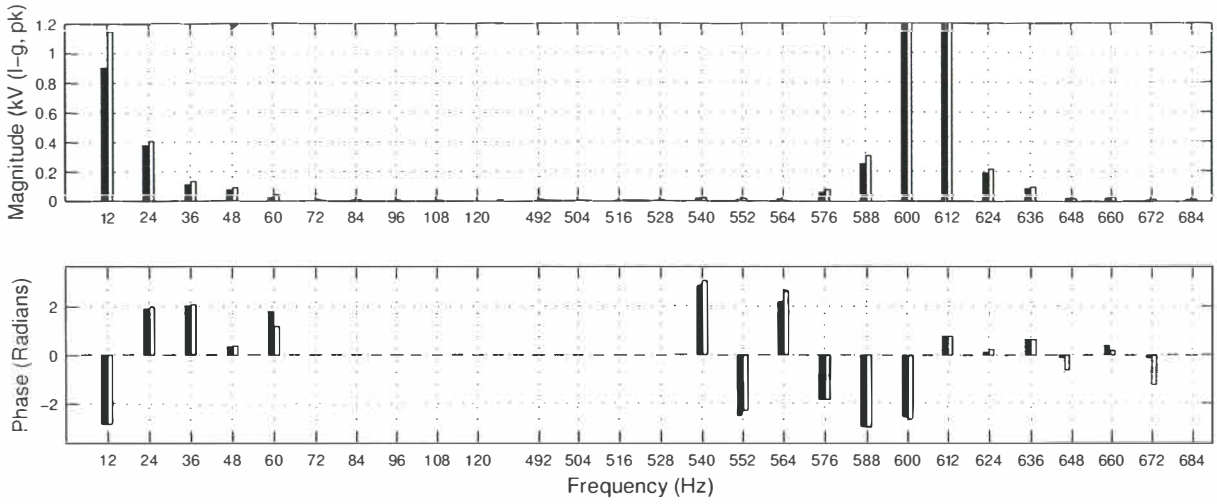

Figure 7.22 DC side comparison for 50-51Hz back-to-back HVDC link. *Black* - Frequency domain, *White* - Time domain.

rectifier side and at frequencies of: 27Hz,39Hz,63Hz and 75Hz on the inverter side. A noticeable difference occurs at 12Hz. This is caused by the lack of PLO modelling in the frequency domain analysis. To demonstrate the effects the PLO has on the dc side voltage spectrum the time domain simulation was re-run with the effective PLO gain reduced to zero. Figure 7.23 shows the new frequency domain comparison with the time domain, without the associated effects of the PLO. As shown, the comparison of the dc voltage at 12Hz is improved. The best way to overcome

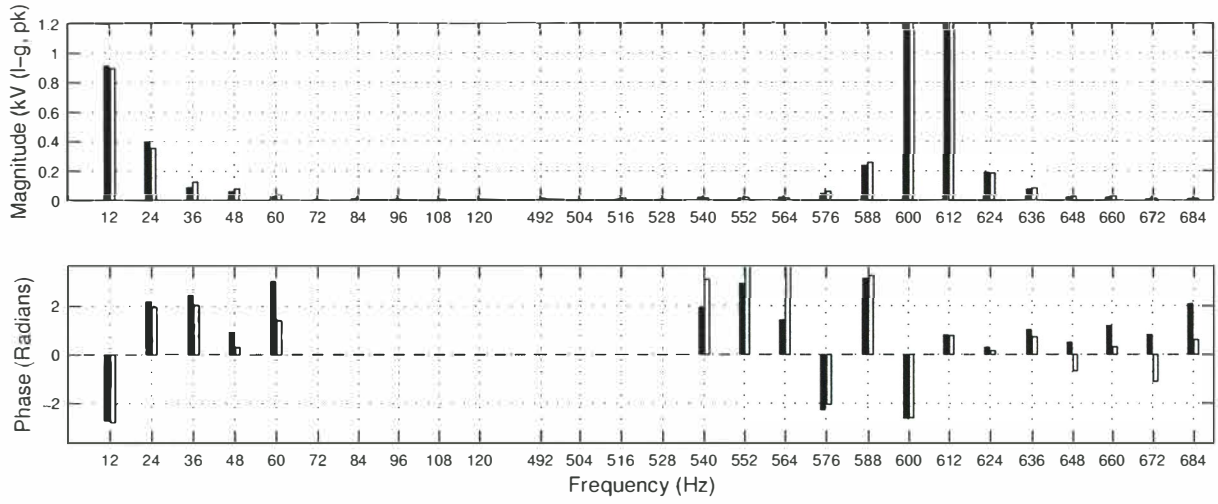

Figure 7.23 DC side comparison for 50-51Hz back-to-back HVDC link, with no PLO in time domain simulation. *Black* - Frequency domain, *White* - Time domain.

this problem is to linearise the effects of the PLO. This will be important in control situations where accurate low frequency modelling is required. However, for harmonic and interharmonic analysis the effects of the PLO are not significant. This is justified as the difference for most frequencies, other than those low frequencies below the fundamental, are negligible.

Figures 7.24 and 7.25 show the main returned ac side voltages at the terminals of both the rectifier and inverter for the 50-51Hz HVDC link.

Once again agreement with time domain simulation is excellent. Of importance in these figures are the low frequency positive sequence interharmonics around the fundamental. The largest in the case of the 50-51Hz HVDC link are the 38Hz distortion on the rectifier side and the 63Hz

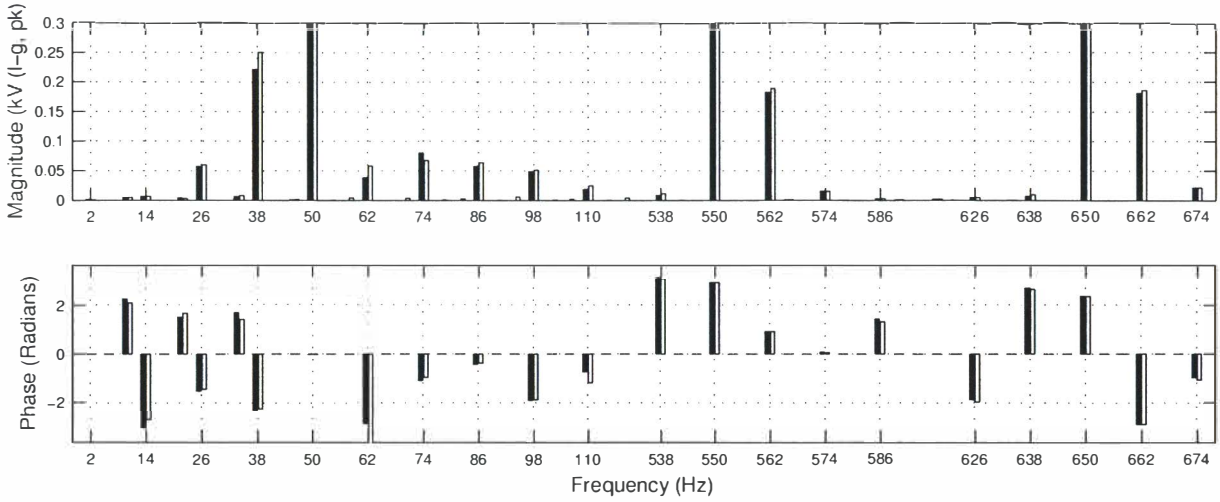

Figure 7.24 Rectifier side comparison for 50-51Hz back-to-back HVDC link. *Black* - Frequency domain, *White* - Time domain.

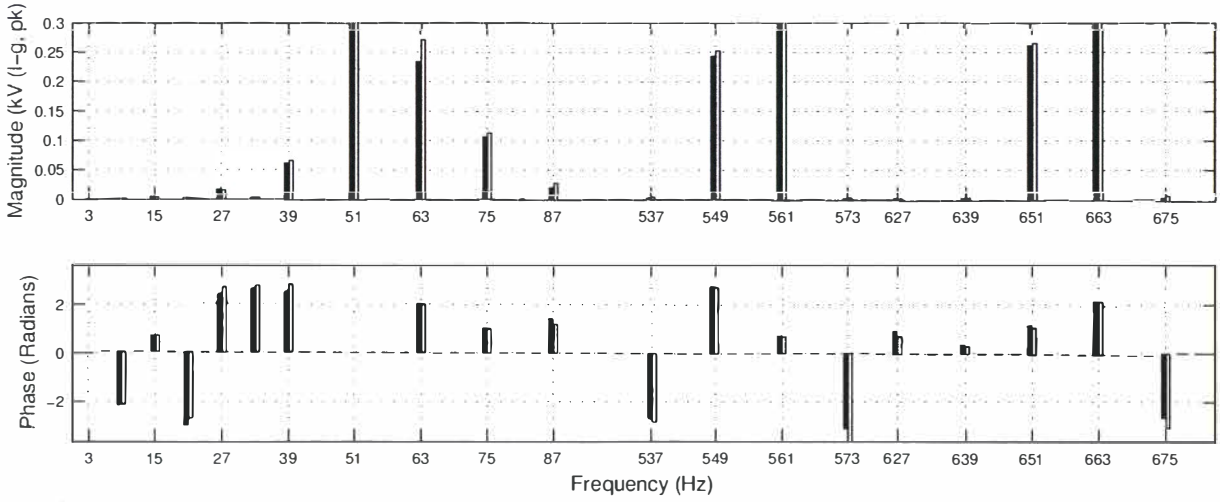

Figure 7.25 Inverter side comparison for 50-51Hz back-to-back HVDC link. *Black* - Frequency domain, *White* - Time domain.

distortion on the inverter side. These frequencies modulate onto a generator rotor at subsynchronous frequencies, and may interact with turbine-generators causing torsional interactions. Section 7.5 discusses these effects in more detail.

In a weak power system, or if the HVDC link is in a power system with untransposed transmission lines, then negative sequence unbalance will be a very common occurrence. The following section describes the distortion-sourced interharmonics resulting from negative sequence unbalance on the 50-51Hz HVDC link.

The negative sequence *distortion sourced* interharmonics on the 50-51Hz back-to-back HVDC link

If a 50-50Hz HVDC link is operating in a weak ac system then, not only are the frequencies on either side of the link likely to differ, but also more than likely there will be negative sequence unbalance on both ac systems. Sections 7.3.1 and 7.3.2 have shown the effect of negative sequence unbalance on the 50-50Hz and 50-60Hz HVDC links, this section shows the result of negative sequence unbalance on the 50-51Hz HVDC link.

The extra returned frequencies on the dc side of the link, resulting from negative sequence unbalance on the 50Hz rectifier can be derived using equations 7.8 and 7.9 with $f_{dck} = 100$Hz. Likewise, if negative sequence unbalance is present on the inverter ac system then returned frequencies can be derived with $f_{dck} = 102$Hz. The main extra returned frequencies are shown in tables 7.7 and 7.8 for the negative sequence unbalance at the 50Hz rectifier and 60Hz inverter respectively.

V_{dc} (Hz)	V_{acpr} (Hz)	V_{acnr} (Hz)	V_{acpi} (Hz)	V_{acni} (Hz)
100	150	50	151	49
500	550	450	551	449
700	750	650	751	649
1100	1150	1050	1151	1049
1300	1250	1250	1351	1249

Table 7.7 Returned frequencies from 12 pulse asynchronous 50-51Hz HVDC link with negative sequence unbalance at the rectifier bus.

V_{dc} (Hz)	V_{acpi} (Hz)	V_{acni} (Hz)	V_{acpr} (Hz)	V_{acnr} (Hz)
102	153	51	152	52
510	561	459	560	460
714	765	663	764	664
1122	1173	1071	1172	1072
1324	1275	1275	1374	1274

Table 7.8 Returned frequencies from 12 pulse asynchronous 50-51Hz HVDC link with negative sequence unbalance at the inverter bus.

Appendix I.3 shows the results for a 0.018pu negative sequence unbalance on the rectifier terminals and appendix I.4 shows the results for a 0.015pu negative sequence unbalance on the inverter terminals. Figures 7.26 and 7.27 show the dc side spectrum for negative sequence unbalance on the rectifier and then on the inverter, respectively. The extra returned frequencies shown are the 2nd (100Hz, 102Hz) and the 10th (500Hz, 510Hz) harmonics.

Figure 7.28 shows the return negative sequence spectrum on the 51Hz inverter terminals resulting from the 0.018pu negative sequence unbalance on the 50Hz rectifier terminals. As shown, a major 0.0115pu 49Hz distortion is produced.

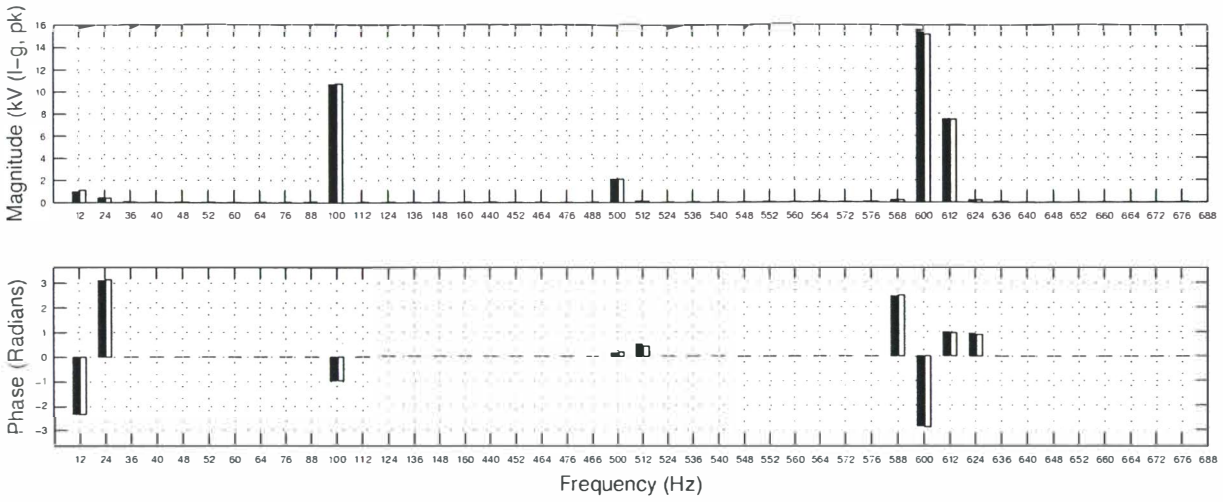

Figure 7.26 DC side comparison for 50-51Hz back-to-back HVDC link with 0.018pu negative sequence voltage distortion on rectifier terminals. *Black* - Frequency domain, *White* - Time domain.

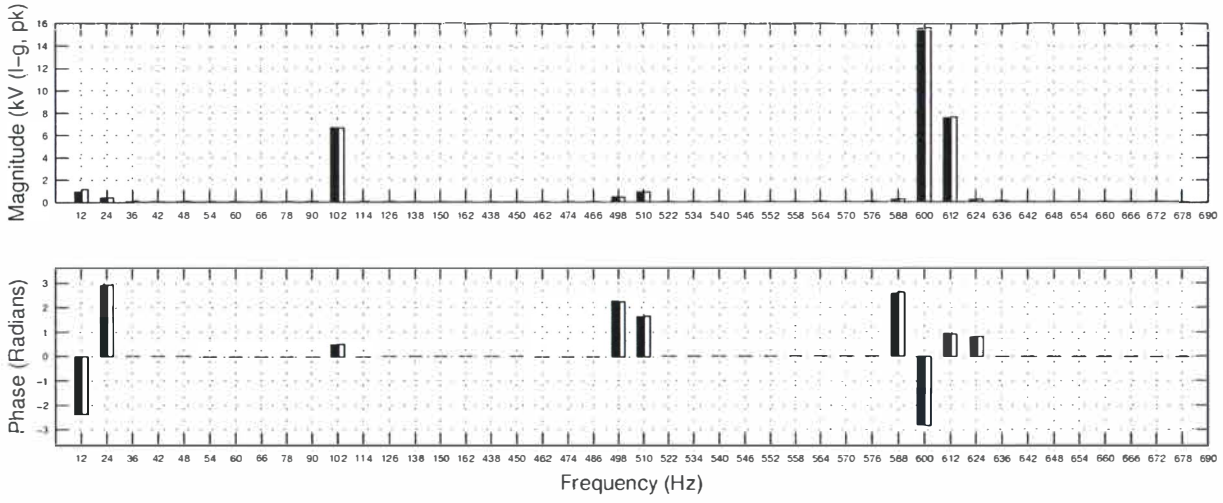

Figure 7.27 DC side comparison for 50-51Hz back-to-back HVDC link with 0.015pu negative sequence voltage distortion on inverter terminals. *Black* - Frequency domain, *White* - Time domain.

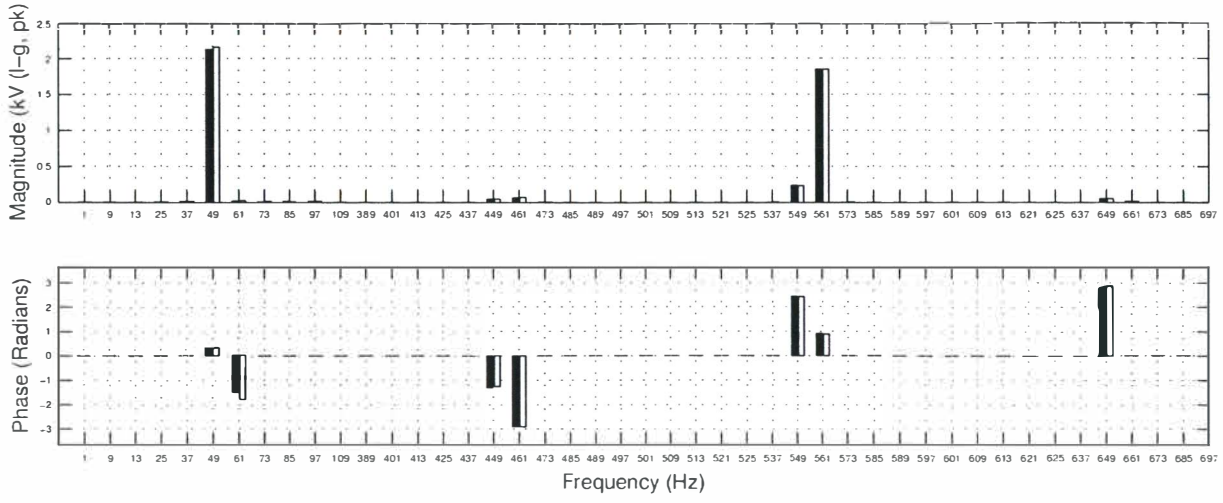

Figure 7.28 Inverter side negative sequence voltage comparison for 50-51Hz back-to-back HVDC link with 0.018pu negative sequence voltage distortion on rectifier terminals. *Black* - Frequency domain, *White* - Time domain.

Likewise, when the negative sequence unbalance is on the 51Hz inverter system a 52Hz negative sequence distortion appears on the 50Hz rectifier. Figure 7.29 shows the resulting negative sequence voltages developed on the rectifier.

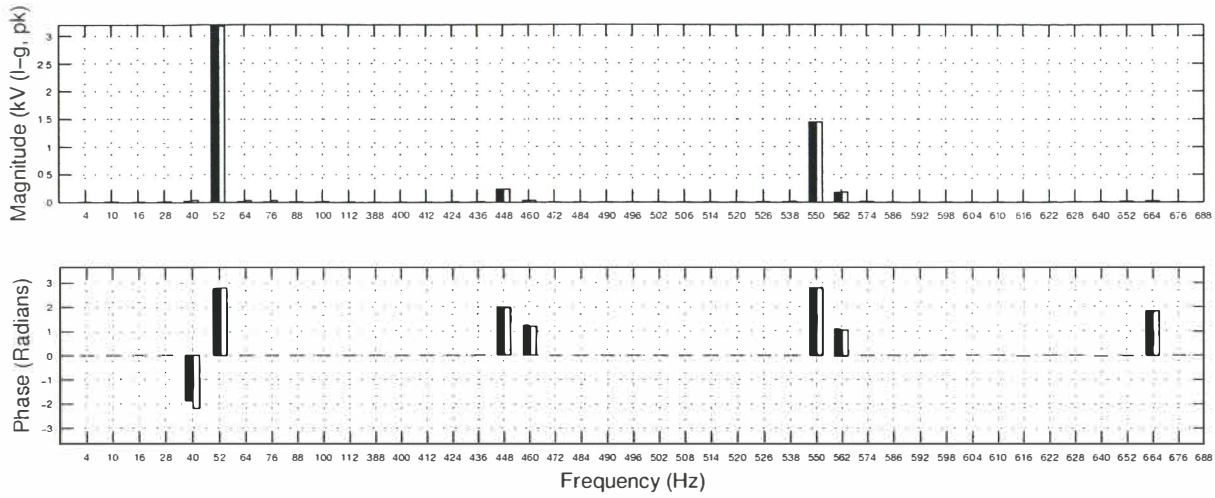

Figure 7.29 Rectifier side negative sequence voltage comparison for 50-51Hz back-to-back HVDC link with 0.015pu negative sequence voltage distortion on inverter terminals. *Black* - Frequency domain, *White* - Time domain.

From observations made in section 7.3.2 and in this section it is obvious that the effects of unbalance on such links can be a major source of interharmonic distortion. The following section discusses the effects of interharmonic distortion on likely subsynchronous resonance problems associated with turbine-generator rotor shafts.

7.5 EFFECTS OF INTERHARMONICS WITH RESPECT TO SSR ON TURBINE-GENERATOR ROTOR SHAFTS

The results of sections 7.3.1,7.3.2 and 7.4.2 have shown the returned operating point and distortion sourced interharmonics generated when HVDC links are operating in both balanced and unbalanced ac systems. Several authors have discussed the possibility of returned interharmonics at subsynchronous frequencies causing turbine-generator rotor shaft oscillation. However, these authors neglect the phase sequence of the returned interharmonics, incorrectly assuming that modulation with a generator will cause subsynchronous resonant frequencies, when in fact, the resulting frequencies will be modulated the opposite way. For example, the 50-60Hz link has a returned 70Hz component on the rectifier side. This is a negative sequence distortion and will modulate onto any electrically close turbine generator rotor shaft at a frequency of 120Hz, not 20Hz as indicated by Yacamini [67] and used in SSR analysis by Hammons [68][69].

Problems may be encountered when low frequency positive sequence frequencies are present on the ac sides of the converter. This happens in asynchronous HVDC links of low frequency differences as shown by the returned low frequencies around the 50-51Hz HVDC link in section 7.4.2. Here, a positive sequence 38Hz and a positive sequence 63Hz are present in reasonable magnitudes on the rectifier and inverter terminals respectively (see figures 7.24 and 7.25), these will modulate onto and electrically close rotor shafts at frequencies of 12Hz. The largest low frequency positive sequence interharmonics occurring around asynchronous HVDC links, with no ac system distortion are given in equations 7.10-7.13 with $n_g = 2$,$n_b = 1$,$n = 0$ and $f_{dck} = 0Hz$. For the 50-51Hz link $f_{band} = 12$Hz and the rectifier ac side frequencies can be described as a positive sequence frequency of $f_{acpr} = 62$Hz and a negative sequence of $f_{acnr} = -38Hz$, which is the same as a positive sequence frequency of 38Hz. Likewise, on the inverter side these equate

to positive sequence frequencies of 39Hz and 63Hz. These returned frequencies modulate onto any turbine-generator rotor shafts at the frequency f_{band} or equivalently the difference in the fundamental frequencies (Δf) multiplied by the pulse number of the link, ($6n_g\Delta f$).

In general, the phase sequence of the returned interharmonics around asynchronous HVDC links is important, especially if possible subsynchronous situations are to be investigated. This is because, like a switching converter, a generator modulates both positive and negative sequence in opposite ways. Situations that result in low frequency positive sequence distortion are cause for concern. In these instances investigation into the subsynchronous operating mode frequencies of nearby turbine-generator shafts may warrant further investigation.

7.6 SUMMARY OF THE GENERAL DIRECT SOLUTION ALGORITHM

This section provides a general procedure for solving the harmonic and interharmonic distortion around general HVDC links. Figure 7.30 is used to illustrate the steps involved, providing reference to equations and sections of the previous chapters where necessary.

There are three general steps required in the analytic algorithm; initialisation, component modelling and the system modelling and solution. These are all discussed in further detail below.

Initialisation: The maximum frequency required, the known fundamental frequencies of the both rectifier and inverter, as well as any known distorting frequencies are used to calculate the returned frequencies around the link. The operating point of the system is then found, either from a single-phase AC/DC load flow, time domain simulation, or just as likely from an actual physical system. The operating point data required are the converter ac system terminal voltages and phase angles, the average dc current, and the firing angles of both the converters[5]. This data is then used to find the average commutating periods of both converters.

Component modelling: Once the operating point and required frequencies around the HVDC link are known, the analytic model described in chapter 5 is used to calculate the converter small signal frequency coupling matrix transfers at those frequencies considered of interest. It is also used to calculate the characteristic ac currents and dc voltage that are used for the base case transfers. It is noted that the calculation of these transfers can be achieved from any accurate HVDC converter model, but must include the phase angle dependence associated with the HVDC converter either using tensor elements or negative frequencies. For example, the iterative model described in chapter 3 can be used or a set of time domain simulations with small signal perturbations used. Though, for all practical purposes, time domain simulation is very slow, hence either iterative or analytic methods are preferred. For calculation of the characteristic harmonics and operating point sourced interharmonics the three transfers a,e and i (in Larsen's equation) are altered to include the characteristic transfers as described earlier in section 7.2.2. Both ac system impedances, and the dc system impedance must be calculated at the correct frequencies and transformed into a diagonal tensor matrix for easy inclusion into the nodal admittance matrix.

System modelling and solution: All calculated transfers from the rectifier and inverter are rearranged from Larson's equation into the more general nodal form. The ac and dc system admittances are added, as described and shown in section 6.3 and the system admittance matrix formed. If the effects of firing angle modulation, acting through the control transfer function are wanted, then these are reduced into the existing transfers. The known and

[5]Other data such as the reactance on the transformers and transformer tap ratio are also required.

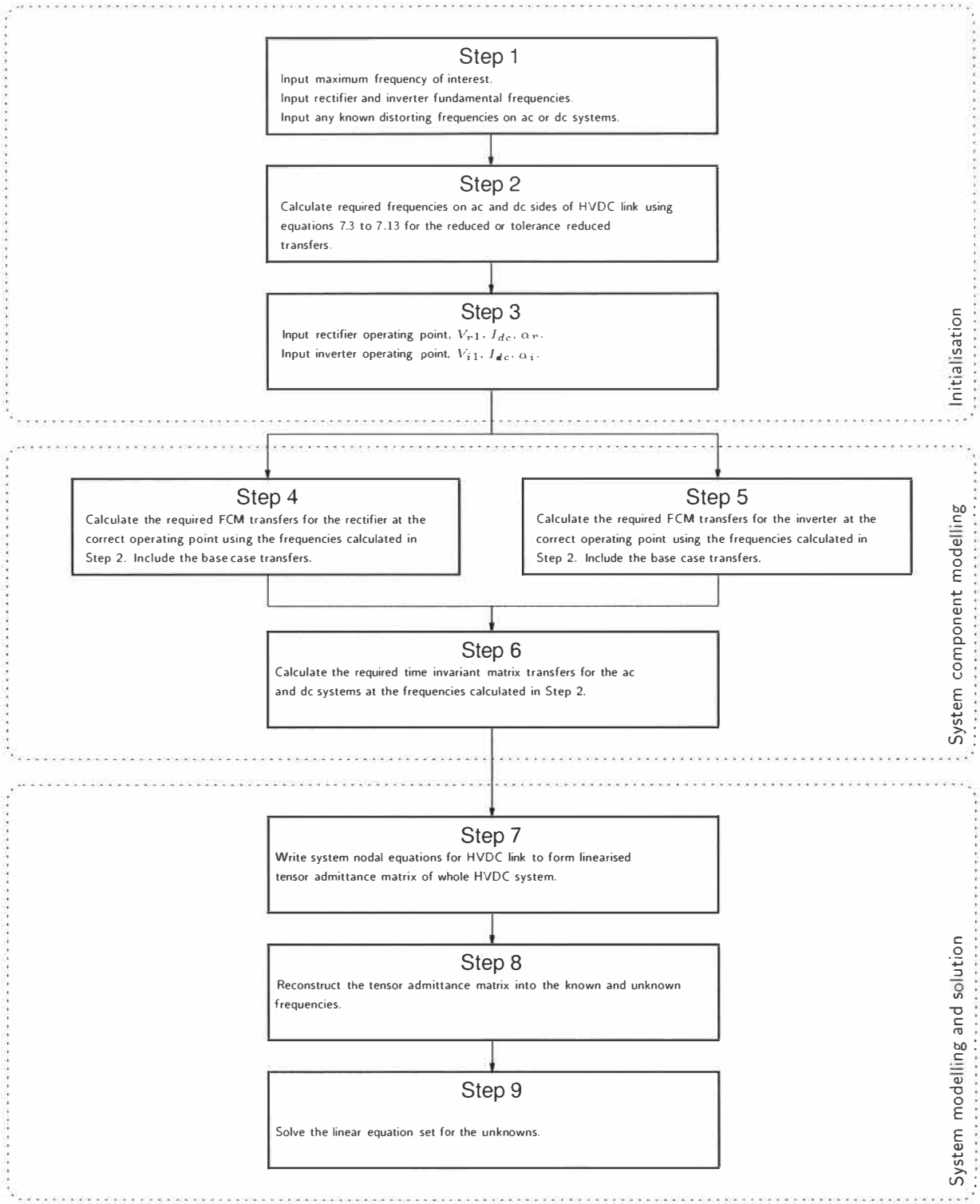

Figure 7.30 Flow diagram showing the general procedure for solving the harmonic and interharmonic cross-modulation around a general HVDC link.

unknown variables of the nodal solution are identified. These are then rearranged and the new system matrix is solved for the unknowns.

7.7 CONCLUSIONS

This chapter has presented a powerful method for predicting the harmonic and interharmonic voltages and currents around the general HVDC link. The technique described uses the fast, accurate linearised frequency domain model, combined with the time variant FCM transfers and simple nodal analysis, to predict both operating point and distortion sourced harmonics and interharmonics with accuracy. Excellent validation with time domain simulation has been shown, and case studies have been used to demonstrate the harmonic and interharmonic cross-modulation through HVDC links.

Several important aspects of direct linearised time variant modelling have been addressed, these include; the significance of an accurate HVDC converter model, and the importance of prior knowledge of the frequencies involved in the modulation process of the link.

A small signal HVDC converter model capable of modelling the effects of switching instant variation is essential for accurate distortion sourced harmonic and interharmonic cross-modulation, while a model which ignores the effect of SIV is still applicable in some asynchronous cases where operating point sourced harmonics and interharmonics are all that are present or required. If distortion sourced harmonic and interharmonics are required then the effects of SIV on the dc side transfers of the HVDC converter must be taken into account. This is particularly important for the cross-modulation of harmonic and interharmonic distortion from one ac system to another.

Examination of the modulating nature of the HVDC link has led to the reduction of the FCMs to a set of transfers at the required (or wanted) frequencies only. This makes these transfers smaller in size and the calculation time significantly faster. This pre-selection of the required frequencies has been shown to be particularly important when modelling asynchronous links with small frequency differences in one or both ac systems. Two frequency selection methods have been described and used, the first giving the exact result and the second using only certain "banded" frequencies about the characteristics.

The effect of subsynchronous interharmonics on the mechanical oscillations of turbine-generator rotor shafts and the importance of the returned phase sequence of the harmonic and interharmonic spectra has been discussed.

The following chapter, using the methods outlined in this chapter, investigates possible conditions that may exacerbate the effects of harmonic and interharmonic distortion through and around HVDC links.

Chapter 8

CRITICAL CONDITIONS FOR HARMONIC AND INTERHARMONIC CROSS-MODULATION

8.1 INTRODUCTION

The coupling between both ac systems of an HVDC link and the individual harmonic and interharmonic currents and voltages are dependent on the HVDC link operating point and ac system impedances at certain frequencies. The larger these couplings, the larger the cross-modulation and the more likely associated problems may occur within the power system. This chapter investigates the conditions required to likely exacerbate harmonic and/or interharmonic cross-modulation problems around the HVDC link.

Central to this problem are the analysis techniques required. Simplified methods provide information and insight, though may lack accuracy. Complex techniques on the other hand, though accurate can tend to lack insight. It is advantageous to be able to approximately predict worst-case operating conditions efficiently. This chapter uses both approaches, focusing on a simplified approach that is then compared with the full linearised solution developed in the previous chapters.

The main variables thought to influence the magnitude of harmonic and interharmonic cross-modulation are the system impedances and the converter operating point. As shown in section 6.4.2, the time variant frequency coupling nature of the converter and link mean the magnitude and angles of all returned voltages and currents are dependent on any single impedance at any one frequency. The operating point on the other hand affects the average commutation period. This alters the spectra of all the switching transfers and hence the resulting magnitudes of the harmonic and interharmonic distortion. This dependence is not as large as that caused by system impedance, but is certainly still cause for concern.

Although all modulated frequencies are involved, the main frequencies are the 3-port frequencies. It is these frequencies that are considered when using a simplified analytic analysis. For the HVDC link the dc system is the common system between rectifier and inverter. For the 3-port frequencies this dc side is represented as a single frequency $k\omega_o$ that modulates to both ac sides at frequencies $(k+1)\omega_o$ and $(k-1)\omega_o$ in positive and negative sequence respectively. Hence, this chapter proposes a simplified analytic analysis using the equivalent 3-port dc side impedance of both the rectifier and inverter to find the worst-case harmonic and interharmonic cross-modulation. An implicit assumption is that high currents and voltages at these frequencies will lead to high currents and voltages at higher order frequencies as well.

Section 8.2 first discusses the dc side impedance representation of the HVDC link. This is then followed by section 8.3 which discusses modelling techniques, concentrating on the simplified approach by formulating analytic equations using Larsen's HVDC converter equation and the ac and dc system equations for the equivalent dc side impedance of each converter.

One advantage of the proposed simplified analysis is that it is attained from the exact small signal model described in chapter 5. The effects of the commutation period and its dynamics remain intact, and the simplifications in this particular instance are the neglect of higher frequency transfers and the effects of control. As described in section 8.3, the equivalent dc side impedance is then simplified further as the average commutation is set to zero. This form of simplification, starting from the exact small signal model, to a simplified analytic equation is by far the best process for deriving simplified analysis techniques. It allows each approximation to be examined, helping determine whether assumptions are valid or not.

The simplified method is used in both sections 8.4 and 8.5 for the analysis of the worst-case cross-modulation resulting from a fundamental negative sequence unbalance on the rectifier ac terminals. These sections look at the effect of ac system impedance and operating point respectively and both use the simplified approach. The loss of accuracy in simplified techniques may provide cause for concern. Hence, throughout this chapter both a simplified technique, using the equivalent dc side impedance derived with the 3-port transfers, and the full linearised solution method are used and compared against one another. For the case studies in sections 8.4 the link is the same as that used in section 7.3.1 with negative sequence unbalance on the rectifier ac side terminals.

A general discussion and conclusions follow using the results of both modelling techniques to give some general 'rules of thumb' on situations that may cause likely worst-case harmonic and interharmonic cross-modulation.

8.2 EQUIVALENT DC SIDE IMPEDANCE REPRESENTATION

The dc system of an HVDC link provides coupling between the two interconnecting ac systems. If no dc system exists, such as in some back-to-back schemes, then the equivalent dc side impedance is the series combination of that seen looking into the dc terminals of each converter. It therefore makes sense to provide an analysis based on the equivalent total dc side impedance of each of the combined HVDC converters.

From the dc side the HVDC converter is best viewed as a voltage source behind an equivalent Thevenin impedance. This impedance performs the same function as a dc side smoothing reactor in that it limits the harmonic and interharmonic coupling between the rectifier and inverter. The impedance is a combination of transformer reactance, ac system impedance, and includes the effects of the commutation period and control. Depending on the accuracy of the analysis required, the dc side impedances can be represented as a full time variant impedance transfer using a FCM, or, for a simplified analysis only the main 3-port frequencies can be used. Solution methods for the equivalent dc side impedance are discussed in more detail in section 8.3. Figure 8.1(a) shows the back-to-back HVDC link with a negative sequence distorting source, V_{acnr}^{k-1} on the rectifier ac system. The equivalent dc side circuit is shown in figure 8.1(b) with the equivalent rectifier distortion transferred to the dc side, V_{dcr}^{k} and the rectifier and inverter represented in terms of the equivalent dc side impedances, Zc_{dcr}^{k} and Zc_{dci}^{k}. For finding the worst-case cross-modulation it is the values of the equivalent dc side impedances which are important, the value of the equivalent dc side voltage distortion being scaled by a constant, in this case transfer j of Larsen's equation.

In its simplest form only the 3-port frequencies are considered and the equivalent dc side impedances can be represented with simple complex numbers in time-invariant form. In this case, a distortion, $k\omega_o$ on the dc side will cause a positive sequence frequency $(k+1)\omega_o$ and a negative sequence frequency $(k-1)\omega_o$ to be produced on the ac sides. Hence, the equivalent dc side impedance at $k\omega_o$ is dependent on the combination of the ac side (and transformer) impedances at $(k+1)\omega_o$ and $(k-1)\omega_o$ frequencies. If the equivalent dc side impedance at $k\omega_o$ is small or near a series resonance point, then the dc currents resulting from either a positive sequence $(k+1)\omega_o$

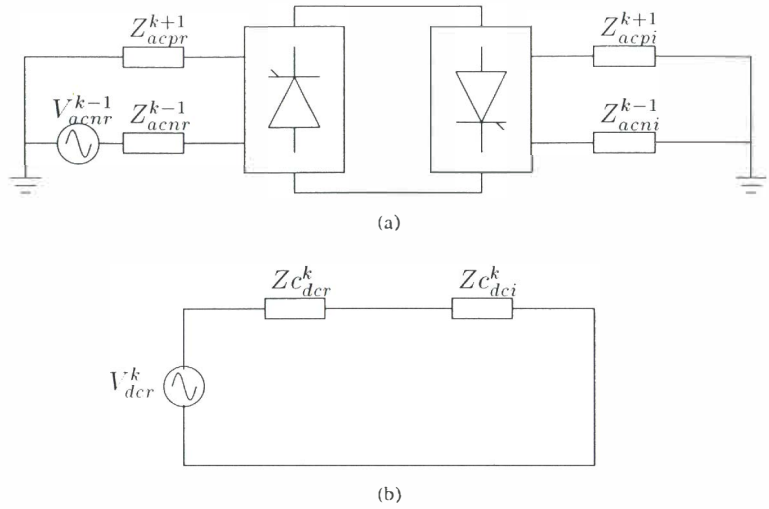

Figure 8.1 Equivalent circuit for back-to-back HVDC link.

distortion or a negative sequence $(k-1)\omega_o$ distortion will be high, and the cross-modulation also high.

Referring to figure 8.1(b), there are two different types of series resonant conditions likely to be encountered. The first is when each individual converter dc side impedance encounters a minimum series resonant condition, the second is when the two combined dc side impedances form a series resonant circuit. In both instances it is likely that the harmonic and interharmonic cross-modulation will be high. When considering the combined impedance approach, the total equivalent dc side impedance will set the dc side current. However, it is likely that the actual individual impedance magnitudes will set voltage levels and if the combined impedance is small but each individual impedance relatively high then this may be cause for concern. Hence, it is likely that this combined series resonant condition will constitute the worst-case situation for harmonic and interharmonic distortion.

The following section investigates the various solution methods for calculating the equivalent dc side impedances around the HVDC link. This is then used in sections 8.4 and 8.5 to investigate the effect of both ac system impedance and operating point variation on the magnitude of the resulting harmonic and interharmonic cross-modulation.

8.3 CALCULATING THE EQUIVALENT DC SIDE IMPEDANCES

The techniques outlined in the previous two chapters have shown the validity and accuracy of the full linearised solution method for calculating the steady state harmonic and interharmonic distortion around HVDC links. This solution is direct and computationally fast allowing many sets of perturbations to be used to find worst-case scenarios. The full solution technique used in this chapter makes use of the memory reduction techniques outlined in section 7.4.1 by considering only the frequencies of interest in the FCMs. This increases computational speed greatly, even for the 50-50Hz system.

The full linearised method is relatively complex, modelling the full frequency interaction and coupling with *time-variant* FCMs. This fails to provide much insight or 'rules of thumb' for the power system engineer. One simplified technique used frequently in the past has been the use of the main diagonal frequency transfers of the full FCMs used previously in Larsen's equation [17][47][49]. These diagonals are *time-invariant* and are by far the largest transfers of distortion having been used for various control situations. These have been discussed in the previous section and are termed the 3-port transfers. Using these, this section concentrates on

the formulation of simplified analytical equations for the equivalent dc side impedance that can be used to help find approximate worse-case scenarios and provide useful insight.

There are various methods used for calculating the equivalent dc side impedance around an HVDC link. Appendix H shows two of these, the first derives the impedance from the full system admittance matrix. This includes the effects of all frequencies and the effects of control and SIV using the full FCMs. The result is a time variant matrix transfer in FCM form. The second assumes the 3-port frequencies only and derives the dc side impedance analytically.

The equivalent dc side impedance, as calculated in equation H.10, is repeated here.

$$Zc_{dc}^{k} = \frac{A_{dc} + B_{dc}}{1 - C_{dc}} - k \tag{8.1}$$

where,

$$A_{dc} = i\left[\frac{cZ_{acp}^{k+1} \quad bgZ_{acp}^{k+1}Z_{acn}^{k-1}}{1 + aZ_{acp}^{k+1} \quad (1 + aZ_{acp}^{k+1})(1 + fZ_{acn}^{k-1})}\right]$$

$$B_{dc} = j\left[\frac{gZ_{acn}^{k-1} \quad ecZ_{acp}^{k+1}Z_{acn}^{k-1}}{1 + fZ_{acn}^{k-1} \quad (1 + aZ_{acp}^{k+1})(1 + fZ_{acn}^{k-1})}\right]$$

$$C_{dc} = \frac{beZ_{acp}^{k+1}Z_{acn}^{k-1}}{(1 + aZ_{acp}^{k+1})(1 + fZ_{acn}^{k-1})}$$

This impedance is dependent on the transfers $a \rightarrow k$ derived in appendix K and the ac side impedances Z_{acp}^{k+1} and Z_{acn}^{k-1}. The effects of control, and hence transfers d, h, l, m, n and o, are ignored as, although this has a significant effect below 75Hz it has only a small effect above this on the equivalent dc side impedance (as shown in figure 8.3).

For a constant operating point the transfers $a \rightarrow k$ stay constant. However, these transfers have been derived in terms of the positive pole rectifier with the dc voltage positive and the dc current positive when flowing out of the converter. Hence, as described in appendix G the signs of transfers c,g and k must be negative for the rectifier and likewise i,j and k for the inverter.

The comparison of this simplified analytic dc side impedance for the CIGRE rectifier is shown in figure 8.2 for frequencies up to 800Hz with the effects of control included. This figure compares the 3-port frequencies only and the full solution method has additional frequencies that are not shown. The comparison between the two methods is very close. Hence, for a reduced solution

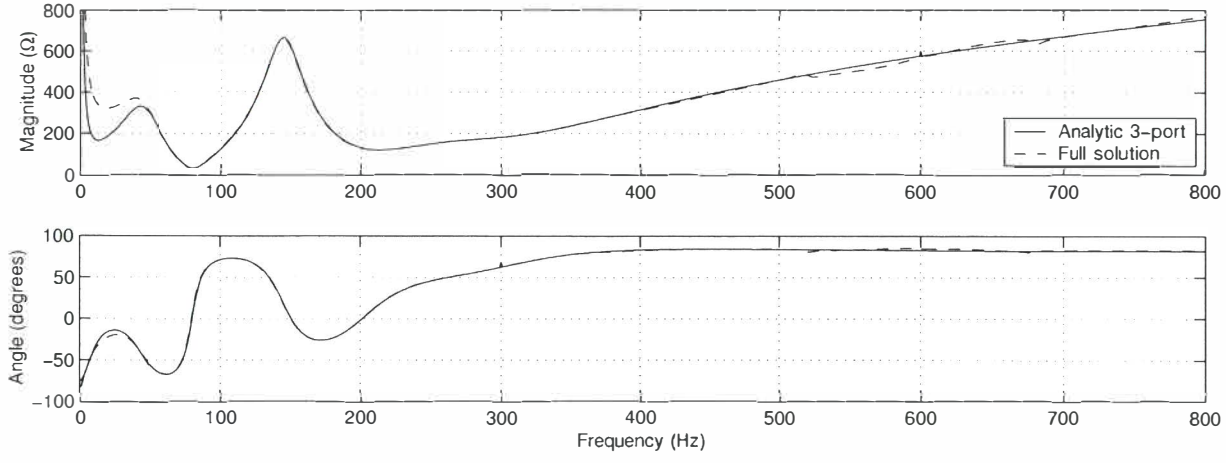

Figure 8.2 Comparison of solution techniques for the CIGRE rectifier equivalent dc side impedance.

of the main frequency interactions around a link, it is thought that the *time-invariant* 3-port transfers can be used with confidence.

The full analytic equation for the dc side impedance (equation 8.1) is still relatively complex, including the effects of SIV and the commutation period but ignoring the effects of control. The effects of control and SIV on the dc side impedance are shown in figure 8.3. As shown, the

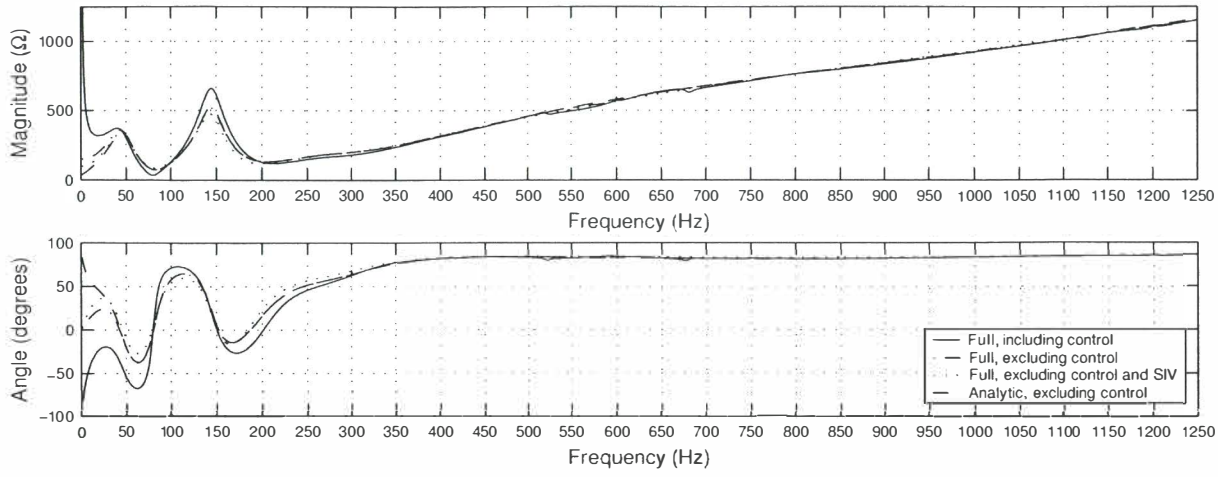

Figure 8.3 The effects of control and SIV on the equivalent dc side impedance of the CIGRE rectifier.

effects are generally small, differing only around parallel resonance points and at frequencies below 300Hz. However, the effects of the PI control are quite noticeable as the frequency tends towards zero. The dominance of the integrator in the constant current controller is the cause of this and at the lowest frequencies means that if less than the ordered current is flowing the error is integrated to alter the firing angle and hence dc voltage. Thus, as shown the controller gives the converter a predominantly capacitive impedance at the lowest frequencies.

From these results it is clear that the equivalent dc side impedance can be approximated above 75Hz using the analytic 3-port transfers and ignoring the effects of control, SIV, and the higher frequency transfers.

Perhaps an easier way to demonstrate the effects of the ac system impedance is to further simplify equation 8.1. To obtain insight into the effects of the ac side and transformer impedances it is useful to consider the equation describing the dc side impedance as the average commutation period μ_o tends towards zero. This results in a significant simplification of the 3-port transfers described in appendix K. As μ_o approaches zero the equivalent dc side impedance for the six pulse converter simplifies to,

$$\begin{aligned} Zc_{dc}^{k}|^{\mu_o \to 0} &= icZ_{acp}^{k+1} + jgcZ_{acn}^{k-1} - k \\ &= \frac{9}{\pi^2}(Z_{acp}^{k+1} + Z_{acn}^{k-1}) + j2X^k + \frac{3X^1}{\pi} \end{aligned} \tag{8.2}$$

where, Z_{acp}^{k+1} and Z_{acn}^{k-1} are the ac system impedances and X^k and X^1 the transformer reactances, all referred to the valve (or secondary side) of the converter transformer. For the 12 pulse converter, with six pulse converters in parallel on the ac side and in series on the dc side the equivalent dc side equation becomes,

$$Zc_{dc}^{k}|^{\mu_o \to 0} = \frac{36}{\pi^2}(Z_{acp}^{k+1} + Z_{acn}^{k-1}) + j4X^k + \frac{6X^1}{\pi} \tag{8.3}$$

The equivalent dc side impedance of the CIGRE rectifier and inverter is shown in figure 8.4 for three values of commutation period. As seen the resonant frequencies are almost completely independent of the commutation period and are accurately predicted by the simplified equation 8.3 when $\mu_o = 0$ in both cases. This is certainly not the case for the damping of the parallel

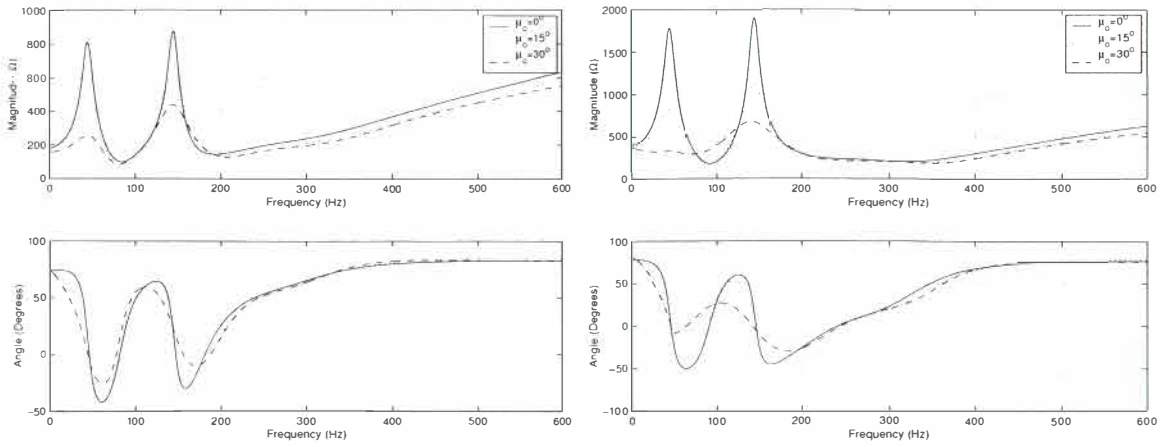

(a) Rectifier (b) Inverter

Figure 8.4 Effect of commutation period on equivalent dc side impedance of rectifier (a), and inverter (b) using equation 8.1.

resonant frequencies which vary significantly with average commutation period. The two parallel resonant impedance peaks become more damped as μ_o is increased while the damping of the series impedance trough remains approximately unchanged. This is described in more detail in section 8.5 which investigates the effects of operating point variation on the cross-modulation of distortion.

There is always a parallel resonance between the ac system and the harmonic filters, usually somewhere above the second harmonic. A single parallel resonance on the ac side results in two parallel resonances on the dc side with an associated series resonance between the two. This is caused by the frequency conversion process of the converter. For the CIGRE benchmark rectifier an ac system parallel resonance close to the second harmonic results in dc side parallel resonances close to the first and third harmonics, with the series resonance near to the second harmonic. For the higher frequency range, the transformer leakage reactance dominates, and the converter impedance is inductive. For the CIGRE HVDC converters, this is equivalent to approximately 0.15 Henries, which interestingly is significant compared to the likely value of a smoothing inductor.

The ac system impedances cause the equivalent dc side impedance to vary between inductive, capacitive and resistive. Figure 8.5 shows the components of the dc side impedance of the CIGRE rectifier and inverter with $\mu_o = 0$. In both cases the total dc impedance magnitude stays reasonably close to, or larger than, the contribution of the transformer leakage reactances, although there are two frequency bands where the impedance may be reduced; one near the second harmonic, and the other from the 4'th to around the 12'th harmonic.

This section has derived a simplified approximation to the equivalent dc side impedance. First, the full dc side impedance was compared with the analytic 3-port dc side impedance with favourable results. The effects of control, SIV and the average commutation period were then all investigated and a further simplification of the dc side impedance has been derived in equations 8.2 and 8.3 ignoring all of these for the six and twelve pulse converters respectively. These simplified equations are only approximate, however, it is hoped they will help provide insight into any likely harmonic and interharmonic cross-modulation problems.

The following section, using these simplified methods investigates the effects of ac system impedance on the magnitude of the harmonic and interharmonic cross-modulation using both the simplified equivalent dc side impedance analysis described in this section and the full solution

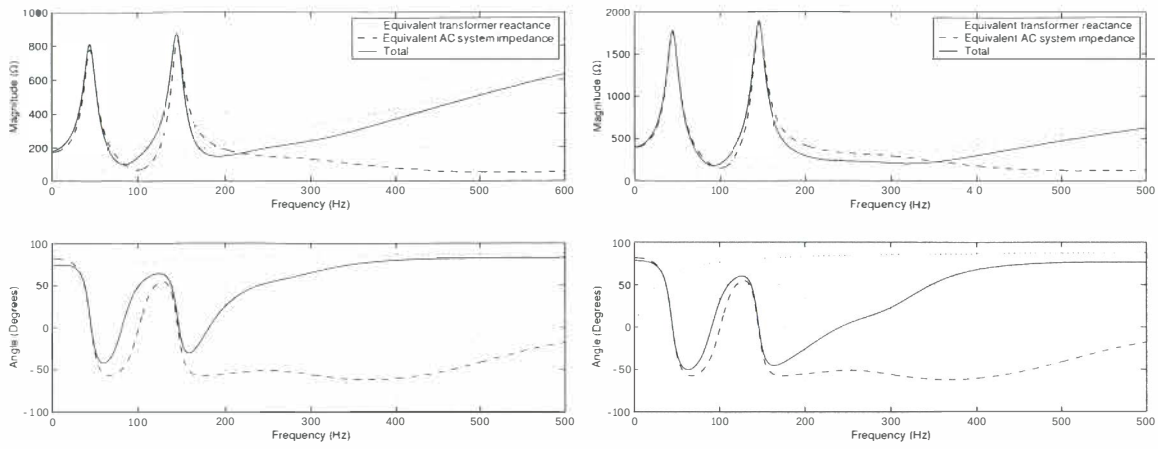

(a) Rectifier (b) Inverter

Figure 8.5 Components of the CIGRE rectifier (a), and inverter (b) dc side impedance at $\mu_o = 0$.

algorithm derived in the previous chapters.

8.4 THE EFFECTS OF SYSTEM IMPEDANCE ON CROSS-MODULATION

The effects of ac system impedance on the resulting harmonic and interharmonic cross-modulation is investigated in this section. Both the simplified dc side impedance analysis and the full solution algorithm are used to predict the worst-case interharmonic cross-modulation. A case study consisting of the back-to-back HVDC link with unbalance on the rectifier terminals is chosen to demonstrate the effectiveness of the simplified prediction method that is compared with the full solution method.

If negative sequence fundamental unbalance is present within the system, then a resulting second harmonic is produced on the dc side. The equivalent dc side impedances of the rectifier and inverter at the second harmonic are what must be investigated in this instance. If these equivalent dc side impedances are found to be small or near a series resonance, then the resulting dc currents will be high and the cross-modulation also high. This section investigates the effects of the third harmonic ac side impedance on the equivalent second harmonic dc side impedance.

8.4.1 Simplified analysis

Referring to figure 8.1(b) the worst situation occurs when the summation of Zc^{k}_{dcr} and Zc^{k}_{dci} is at a minimum. This can occur when each of the individual impedance magnitudes are at a minimum or when the summation of the two is at a minimum. This section, assuming unbalance on the rectifier terminals, calculates the worst-case third harmonic impedances for both the individual rectifier and inverter impedances as well as the combined dc side impedance using the simplified dc side equivalent described in section 8.2.

The individual worst-case third harmonic impedances are easily calculated using equations 8.2 and 8.3 with the correct values of ac system and transformer impedances. Table 8.1 gives values of the ac side impedances and transformer impedances around the CIGRE benchmark link at the fundamental and third harmonics. Note that these impedances are referred to the valve (or secondary) side of the converter transformer.

Impedance	Frequency	Rectifier	Inverter
Z^3_{acp}	$3\omega_o$	$14.8 - j24.5$	$19.3 - j20.2$
Z^1_{acn}	ω_o	$3.4 + j23.6$	$8.2 + j22.0$
X^2	$2\omega_o$	26.90	26.90
X^1	ω_o	13.45	13.45

Table 8.1 3-port impedances around the CIGRE link for negative sequence unbalance, referred to the valve side of the converter transformer.

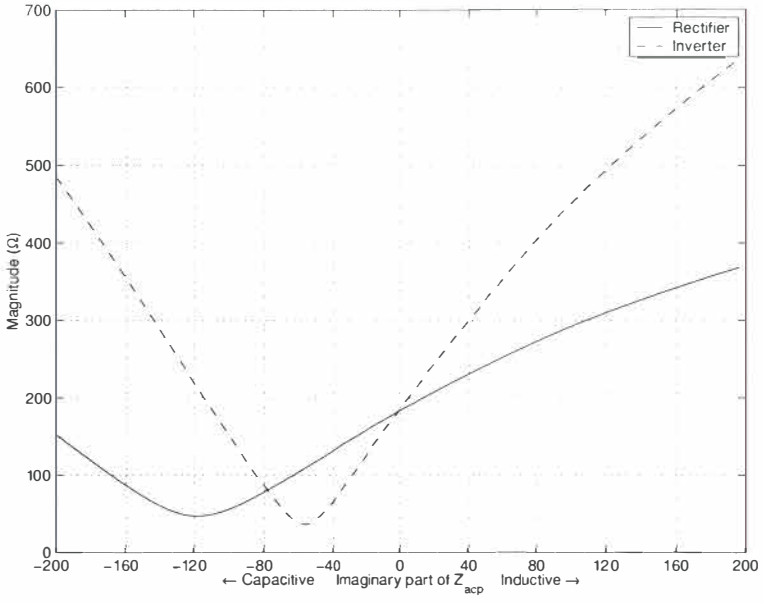

Figure 8.6 Equivalent 100Hz dc side impedance of rectifier and inverter while varying the imaginary part of Z^3_{acp}.

Assuming that the transformer and the fundamental impedances stay constant, then the worst-case third harmonic impedance for an equivalent second harmonic dc side series resonance can be approximated using equation 8.3 for the 12 pulse CIGRE converters. Using the CIGRE values of X^2, X^1 and Z^1_{acn} in table 8.1 the worst-case third harmonic impedances (Z^3_{acp}) for the individual rectifier and inverter will be ones that cancel the imaginary part, causing the equivalent dc side impedance to be at a minimum and resistive. This very simple approach equates to a third harmonic capacitive impedance of $-j141\Omega$ for the rectifier and for the inverter a third harmonic capacitive impedance of $-j60\Omega$, both referred back to the ac system (or primary) side of the converter transformers.

The same analysis is repeated using equation 8.1, including the effects of SIV and the average commutation period. Figure 8.6 shows the values of the equivalent dc side impedance for both the rectifier and inverter while varying the complex part of the third harmonic impedance for each. In this instance the minimum rectifier dc side impedance occurs when the rectifier third harmonic impedance is $-j120\Omega$ and the inverter third harmonic impedance is $-j56\Omega$, both referred to the ac system side of the converter transformers.

The above results indicate the value of the third harmonic impedances that produce individual minimum dc side impedances in both the rectifier and inverter. When the equivalent dc side impedances are combined the results differ in that it is now the combination of the two impedances that must be at a minimum. This resonant condition is the most important for cross-modulation as it is the effective total impedance between both ac systems. In principle,

the larger the individual converter impedances, the larger the transferred voltages. For example, the dc side induced voltage would be small when the individual rectifier and inverter dc side impedances are minimum. However, if there is a combined series resonance where the overall dc side impedance is small, but the rectifier is inductive and the inverter capacitive, then the dc side voltages will be larger.

With this train of thought the total equivalent dc side impedance will set the harmonic current flows, and then actual impedance magnitudes will set voltage levels. Figure 8.7 shows a contour plot of the imaginary part of the total dc side impedance, Zc_{dct}, as the imaginary parts of the rectifier and inverter third harmonic impedance are varied. The bold lines indicate the series

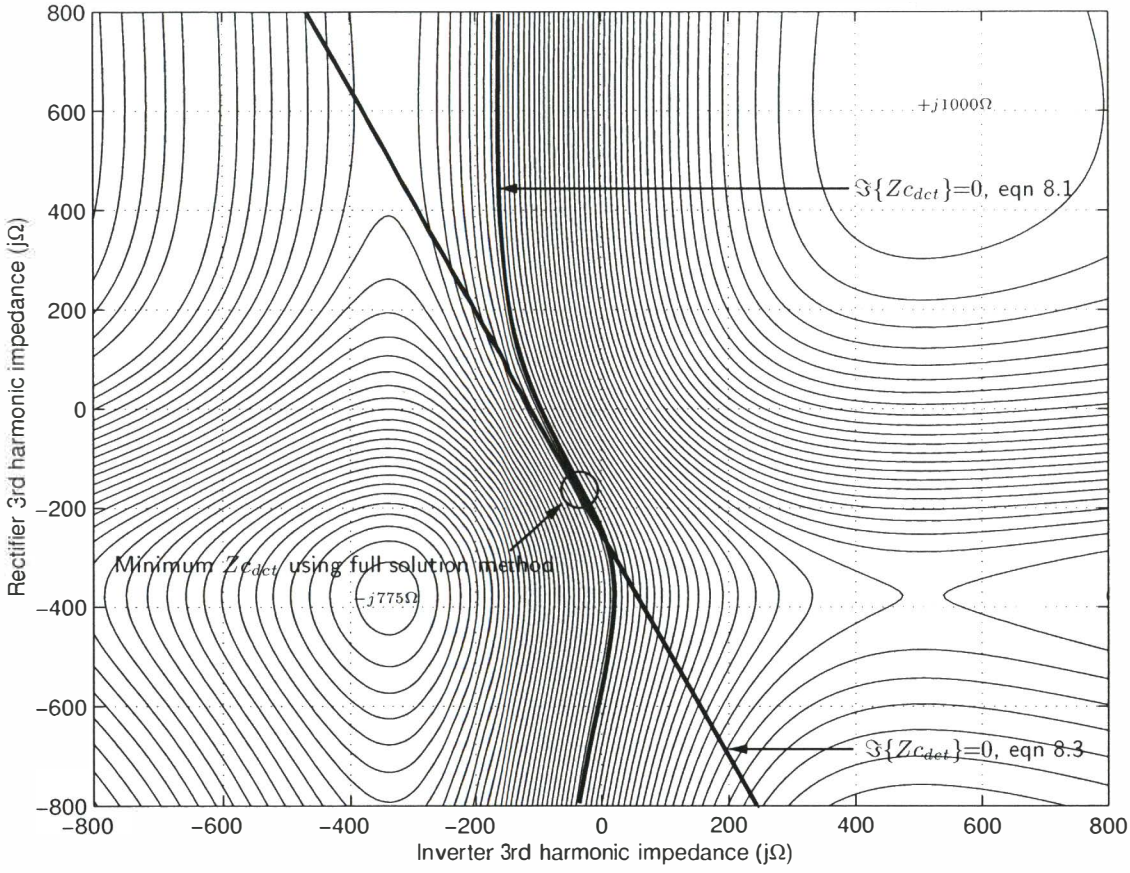

Figure 8.7 Contour plot of the imaginary part of the equivalent total dc side impedance Zc_{dct} at 100Hz using equation 8.1 while varying the rectifier and inverter third harmonic impedance. The minimum imaginary parts are shown in bold for both equation 8.1 and the simplified equation 8.3. Contours are those described using equation 8.1 and are spaced by $j25\Omega$.

resonant conditions using the simplified equations 8.1 (without control but including SIV and μ_o) and 8.3 (without control, SIV, and assuming $\mu_o = 0$). It is these conditions, where the imaginary part of the total dc side impedance is zero, that cross-modulation problems are likely. The contours are obtained using the simplified dc side impedance equation (equation 8.1) which includes and effects of SIV, μ_o but excludes the effects of control. As shown the peaks of $-j775\Omega$ and $j1000\Omega$ indicate the peak capacitive and inductive equivalent total 100Hz dc side impedance respectively. Notably these occur when the third harmonic impedances are both either capacitive or inductive.

As discussed above, maximum cross-modulation is likely to occur when the total combined dc side impedance is small, setting the dc current magnitude, and each equivalent dc side impedance high, setting the voltage magnitudes. Figure 8.7 shows the cases where the imaginary part of

the total dc side impedance is zero. One possible worst-case representation of this case is shown in figure 8.8. The curves Zc_{dcr} and Zc_{dci} show the equivalent rectifier and inverter dc side impedances as the imaginary part of the rectifier and inverter third harmonic impedance are varied. The curve Zc_{dct} is just one possible combination of these two impedances and has been chosen as it represents the worst-case condition when using the full solution algorithm, described in the following section. As shown, the values Zc_{dcr}^{min} and Zc_{dci}^{min} show the rectifier and

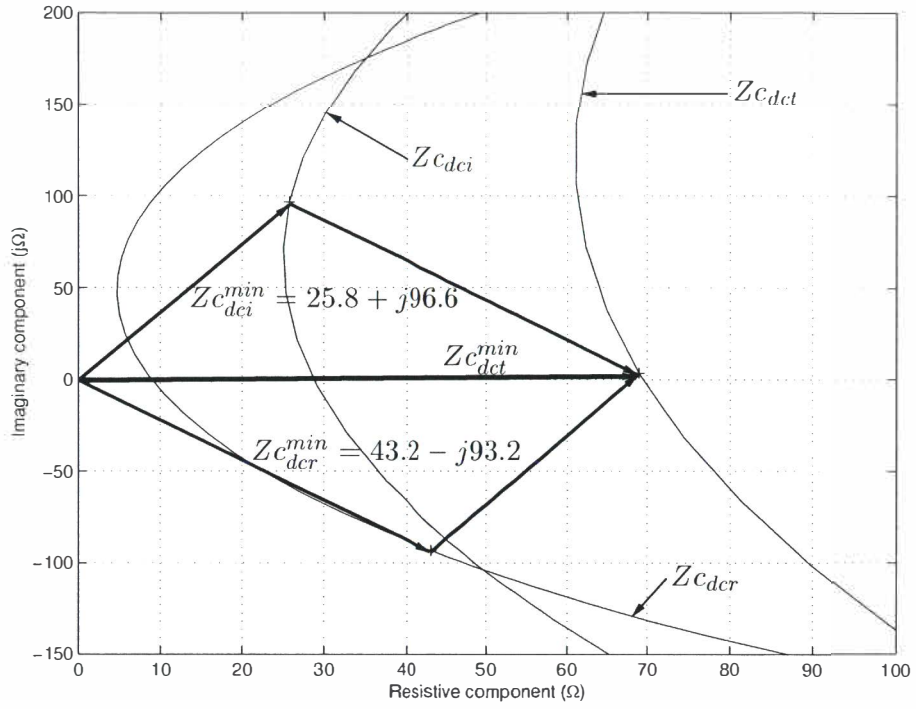

Figure 8.8 Vector addition of equivalent rectifier and inverter 100Hz dc side impedances giving a near worst-case situation with individual high impedance magnitudes but low combined impedance.

inverter equivalent dc side impedances that combine to give a near minimum dc side impedance. Although this does not give the minimum total dc side impedance, it gives a total dc side impedance close to the minimum and one where the individual impedance values Zc_{dcr}^{min} and Zc_{dci}^{min} are relatively high. In this case the rectifier is capacitive and inverter inductive as shown. These values relate to the worst-case capacitive third harmonic impedances found using the full solution method in section 8.4.2 of approximately $-j181\Omega$ on the rectifier and $-j29\Omega$ on the inverter.

8.4.2 Full analysis

The full linearised solution algorithm is used in this section to calculate the voltages around the link while varying the third harmonic impedances in both the rectifier and inverter ac systems. In this instance the effects of control, SIV and all returned frequencies are modelled. The case study is the same as that used in the previous section and in section 7.3.1, with unbalance on the rectifier terminals. The operating point is assumed to stay constant, so the impedance values at 50Hz and the negative sequence voltage magnitude are also considered to remain constant. The link is modelled in full, using the reduced frequency set to improve memory and solution time. This method is more accurate, but lacks the insight provided by the simplified analysis.

Figure 8.9 shows the voltage transfers about the HVDC link while varying the imaginary parts of the third harmonic impedances on the rectifier and inverter. It is assumed that the resistive parts of the third harmonic system impedances are zero. To generate these figures the full

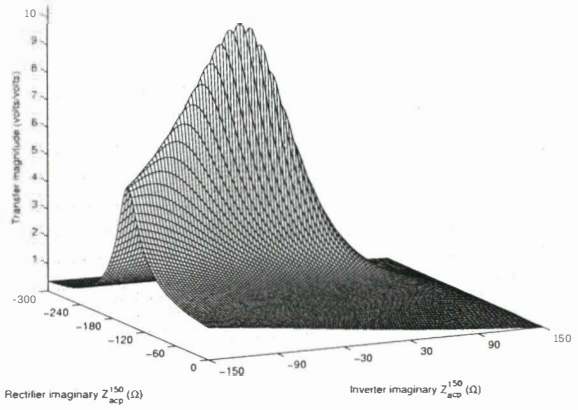

(a) Rectifier 150Hz positive sequence voltage transfer magnitude (volts/volts).

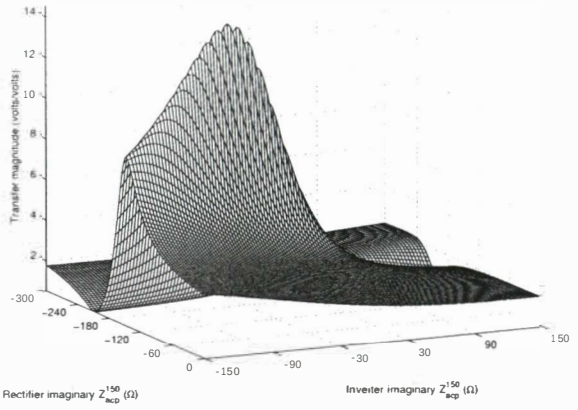

(b) DC side 100Hz voltage transfer magnitude (volts/volts).

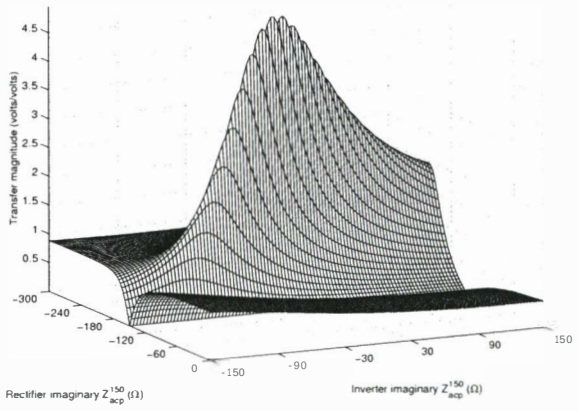

(c) Inverter 150Hz positive sequence voltage transfer magnitude (volts/volts).

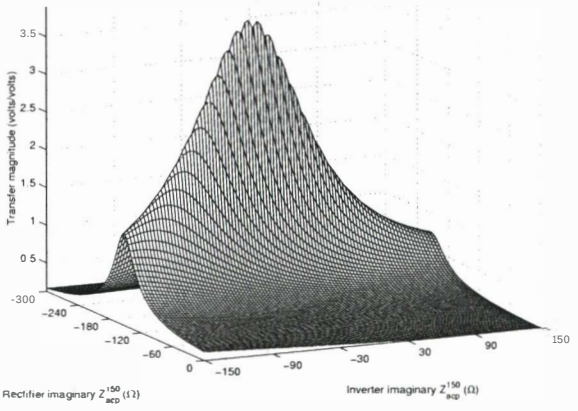

(d) Inverter 50Hz dc side voltage transfer magnitude (volts/volts).

Figure 8.9 Magnitude of voltage transfers around back-to-back link while varying the imaginary parts of both the rectifier Z_{acpr}^{150} and inverter Z_{acpi}^{150} impedance, with no resistive component.

algorithm was run $101^2 = 10201$ times while varying the rectifier impedance from $-j300\Omega$ to 0Ω and the inverter impedance from $-j150\Omega$ to $j150\Omega$, both in $j3\Omega$ perturbations.

In figure 8.9, the magnitude of the transfers of distortion can be quite high. For the transfer to the DC side 100Hz voltage this is fourteen times the unbalance, while the transfers through the link to the inverter terminal voltage are close to five times the magnitude for the third harmonic and four times for the transfer of unbalance. This transfer of unbalance is ten times the normal value with the standard CIGRE third harmonic impedances. The third harmonic impedances that match the resonance peaks and the magnitude of these peaks are given in table 8.2. These

Voltage transfer	Rectifier Z_{acp}	Inverter Z_{acp}	Transfer magnitude
Rectifier V_{acp}^{150}	$-j189$	$-j27$	10.4
DC side V_{dc}^{100}	$-j198$	$-j24$	14.5
Inverter V_{acn}^{50}	$-j177$	$-j30$	3.9
Inverter V_{acp}^{150}	$-j159$	$-j36$	5.0

Table 8.2 Worst-case third harmonic impedances around the CIGRE link for different 3-port voltage transfers resulting from negative sequence unbalance on the rectifier terminals.

results are all in approximately the same region for each of the different voltage transfers, the average being $-j181\Omega$ for the rectifier and $-j29\Omega$ for the inverter. These third harmonic impedances fall on the series resonant lines shown in figure 8.7 using the simplified equations 8.1 and 8.3. Table 8.3 compares the simplified individual and combined dc side impedance approach of the previous section with the average of the full solution method above. Both simplified re-

Prediction method	Rectifier Z_{acp}	Inverter Z_{acp}
Individual converters simplified eqn (8.1)	$-j120$	$-j56$
Individual converters simplified eqn (8.3)	$-j141$	$-j60$
Combined converters simplified eqn (8.1)	See figure 8.7	
Combined converters simplified eqn (8.3)	See figure 8.7	
Full solution method	$-j181$	$-j29$

Table 8.3 Worst-case third harmonic impedances around the CIGRE link for negative sequence unbalance.

sults compare reasonably well with the full solution method. However, the individual converter impedance resonance conditions give only 'ball-park' results while the combined converter impedance technique, dependent on two variables, gives the correct region (as indicated by the bold lines in figure 8.7) but is unable to predict the exact worst-case condition. This indicates that simplified methods, and in particular the combined equivalent dc side impedance, are valuable tools for the fast prediction of approximate worst-case conditions.

As an aside, figures 8.10(a) and (b) show the effect that third harmonic impedance plays on the negative sequence ninth harmonic voltage magnitudes about the link. The maximum third harmonic impedances that give the maximum ninth harmonic voltages are described in table 8.4.

These results correlate with those in table 8.2 for the main 3-port frequencies. This is particularly seen by the similar values of the third harmonic impedance required for the inverter voltage transfers V_{acn}^{50} and V_{acn}^{450}.

Figures 8.11 and 8.12 show the comparison of the HVDC link terminal voltages for the back-to-back CIGRE link with normal and worst-case third harmonic impedance values. In this case the third harmonic impedances on the rectifier and inverter are $-j181\Omega$ and $-j29\Omega$ respectively and a 0.015pu (5.33kV, l-g) fundamental negative sequence voltage unbalance exists on the rectifier

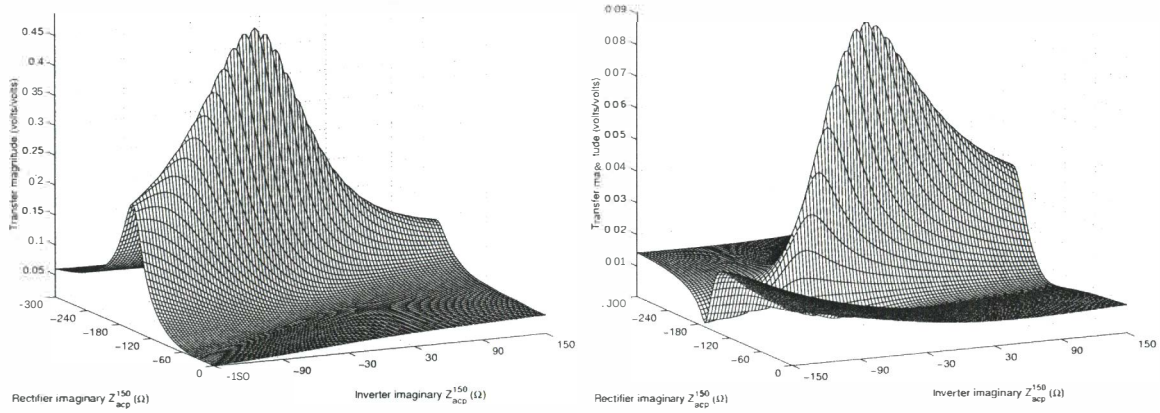

(a) Rectifier 450Hz negative sequence voltage transfer magnitude (volts/volts).

(b) Inverter 450Hz negative sequence voltage transfer magnitude (volts/volts).

Figure 8.10 Magnitude of ninth harmonic voltage transfers around back-to-back link while varying the imaginary parts of both the rectifier Z^{150}_{acpr} and inverter Z^{150}_{acpi} impedance, with no resistive component.

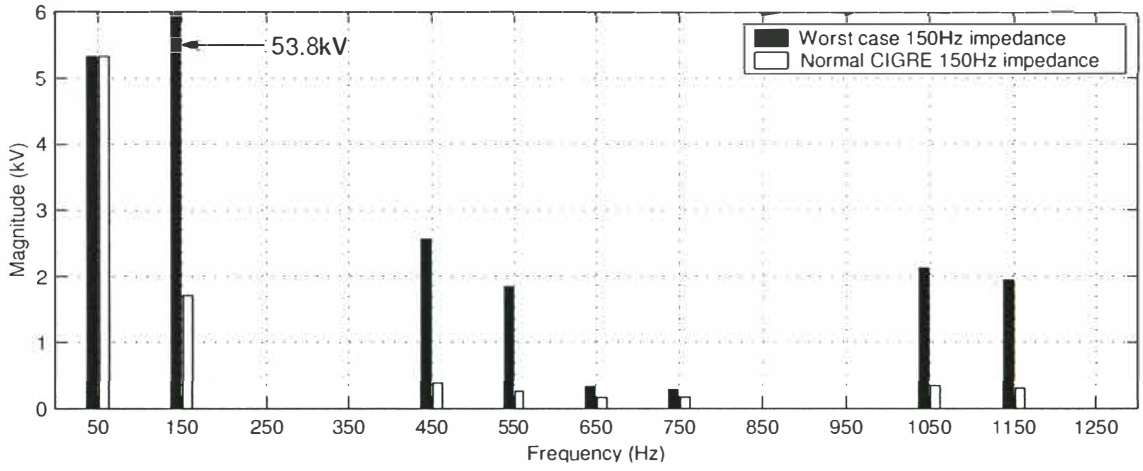

Figure 8.11 Difference in rectifier terminal voltage spectra resulting from a 0.015pu (5.33kV, l-g) fundamental unbalance on the rectifier terminals.

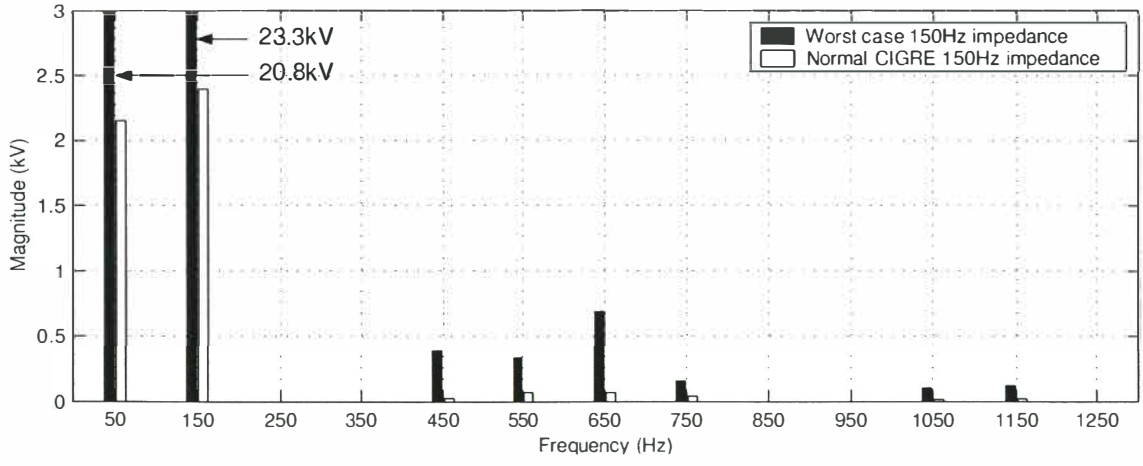

Figure 8.12 Difference in inverter terminal voltage spectra resulting from a 0.015pu (5.33kV, l-g) fundamental unbalance on the rectifier terminals.

Voltage transfer	Rectifier Z_{acp}	Inverter Z_{acp}	Transfer magnitude
Rectifier V_{acn}^{450}	$-j147$	$-j39$	0.09
Inverter V_{acn}^{450}	$-j180$	$-j30$	0.49

Table 8.4 Worst-case third harmonic impedances around the CIGRE link for the ninth harmonic voltage transfers resulting from negative sequence unbalance on the rectifier terminals.

terminals. As shown, there is a large difference in the two results. The fundamental voltage unbalance and third harmonic voltages on the inverter terminals are now approximately 10 times larger while the rectifier third harmonic is 31.5 times its original magnitude.

In this instance, the cross-modulation is also dependent on the impedance at 50Hz or the short circuit ratio of both ac systems. In this study the impedance of the CIGRE ac systems at 50Hz are relatively weak, the short circuit ratio being $2.5\angle -84$ for the rectifier and $2.5\angle -74$ for the inverter as indicated by the CIGRE benchmark model [62]. This is effectively per unit admittance. The effects of these admittances will be similar to the third harmonic impedances as, using simplified equation 8.3 they add together with the third harmonic impedances. Several key points are discussed below;

- If the system is weak (low SCR), the likelihood of unbalance is generally higher than a strong (high SCR) system.
- The effect of the reactive compensation capacitors (including the filters) must be taken into account. These can cause significant parallel resonances that can significantly increase the effective ac system impedance at 50Hz, hence lowering the effective system strength. Weak ac systems mean high impedance and this will generally add to the equivalent total dc side impedance.
- Very strong ac systems may be candidates for the cross-modulation of harmonic currents from connecting weak ac systems.
- The resistive damping of the ac systems at fundamental frequency is very important. The lower the resistive component the more the likelihood of cross-modulation problems.

The following section, using both the techniques in this section and in section 8.4.1, takes into account the effects of operating point on the transfers of distortion around the link and hence the magnitude of the harmonic cross-modulation.

8.5 THE EFFECTS OF OPERATING POINT ON CROSS-MODULATION

It has been shown that the effects of impedance can cause large differences in the returned voltages and currents around the HVDC link. This section follows section 8.4 by investigating the effects that operating point has on the transfers, and hence the resulting cross-modulation magnitude around the link. Once again, the case study is the same as that used in the previous section and in section 7.3.1.

8.5.1 The effects of operating point on the 3-port transfers

The operating point has been defined clearly in section 4.3 and is dependent on the fundamental voltage magnitude and angle, $V_1\angle\varphi$, the firing angle, α_o, and the average commutation period, μ_o. The effect of operating point on each individual 3-port transfer can be seen in their analytic representation, as shown in appendix K.

Table 8.5 lists each of the 3-port transfers with there associated operating point dependences. As

Transfer	Magnitude dependence	Angle dependence
a	μ_o	μ_o
b	μ_o	μ_o, α_o, φ
c	μ_o	μ_o, α_o, φ
d	μ_o, V_1, α_o	μ_o, α_o, φ
e	μ_o	μ_o, α_o, φ
f	μ_o	μ_o
g	μ_o	μ_o, α_o, φ
h	μ_o, V_1, α_o	μ_o, α_o, φ
i	μ_o	μ_o, α_o, φ
j	μ_o	μ_o, α_o, φ
k	μ_o	μ_o
l	α_o	μ_o

Table 8.5 Operating point dependence on the 3-port transfers.

shown, all transfers are dependent on the average commutation period μ_o and all are magnitude dependent on the commutation period except l which is magnitude dependent on the average firing angle α_o. There also exists angle dependence with the fundamental voltage angle φ, the commutation period and the firing angle. The major effect on these transfers, and hence on the magnitude of the harmonic and interharmonic cross-modulation is the effect of the average commutation period.

The average commutation period is defined by the well known equation,

$$\mu_o = cos^{-1}[cos\alpha_o - \frac{2X_c I_{dc}}{\sqrt{3}NV_1}] - \alpha_o \tag{8.4}$$

To keep the investigation as realistic as possible only values between 0 and 30 degrees are investigated by varying the value of the dc current from 0kA to 2.4kA. The firing angles and fundamental voltage and commutating reactance are assumed to remain constant. In this instance the ac system remains unchanged, although realistically the parallel resonance effects of the power factor correction capacitors and the change in transfer tap ratios will alter the system impedance. This is a little unrealistic but shows the general effect of the commutation period on the transfer of distortion. Figure 8.13 shows the change in the average commutation period for both the rectifier and inverter for different dc current operating points.

Figure 8.14 shows the effects of the average commutation period on the transfers from ac voltage to ac current when $k = 2$. As shown, these transfers are fully dependent on the average commutation period, being zero when $\mu_o = 0$.

These transfers are by far the most dependent of the transfers in Larsen's equation but their magnitude remains small compared to the other transfers. Figures 8.15 and 8.16 show the transfers from dc current to ac current and ac voltage to dc voltage, for both the rectifier and inverter.

Unlike figure 8.14, both the current to current and voltage to voltage transfers of figures 8.15 and 8.16 show only slight dependence on the average commutation period varying only by up to 10% of their magnitude over the range of commutation periods. Both transfers are also significantly larger in magnitude than the $ac \rightarrow ac$ transfers and are hence more dominant.

Figure 8.17 shows the variation of the dc current to dc voltage transfer k with average commutation period for both the rectifier and inverter. As shown in equations 8.2 and 8.3 this

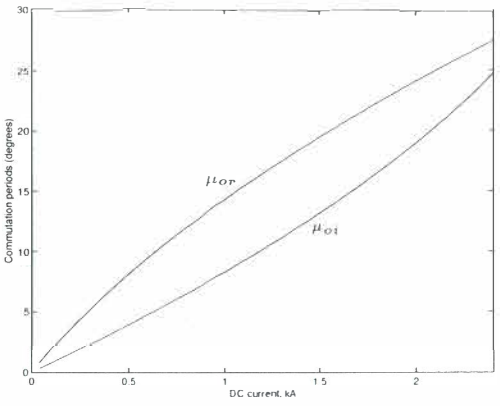

Figure 8.13 Rectifier and inverter average commutation periods for varying I_{dc}.

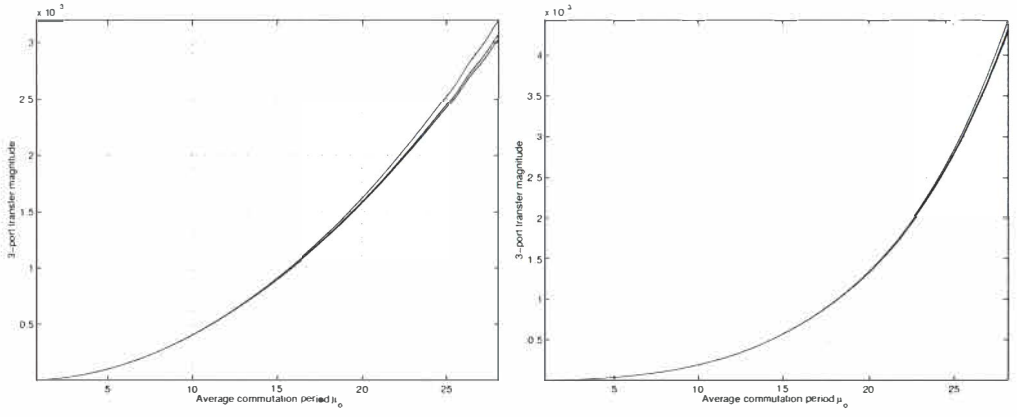

(a) Rectifier (b) Inverter

Figure 8.14 3-port ac --› ac transfer magnitudes with varying average commutation period. (a) Rectifier transfers a, b, e and f. (b) Inverter transfers a, b, e and f, for $k = 2$.

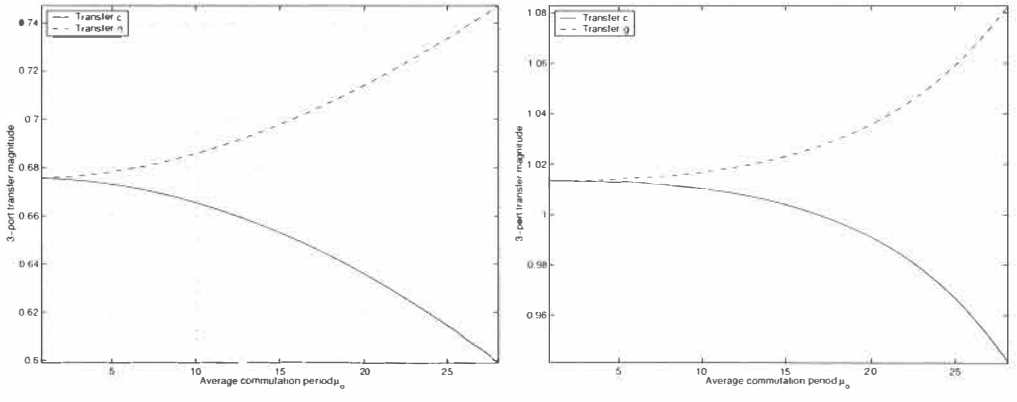

(a) Rectifier (b) Inverter

Figure 8.15 3-port dc --› ac transfer magnitudes with varying average commutation period. (a) Rectifier transfers c and g. (b) Inverter transfers c and g, for $k = 2$.

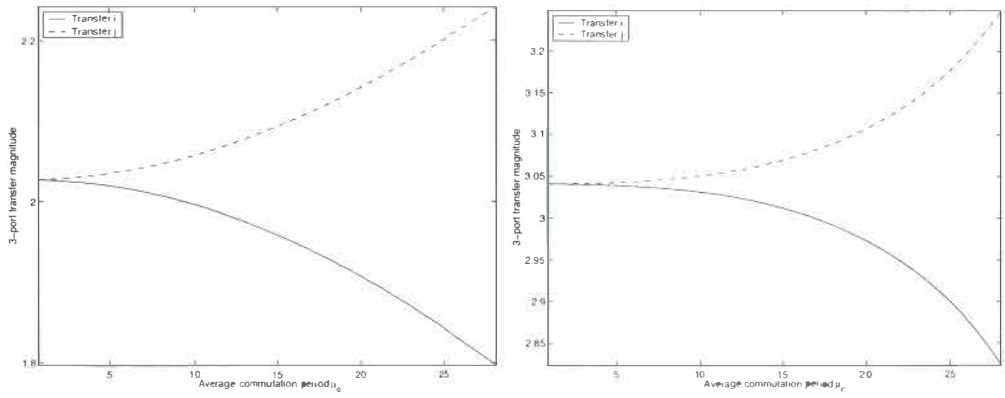

(a) Rectifier (b) Inverter

Figure 8.16 3-port $ac \dashrightarrow dc$ transfer magnitudes with varying average commutation period. (a) Rectifier transfers c and g. (b) Inverter transfers c and g, for $k = 2$.

transfer is dominated by the reactance of the converter transformers but is scaled by the average commutation period. The magnitude of transfer k varies by up to over 20% as the commutation periods increase up to over 25^o. This dependence is more significant than either of the transfers in figures 8.15 or 8.16. These results reinforce the simplified equivalent dc side impedance equa-

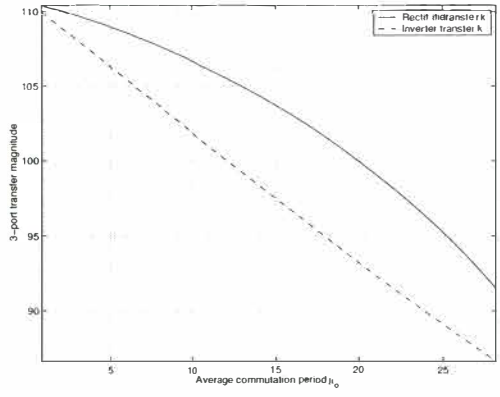

Figure 8.17 3-port $dc \dashrightarrow dc$ transfer magnitudes with varying average commutation period for both the rectifier and inverter, for $k = 2$.

tions 8.2 and 8.3 where the effects of the average commutation period are ignored. However, in this section, it is the effects of average commutation period on the equivalent dc side impedance that are required and hence these simplified equations are no longer of any use.

8.5.2 Finding worst-case operating point for cross-modulation resulting from negative sequence unbalance

Unlike the variation of ac system impedance, the operating point variation generally causes only comparatively small changes in the resulting cross-modulation magnitudes. This has been seen by the variation of the transfers in figures 8.14 to 8.17 and with the reasonable results in section 8.3 for the dc side impedance ignoring the effects of the commutation period.

Figure 8.4 shows the effect of the 3-port equivalent dc side impedance of the rectifier and inverter for three different values of average commutation period μ_o. The effect of increasing commutation period on the equivalent dc side impedance is an increase in the damping of the resonant peaks.

However, the effect of the commutation period on the equivalent dc side impedance at $k = 2$ is very small. This section uses the same simplified approach as that used in section 8.4 to look at the effect of operating point on the equivalent dc side impedance for the cross-modulation resulting from negative sequence unbalance. However, as equations 8.2 and 8.3 assume $\mu_o = 0$ they are no longer of any use and only equation 8.1 is valid. Once again the results of this section are compared with the results gained using the full solution method.

Simplified analysis

Following the approach taken in section 8.4 figure 8.18 shows the equivalent dc side impedance of both the rectifier, inverter and their combined equivalent dc side impedance at 100Hz as the dc current varies from 0 to 2.4kA and the average commutation periods vary as indicated in figure 8.13.

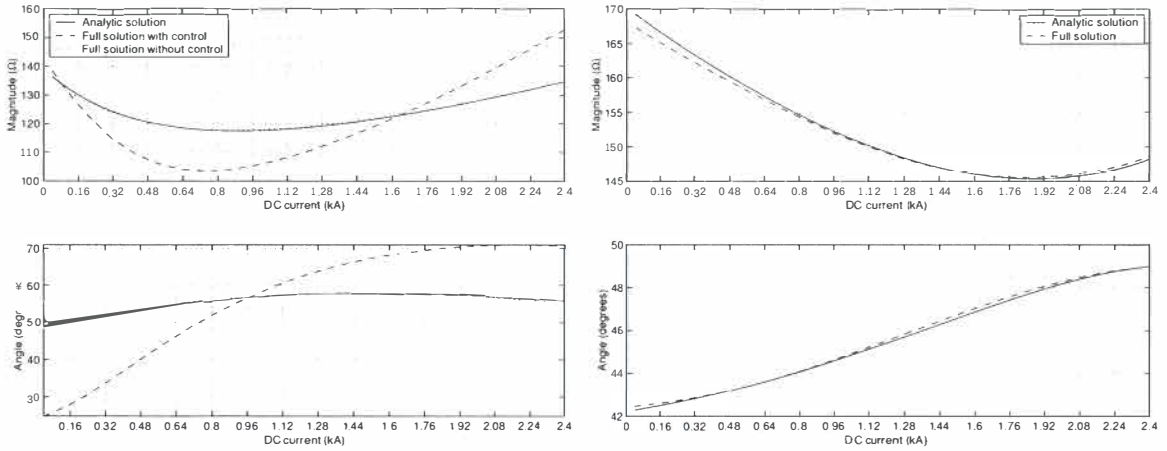

(a) Rectifier

(b) Inverter

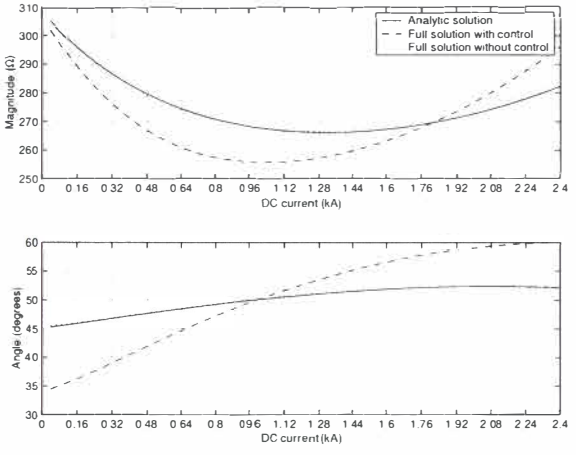

(c) Rectifier plus Inverter

Figure 8.18 Effects of average commutation period μ_o on the 100Hz dc side impedance, (a) Rectifier, (b) Inverter, (c) Rectifier plus Inverter.

This 100Hz impedance is calculated for the same operating point as used in the previous sections. Figures 8.18(a) and (b) show the difference in the dc side equivalent impedances of the single

rectifier and inverter using both the simplified 3-port analytic technique (equation 8.1) and the full solution technique using equation H.3 in appendix H, with and without the effects of control on the rectifier side. As shown agreement is good, though the effects of control do have a noticeable effect on the rectifier impedance.

Figure 8.18(a) indicates that the resulting distortion on the rectifier will be large at low dc currents but will steadily decrease as the dc current and equivalent dc side impedance increase. Likewise, figure 8.18(b) indicates that higher values of dc current will cause higher distortion on the inverter side as the dc side impedance decreases. Figure 8.18(c) however, indicates that the worst-case combined dc side impedance is likely to be around the normal operating point for the standard HVDC link, ie, when the dc current is between 0.9-1.3pu.

As seen in figure 8.4 the effect of the commutation period will cause larger associated effects if the equivalent dc side distorting frequency falls on a parallel resonant frequency. The effect of the commutation period on these frequencies is quite considerable and, though cross-modulation problems would be unlikely at these frequencies (due to the high dc side impedance), the difference in the returned cross-modulation spectra will be large over the range of different operating values. The following section verifies these results using the full solution algorithm.

Full analysis

Figures 8.19 (a) and (b) show the effect of different dc side currents on the transfers from negative sequence voltage at the rectifier to different voltage transfers around the link. The first figure shows the 3-port frequencies only while the second figure shows the transfers to higher frequencies. Both figures are the result of the full solution technique.

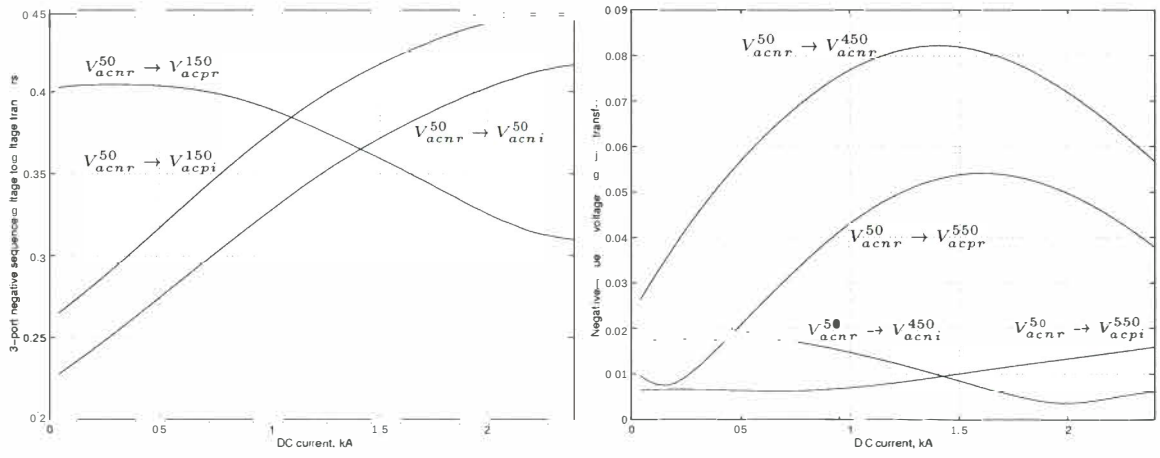

(a) 3-port voltage transfers

(b) Higher frequency voltage transfers

Figure 8.19 Negative sequence voltage to voltage transfers.

As shown, the predicted increase in the inverter 3-port voltages is seen in figure 8.19(a) for both the transfer of unbalance and the positive sequence third harmonic. Likewise, figure 8.19(a) shows the decrease in the rectifier positive sequence third harmonic. Figure 8.19(b) shows the effects of the operating point on the returned higher frequencies. The simplified analysis can not predict these, and if higher frequencies are problematic then the full solution algorithm must be used.

The effects of the power factor correction capacitors and transformer tap ratio have been ignored. These play an important role by varying the parallel resonant points of the ac system and hence

equivalent dc side impedance. The 100Hz dc side impedance is dependent on both the 50Hz and 150Hz ac side impedances and the effect of increased capacitance at higher firing angles will decrease the parallel resonant frequency. This will simply increase the effective impedance of the rectifier 50Hz ac system and more than likely will result in reduced cross-modulation.

The results of this section have indicated that the effects of operating point variation are generally smaller than the effects of impedance variation. However, all links will vary their dc current in accordance with the required power transfer and the harmonic cross-modulation will differ as a result. The following section provides a discussion of the results obtained within this chapter and attempts to provide some 'rules of thumb' for likely worst-case operating conditions.

8.6 DISCUSSION

The results of sections 8.4 and 8.5 indicate that under certain operating conditions harmonic and interharmonic cross-modulation will be high. The simplified analysis described in section 8.3 has given insight into the likely conditions required to cause harmonic and interharmonic cross-modulation problems based on the equivalent dc side impedance. Both individual converter dc side impedances and the dc side combined impedance have been investigated. It is clear that the combined impedance gives better results for overall cross-modulation problems. Section 8.4 has investigated the effect of ac side impedance while section 8.5 has investigated the effects of operating point on these equivalent dc side impedances. The results are discussed here and simple 'rules of thumb' are formulated.

8.6.1 The effects of ac system impedance

The effect of the ac system impedance on the harmonic and interharmonic cross-modulation has been demonstrated using fundamental unbalance on the rectifier terminals as a case study. This results in the main transfer of both fundamental negative sequence unbalance and positive sequence third harmonics around the link. It is hence the variation of impedance at these frequencies that must be taken into account.

The results indicate that capacitive third harmonic impedances and a strong ESCR are required, both with minimal resistive damping. However, if the ESCR is strong, unbalance on the terminals will be minimal. This indicates that links connecting a strong ac system to a weak unbalanced ac system may be likely candidates for associated cross-modulation problems from the weak to the strong system. For example if the rectifier ac system is weak it is more likely there will be a substantial unbalance on the rectifier terminals. If the inverter ac system is strong with little resistive damping then this would indicate a good case for the transfer of unbalance through the link to the inverter terminals.

Both prediction methods lead to some approximate 'rules of thumb' for worst-case harmonic and interharmonic distortion;

- If the combined equivalent dc side impedance of the link is small and falls on a series resonant condition at a problem frequency, then cross-modulation problems are likely. This will be particularly pronounced if each individual converter dc side impedance is high, but the combined impedance low. This has been seen in figure 8.8. Perhaps a good indicator, in similar stance with the SCR, ESCR, etc, could be written as, $CMF = \frac{|Zc_{dcr}|+|Zc_{dci}|}{|Zc_{dcr}+Zc_{dci}|}$, where CMF stands for Cross-Modulation Factor. Here a low cross-modulation would be close to 1, never below, while a high cross-modulation, such as that in figure 8.8 would indicate a value near 3.
- Resistive damping is very important. The lower the resistance, the larger the cross-modulation. In such circumstances the CMF would also be larger, indicating increased

cross-modulation. As discussed previously, low resistance strong ac systems tend to have minimal unbalance and this must be taken into account. Hence, it is likely that a strong ac system connected to a weak one may be a candidate for problems.

- Most problem situations, such as the negative sequence case, will require capacitive ac system impedances at the returned 3-port problem frequencies. This is required to cancel the reactive nature of the converter transformers. Problems are unlikely at higher frequencies where the converter reactance dominates.

The simplified approach used within this chapter should not be underestimated, it is relatively straight forward to use and has given the same approximate results as shown by the full solution method for predicting the worst-case impedance combinations around the HVDC link. In general the approximate 'rules of thumb' for looking for possible worst-case harmonic and interharmonic distortion could be stated simply as;

- Capacitive ac system impedances at the 3-port frequencies.
- Low resistance ac system impedances at the 3-port frequencies.

If these conditions exist then further investigation, such as calculating the equivalent dc side impedances and possible cross-modulation factor is warranted.

8.6.2 The effects of operating point

The operating point has been investigated by varying the dc current, keeping the firing angles, transformer tap ratios and power factor correction capacitors constant. Though the firing angles are likely to remain approximately constant it is certain the transformer tap ratios and power factor correction capacitors will change with differing operating point. These changes result in ac side parallel resonances moving and alter the ac side impedance viewed from the converter terminals. It is recognised that the methods in both section 8.4 and 8.5 must ultimately be used in conjunction with one another. However, for the purposes of the work described within this chapter the effects of the dc current and hence average commutation have been considered in isolation from the effects of varying ac system impedance.

The results show that though operating point change does play a role, its effect is not as strong as that of the ac system impedance. The effects of the operating point on the individual transfers of distortion around the link have been shown in figures 8.14 to 8.17 and the resulting effects on the dc side impedance in figure 8.18 for negative sequence unbalance. These results compare approximately with the results of the full solution in figure 8.19(a).

One important observation of the effects of the commutation period on the equivalent dc side impedance can be seen in figure 8.4 when looking at the effects of the average commutation period. It can be seen that increasing commutation period gives more damping in the resonant peaks. Hence, although the effect of operating point was small in the unbalanced case, the effect of operating point may be significant at other frequencies. However, it is likely to be significant when the impedance is high and hence cross-modulation problems unlikely. As discussed in the previous section the cross-modulation factor (CMF) could also be used as an indicator.

8.7 CONCLUSIONS

The conditions that effect the magnitude of harmonic and interharmonic cross-modulation around the HVDC link are largely associated with the impedance of the connecting ac systems, and lesser so with the operating point. Resonant conditions in both rectifier and inverter ac systems can effect the transfer of waveform distortion through and around an HVDC link.

This chapter has used an HVDC link in back-to-back configuration with fundamental unbalance on the rectifier terminals as a case study. Two methods have been used to predict the worst-case ac system impedance conditions, a simplified approach based on the equivalent dc side impedance of each converter, and the full solution technique described in the previous chapters. The simplified approach has derived a simple equation for the equivalent dc side impedance, using this to predict the likely worst-case ac system impedance and operating point conditions when a series resonant condition is encountered. This in general requires one converter to look inductive and the other capacitive. Due to the high inductive nature of the equivalent dc side impedance this will generally require capacitive impedances on both ac sides, cancelling much of the effect of the transformer reactances. A possible factor, the cross-modulation factor (CMF) has been discussed for indicating the worst-case cross-modulation.

Chapter 9

CONCLUSIONS AND FUTURE WORK

9.1 CONCLUSIONS

Many tools and techniques are widely available to investigate the steady state power quality around HVDC links. However, of these, none are capable of modelling the HVDC link quickly and accurately for steady state waveform distortion. Time domain methods are accurate but slow, the reverse being true for most linearised frequency domain methods. Numerical iterative frequency domain methods have shown promise with reasonably fast and accurate results, but due to their complexity have failed to provide much insight into waveform distortion interactions.

With this in mind, an investigation into the linearity of the HVDC converter in the frequency domain, using a simple and accurate numerical frequency domain model has been performed. The results have revealed not only the sensitivity of the device to small signal distortion, but have also helped aid in the understanding of the complicated effects during the commutation period. In particular, the effects of Switching Instant Variation (SIV) on the transfers of distortion around the converter have proved a pivotal role. These results have lead to the development of an improved accurate small signal HVDC model in the frequency domain.

The small signal frequency domain analysis of the HVDC converter is achieved by writing analytic equations describing the returned spectra from some applied small signal distortion. These spectra consist of both linear first order and non-linear higher order parts. The linear first order parts are identified, and it is these spectra that are derived in the small signal sense. The linearised spectra are described using sampled Partial Steady State (PSS) and Partial Transient (PT) responses to a linear circuit describing the switching state. The Fourier series of these spectra are then added giving the total resulting steady state response to the small signal distortion.

The time varying nature of the converter results in frequency coupling. This is including using Frequency Coupling Matrices (FCMs) which, assuming linearity and superposition are built from a series of small signal spectra at different distorting frequencies. A system equation (Larsen's equation) describes the coupling of phase sequence voltage and dc current distortion to phase sequence current and dc voltage around the current sourced HVDC converter. The FCMs are used within this system equation resulting in a concatenated matrix equation fully describing the frequency modulating nature of the single converter system. Inclusion of ac and dc systems are achieved by converting the system equation to nodal form and the system then easily solved for the unknown variables.

The extension of the single converter system to a full HVDC link is simple and the full nodal system equation has been written and solved for several different case studies. The effects of the most common form of power system distortion, fundamental negative sequence unbalance, have been modelled on both the 50-50Hz and 50-60Hz link and the validity of the method proven with excellent correlation with time domain PSCAD/EMTDC simulation. The effect of SIV on the

harmonic cross-modulation on the 50-50Hz back-to-back HVDC link is shown, being particularly pronounced for the transfers to dc voltage and hence the cross-modulation of distortion through the link.

Asynchronous links with small frequency differences cause problems. The system equation and FCMs become very large as many different frequencies are involved. This has lead to the development of a reduced frequency set for memory reduction in the FCMs. The memory requirements and speed of matrix inversion are presented by comparing the full frequency method with two different frequency reduced methods. Both reduced frequency methods give accurate results with greatly improved computational memory and modelling speed. Using these reduced frequency methods, both operating point and distortion sourced interharmonics are investigated on a 50-51Hz back-to-back link. Resulting positive sequence frequencies in the subsynchronous range are identified for possible rotor torque problems and a simple equation, simply the difference in ac system frequencies multiplied by the HVDC link pulse number is used to predict these frequencies.

Finally, possible worst-case scenarios for harmonic and interharmonic distortion are investigated. A simplified analysis is formulated based on the equivalent 3-port dc side impedance. This is used to predict possible worst-case harmonic and interharmonic cross-modulation scenarios for the effects of different ac system impedance and operating points. The results indicate that ac system impedance at the '3-port' frequencies are very important in the transfer of distortion through and around the link. Validation of the simplified technique against the full solution method is achieved and good 'rules of thumb' proposed for the worst-case transfers of distortion.

9.2 FUTURE WORK

The future of electric power is assured. As non-renewable energy supplies are exhausted alternative energy resources must be found. Many solutions to these problems are dependent on the use of power electronic switching devices for the efficient and reliable transfer of power. One such example is the increasing awareness of the efficiency of having small power generation close to the load. Another example is the use of electric power in the transportation industry. Many of these devices require power electronic switching devices to convert electric energy in one form into a more usable form.

Though this thesis has been based on the modelling of the HVDC converter and link, much work remains on the small signal modelling of other power electronic devices. Small signal linearised modelling is very powerful and can be used for not only the analysis of harmonic and interharmonic problems, but also for the modelling of transient control and small signal stability problems. As far as steady state waveform distortion is concerned, this thesis has given a good framework for the linearised steady state time-variant modelling for such devices. This includes the use of tensors, FCMs and the nodal analysis. These techniques can be easily applied to other situations such as that found in distributed generation and in the transportation industry. The following sections discuss some possible future developments of the work carried out within this thesis.

9.2.1 Small signal power electronic device modelling

With the exception of the capacitor commutated converter, the HVDC converter is perhaps one of the hardest power electronic devices to model in the small signal sense. The reason is the commutation period and the effect distortion plays on this. Before developing small signal linearised models, investigation into the suitability of the device to be modelled is required. For the HVDC converter this was achieved using an iterative frequency domain model assuming the converter was non-linear. The effects of distortion on the commutation period dynamics were

investigated and much insight gained. This non-linear analysis is required for all power electronic switching devices, determining their linearity, or sensitivity, of the operating point to applied distortion. Once this sensitivity is known, the accuracy of a linearised small signal model will also be known and confidence can be gained for further linearised development.

As an example, it is known that single and three phase voltage sourced diode rectifiers can be linearised about a base operating point [?], however, how sensitive are the operating points? The sensitivity and hence accuracy of such small signal models must be determined.

Another example is that of voltage sourced converters utilising GTO switches and PWM technology such as ABB's 'HVDC light'. These devices are becoming increasingly popular on offshore wind farms, oil platforms and distributed generation gas/steam turbines. Converters using this switching topology are thought to be almost completely linear due to the controlled nature of the turn on and turn off switching instants. Similar techniques to those used within this thesis could be further developed for such situations.

The increasing use of small generators on the power system, combined with devices such as gas/steam turbines may create an interesting area for the analysis of steady state waveform distortion. Harmonic and interharmonic currents generated by the switching devices may interact with the high speed rotor shaft assemblies causing unwanted vibration and possible early mechanical fatigue. Furthermore a combination of these devices may result in low frequency oscillations, such as subsynchronous resonance and also possible inter-area oscillations may also result. These are more likely the result of control problems but can be analysed using small signal stability techniques. Further investigation is required into such problems, not only for gas turbines, but also for the various wind turbines and other small generation schemes now becoming widely available. Small signal models of these machines combined with small signal models of the switching plant are required.

9.2.2 Generalised frequency domain analysis

A generalised modular framework for the analysis of multiple power electronic devices and the power transmission networks in which they are connected is required. The generalised analysis is a two-step process involving firstly a single or perhaps three phase AC/DC load flow to obtain the operating point, then a linearised analysis of the system similar to that described within this thesis. Software will be required that ties the load flow and full nodal analysis using the FCMs together forming the overall system admittance matrix for the harmonic and interharmonic analysis, or a state matrix for eigenvalue small signal stability type analysis.

Once achieved, full solutions of power systems containing multiple power electronic switching devices can be solved quickly and accurately. This could be especially useful in systems where distributed or embedded generation are to be used or simply where many different power electronic devices are connected to the network.

9.2.3 Simplified analysis

The simplified analysis described in chapter 8 has been used with success to determine approximate 'rules of thumb' for finding worst-case cross-modulation conditions. The use of such methods is important when considering a multitude of operating points and could be extremely valuable in the design and analysis stages of filter installation or power system network changes. The simplified 3-port equations can be simplified further, calculated at dc, and used for small signal transient control analysis. This has been and is still currently under research within the department.

Appendix A

LIST OF FIGURES AND TABLES

LIST OF FIGURES

LIST OF TABLES

Appendix B

HVDC LINKS WORLDWIDE

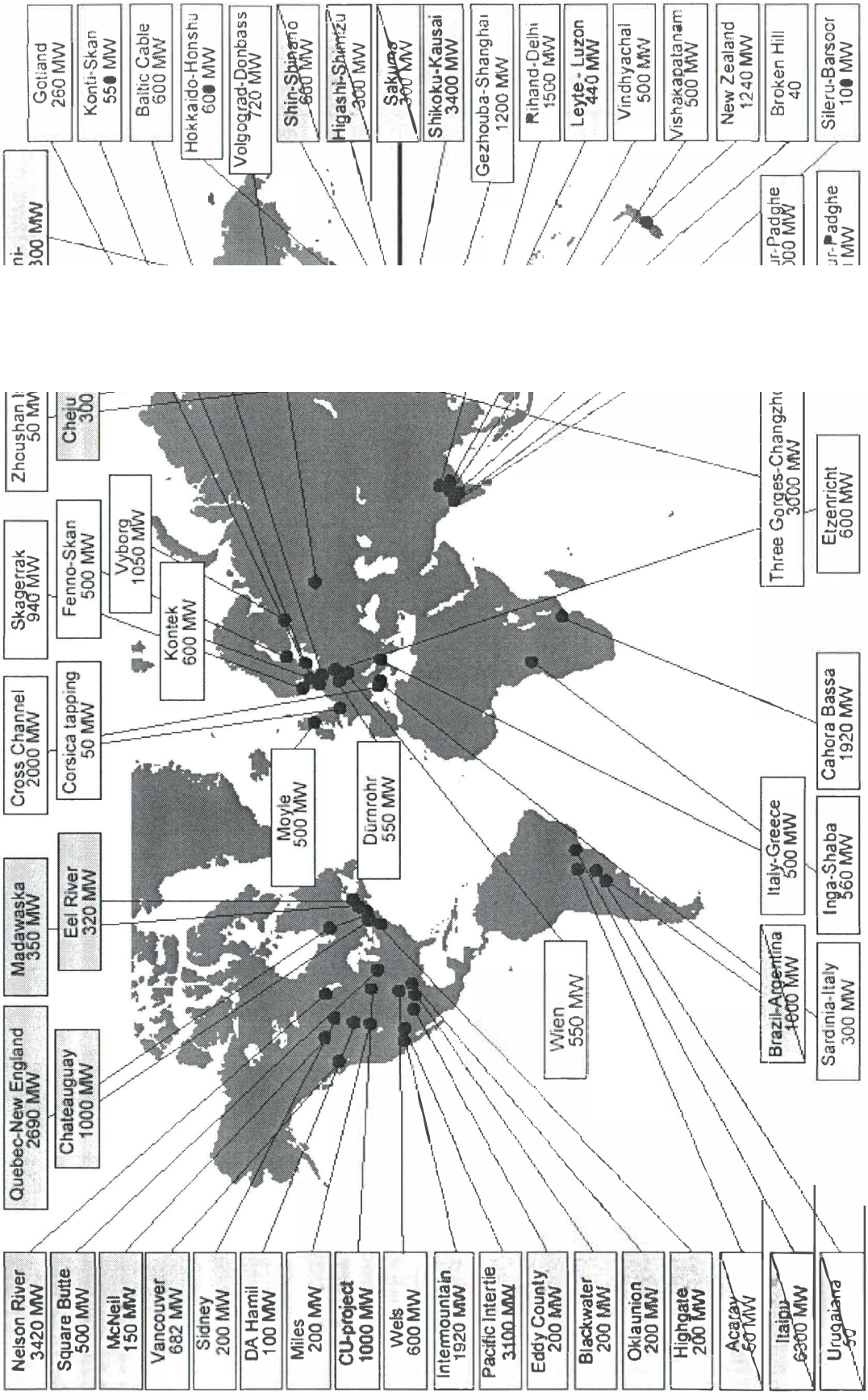

Figure B.1 HVDC links worldwide, *Courtesy [2].*

Appendix C

MULTI-PERTURBATION SIMULATIONS IN THE TIME DOMAIN PROGRAM PSCAD/EMTDC

This appendix describes the methods used for the time domain PSCAD/EMTDC validation of the analytic transfers and ac/dc side impedances. To validate the frequency dependent transfers in the time domain either an automatic time variable distorting source is required or multiple time domain simulations must be run at each distortion frequency. The later is very time consuming, hence the former has been chosen, but requires an additional automated PSCAD/EMTDC component. A specialised component called 'autogain' has been created in the pseudo PSCAD/FORTRAN scripting language used for such components. This has allowed a normal gain component to change its gain after linear time intervals and has also allowed data output of the chosen variables to be written to file at the required specified time intervals.

Most of the time domain simulations used within this thesis have been perturbed from 10 to 1250Hz in 10Hz steps with a suitably small signal distortion for the required transfer or impedance to be validated. In most cases this was achieved by applying distortion to the system every 0.5 seconds giving a total simulation time in PSCAD/EMTDC of $5 + 125 \times 0.5 = 67.5$ seconds. After applying each distorting frequency the system was allowed to settle for 0.4 seconds before the time domain data (3 phase ac currents and dc voltage) was written to an output file for the remaining 0.1 seconds. This was achieved simply by adjusting the PRINT step to 2×10^{-5} accordingly. The resulting data files are very large being 5000 rows of data points for each 0.1 second of recorded data. Hence, a data file with x variables (columns) of recorded data would use approximately $125 \times 5000 \times (x + 1) \times 16 = 10(x + 1)$ Megabytes of disk space, the $(x + 1)$ used as the time vector is recorded in the first column.

These data files were then loaded into MATLAB using a specialised MATLAB function called PSCADdata. This function requires both the main perturbed time domain data file for input as well as a base case (unperturbed) input data file. As well as this the function requires the column position of each variable so it can identify the three phase ac currents and dc voltage or other variable to be FFT'd. The output is the returned small signal frequency domain data (minus the base case spectrum) in a frequency cross-coupling matrix form. Two transfers are given for the ac current in both positive and negative sequence.

The MATLAB file splits the time domain PSCAD/EMTDC data into 125 different matrices by finding the discontinuity in the time vector (column one of the data file). Phase sequence transformation on the ac currents followed by the FFT on each column follows. The results are then placed into the appropriate column of the appropriate matrix. These matrices can then be used for validation against the small signal analytic model.

Appendix D

HVDC TEST SYSTEMS

D.1 THE STANDARD CIGRE HVDC BENCHMARK MODEL

The CIGRE HVDC benchmark model [62] has been designed to give a simple, yet operationally difficult test system for encouraging comparisons of performance between different computer models. The primary reason for such a test system is for the analysis of different control strategies, while a secondary purpose is to provide a reference for various simulating programs. The system is shown in figure D.1 below with the main parameters given in table D.1. Figure D.2 (a) and (b) show the individual CIGRE rectifier and inverter test systems with the same ac and dc systems and parameters used in table D.1. In these cases a constant dc voltage source is used to represent the opposite converter. Figure D.3(a) shows the rectifier ac system impedance magnitude and phase angle (Z_{acr}), while figures D.3(b) and (c) show the inverter ac system (Z_{aci}), and dc system (Z_{dc}) respectively. The individual components making up these systems, including the filters and Thevenin equivalent impedances can be found in [62].

Parameter	Rectifier	Inverter
AC source voltage (RMS), $V_{s(r,i)}$	$375.36\angle 22.18^o$	$215.05\angle -23.14^o$
Primary side transformer terminal voltage (RMS), $V_{1(r,i)}$	$345\angle 0^o$	$230\angle 0^o$
Secondary side transformer terminal voltage (RMS), $V_{2(r,i)}$	211.42	211.42
Transformer MVA rating	598	598
Transformer turns ratio	0.6128	0.9192
Base system impedance (1000MW base)	119.03Ω	52.90Ω
Base transformer impedance, secondary side	74.75Ω	74.75Ω
Base transformer impedance, primary side	199.04Ω	88.46Ω
Per unit transformer leakage reactance (primary side base)	0.18	0.18
Transformer reactance on secondary side base	13.45Ω	13.45Ω
Average firing angle, $\alpha_{o(r,i)}$	15.0^o	141.81^o
Average commutation period, $\mu_{o(r,i)}$	23.19^o	23.19^o
DC, dc side current, I_{dc}	$2kA$	$2kA$

Table D.1 Operating parameters of the CIGRE 50-50Hz HVDC benchmark model.

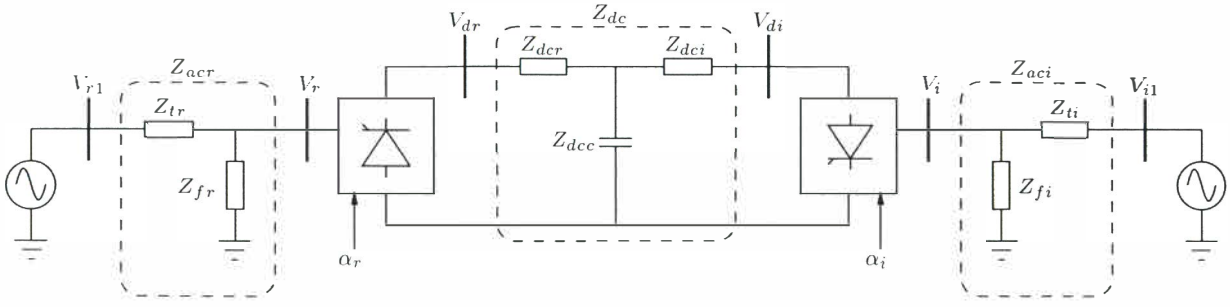

Figure D.1 Full CIGRE benchmark test system.

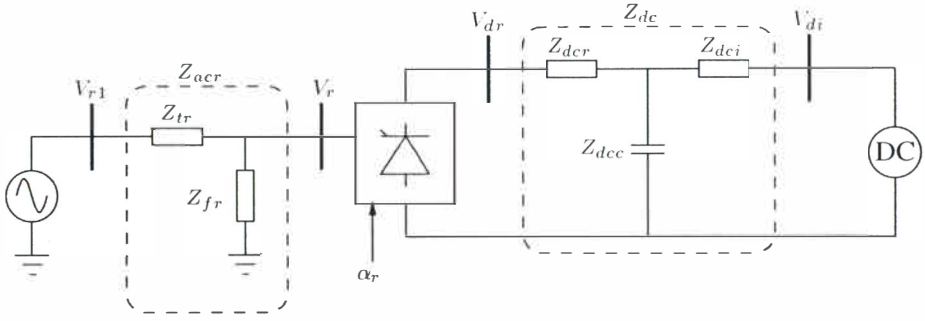

(a) CIGRE rectifier benchmark test system.

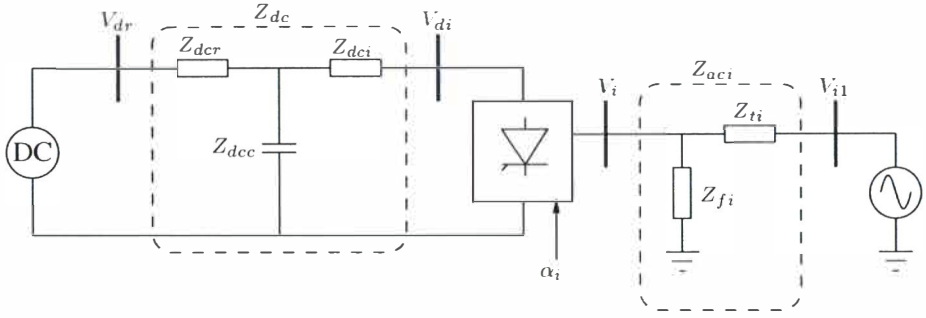

(b) CIGRE inverter benchmark test system.

Figure D.2 CIGRE rectifier and inverter benchmarks.

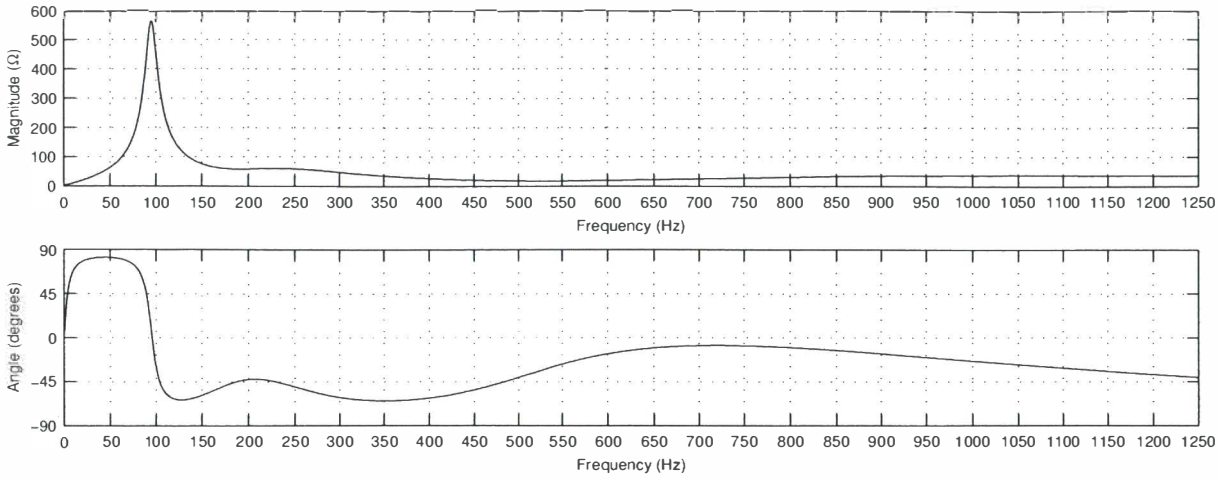

(a) CIGRE rectifier ac system impedance, Z_{acr}.

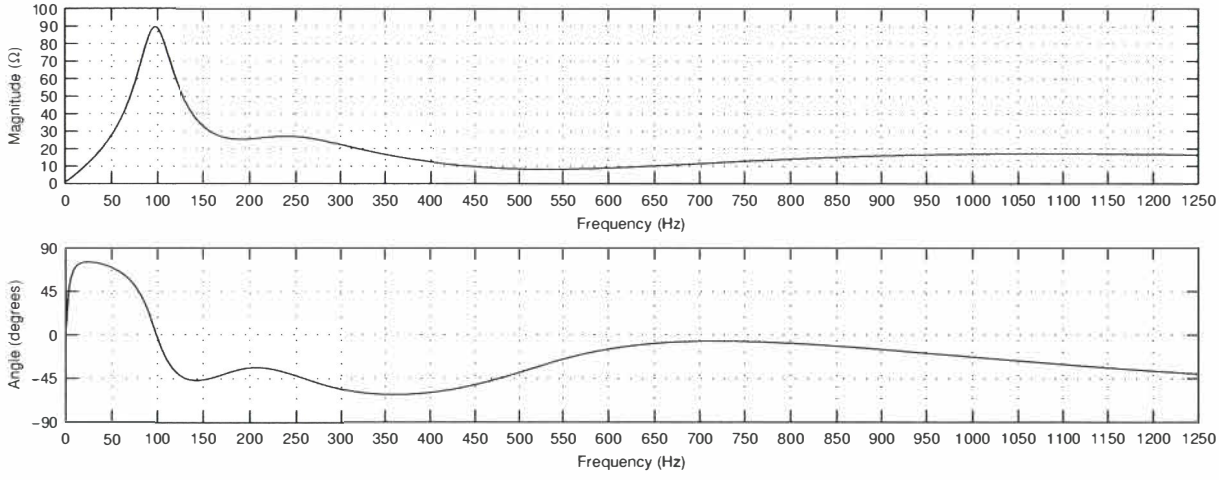

(b) CIGRE inverter ac system impedance, Z_{aci}.

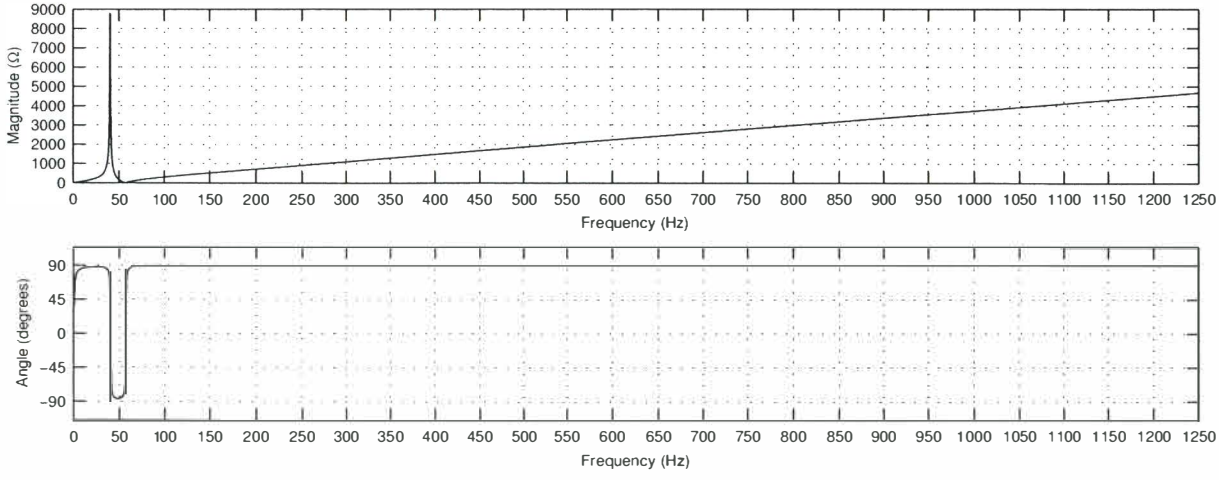

(c) CIGRE dc system impedance, Z_{dc}.

Figure D.3 CIGRE rectifier and inverter benchmarks.

D.2 THE BACK-TO-BACK HVDC BENCHMARK MODEL

The back-to-back schemes used within this thesis are simply the CIGRE system without the dc system, as shown in figure D.4. The load flow conditions change due to the voltage drop across the dc system being zero. For simplicity the ac and dc systems remain the same as those depicted in figure D.3 except when the link is operated in asynchronous power transfer mode connecting two different system frequencies such as the 50-60Hz back-to-back link shown in chapter 7. In this case the 60Hz system has been scaled accordingly. Leaving the impedances the same as the CIGRE model presents a non-ideal power load flow condition. However, for the purposes of this thesis this is not considered important, especially where harmonic and interharmonic validation is concerned.

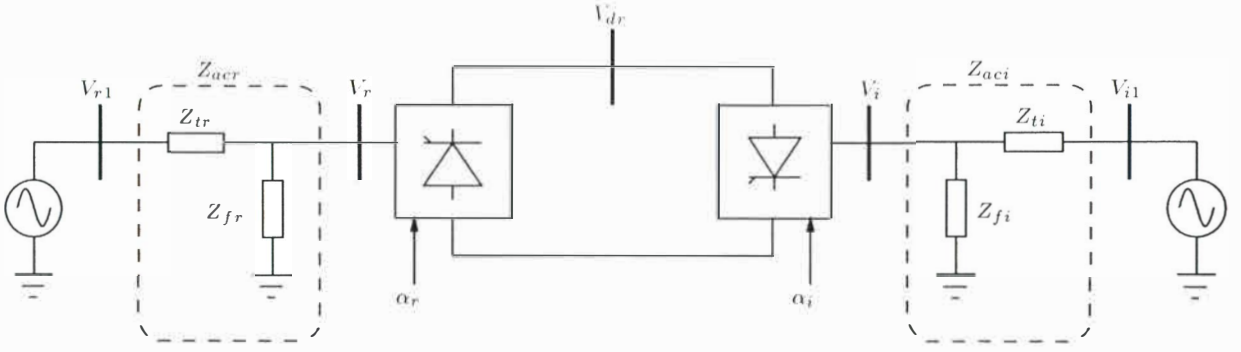

Figure D.4 Modified back-to-back CIGRE HVDC link.

Appendix E

PDM, AMIT AND PAM

This appendix describes the derivation of the Area Modulated Impulse Train (AMIT) from Schwartz's Pulse Duration Modulated (PDM) spectrum [70], then uses this spectrum to derive the Pulse Amplitude Modulated (PAM) spectrum. Both the AMIT and PAM spectra are required in the derivation of the algebraic converter model described in chapter 5. The AMIT spectrum is a first order linearisation of Schwartz's PDM spectrum. It is used to model the linearised effects of the SIV on the transfers associated with dc voltage. Wood [3] used Schwartz's full PDM spectrum, showing all higher order frequencies generated by the SIV for the HVDC converter, this work is repeated here. The first order AMIT spectrum is then derived from the full PDM spectrum and is shown to be equivalent to an area or amplitude modulated impulse train.

E.1 SCHWARTZ'S PULSE DURATION MODULATED (PDM) SPECTRUM

In Schwartz's analysis the PDM waveform is generated by adding the modulating signal to a steady state sawtooth sweep voltage. The pulse is initiated at the beginning of each voltage sweep, and is terminated when the sweep crosses a preset threshold. The unmodulated sweep waveform, threshold, and resulting pulses are shown in figure E.1

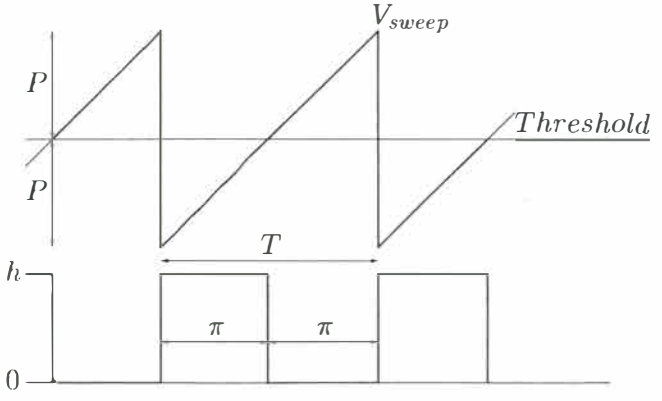

Figure E.1 Unmodulated PDM wave shapes

Letting the sweep be as shown in figure E.1, the modulation signal $Qcos(qt)$, and the pulse height h, Schwartz calculates the resulting frequency spectrum,

$$
\begin{aligned}
E(t) &= \frac{h}{2} - \frac{hQ}{2P}cos(qt) + \frac{h}{\pi}\sum_{m=1}^{\infty}\left[(-1)^m - J_o\left(\frac{m\pi Q}{P}\right)\right]\frac{sin(mpt)}{m} \\
&- \frac{h}{\pi}\sum_{m=1}^{\infty}\sum_{n=1}^{\infty}\frac{J_n\left(\frac{m\pi Q}{P}\right)}{m}sin\left[(mp+nq)t+\frac{n\pi}{2}\right] \\
&- \frac{h}{\pi}\sum_{m=1}^{\infty}\sum_{n=1}^{\infty}\frac{J_n\left(\frac{m\pi Q}{P}\right)}{m}sin\left[(mp-nq)t+\frac{n\pi}{2}\right]
\end{aligned}
\tag{E.1}
$$

where p is the angular sweep frequency, which will now be known as ω_o.

Redefining the PDM in terms of the pulse angular position (radians) as $bcos(k\omega_o t + \delta_k)$, results in the substitutions, $Q = \frac{-Pb}{\pi}$ and $q = k\omega_o$. Also, $h = 1$. The frequency spectrum then becomes,

$$
\begin{aligned}
E(\omega_o t) &= \frac{1}{2} - \frac{b}{2\pi}cos(k\omega_o t + \delta_k) + \frac{h}{\pi}\sum_{m=1}^{\infty}\left[(-1)^m - J_o(mb)\right]\frac{sin(m\omega_o t)}{m} \\
&- \frac{1}{\pi}\sum_{m=1}^{\infty}\sum_{n=1}^{\infty}\frac{J_n(mb)}{m}sin\left[(m+nk)\omega_o t + n\delta_k - \frac{n\pi}{2}\right] \\
&- \frac{1}{\pi}\sum_{m=1}^{\infty}\sum_{n=1}^{\infty}\frac{J_n(mb)}{m}sin\left[(m-nk)\omega_o t + n\delta_k - \frac{n\pi}{2}\right]
\end{aligned}
\tag{E.2}
$$

When modelling the SIV, only the change in the PDM spectrum that results from an existing wave being modulated needs to be considered. The spectrum of the unmodulated pulse train is therefore subtracted from the modulated pulse train to define the harmonic contribution of the modulation.

The unmodulated pulse train has the spectrum,

$$
E(\omega_o t) = \frac{1}{2} + \frac{1}{\pi}\sum_{m=1}^{\infty}[(-1)^m - 1]\frac{sin(m\omega_o t)}{m} \tag{E.3}
$$

Thus the contribution of modulation to the harmonic spectrum is,

$$
\begin{aligned}
PDM(\omega_o t) &= \frac{b}{2\pi}cos(k\omega_o t + \delta_k) + \frac{1}{\pi}\sum_{m=1}^{\infty}\left[1 - J_o(mb)\right]\frac{sin(m\omega_o t)}{m} \\
&- \frac{1}{\pi}\sum_{m=1}^{\infty}\sum_{n=1}^{\infty}\frac{J_n(mb)}{m}sin\left[(m+nk)\omega_o t + n\delta_k - \frac{n\pi}{2}\right] \\
&- \frac{1}{\pi}\sum_{m=1}^{\infty}\sum_{n=1}^{\infty}\frac{J_n(mb)}{m}sin\left[(m-nk)\omega_o t + n\delta_k - \frac{n\pi}{2}\right]
\end{aligned}
\tag{E.4}
$$

As shown, higher order frequencies are present in the PDM spectrum with non-linear n^{th} order Bessel function multipliers. In the linearised model the switching instant modulation magnitude and angle, $b\angle\delta$, are acquired through small signal linearisation techniques as shown in chapter 5 and given in table 5.3. These signals themselves are small and as $b\angle\delta \rightarrow 0$ the non-linear Bessel

function multipliers can be effectively linearised. Figure E.2 shows the non-linear variation in the Bessel function multipliers for the 0^{th} and 1^{st} order terms. In this instance, $J_o(mb)|^{b\to 0} \to 1$,

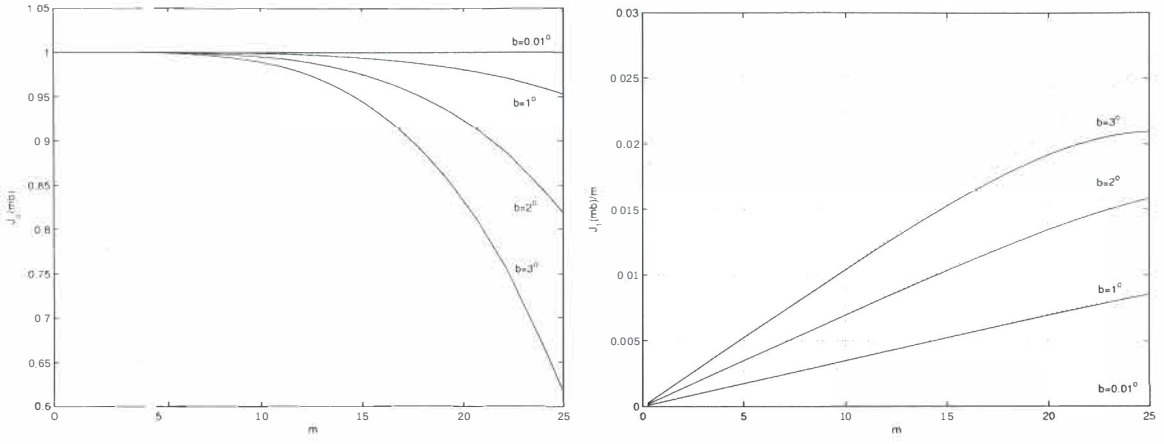

(a) 0^{th} order Bessel functions, $J_o(mb)$

(b) 1^{st} order Bessel functions, $\frac{J_1(mb)}{m}$ and linearised approximation, $\frac{b}{2}$ - dotted

Figure E.2 Effect of frequency m and b at $0.01°, 1°, 2°$ and $3°$ on Bessel function multipliers

$\frac{J_1(mb)}{m}|^{b\to 0} \to \frac{b}{2}$ and all higher order Bessel functions $\frac{J_n(mb)}{m}|^{b\to 0} \to 0$. Hence, in the small signal linearised sense, equation E.4 can be rewritten as,

$$PDM(\omega_o t)|^{b\to 0} = +\frac{b}{2\pi}cos(k\omega_o t + \delta) + \frac{b}{2\pi}\sum_{m=1}^{\infty} cos((m+k)\omega_o t + \delta) + \frac{b}{2\pi}\sum_{m=1}^{\infty} cos((m-k)\omega_o t - \delta) \tag{E.5}$$

This is mathematically the same as a sampled *Dirac comb* or area modulated impulse train, AMIT. The following section derives the AMIT spectrum from the *ideal sampling function.*

E.2 THE AREA MODULATED IMPULSE TRAIN, AMIT SPECTRUM

Figure E.3 shows the *ideal sampling function*, or *Dirac comb*, with its time and frequency domain representations. Part (a) and (b) show the conversion from seconds to radians, 2π being the fundamental period. The area modulated impulse train can be found from time domain multiplication of the wave shape in figure E.3 with is required modulating signal. Equation E.6 shows the relationship from the delta function to positive frequency sinusoidal form.

$$\sum_{m=-\infty}^{\infty} \delta(\omega_o t - 2m\pi) = \frac{1}{2\pi} + \frac{1}{2\pi}\sum_{m=1}^{\infty} cos(m\omega_o t) \tag{E.6}$$

The modulating signal is simply a sinusoidal frequency, $bcos(k\omega_o t + \delta)$ and when multiplied in the time domain with equation E.6 gives the required AMIT spectrum required for the dc voltage transfers. This process is shown in figure E.4. The area modulated delta functions are presented as amplitude modulated functions which are mathematically identical. The multiplication gives

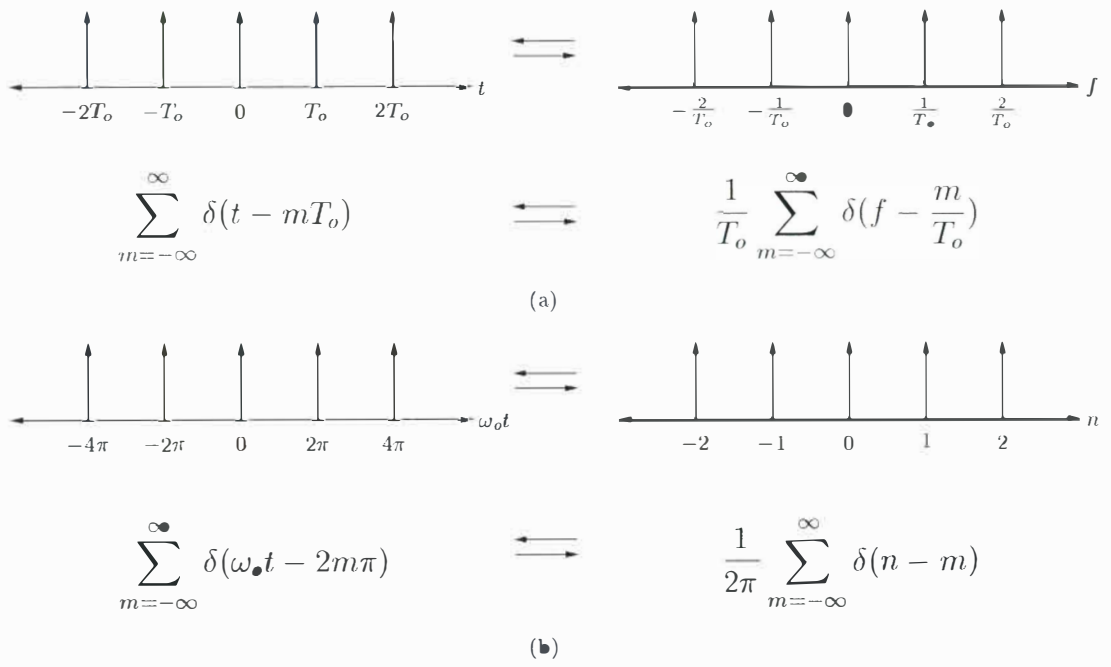

Figure E.3 Time and frequency domain representation of ideal sampling function, (a) seconds, (b) radians.

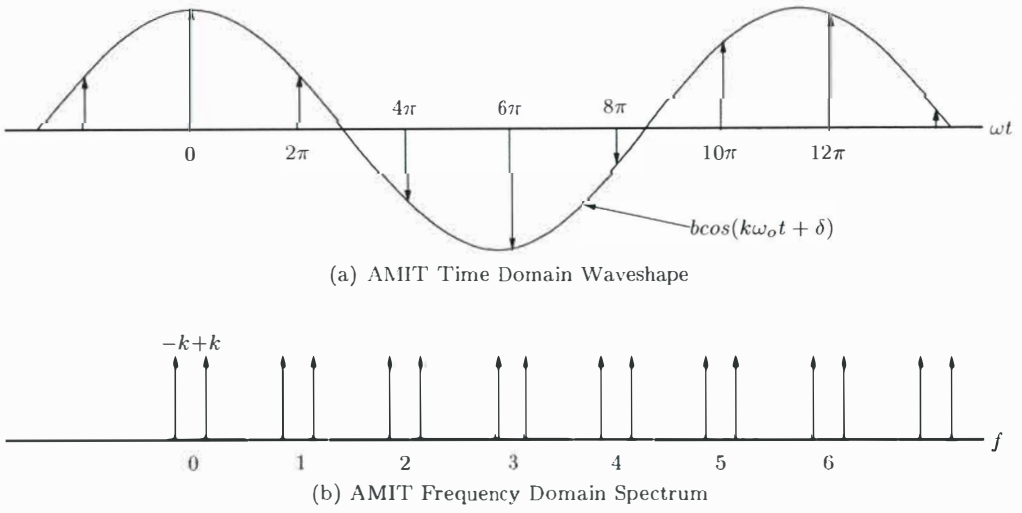

Figure E.4 Time and frequency domain representation of AMIT wave shape.

the required AMIT spectra, ie.

$$AMIT(\omega_o t) = +\frac{b}{2\pi}cos(k\omega_o t + \delta) + \frac{b}{2\pi}\sum_{m=1}^{\infty} cos((m+k)\omega_o t + \delta) + \frac{b}{2\pi}\sum_{m=1}^{\infty} cos((m-k)\omega_o t - \delta) \tag{E.7}$$

This is the area modulated delta function required for the small signal transfers to dc voltage. It is identical to equation E.5.

E.3 THE PULSE AMPLITUDE MODULATED, PAM SPECTRUM

The PAM spectrum is required in the calculation of the transfers to ac current. Fortunately the effect of calculated by convolving the AMIT spectrum with a rectangular pulse of width $\frac{\mu_o}{\omega_o}$ seconds, time shifted by $\frac{\mu_o}{2\omega_o}$ seconds. This is shown in figure E.5(a) and (b) respectively. The Fourier transform for a rectangular pulse centred on the origin is,

$$\begin{aligned} RP(k) &= \int_{-\frac{\mu_o}{2\omega_o}}^{\frac{\mu_o}{2\omega_o}} e^{-j2\pi kft}dt \\ &= \frac{1}{\pi kf}sin(\pi kf\frac{\mu_o}{\omega_o}) \\ &= \frac{\mu_o}{\omega_o}sinc(kf\frac{\mu_o}{\omega_o}) \end{aligned} \tag{E.8}$$

A time shift of $\frac{\mu_o}{2\omega_o}$ must by applied to this transform before convolution with the AMIT spectra. This is given as,

$$RP(k) = \frac{\mu_o}{\omega_o}sinc(kf\frac{\mu_o}{\omega_o}).e^{-jk\frac{\mu_o}{2}} \tag{E.9}$$

Convolution of the AMIT spectrum (equation E.7), with the Fourier transform of the phase

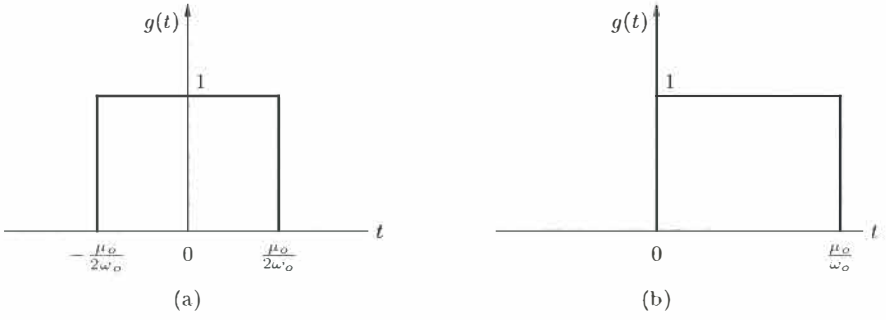

Figure E.5 Representation of rectangular pulse, (a) - centred at zero, (b) - time shifted by $\frac{\mu_o}{2\omega_o}$.

shifted rectangular pulse (equation E.9) gives the PAM spectrum required for the transfers to ac current. This is shown in figure E.6 and derived in equation E.10 below.

$$\begin{aligned} PAM(\omega_o t) = &+ \frac{b\mu_o}{2\pi}sinc(\frac{k\mu_o}{2\pi})cos(k\omega_o t - k\frac{\mu_o}{2} + \delta) \\ &+ \frac{b\mu_o}{2\pi}\sum_{m=1}^{\infty} sinc((m+k)\frac{\mu_o}{2\pi})cos((m+k)\omega_o t - (m+k)\frac{\mu_o}{2} + \delta) \\ &+ \frac{b\mu_o}{2\pi}\sum_{m=1}^{\infty} sinc((m-k)\frac{\mu_o}{2\pi})cos((m-k)\omega_o t - (m-k)\frac{\mu_o}{2} - \delta) \end{aligned} \tag{E.10}$$

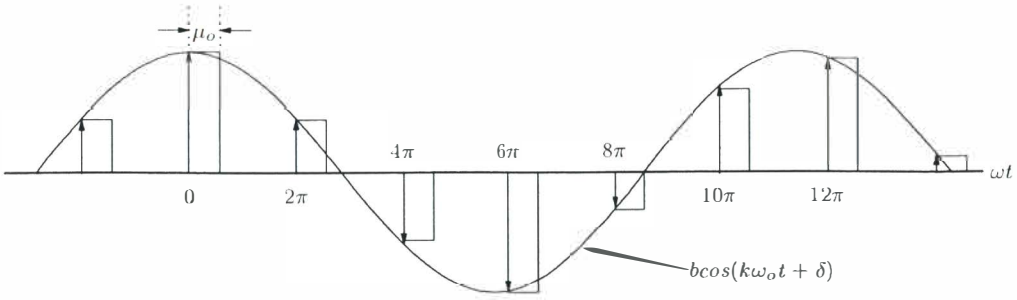

(a) PAM Time Domain Waveshape

Figure E.6 Time domain representation PAM wave shape.

Appendix F

THE SPARSE MATRIX TRANSFERS

This appendix shows sparsity plots of the frequency cross coupling matrix transfers used throughout this thesis. The '+' signs indicate the direct terms while the '$\otimes$' signs indicate the conjugated terms. The light grey terms indicate the additional transfers required for the 6-pulse converter while the black transfers indicate the transfers required for the 12-pulse converter only.

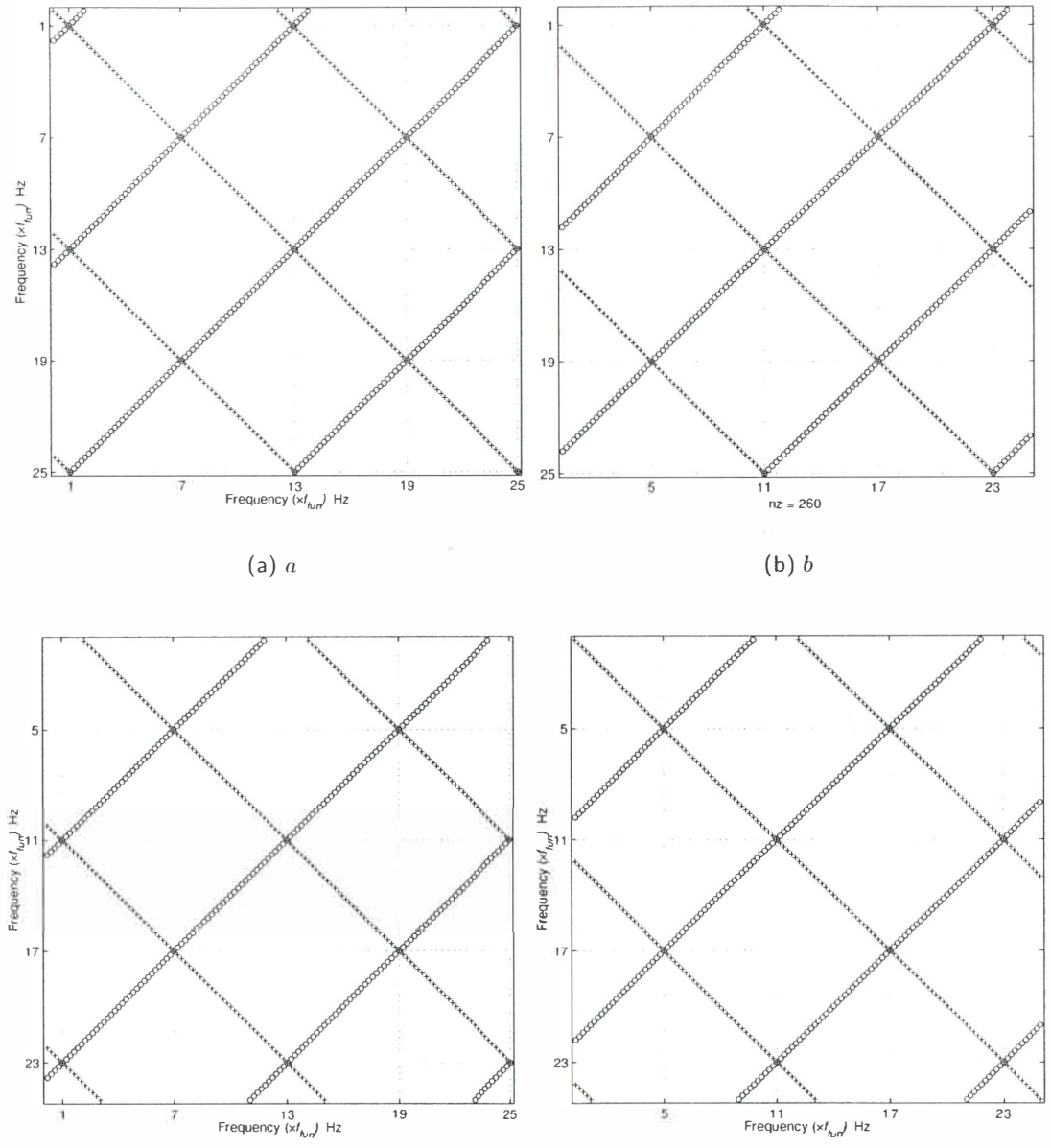

(a) a (b) b

(c) e (d) f

Figure F.1 CIGRE rectifier $V_{ac} \rightarrow I_{ac}$ transfers.

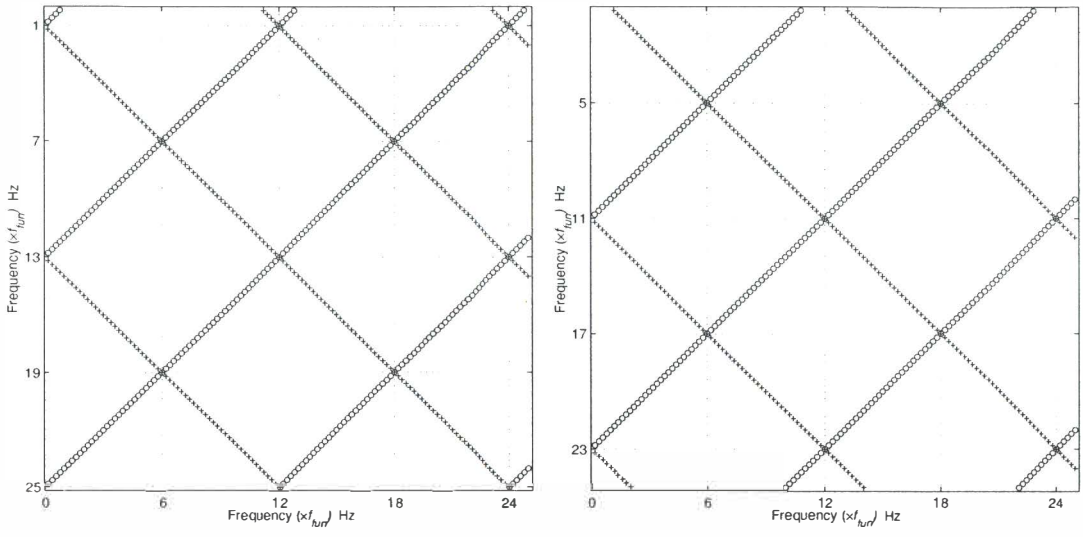

(a) c (b) g

Figure F.2 CIGRE rectifier $I_{dc} \rightarrow I_{ac}$ transfers.

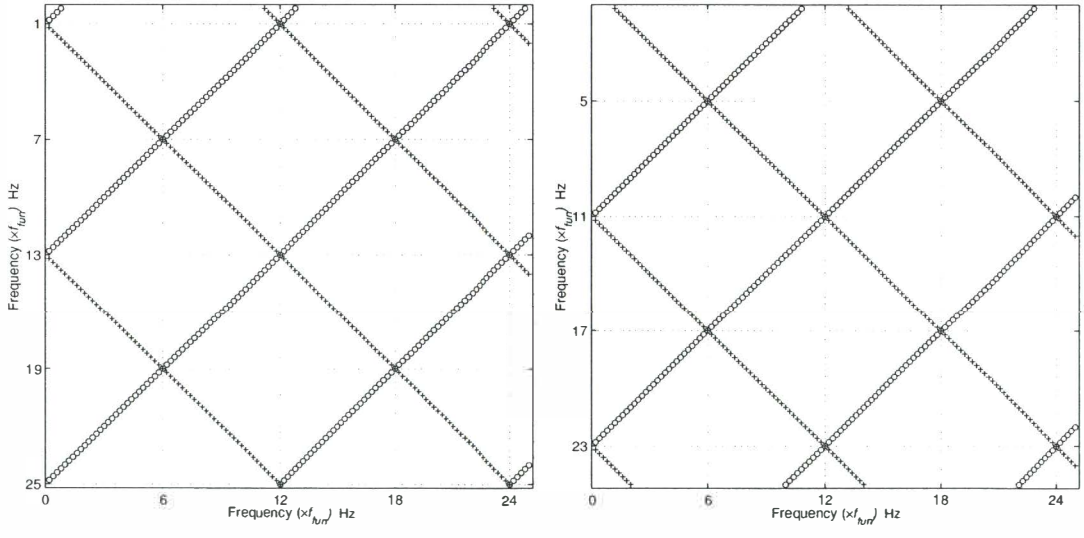

(a) d (b) h

Figure F.3 CIGRE rectifier $\alpha \rightarrow I_{ac}$ transfers.

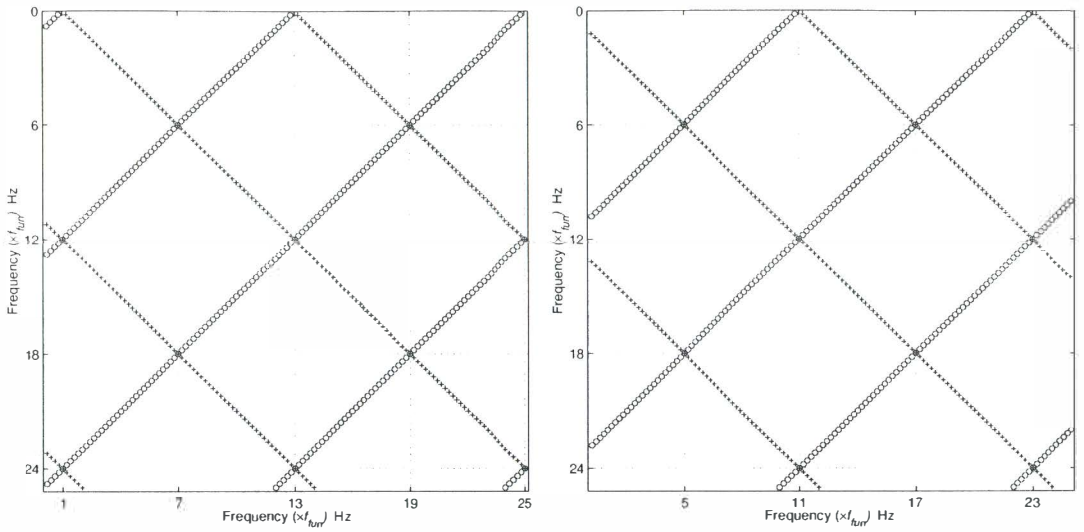

(a) i (b) j

Figure F.4 CIGRE rectifier $I_{ac} \rightarrow V_{dc}$ transfers.

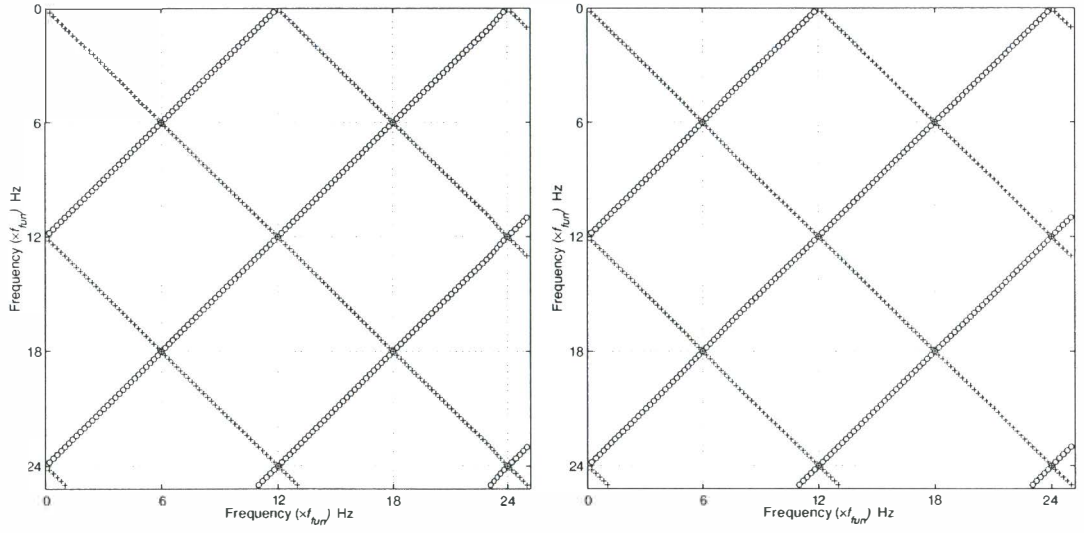

(a) k (b) l

Figure F.5 CIGRE rectifier $I_{dc}, \alpha \rightarrow V_{dc}$ transfers.

Appendix G

CONFIGURATION OF TRANSFERS IN LARSEN'S EQUATION

There are two important considerations that must be considered when modelling the rectifier and inverter using Larsen's equation. These are the direction of all the currents into and out of the converter and the orientation of the dc side voltage.

The frequency dependent cross coupling transfers of Larsen's equation are derived in both the analytic and iterative frequency domain models as viewing positive distorting ac currents into the converter and the positive dc current out of the converter. This convention was used as it is the same as the power flow at fundamental and dc. The models were derived in the rectifier sense and hence the dc voltage is orientated in the positive direction. The orientation of the currents and voltages in the derived models is shown in figure G.1(a).

Figures G.1(b) and G.1(c) show the converter and the direction of the currents and voltages around the converter for rectification (b), and for inversion (c) respectively. In both instances all currents are positive when derived into the converter, as required for conventional nodal analysis.

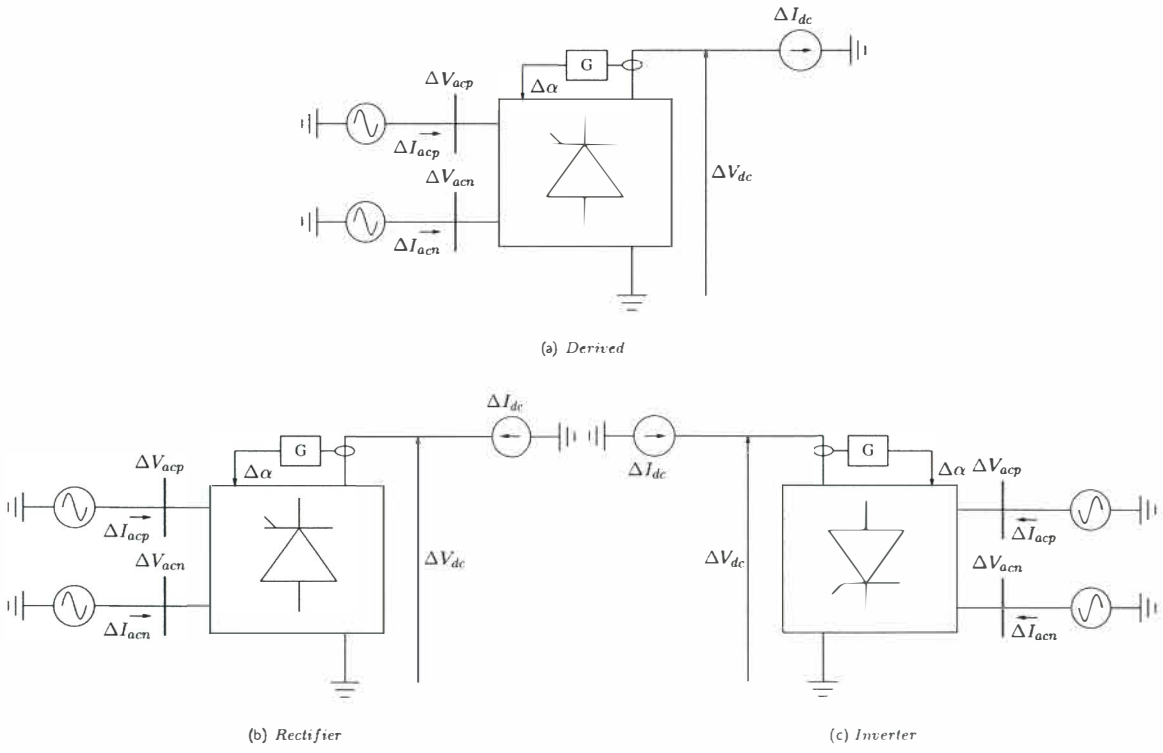

Figure G.1 Converter modes of operation.

Hence, when the converter transfers are derived with all current sources into the converter as in

figure G.1(b), Larsen's equation for the rectifier becomes,

$$\begin{bmatrix} \Delta I_{acp} \\ \Delta I_{acn} \\ \Delta V_{dc} \\ 0 \end{bmatrix} = \begin{bmatrix} a & b & -c & d \\ e & f & -g & h \\ i & j & -k & l \\ 0 & 0 & -G & 1 \end{bmatrix} \begin{bmatrix} \Delta V_{acp} \\ \Delta V_{acn} \\ \Delta I_{dc} \\ \Delta \alpha \end{bmatrix} \tag{G.1}$$

and for the inverter becomes,

$$\begin{bmatrix} \Delta I_{acp} \\ \Delta I_{acn} \\ \Delta V_{dc} \\ 0 \end{bmatrix} = \begin{bmatrix} a & b & c & d \\ e & f & g & h \\ -i & -j & -k & -l \\ 0 & 0 & G & 1 \end{bmatrix} \begin{bmatrix} \Delta V_{acp} \\ \Delta V_{acn} \\ \Delta I_{dc} \\ \Delta \alpha \end{bmatrix} \tag{G.2}$$

Appendix H

THE HVDC CONVERTER IMPEDANCE

This appendix uses Larsen's equation [34] to derive the ac side phase sequence and dc side impedances around the CIGRE test system rectifier and inverter. Presented are the 3-port impedances which are the most dominate terms of the impedance transfers. The effects of the control transfer function, the switching instant variation (SIV) and a comparison between the two solution techniques described in this appendix are shown.

In chapter 6, equations 6.15 to 6.20 demonstrate the conversion of Larsen's equation into the more general nodal form, including the ac and dc side system admittances. In this form the positive, negative and dc side admittance/impedance transfers can be found by partitioning the matrix accordingly, then solving for the required variables associated with the wanted impedance.

H.1 FULL MATRIX SOLUTION OF CONVERTER IMPEDANCES

The following equations give the positive (Zc_{acp}), negative (Zc_{acn}) and dc (Zc_{dc}) side small signal impedance viewed while looking into both the ac and dc terminals of the HVDC converter respectively. The full matrix solution uses the full FCMs and includes the all associated effects resulting from higher frequency cross modulation and control.

The positive sequence impedance of the converter can be described in matrix form as:

$$Zc_{acp} = [A - BD^{-1}C - Y_{acp}]^{-1} \tag{H.1}$$

where, $A = [Y^*_{11} + Y_{acp}]$, $B = \begin{bmatrix} Y^*_{12} & Y^*_{13} \end{bmatrix}$, $C = \begin{bmatrix} Y^*_{21} \\ Y^*_{31} \end{bmatrix}$ and $D = \begin{bmatrix} Y^*_{22}+Y_{acn} & Y^*_{23} \\ Y^*_{32} & Y^*_{33}+Y_{dc} \end{bmatrix}$

The negative sequence impedance of the converter can be described similarly as,

$$Zc_{acn} = [A - BD^{-1}C - Y_{acn}]^{-1} \tag{H.2}$$

but this time, $A = [Y^*_{22} + Y_{acn}]$, $B = \begin{bmatrix} Y^*_{21} & Y^*_{23} \end{bmatrix}$, $C = \begin{bmatrix} Y^*_{12} \\ Y^*_{32} \end{bmatrix}$ and $D = \begin{bmatrix} Y^*_{11}+Y_{acp} & Y^*_{13} \\ Y^*_{31} & Y^*_{33}+Y_{dc} \end{bmatrix}$

and the dc side impedance as,

$$Zc_{dc} = [D - CA^{-1}B - Y_{dc}]^{-1} \tag{H.3}$$

where, $A = \begin{bmatrix} Y^*_{11}+Y_{acp} & Y^*_{12} \\ Y^*_{21} & Y^*_{22}+Y_{acn} \end{bmatrix}$, $B = \begin{bmatrix} Y^*_{13} \\ Y^*_{23} \end{bmatrix}$, $C = \begin{bmatrix} Y^*_{31} & Y^*_{32} \end{bmatrix}$ and $D = [Y^*_{33} + Y_{dc}]$

These matrix equations solve for the impedance around the converter and include all frequency cross-coupling associated in the transfers as well as the associated converter control action if required. SIV can be included or excluded in the individual transfers as required, showing its

contribution on the converter impedance. The following section describes the analytic derivation of the 3-port impedances around the converter.

H.2 ANALYTIC SOLUTION USING 3-PORT TRANSFERS

If only the 3-port frequencies are required or needed then the impedance transfers can be written in analytic form straight from Larsen's equation and the associated ac and dc system equations.

$$\begin{bmatrix} \Delta I_{acp}^{k+1} \\ \Delta I_{acn}^{k-1} \\ \Delta V_{dc}^{k} \\ 0 \end{bmatrix} = \begin{bmatrix} a & b & c & d \\ e & f & g & h \\ i & j & k & l \\ m & n & o & 1 \end{bmatrix} \begin{bmatrix} \Delta V_{acp}^{k+1} \\ \Delta V_{acn}^{k-1} \\ \Delta I_{dc}^{k} \\ \Delta \alpha^{k} \end{bmatrix} \tag{H.4}$$

$$\Delta V_{dc}^{k} = -\Delta I_{dc}^{k} Z_{dc}^{k} \tag{H.5}$$

$$\Delta V_{acp}^{k+1} = -\Delta I_{acp}^{k+1} Z_{acp}^{k+1} \tag{H.6}$$

$$\Delta V_{acn}^{k-1} = -\Delta I_{acn}^{k-1} Z_{acn}^{k-1} \tag{H.7}$$

The inputs to Larsen's equation are ΔV_{acp}^{k+1} and ΔV_{acn}^{k-1}, the positive and negative sequence applied voltage distortions, and ΔI_{dc}^{k} and $\Delta \alpha^{k}$ the DC current and firing angle distortions. The outputs are the resulting ac side currents ΔI_{acp}^{k+1} and ΔI_{acn}^{k-1} and dc side voltage, ΔV_{dc}^{k}. The transfers $a \rightarrow l$ are the linearised 3-port transfers given in appendix K while transfers m,n and o represent the effect of feedback through the firing angle control system. In order to model the converter in positive pole rectifier and inverter configurations the sign of a number of the transfers must be changed, as described in appendix G. Note the symbol k is used to represent both a transfer and the dc side frequency divided by the fundamental frequency on the converter, ie, $k = f_{dc}^{k}/f_{base}$.

For the positive sequence admittance looking into the converter, Larsen's equation H.4 and the systems equations H.5 to H.7 are solved giving,

$$Yc_{acp}^{k+1} = A_p + \frac{B_p C_p}{Z_{dc} - D_p} \tag{H.8}$$

where, $A_p = a - \frac{ebZ_{acn}^{k-1}}{1+fZ_{acn}^{k-1}}$, $B_p = c - \frac{gbZ_{acn}^{k-1}}{1+fZ_{acn}^{k-1}}$, $C_p = i - \frac{jeZ_{acn}^{k-1}}{1+fZ_{acn}^{k-1}}$ and $D_p = k - \frac{jgZ_{acn}^{k-1}}{1+fZ_{acn}^{k-1}}$. Likewise, the negative sequence admittance looking into the converter can be written as,

$$Yc_{acn} = A_n + \frac{B_n C_n}{Z_{dc} - D_n} \tag{H.9}$$

where, $A_n = f - \frac{ebZ_{acp}^{k+1}}{1+aZ_{acp}^{k+1}}$, $B_n = g - \frac{ecZ_{acp}^{k+1}}{1+aZ_{acp}^{k+1}}$, $C_n = j - \frac{ibZ_{acp}}{1+aZ_{acp}}$ and $D_n = k - \frac{icZ_{acp}^{k+1}}{1+aZ_{acp}^{k+1}}$, and the dc side impedance written as,

$$Zc_{dc}^{k} = \frac{A_{dc} + B_{dc}}{1 - C_{dc}} - k \tag{H.10}$$

where, $A_{dc} = i\left[\frac{cZ_{acp}^{k+1}}{1+aZ_{acp}^{k+1}} - \frac{bgZ_{acp}^{k+1}Z_{acn}^{k-1}}{(1+aZ_{acp}^{k+1})(1+fZ_{acn}^{k-1})}\right]$, $B_{dc} = j\left[\frac{gZ_{acn}^{k-1}}{1+fZ_{acn}^{k-1}} - \frac{ecZ_{acp}^{k+1}Z_{acn}^{k-1}}{(1+aZ_{acp}^{k+1})(1+fZ_{acn}^{k-1})}\right]$, $C_{dc} = \frac{beZ_{acp}^{k+1}Z_{acn}^{k-1}}{(1+aZ_{acp}^{k+1})(1+fZ_{acn}^{k-1})}$.

These equations show the small signal impedance around the HVDC converter. Though they calculate only the main 3-port frequencies they are useful for gaining insight into likely problems and the used in chapter 8 to help identify worst-case operating conditions for harmonic and interharmonic cross-modulation.

H.3 CIGRE RECTIFIER IMPEDANCE

This section uses the above equations to show the effective 3-port impedance for both positive, negative and dc side impedances around the CIGRE rectifier. Figure H.1 shows the comparison between the impedances calculated using the full matrix reduction and 3-port solution techniques described in sections H.1 and H.2 respectively. The operating point is that of the standard CIGRE benchmark model described in appendix D. Figure H.2 shows the effect of including the standard PI control transfer function and figure H.3 shows the effect of the SIV on the 3-port impedances of the rectifier.

H.4 CIGRE INVERTER IMPEDANCE

This section uses the above equations to show the effective 3-port impedance for both positive, negative and dc side impedances around the CIGRE inverter at the operating point described in appendix D. Similar to the rectifier, figure H.4 shows the comparison between the impedances calculated using the full matrix reduction and 3-port solution techniques described in sections H.1 and H.2 respectively. Figure H.5 shows the effect of the SIV on the 3-port impedances around the inverter.

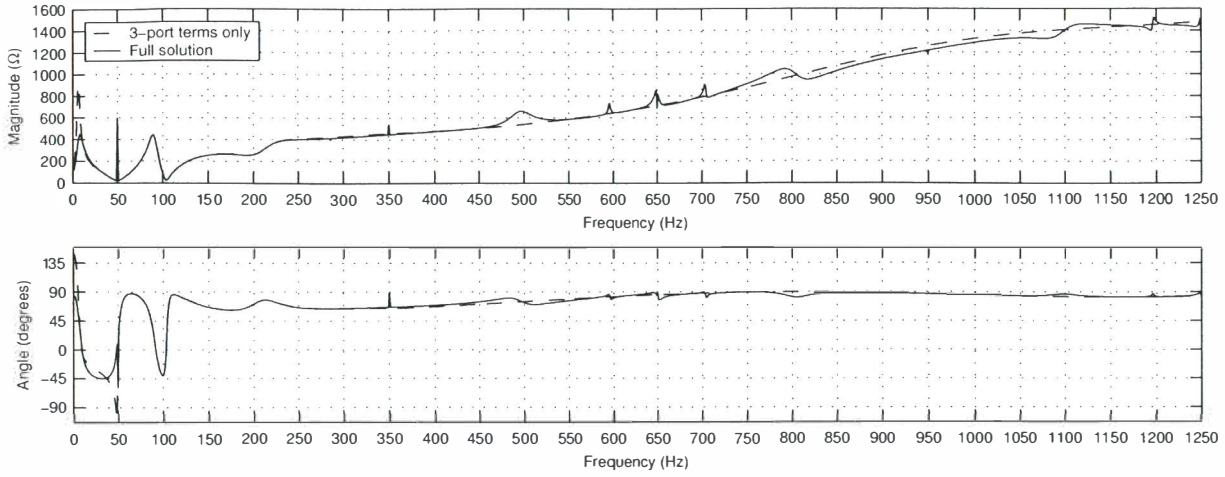

(a) CIGRE rectifier positive sequence impedance.

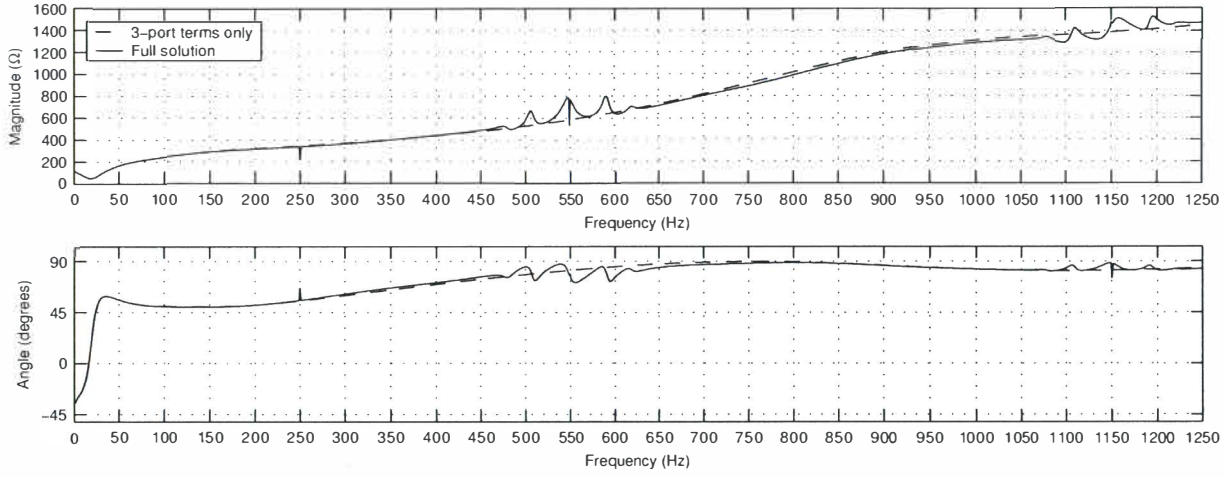

(b) CIGRE rectifier negative sequence impedance.

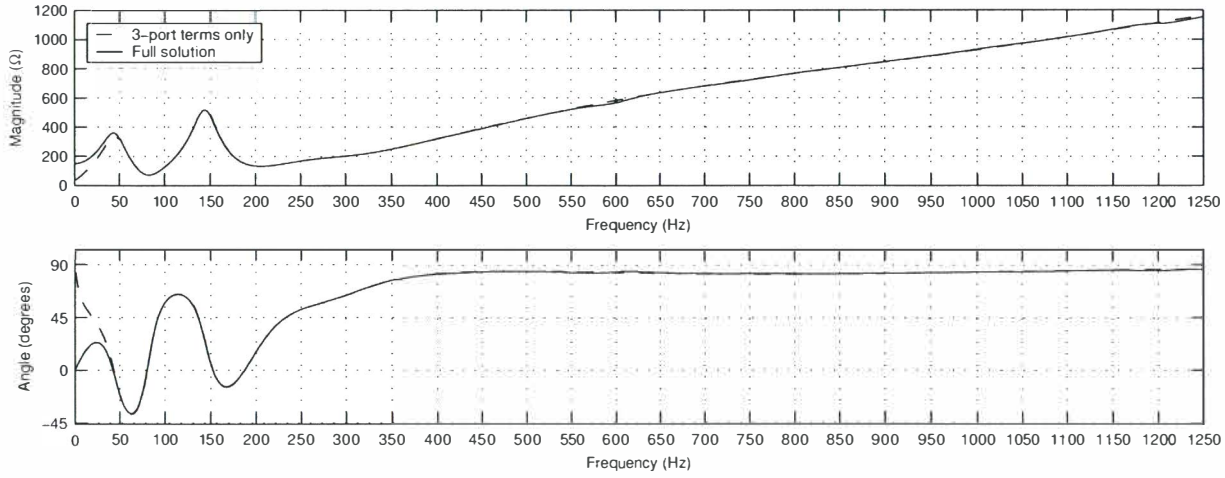

(c) CIGRE rectifier dc side impedance.

Figure H.1 Comparison solution techniques for the impedances around the CIGRE rectifier.

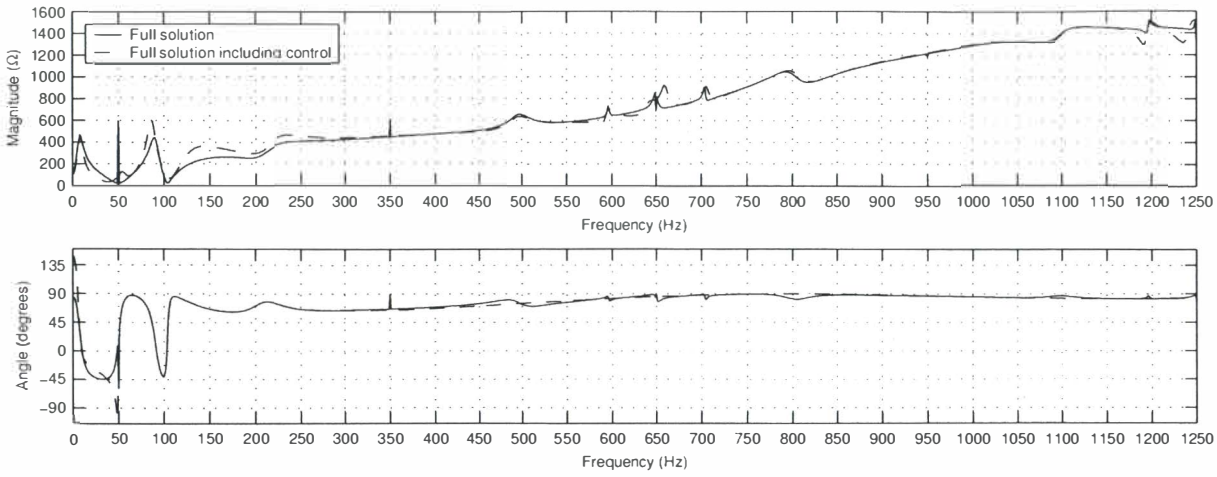

(a) CIGRE rectifier positive sequence impedance.

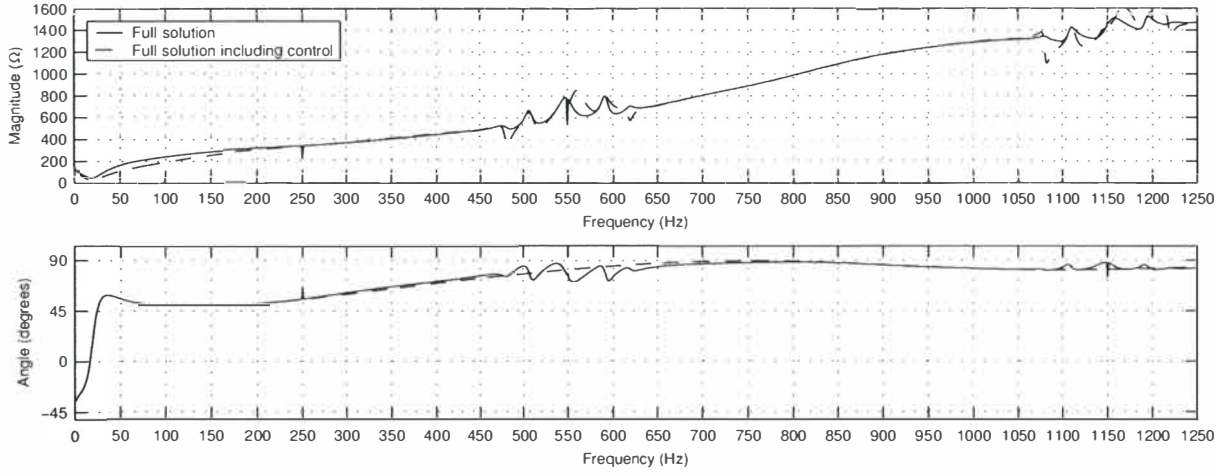

(b) CIGRE rectifier negative sequence impedance.

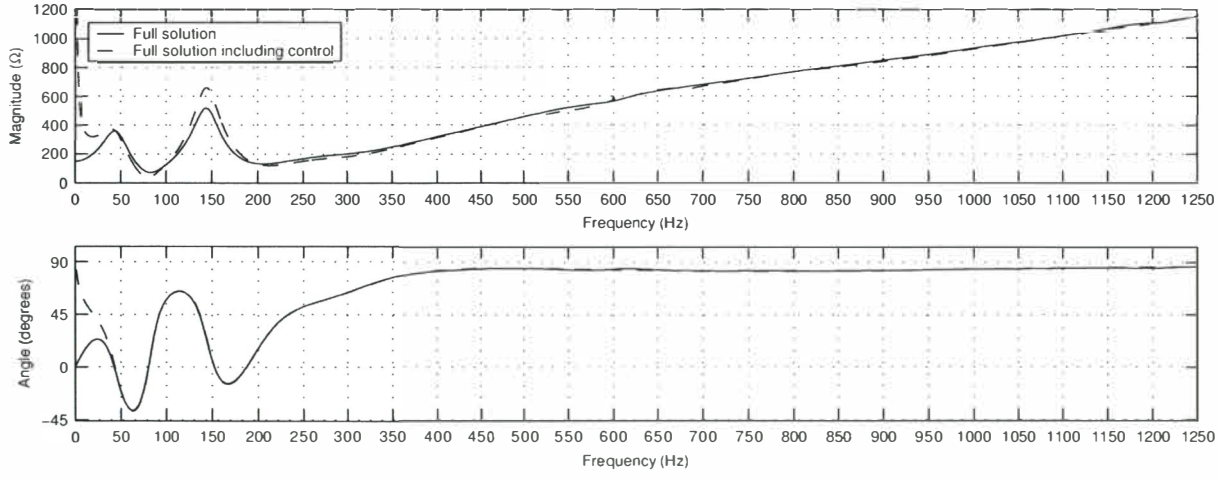

(c) CIGRE rectifier dc side impedance.

Figure H.2 Effect of firing angle control on 3-port impedance around the CIGRE rectifier.

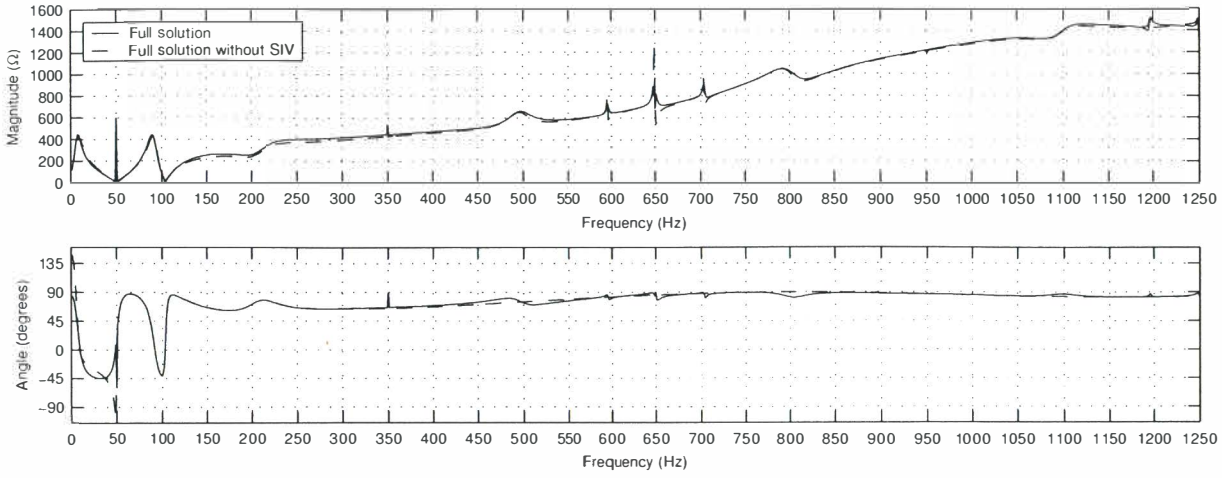

(a) CIGRE rectifier positive sequence impedance.

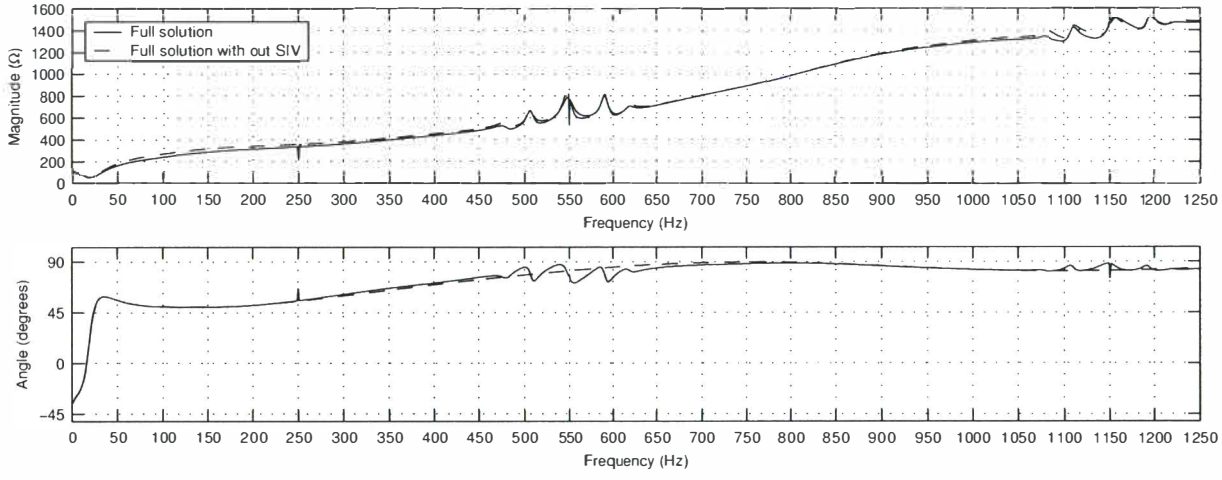

(b) CIGRE rectifier negative sequence impedance.

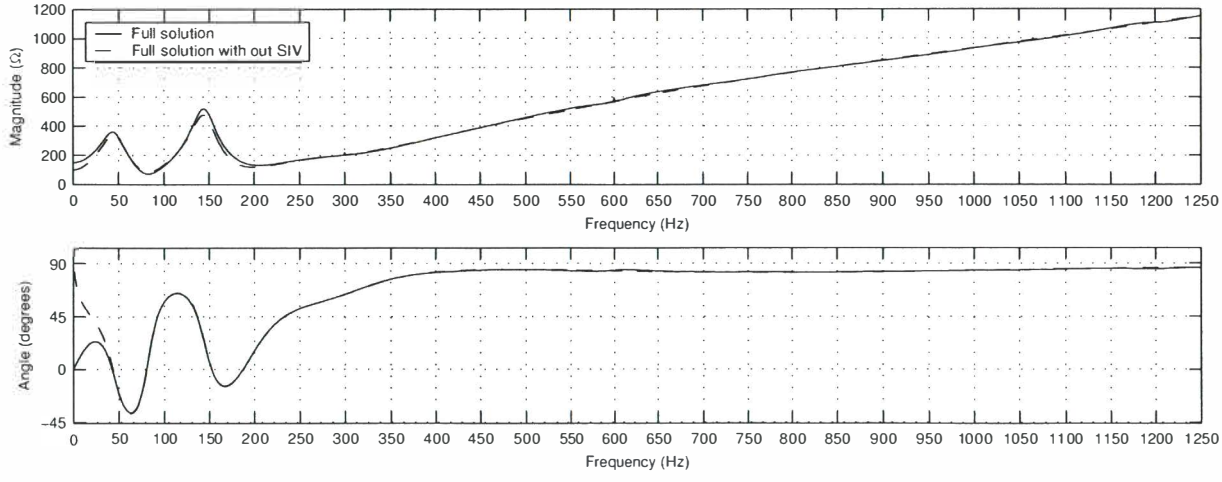

(c) CIGRE rectifier dc side impedance.

Figure H.3 Effect of SIV on 3-port impedance around the CIGRE rectifier.

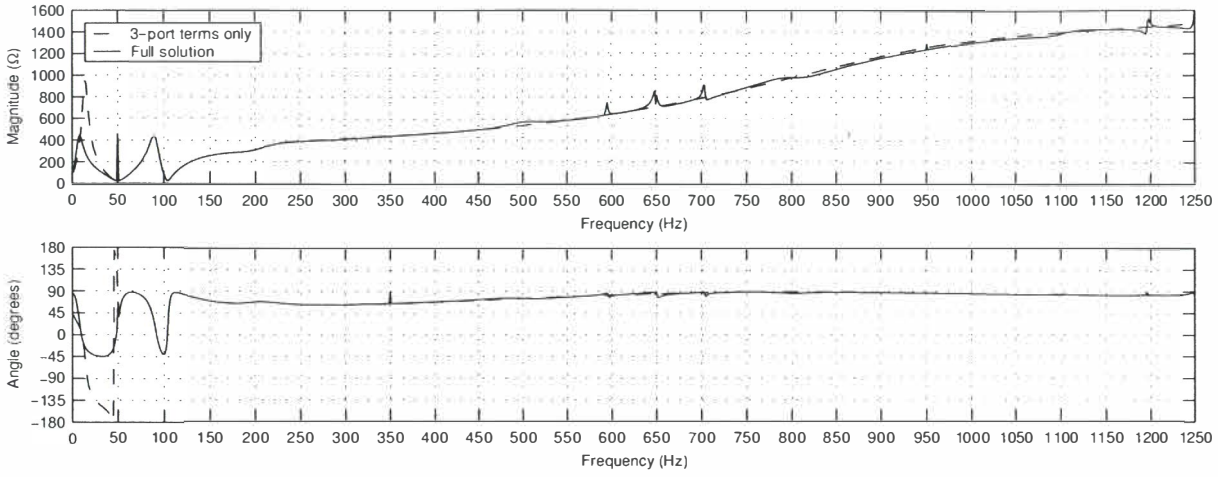

(a) CIGRE inverter positive sequence impedance.

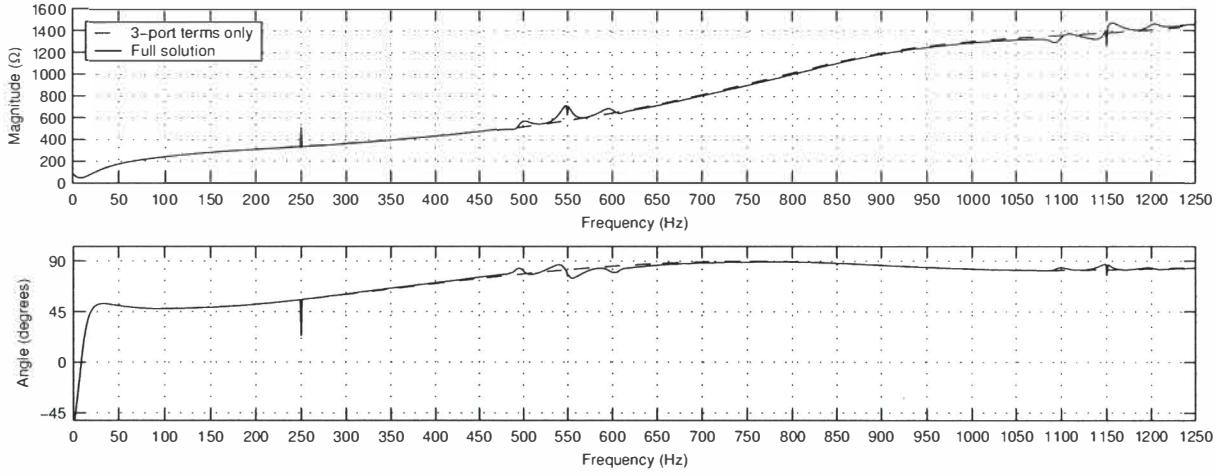

(b) CIGRE inverter negative sequence impedance.

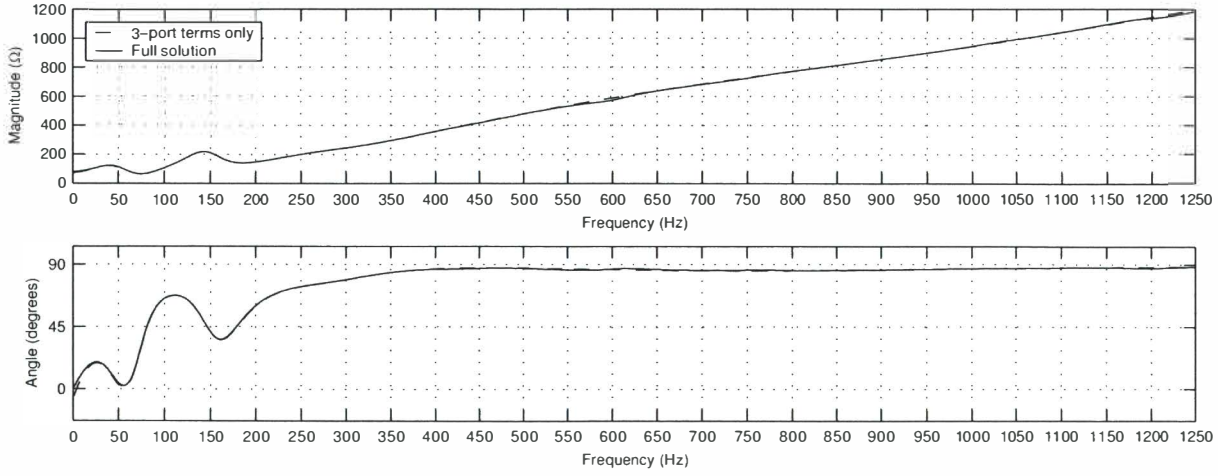

(c) CIGRE inverter dc side impedance.

Figure H.4 Comparison solution techniques for the impedances around the CIGRE inverter.

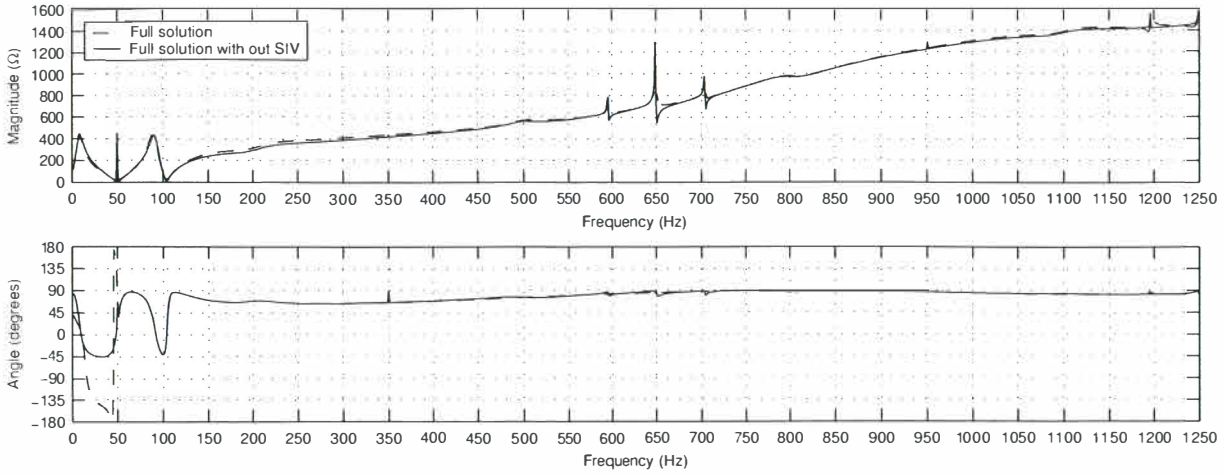

(a) CIGRE inverter positive sequence impedance.

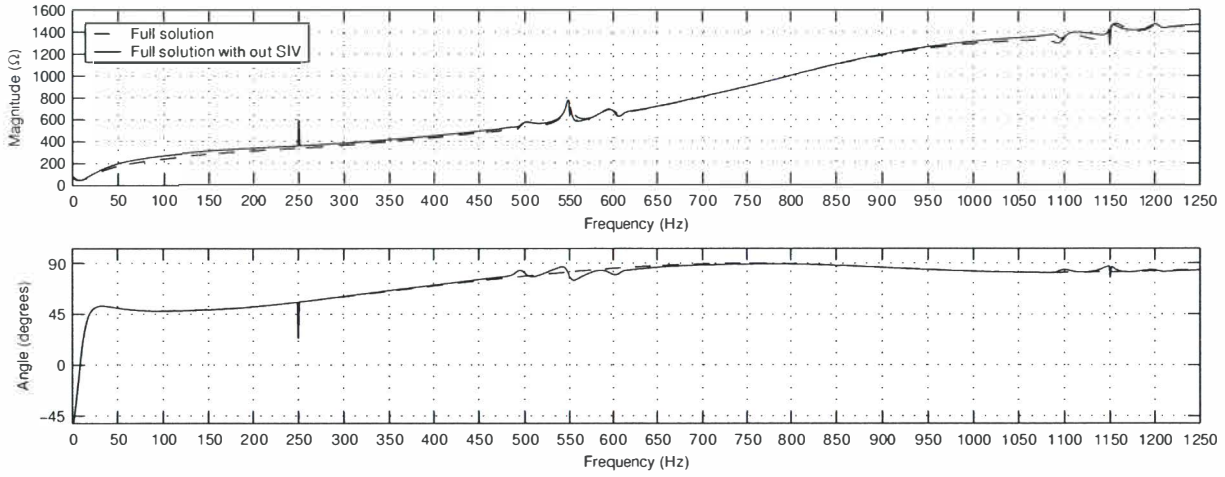

(b) CIGRE inverter negative sequence impedance.

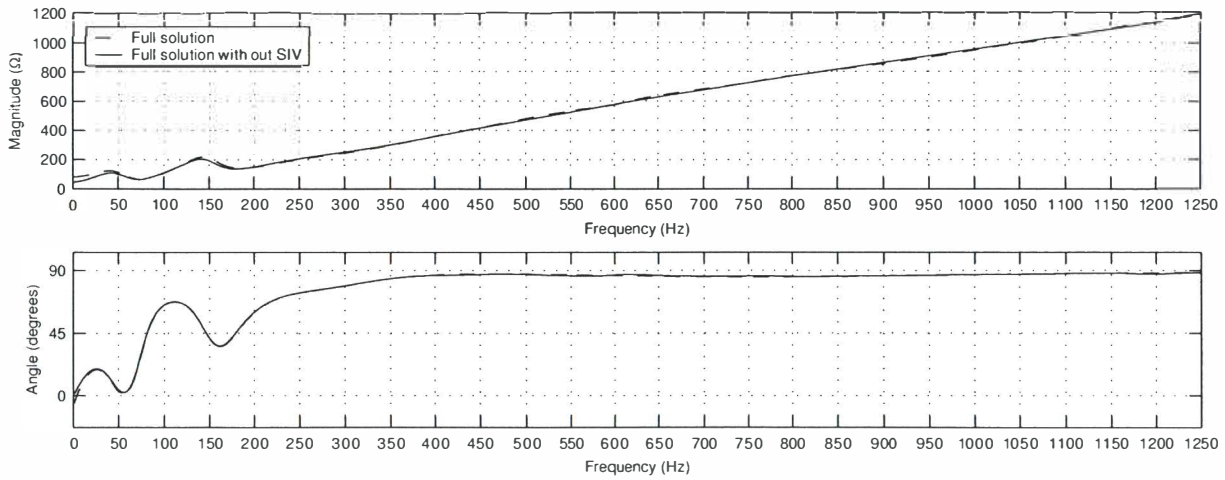

(c) CIGRE inverter dc side impedance.

Figure H.5 Effect of SIV on 3-port impedance around the CIGRE inverter.

Appendix I

INTERHARMONIC RESULTS AROUND BACK-TO-BACK HVDC LINKS

I.1 THE 50-60HZ BACK-TO-BACK LINK WITH UNBALANCE AT THE RECTIFIER

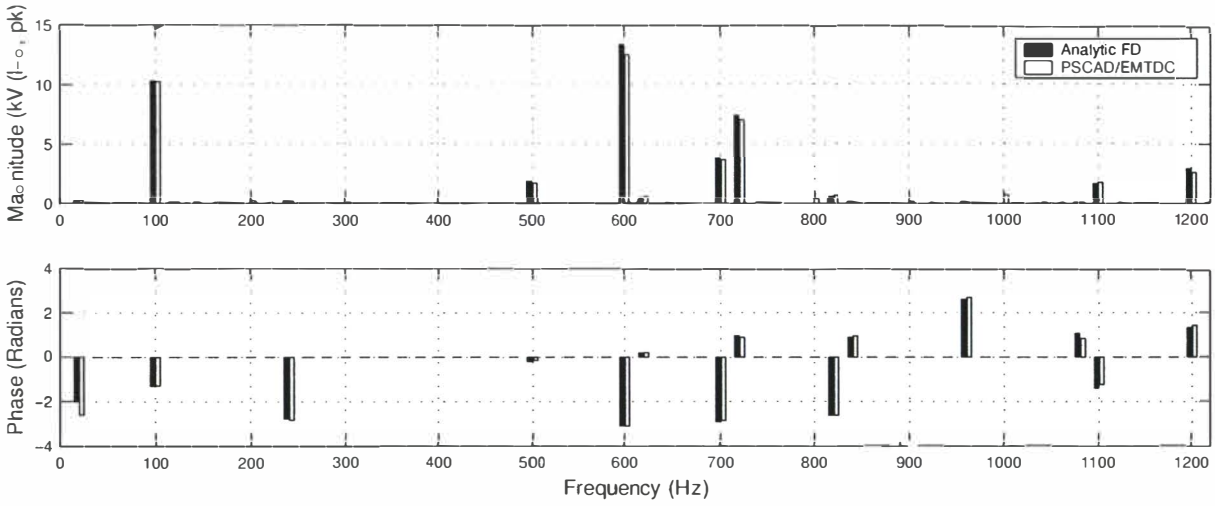

Figure I.1 Resulting DC side voltage spectrum on 50-60Hz link with a 0.024pu unbalance on the rectifier terminals.

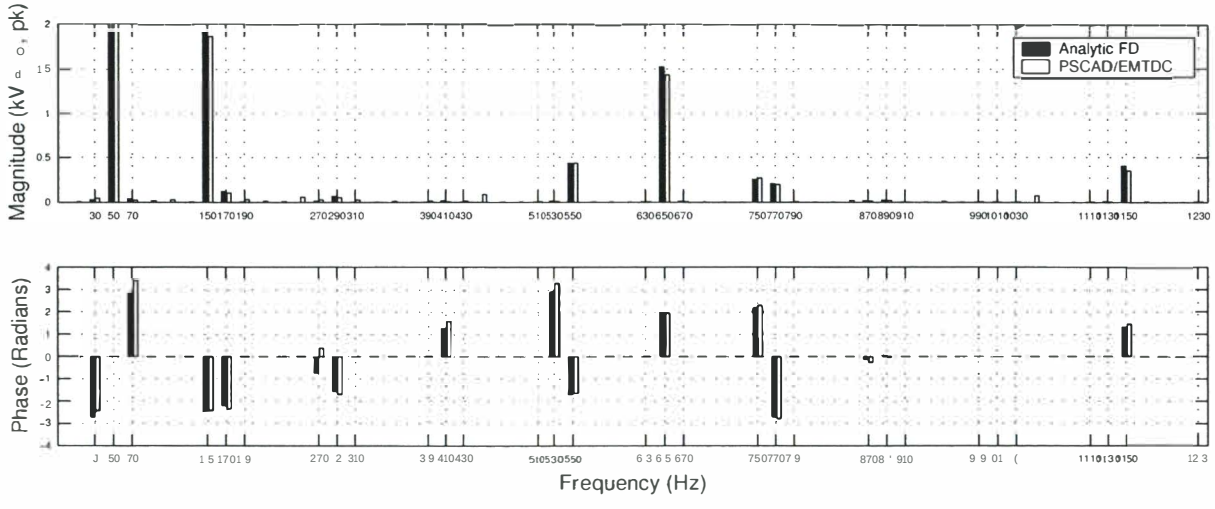

Figure I.2 Resulting positive sequence spectrum on rectifier terminals with a 0.024pu unbalance on rectifier terminals.

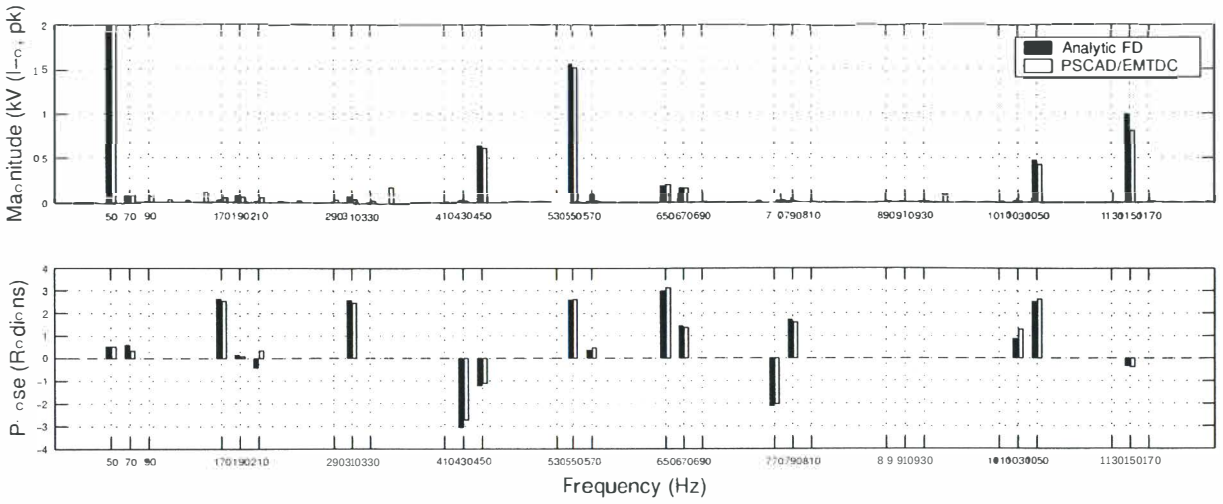

Figure I.3 Resulting negative sequence spectrum on rectifier terminals with a 0.024pu unbalance on rectifier terminals.

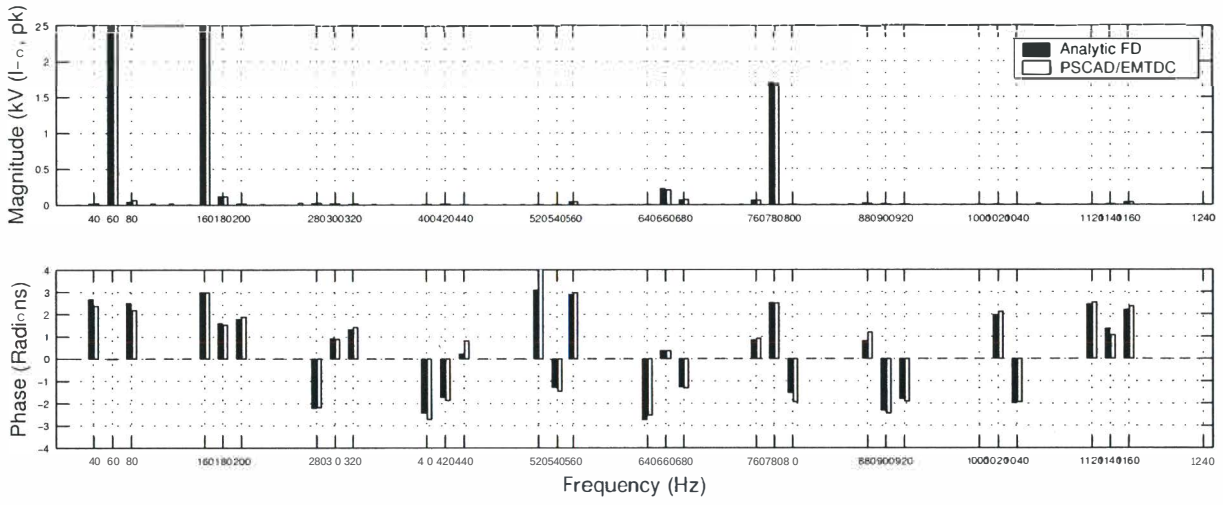

Figure I.4 Resulting positive sequence spectrum on inverter terminals with a 0.024pu unbalance on rectifier terminals.

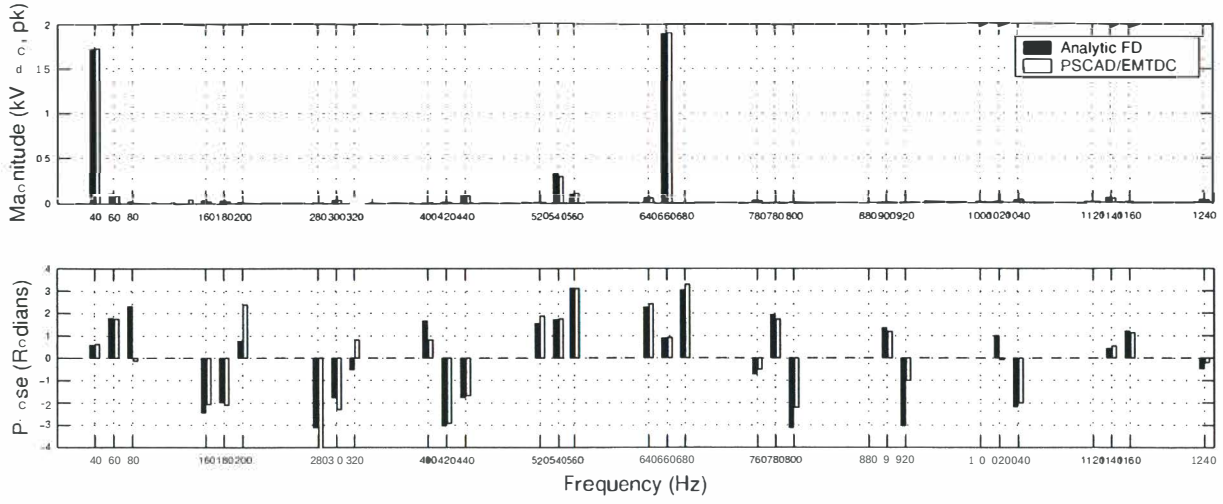

Figure I.5 Resulting negative sequence spectrum on inverter terminals with a 0.024pu unbalance on rectifier terminals.

I.2 THE 50-60HZ BACK-TO-BACK LINK WITH UNBALANCE AT THE INVERTER

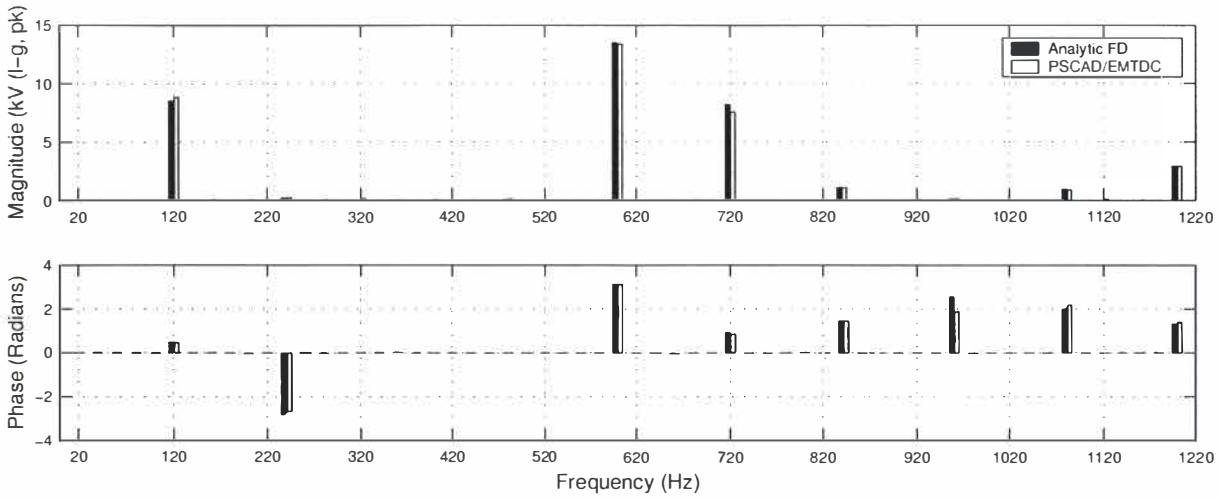

Figure I.6 Resulting DC side voltage spectrum on 50-60Hz link with a 0.017pu unbalance on the inverter terminals.

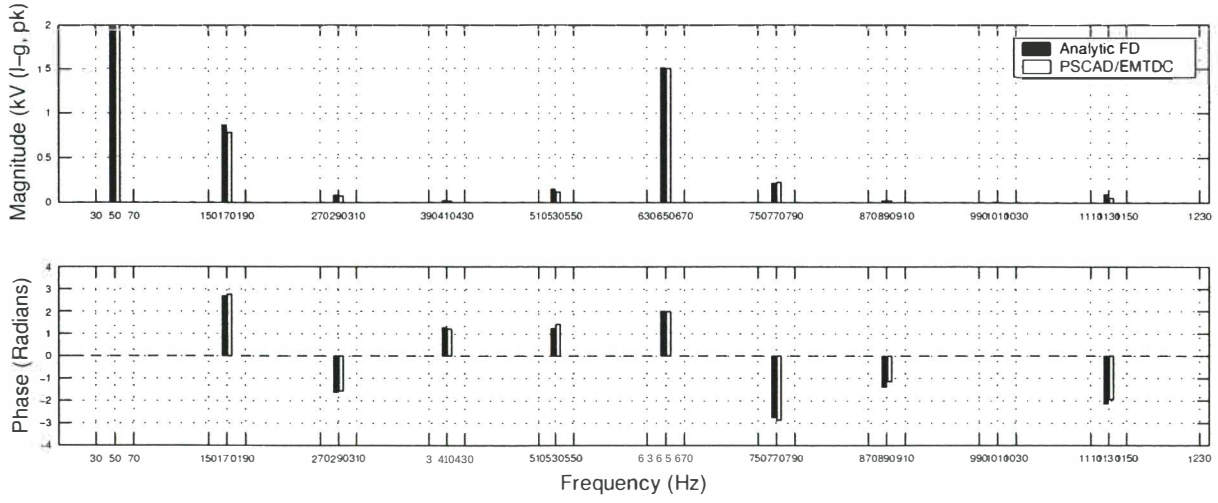

Figure I.7 Resulting positive sequence spectrum on rectifier terminals with a 0.017pu unbalance on inverter terminals.

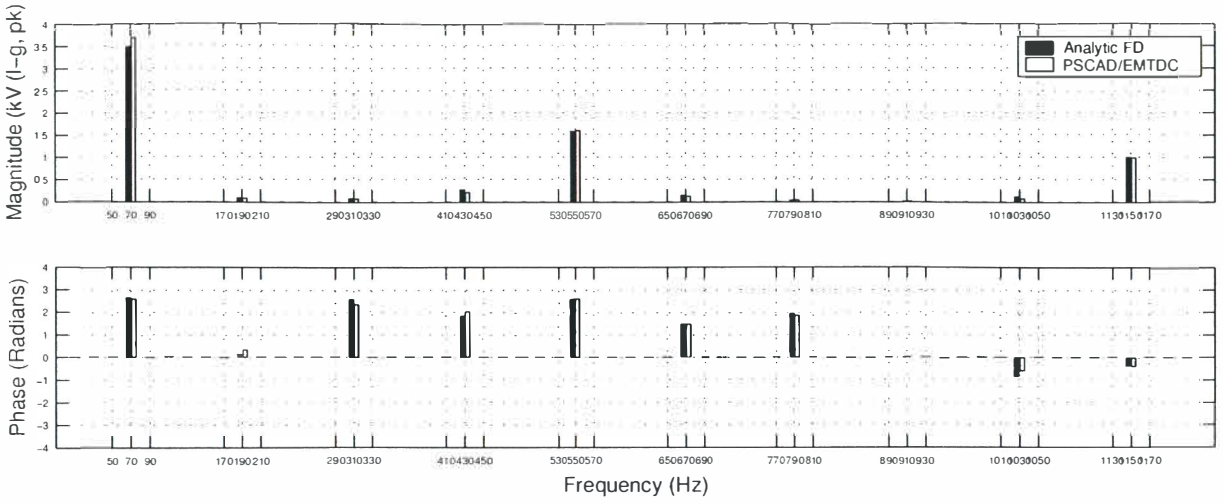

Figure I.8 Resulting negative sequence spectrum on rectifier terminals with a 0.017pu unbalance on inverter terminals.

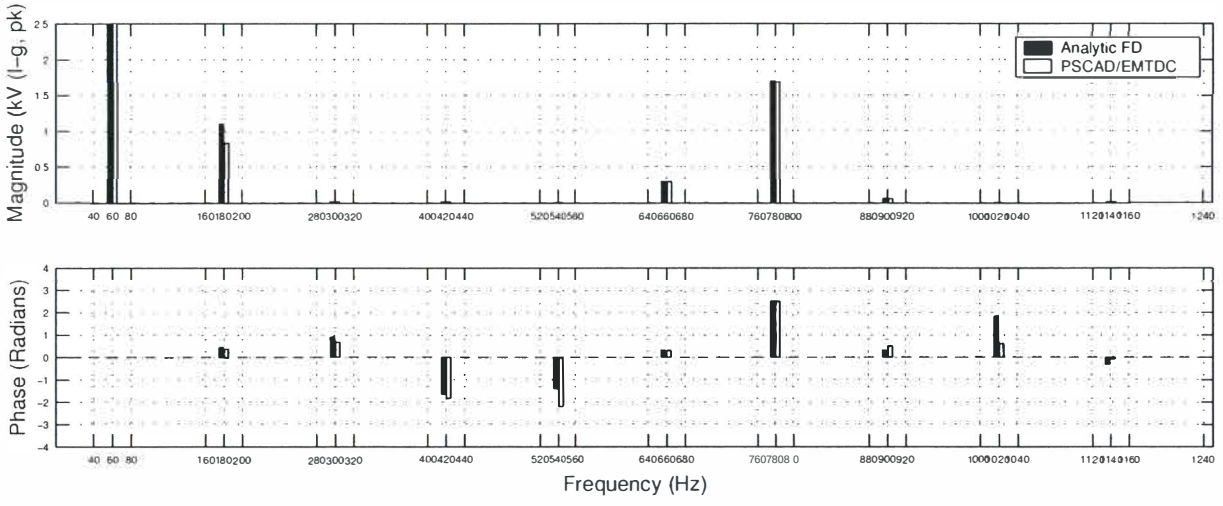

Figure I.9 Resulting positive sequence spectrum on inverter terminals with a 0.017pu unbalance on inverter terminals.

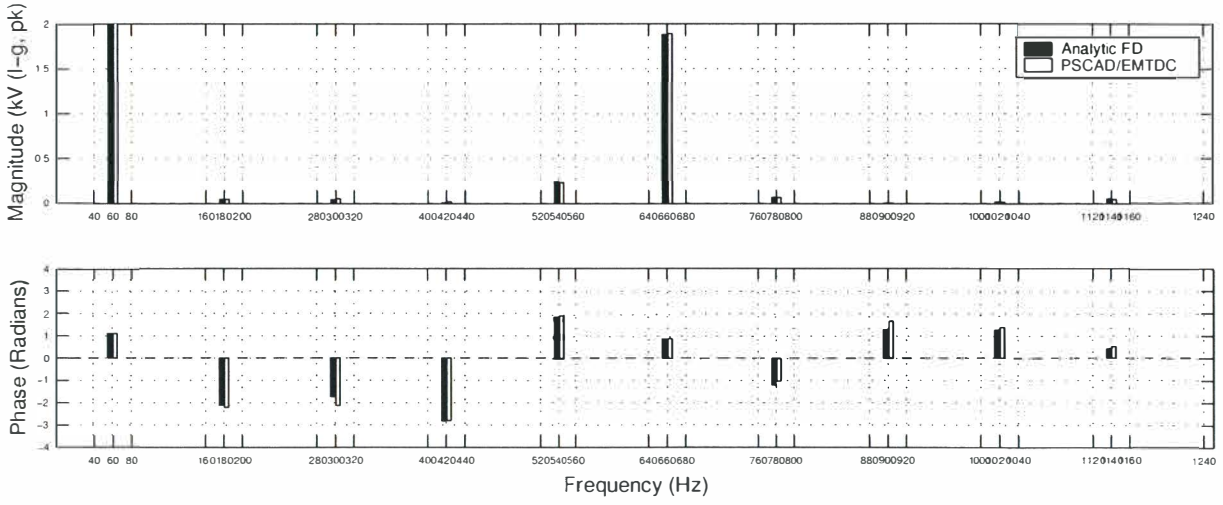

Figure I.10 Resulting negative sequence spectrum on inverter terminals with a 0.017pu unbalance on inverter terminals.

I.3 THE 50-51HZ BACK-TO-BACK LINK WITH UNBALANCE AT THE RECTIFIER

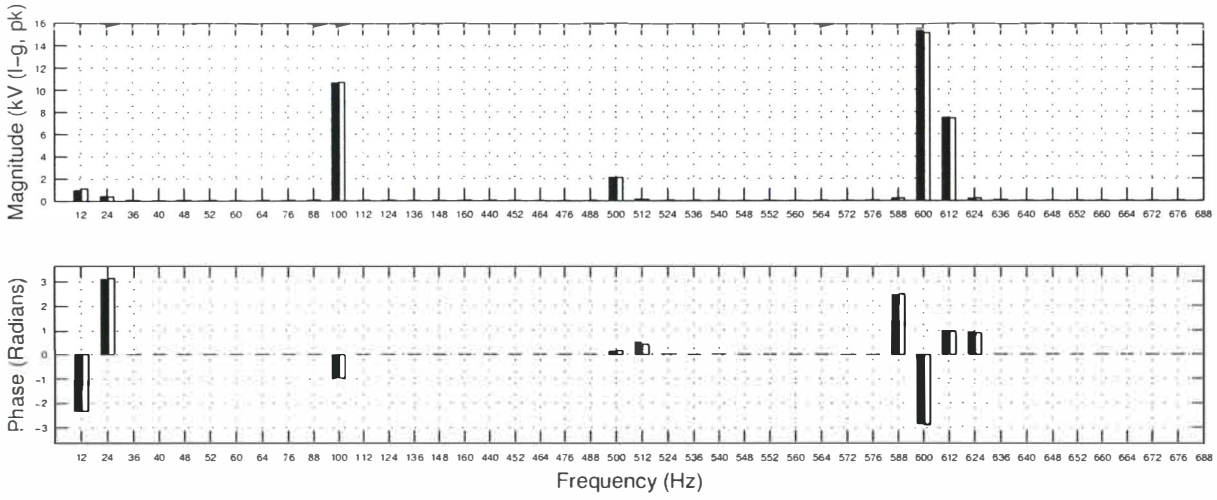

Figure I.11 DC side comparison for 50-51Hz back-to-back HVDC link with 0.018pu voltage unbalance on the rectifier terminals. *Black*–Frequency Domain, *White*–Time Domain.

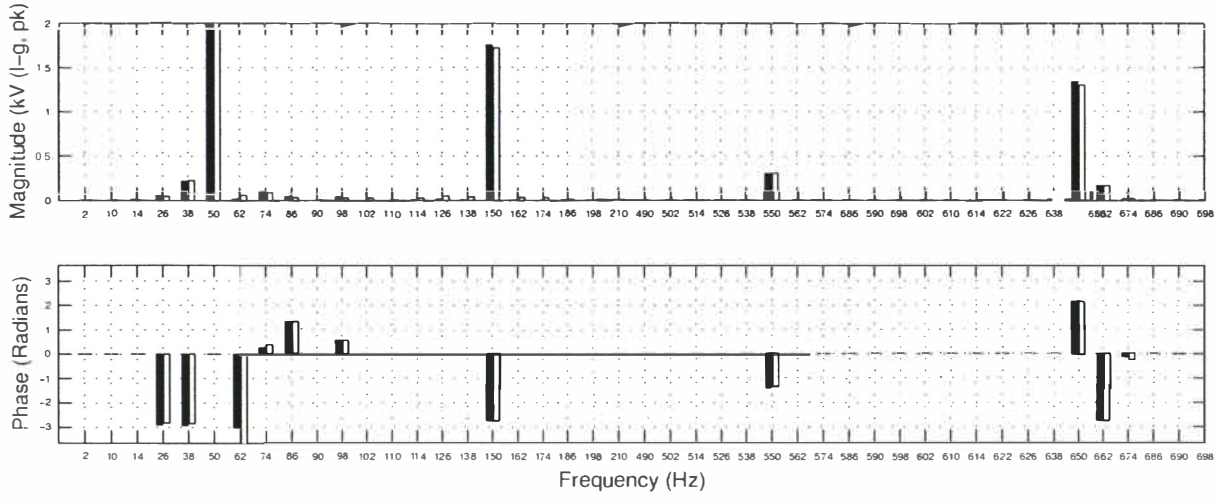

Figure I.12 Rectifier side positive sequence voltage comparison for 50-51Hz back-to-back HVDC link with 0.018pu voltage unbalance on rectifier terminals. *Black*–Frequency Domain, *White*–Time Domain.

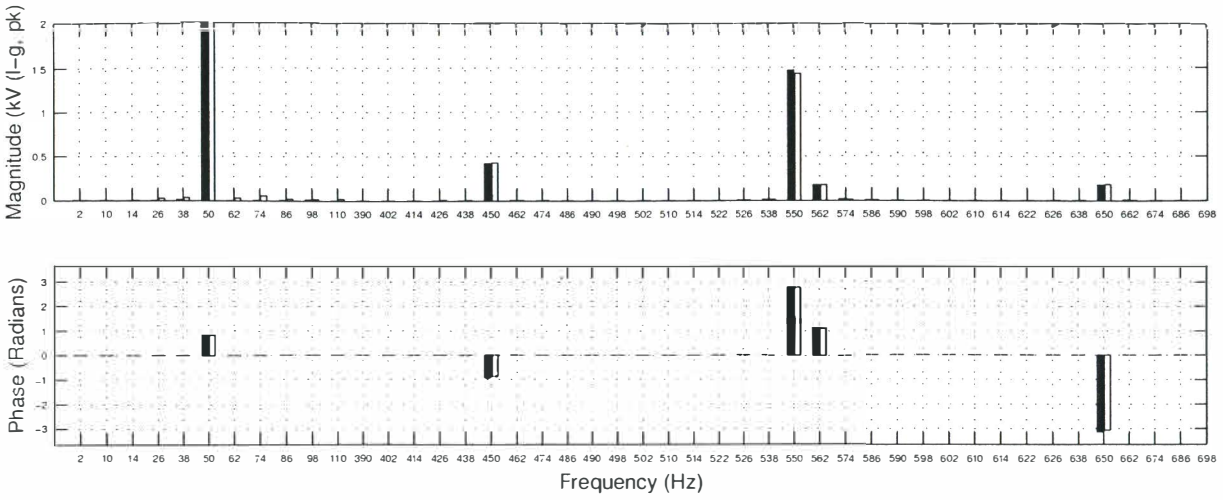

Figure I.13 Rectifier side negative sequence voltage comparison for 50-51Hz back-to-back HVDC link with 0.018pu voltage unbalance on rectifier terminals. *Black*–Frequency Domain, *White*–Time Domain.

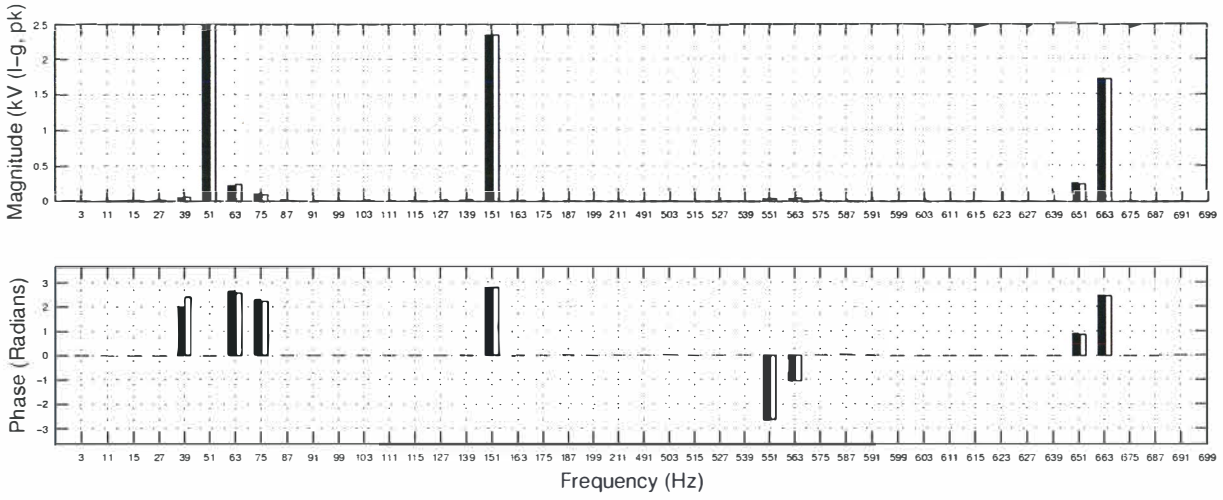

Figure I.14 Inverter side positive sequence voltage comparison for 50-51Hz back-to-back HVDC link with 0.018pu voltage unbalance on rectifier terminals. *Black*–Frequency Domain, *White*–Time Domain.

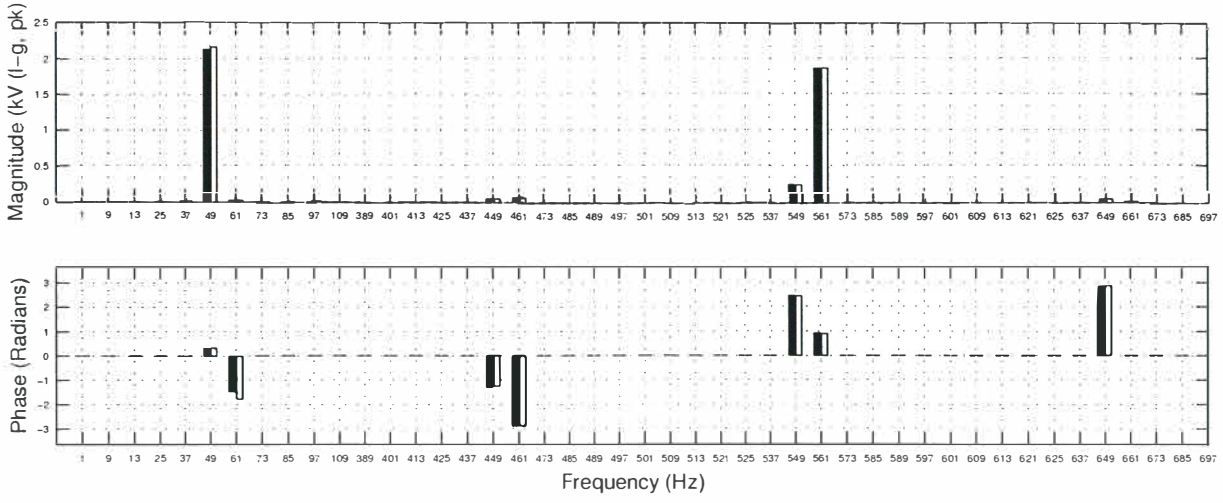

Figure I.15 Inverter side negative sequence voltage comparison for 50-51Hz back-to-back HVDC link with 0.018pu voltage unbalance on rectifier terminals. *Black*–Frequency Domain, *White*–Time Domain.

I.4 THE 50-51HZ BACK-TO-BACK LINK WITH UNBALANCE AT THE INVERTER

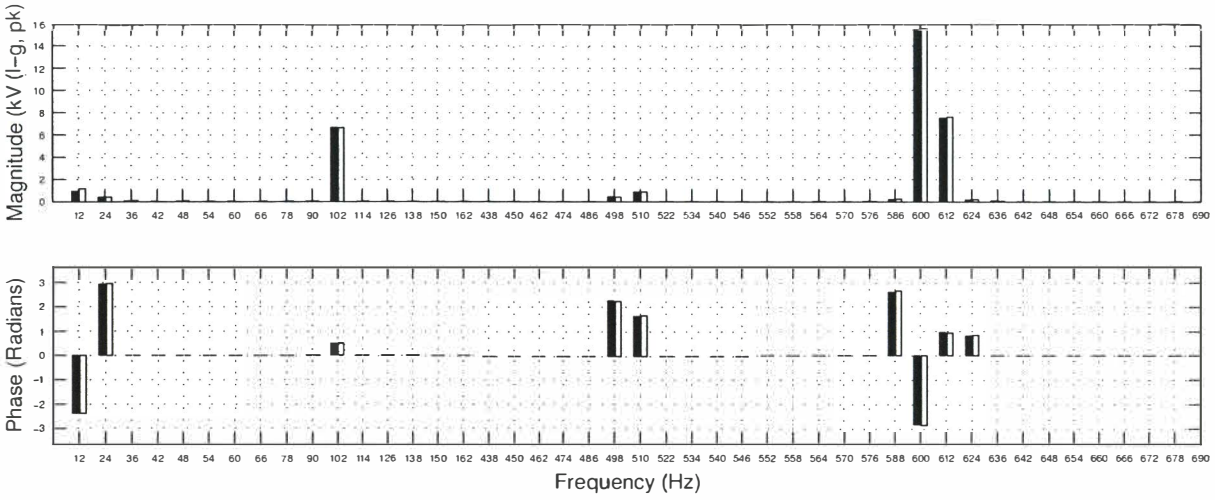

Figure I.16 DC side comparison for 50-51Hz back-to-back HVDC link with 0.015pu voltage unbalance on inverter terminals. *Black*–Frequency Domain, *White*–Time Domain.

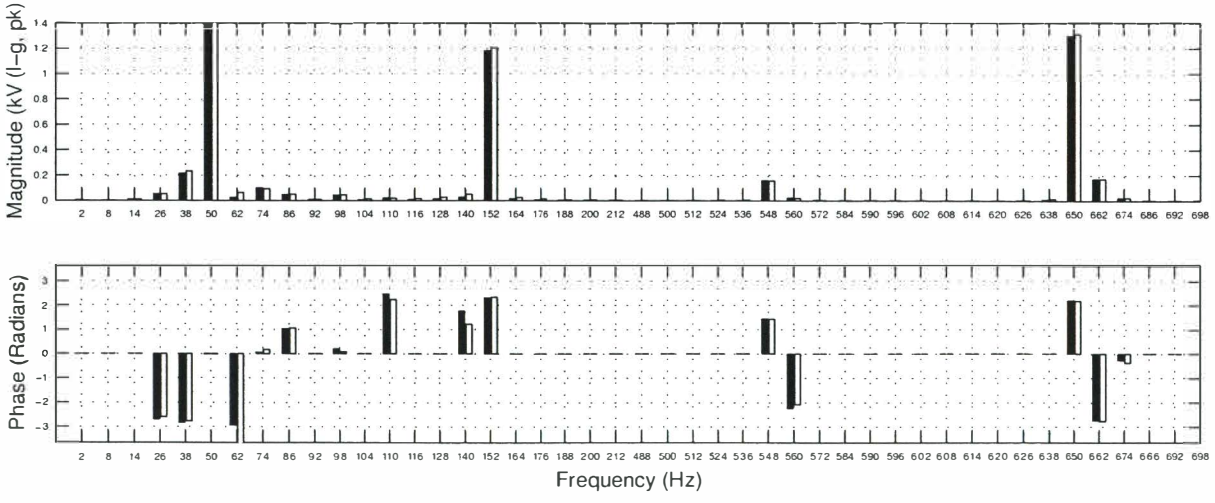

Figure I.17 Rectifier side positive sequence voltage comparison for 50-51Hz back-to-back HVDC link with 0.015pu voltage unbalance on inverter terminals. *Black*–Frequency Domain, *White*–Time Domain.

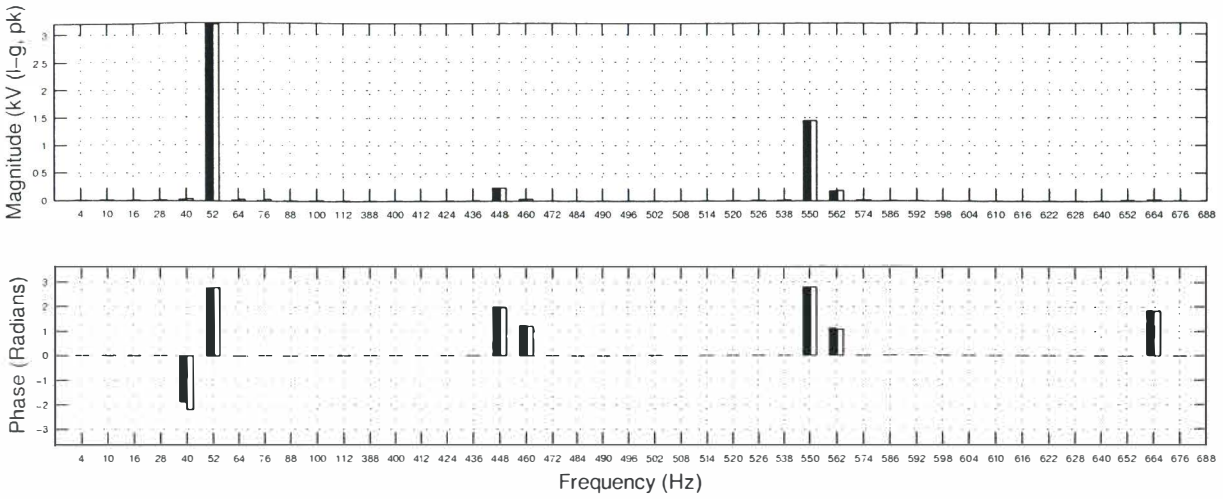

Figure I.18 Rectifier side negative sequence voltage comparison for 50-51Hz back-to-back HVDC link with 0.015pu voltage unbalance on inverter terminals. *Black*–Frequency Domain, *White*–Time Domain.

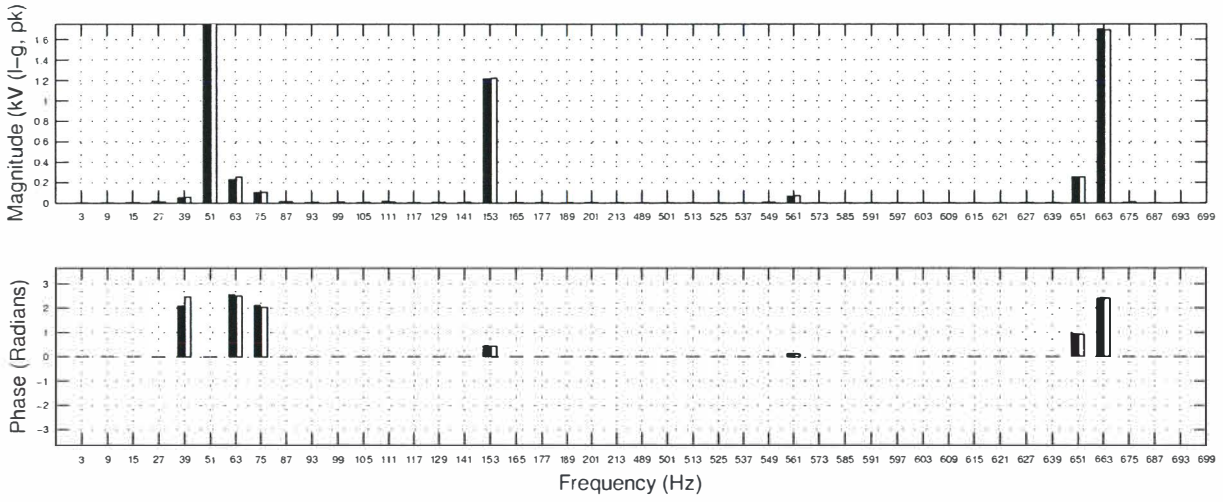

Figure I.19 Inverter side positive sequence voltage comparison for 50-51Hz back-to-back HVDC link with 0.015pu voltage unbalance on inverter terminals. *Black*–Frequency Domain, *White*–Time Domain.

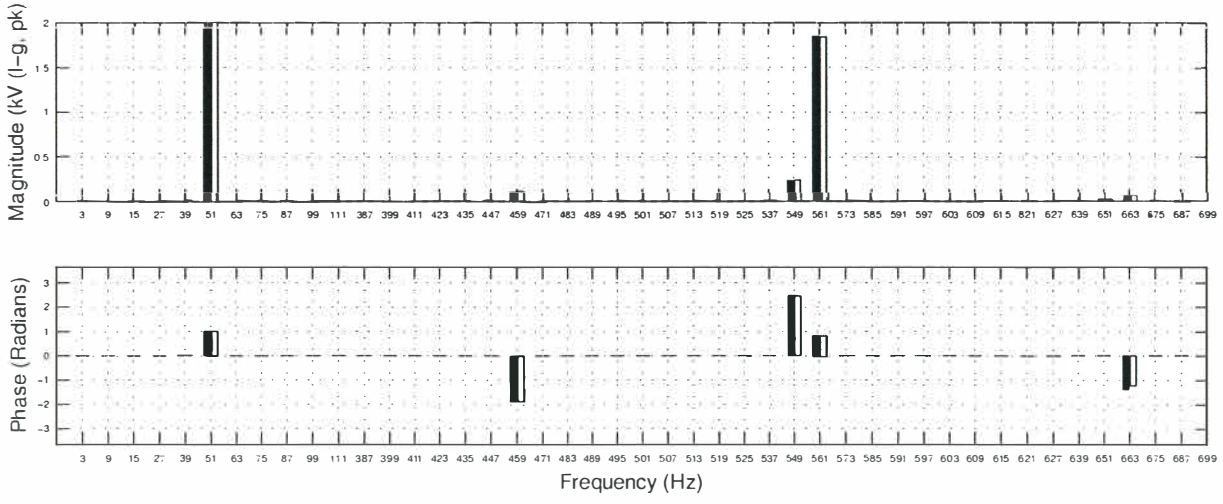

Figure I.20 Inverter side negative sequence voltage comparison for 50-51Hz back-to-back HVDC link with 0.015pu voltage unbalance on inverter terminals. *Black*–Frequency Domain, *White*–Time Domain.

Appendix J

ASYNCHRONOUS LINK DC SIDE TRANSFERS

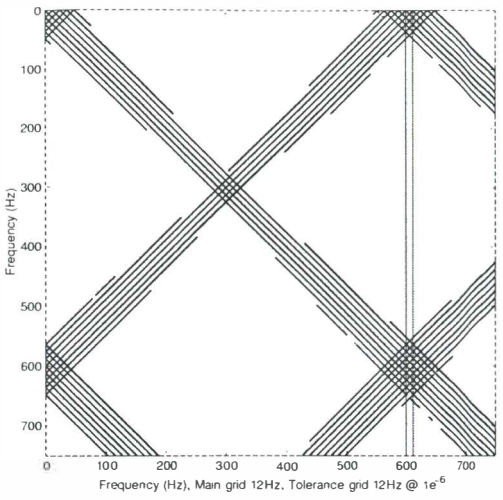

(a) 50 - 51Hz HVDC link.

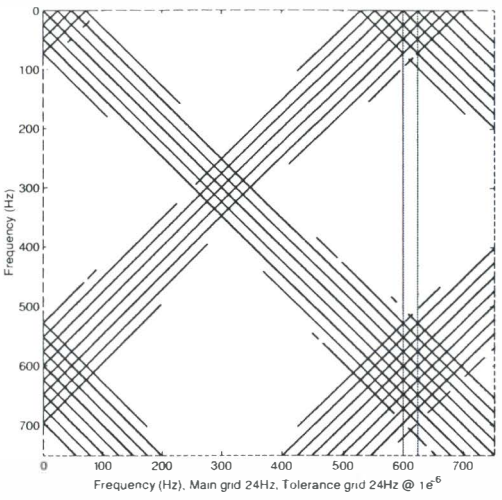

(b) 50 - 52Hz HVDC link.

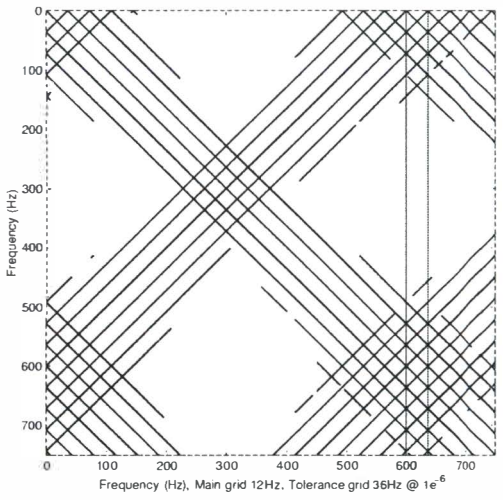

(c) 50 - 53Hz HVDC link.

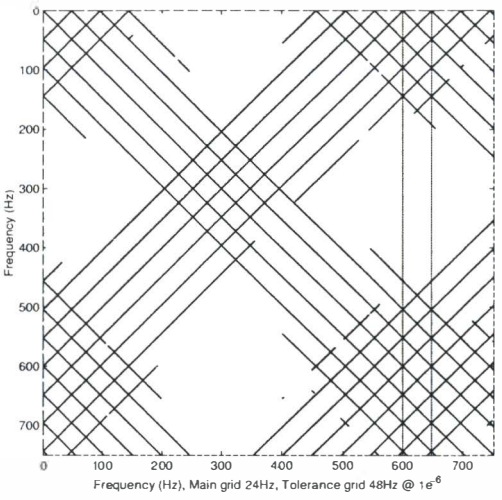

(d) 50 - 54Hz HVDC link.

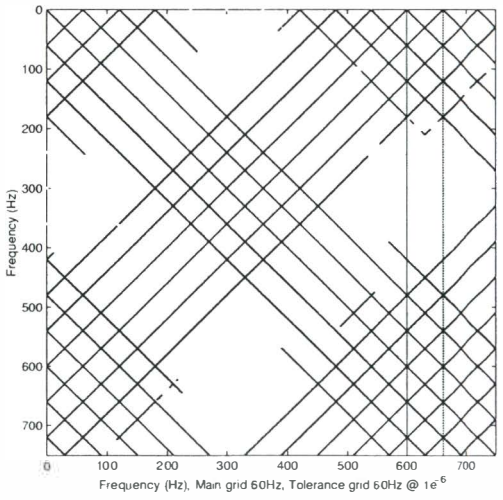

(e) 50 - 55Hz HVDC link.

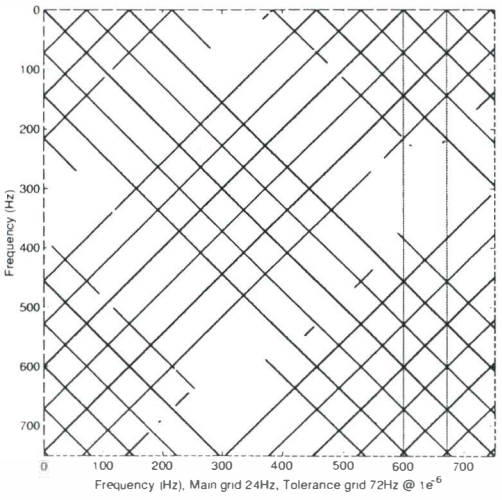

(f) 50 - 56Hz HVDC link.

Figure J.1 Reduced DC side admittance transfers for asynchronous links. Shown are the reduced grid pattern (light grey), and tolerance reduced grid pattern (black) which indicate the required frequency transfers for both a full and partial linearised solution.

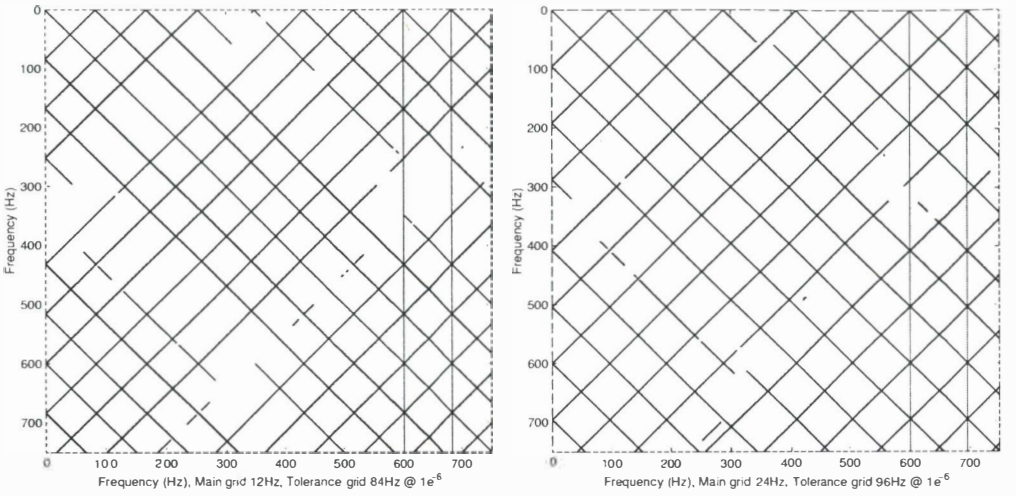

(a) 50 - 57Hz HVDC link.

(b) 50 - 58Hz HVDC link.

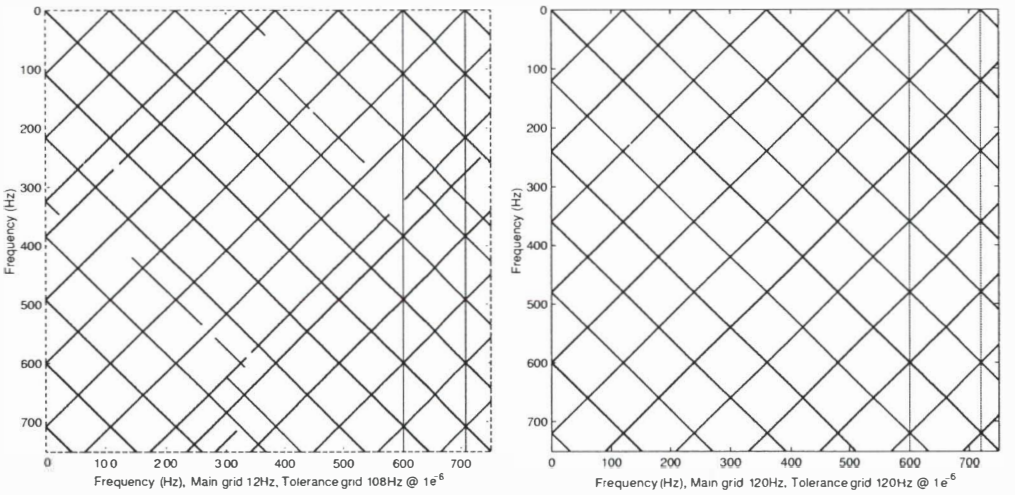

(c) 50 - 59Hz HVDC link.

(d) 50 - 60Hz HVDC link.

Figure J.2 Reduced DC side admittance transfers for asynchronous links. Shown are the reduced grid pattern (light grey), and tolerance reduced grid pattern (black) which indicate the required frequency transfers for both a full and partial linearised solution.

Appendix K

THE 3-PORT FREQUENCY TRANSFERS

This appendix analytically describes the *time-invariant* 3-port frequency cross-coupling transfers associated with the HVDC converter. Larsen [34] recognised the modulating relationships between the different phase sequences and described the 3-port method for the specific case of negative sequence unbalance. However, the 3-port transfers extend over the frequency range of interest and can be described as the main diagonal terms in the frequency cross-coupling matrices described in appendix F. Only 3 frequencies are ever considered in the modulation process of the converter, these being at frequency $k\omega_o$ on the dc side and frequencies $(k-1)\omega_o$ in negative sequence and $(k+1)\omega_o$ in positive sequence on the ac side. These are the frequencies in the first row of table 3.1. All other frequency cross modulation is ignored under the assumption that the 3-port transfers remain the dominant frequency cross-coupling transfers. Larsen's equation is given below in equation K.1 and equations K.3 to K.14 analytically describe the direct parts of the 3-port transfers.

$$\begin{bmatrix} \Delta I_{acp}^{k+1} \\ \Delta I_{acn}^{k-1} \\ \Delta V_{dc}^{k} \\ 0 \end{bmatrix} = \begin{bmatrix} a & b & c & d \\ e & f & g & h \\ i & j & k & l \\ m & n & o & 1 \end{bmatrix} \begin{bmatrix} \Delta V_{acp}^{k+1} \\ \Delta V_{acn}^{k-1} \\ \Delta I_{dc}^{k} \\ \Delta \alpha^{k} \end{bmatrix} \tag{K.1}$$

The inputs to Larsen's equation are ΔV_{acp}^{k+1} and ΔV_{acn}^{k-1}, the positive and negative sequence applied voltage distortions, and ΔI_{dc}^{k} and $\Delta \alpha^{k}$ the DC current and firing angle distortions. The outputs are the resulting ac side currents ΔI_{acp}^{k+1} and ΔI_{acn}^{k-1} and dc side voltage, ΔV_{dc}^{k}. The transfers $a \rightarrow l$ are the linearised 3-port transfers given in the appendix while transfers m,n and o represent the effect of feedback through the firing angle control system. In order to model the converter in positive pole rectifier and inverter configurations the sign of a number of the transfers must be changed, as described in appendix G. Note the symbol k is used to represent both a transfer and the dc side frequency divided by the fundamental frequency on the converter, ie, $k = f_{dc}^{k}/f_{base}$.

Figure K.1 shows the sparse matrix structure of the 3-port transfers. The 'direct' parts of the 3-port analytic transfers are derived using the full *time-variant* small signal transfers described in chapter 5 and are given below.

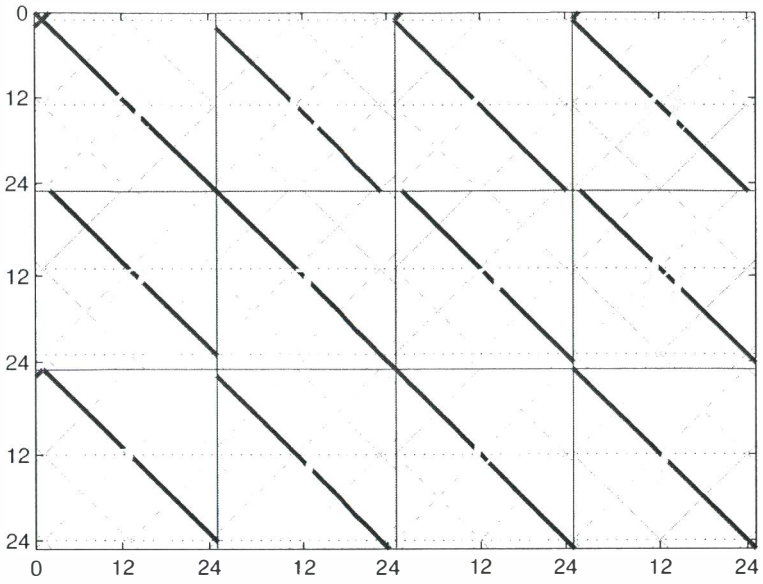

Figure K.1 Sparse structure of equation K.1 showing the '3-port' transfers in bold.

K.1 THE DIRECT '3-PORT' TRANSFERS

The 3-port model of the 6-pulse HVDC converter is described by the transfers

$$a = -j\frac{3\mu_o}{2\pi X(k+1)}\left[1 - sinc((k+1)\mu_o/2\pi)\,\underline{/-(k+1)\mu_o/2}\right] \quad \text{(K.2)}$$

$$f = -j\frac{3\mu_o}{2\pi X(k-1)}\left[1 - sinc((k-1)\mu_o/2\pi)\,\underline{/-(k-1)\mu_o/2}\right] \quad \text{(K.3)}$$

$$b = -j\frac{3}{2\pi X(k-1)}\underline{/-2(\alpha_o-\phi)}\left[sin(\mu_o)\underline{/-\mu_o} - \mu_o sinc((k+1)\mu_o/2\pi)\,\underline{/-(k+1)\mu_o/2}\right] \quad \text{(K.4)}$$

$$e = -j\frac{3}{2\pi X(k+1)}\underline{/+2(\alpha_o-\phi)}\left[sin(\mu_o)\underline{/+\mu_o} - \mu_o sinc((k-1)\mu_o/2\pi)\,\underline{/-(k-1)\mu_o/2}\right] \quad \text{(K.5)}$$

$$c = \underline{\frac{\sqrt{3}}{\pi}/-(\alpha_o-\phi)}\left[-j - sin(\mu_o/2)\underline{/-\mu_o/2}\ (\mu_o/2)sinc((k+1)\mu_o/2\pi)\,\underline{/-(k+1)\mu_o/2}\right] \quad \text{(K.6)}$$

$$g = \underline{\frac{\sqrt{3}}{\pi}/+(\alpha_o-\phi)}\left[+j - sin(\mu_o/2)\underline{/+\mu_o/2}\ (\mu_o/2)sinc((k-1)\mu_o/2\pi)\,\underline{/-(k-1)\mu_o/2}\right] \quad \text{(K.7)}$$

$$d = -\frac{3V_1\mu_o}{2\pi X}sin(\alpha_o)\underline{/-(\alpha_o-\phi)sinc((k+1)\mu_o/2\pi)\,/-(k+1)\mu_o/2} \quad \text{(K.8)}$$

$$h = -\frac{3V_1\mu_o}{2\pi X}sin(\alpha_o)\underline{/+(\alpha_o-\phi)inc((k-1)\mu_o/2\pi)\,/-(k-1)\mu_o/2} \quad \text{(K.9)}$$

$$i = \underline{\frac{3\sqrt{3}}{\pi}/+(\alpha_o-\phi)}\left[+j - sin(\mu_o/2)\underline{/+\mu_o/2}\ (\mu_o/2)\underline{/+\mu_o}sinc((k+1)\mu_o/2\pi)\,\underline{/-(k+1)\mu_o/2}\right] \quad \text{(K.10)}$$

$$j = \underline{\frac{3\sqrt{3}}{\pi}/-(\alpha_o-\phi)}\left[-j - sin(\mu_o/2)\underline{/-\mu_o/2}\ (\mu_o/2)\underline{/-\mu_o}sinc((k-1)\mu_o/2\pi)\,\underline{/-(k-1)\mu_o/2}\right] \quad \text{(K.11)}$$

$$k = -jkX(2 - 3\mu_o/2\pi) - (3X/\pi)cos(k\mu_o/2)\underline{/-k\mu_o/2} \quad \text{(K.12)}$$

$$l = -\frac{3\sqrt{3}V_1}{2\pi}sin(\alpha_o)\left[1 + \underline{/-k\mu_o}\right] \quad \text{(K.13)}$$

where the AC side variables are written in terms of their equivalent dc side frequencies. All ac side variables are referred to the valve side of the converter transformer. To model higher pulse converters it is necessary to scale the transfers in accordance with the series and parallel connections on the ac and dc sides. This means all transfers are scaled by the number of six pulse groups (n_g) and either the transformer ratio squared N^2 or just the transformer ratio N.

For the 12 pulse series connected converter the transfers a,b,e and f are scaled by N^2 transferred to the secondary side. The transfers c,g,d,h,i and j are transfers from *voltage* --› *voltage* and *current* --› *current* through the converter and are scaled by the transformer ratio N.

K.2 COMPARISON BETWEEN ANALYTIC AND TIME DOMAIN 3-PORT TRANSFERS

This section shows the comparisons made between the derived analytic model and the PSCAD/-EMTDC time domain simulation for the direct 3-port frequency transfers. The test system is the CIGRE rectifier and inverter with the operating conditions given in appendix D with strong (effectively no impedance) ac and dc system systems. The analytic model has been solved with all direct and conjugated frequency cross coupling transfers in place. The direct 3-port transfers have then been plotted and are identical to those described by the above equations except for the sharp spikes occurring where the direct and conjugated parts of the transfers are at the same frequency.

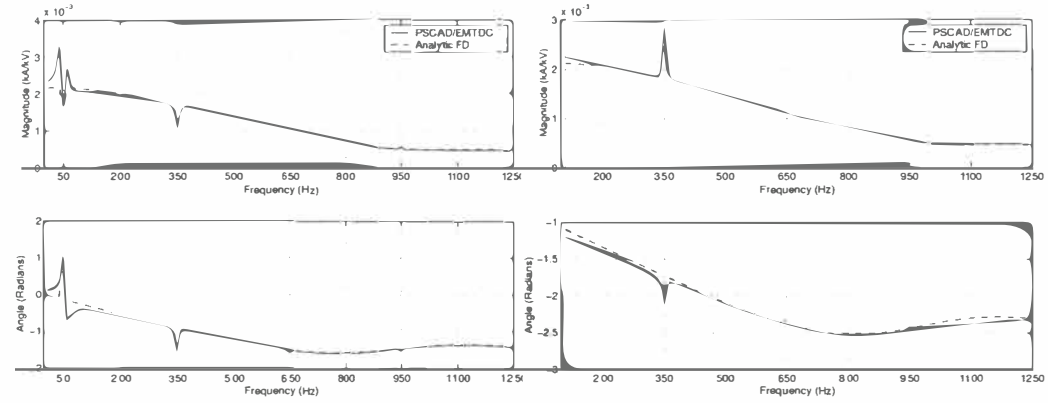

(a) a (b) b

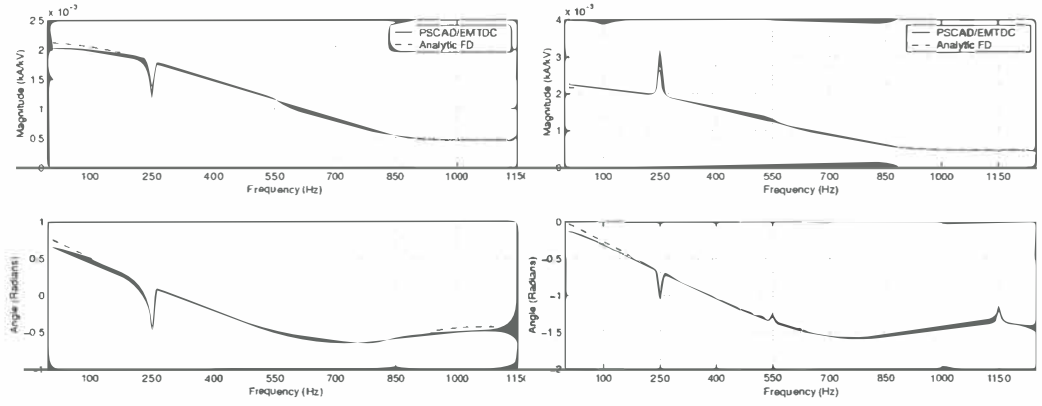

(c) e (d) f

Figure K.2 CIGRE rectifier $V_{ac} \rightarrow I_{ac}$ transfers.

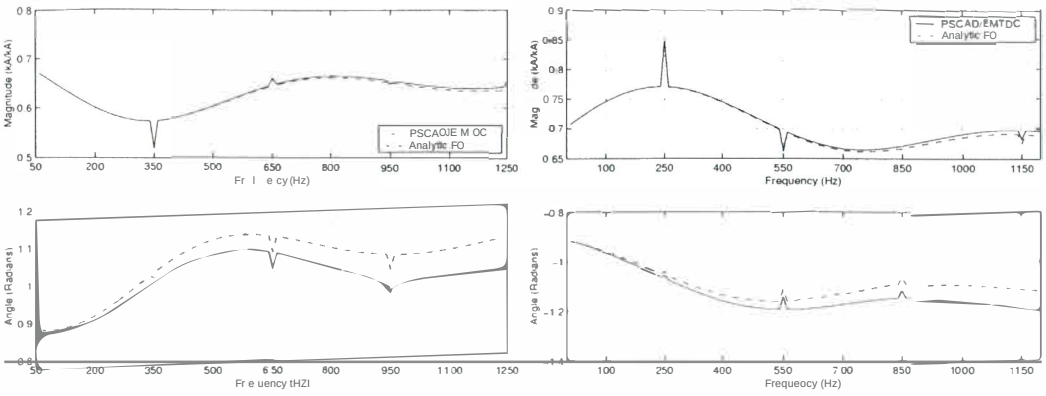

(a) c (b) g

Figure K.3 CIGRE rectifier $I_{dc} \dashrightarrow I_{ac}$ transfers.

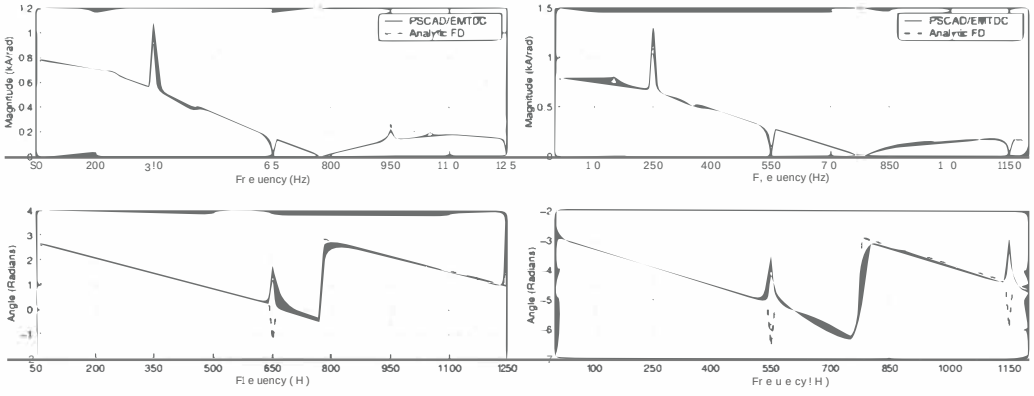

(a) d (b) h

Figure K.4 CIGRE rectifier $\alpha \dashrightarrow I_{ac}$ transfers.

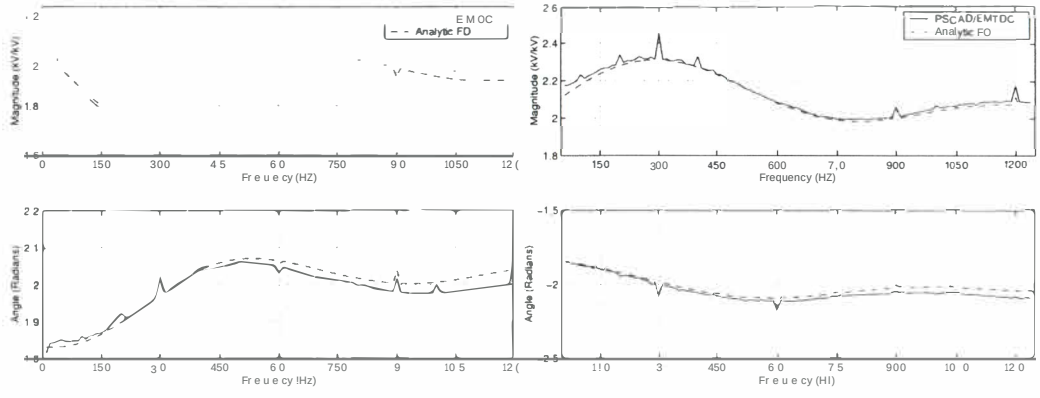

(a) i (b) j

Figure K.5 CIGRE rectifier $I_{ac} \dashrightarrow V_{dc}$ transfers.

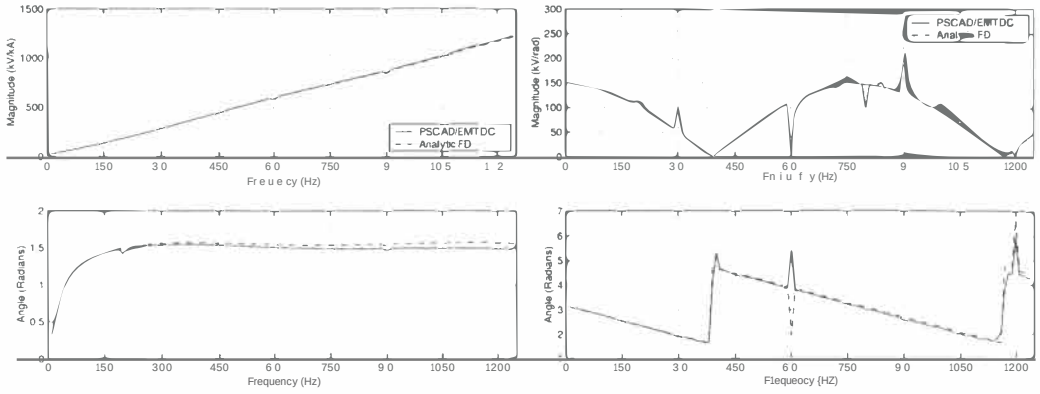

(a) k (b) l

Figure K.6 CIGRE rectifier $I_{dc}, \alpha \rightarrow V_{dc}$ transfers.

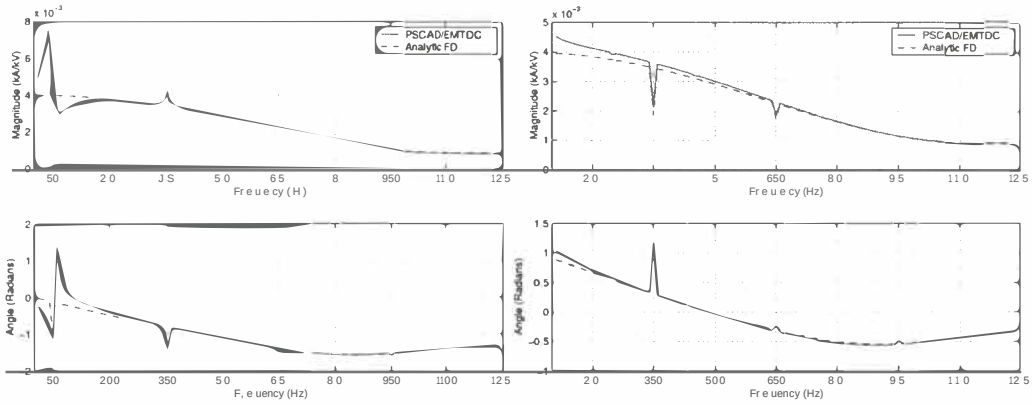

(a) a (b) b

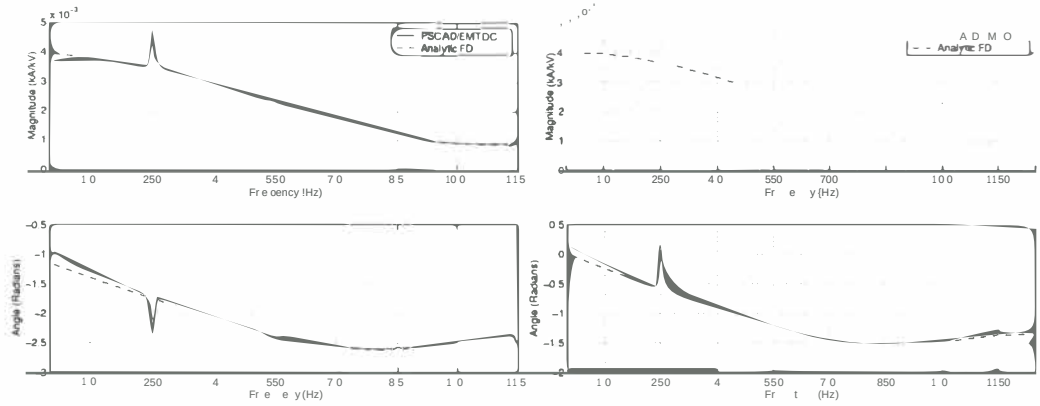

(c) e (d) f

Figure K.7 CIGRE inverter $V_{ac} \rightarrow I_{ac}$ transfers.

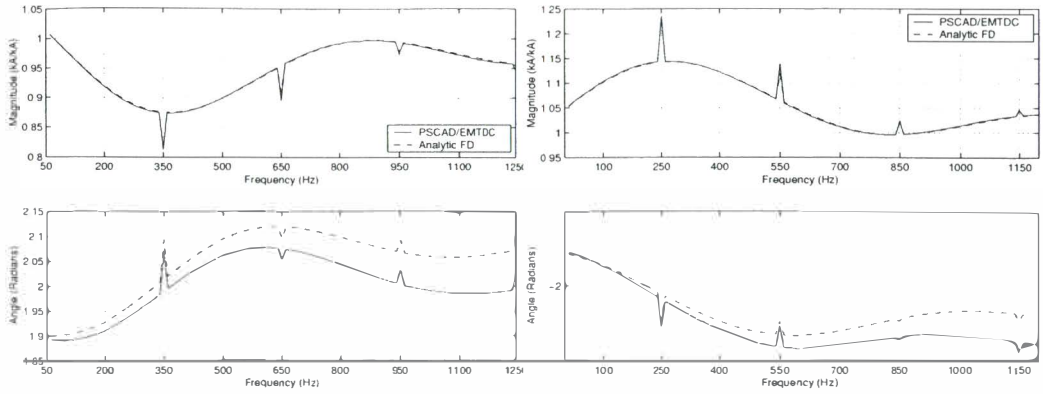

(a) c (b) g

Figure K.8 CIGRE inverter $I_{dc} \rightarrow I_{ac}$ transfers.

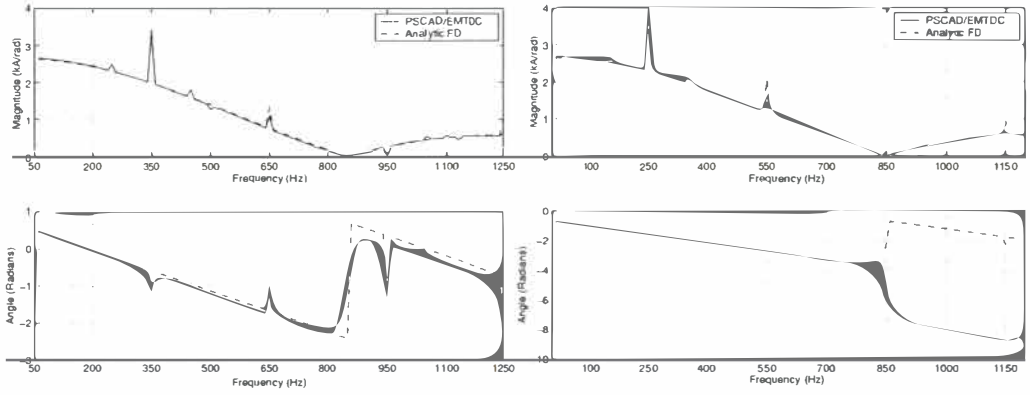

(a) d (b) h

Figure K.9 CIGRE inverter $\alpha \rightarrow I_{ac}$ transfers.

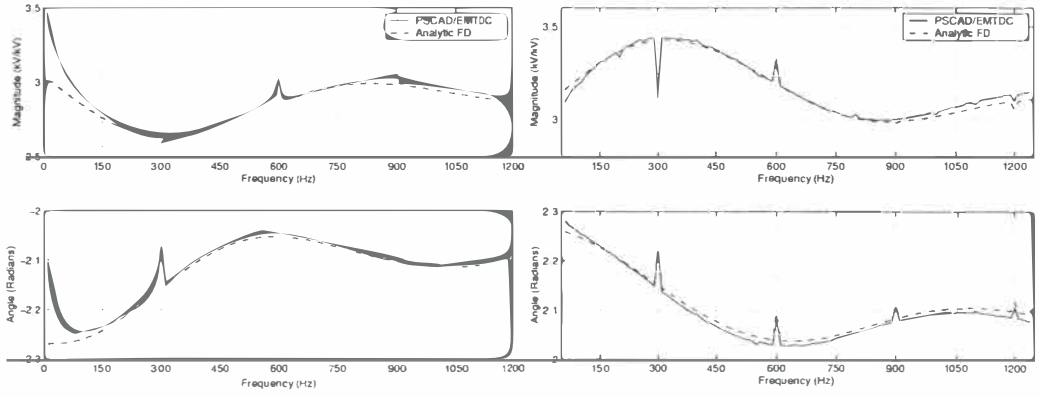

(a) i (b) j

Figure K.10 CIGRE inverter $I_{ac} \rightarrow V_{dc}$ transfers.

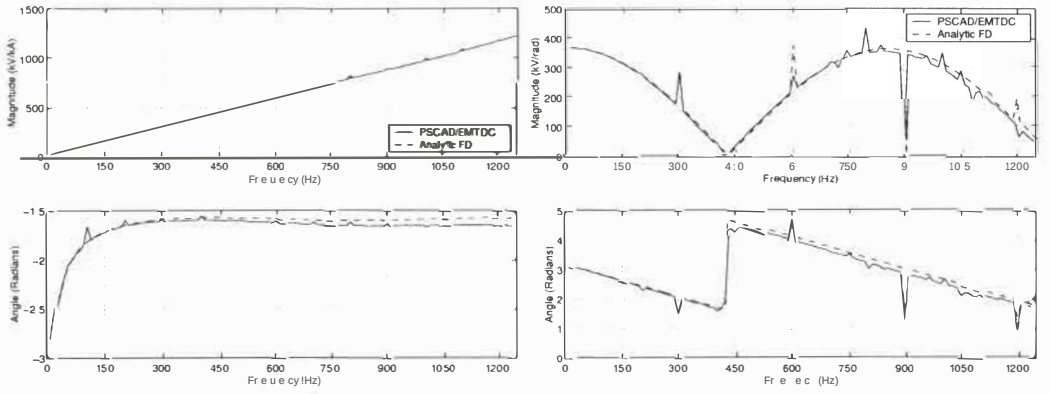

(a) k (b) l

Figure K.11 CIGRE inverter $I_{dc}, \alpha \rightarrow V_{dc}$ transfers.

Appendix L

PUBLICATIONS

The following is a list of publications resulting from the work described within this thesis.

1. D.J. Hume, A.R. Wood and C.M. Osauskas, *"The effect of AC system impedance on the cross-modulation of distortion in HVDC links"*. Accepted for the 10th ICHQP Conference - Rio de Janeiro, Brazil. October 6-9 2002.

2. D.J. Hume, A.R. Wood and C.M. Osauskas, *"Frequency domain modelling of interharmonics in HVDC systems"*. Accepted for publication for the IEE Proceedings on Generation Transmission and Distribution.

3. C.M. Osauskas, D.J. Hume and A.R. Wood, *"Small signal frequency domain model of an HVDC converter"*, IEE Proceedings on Generation Transmission and Distribution, vol. 148, no. 6, pp 573–578, November 2001.

4. A.R. Wood, C.M. Osauskas and D.J. Hume, *"Small signal modelling of HVDC transmission systems"*, 7th International Conference on AC-DC Power Transmission, No. 485, pp 107-112, IEE London, UK. November 28-30 2001.

5. A.R. Wood, D.J. Hume and C.M. Osauskas, *"A review of linear analysis techniques for HVDC and FACTS device waveform distortion"*, 9th ICHQP Conference Paper - Orlando, Florida, USA. October 1-4 2000.

6. A.R. Wood, D.J. Hume and J. Arrillaga, *"Cross-modulation of harmonics in HVDC schemes"*. Technical Brochure, CIGRE Working Group 14.25. Summary - Electra No 184, June 1999. Ref 143.

7. A.R. Wood, D.J. Hume and J. Arrillaga, *"On the elimination of the smoothing reactor from back-to-back HVDC interconnections"*. CIGRE conference paper, 1999.

8. D.J. Hume, A.R. Wood, B.C. Smith and J. Arrillaga, *"Linearised direct harmonic solution method for a back-to-back HVDC link"*. 8th ICHQP Conference Paper - Athens, Greece. October 14-16 1998.

REFERENCES

[1] J. Arrillaga. Power quality following deregulation. *Proceedings of the IEEE*. 88(2):246 to 261, February 2000.

[2] J.P. Charpentier R Rudervall and R Sharma. High voltage direct current (hvdc) transmission systems technology review paper. *Energy Week 2000, Washington, D.C, USA,*, March 2000.

[3] A. R. Wood. *An analysis of non-ideal HVDC convertor behaviour in the frequency domain, and a new control proposal.* PhD thesis, Department of Electrical and Electronic Engineering, University of Canterbury, Christchurch, New Zealand, November 1993.

[4] B.C. Smith. *A harmonic domain model for the interaction of the HVDC convertor with ac and dc systems.* PhD thesis, University of Canterbury, New Zealand, 1996.

[5] G.N. Bathurst. *A Newton solution for the harmonic analysis of power systems with multiple non-linear devices.* PhD thesis, Electrical Engineering department, University of Canterbury, New Zealand, April 1999.

[6] G.N. Bathurst, N.R. Watson, and J. Arrillaga. Adaptive frequency-selection method for a newton solution of harmonics and interharmonics. *IEE Proceedings on Generation, Transmission and Distribution*, 147(2):126–130, March 2000.

[7] B.C. Smith, N.R. Watson, A.R. Wood, and J. Arrillaga. Newton solution for the steady-state interaction of AC/DC systems. *IEE Proceedings on Generation, Transmission and Distribution*, 143(2):200–207, March 1996.

[8] J. Arrillaga. *High Voltage Direct Current Transmission.* Peter Peregrinus Ltd, London, U.K., 1983.

[9] B.R. Andersen, D.R. Monkhouse, R.S. Whitehouse, J.D.G. Williams, V.K. Prasher, and Devinder Kumar. Commisioning the 1000MW back to back HVDC link at chandrapur, india. *CIGRE*, 1, 1998.

[10] M.J. Luckett, N.M. MacLeod, and D.J. Young. Aspects of filter design for the Chandrapur 2x500MW HVDC back-to-back converter station. *IEE Sixth International Conference on AC and DC Power Transmission*, (423):191–196, April 1996.

[11] G H Robinson. Experience with harmonics: New zealand hvdc transmission scheme. *IEE conference publication, in 'High voltage dc transmission'*, (22):442 to 444, 1966.

[12] Y. Kraichik Y. Kazachkov, A. Boyarsky. The third harmonic in the russia-finland dc interconnection. *IEEE Transactions on Power Delivery*, 9(4):2009–2017, October 1994.

[13] Pal Otto Eide, R. Fredheim, Jan Spanberg, Bernt Bergdahl, and Lars-Erik Juhlin. Simulation of harmonic problems in the kristiansand hvdc station. *PSCC Conference*, June 1999.

[14] D.L. Dickmander, S.Y. Lee, G.L. Désilets, and M. Granger. Ac/dc harmonic interactions in the presence of gic for the quebec-new england phase ii hvdc transmission. *IEEE Transactions on Power Delivery*, 9(1):68 to 78, January 1994.

[15] E. Mollerstedt and B. Bernhardsson. Out of control because of harmonics - an analysis of the harmonic response of an inverter locomotive. *IEEE sontrol systems magazine*, pages 70–81, August 2000.

[16] M. Hernes and B. Gustavsen. Simulation of shaft vibrations due to interaction between turbine-generator train and power electonic converters at the visund oil platform. *PCC-Osaka*, page 1381 to 1386, 2002.

[17] A R Wood and J Arrillaga. Hvdc convertor waveform distortion - a frequency domain analysis. *IEE proceedings Pt C*, 142(1):88 to 96, January 1995.

[18] Wood A.R., Hume D.J., and Arrillaga J. On the elimination of the smoothing reactor from back-to-back hvdc interconnections. *Cigre conference paper*, 1999.

[19] T. Ino, R.M. Mathur, M.R. Iravani, and S.Sasaki. Validation of digital simulation of dc links - part ii. *IEEE Transactions on Power Apparatus and Systems*, 104(9):2596 to 2603, September 1985.

[20] D. A. Woodford, A. M. Gole, and R. W. Menzies. Validation of digital simulation of hvdc transients by field tests. *IEE conf. publ. on AC and DC power transmission*, (255):377 to 381, 1985.

[21] M Fauri. Harmonic modelling of non-linear load by means of cross frequency admittance matrix. *IEEE Transactions on Power Systems*, 12(4):1632–1638, November 1997.

[22] P. Marino R. Carbone, A. Lo Schiavo and A. Tesla. A new method based on periodic convolution for sensitivity analysis of multi-stage conversion systems. *9th International Conference on Harmonics and quality of power*, 1:69–74, October 2000.

[23] N.M. Wereley. *Analysis and control of linear periodically time varying systems.* PhD thesis, Department of Aeronautics and Astronautics, MIT, 1991.

[24] J. Usaola. Multifrequency analysis with time-domain simulation. *European Transactions on Electric Power*, 6(1):53 to 60, January 1996.

[25] B.C. Smith, N.R. Watson, A.R. Wood, and J. Arrillaga. Harmonic tensor linearisation of hvdc converters. *IEEE Transactions on Power Delivery*, 13(4):1244 to 1250, October 1998.

[26] G.N. Bathurst, B.C. Smith, N.R. Watson, and J. Arrillaga. Modelling of HVDC transmission systems in the harmonic domain. *IEEE Transactions on Power Delivery*, 14(3):1075–1079, July 1999.

[27] B.C. Smith, N.R. Watson, A.R. Wood, and J. Arrillaga. Steady state model of the ac/dc convertor in the harmonic domain. *IEE proceedings Pt C*, 142(2):109 to 118, March 1995.

[28] B.C. Smith, N.R. Watson, A.R. Wood, and J. Arrillaga. A newton solution for the steady state interaction of ac/dc systems. *IEE Proceedings on Generation, Transmission and Distribution*, 143(2):200 – 210, March 1996.

[29] B.C. Smith, J. Arrillaga, A.R. Wood, and N.R. Watson. A review of iterative harmonic analysis for AC-DC power systems. *IEEE Transactions on Power Delivery*, 13(1):180–185, January 1998.

[30] G.N. Bathurst, B.C. Smith, N.R. Watson, and J. Arrillaga. Harmonic domain modelling of high pulse converters. *IEE Proc.-Electr. Power Appl.* 146(3):335–340, May 1999.

[31] G.N. Bathurst, N.R. Watson, and J. Arrillaga. Modelling of bipolar HVDC links in the harmonic domain. *IEEE Transactions on Power Delivery*, 15(3):1034–1038, July 2000.

[32] G.N. Bathurst, N.R. Watson, and J. Arrillaga. A harmonic domian solution for systems with multiple high-power AC/DC converters. *IEE Proceedings on Generation, Transmission and Distribution*, 148(4):312–318, July 2001.

[33] D.J. Hume, A.R. Wood, B.C. Smith, and J. Arrillaga. Linearised direct harmonic solution method for a back-to-back hvdc link. *ICHQPs Conference, 14-16 sept. 1998, Athens, Greece.*, October 1998.

[34] E V Larsen, D H Baker, and J C McIver. Low order harmonic interaction on ac/dc systems. *IEEE Transactions on Power Delivery*, 4(1):493–501, January 1989.

[35] M. Sakui and H. Fujita. Line harmonic current of three phase thyristor bridge rectfier with dc current ripple and overlap angle. *Trans IEE Japan*, 105-B(9):717 to 724, September 1985.

[36] M. Sakui, H. Fujita, and M. Shioya. A method for calculating harmonic currents of a three phase bridge uncontrolled rectifier with dc filter. *IEEE Transactions on Industrial Electronics*, 36(3):434 to 440, August 1989.

[37] M. Sakui and H. Fujita. Calculation of harmonic currents in a three phase convertor with unbalanced power supply conditions. *IEE Proceedings Pt. B*, 139(5):478 to 484, September 1992.

[38] L. Hu and R. Yacamini. Harmonic transfer through convertors and hvdc links. *IEEE Transactions on Power Electronics*, 7(3):514 to 525, July 1992.

[39] L. Hu and R. Yacamini. Calculation of harmonics and interharmonics in hvdc schemes with low dc side impedance. *IEEE Proceedings-C*, 140(6):469 to 476, November 1993.

[40] L. Hu and L. Ran. Direct method for calculation of ac side harmonics and interharmonics in an hvdc system. *IEE Proceedings on Generation, Transmission and Distribution*, 147(6):329–335, November 2000.

[41] C.M. Osauskas and A R Wood. A frequency domain model of a thyristor controlled reactor. *ICHQPs Conference, 14-16 sept. 1998, Athens, Greece.*, October 1998.

[42] H. D. Laird, S. D. Round, and R.M. Duke. A frequency domain analytical model of an uncontrolled single-phase voltage-source rectifier. *IEEE Transactions on Industrial Electronics*, 47(3):525–531, June 2000.

[43] E.V. Persson. Calculation of transfer functions in grid controlled convertor systems. *IEE Proceedings*, 117(5):989 to 997, May 1970.

[44] J.P. Sucena-Paiva and L.L. Freris. Stability of a dc transmission link between weak ac systems. *IEE Proceedings*, 121(6):508 to 515, June 1974.

[45] A.R. Wood and J. Arrillaga. The frequency dependent impedance of an hvdc converter. *IEEE Transactions on Power Delivery*, 10(3):1635 to 1641, July 1995.

[46] A.R. Wood and J. Arrillaga. Composite resonance; a circuit approach to the waveform distortion dynamics of an hvdc converter. *IEEE Transactions on Power Delivery*, 10(4):1882 to 1888, October 1995.

[47] S. Chen, A.R. Wood, and J. Arrillaga. Hvdc converter core saturation instability; a frequency domain analysis. *IEE Proceedings Pt. C*, 143(1):75 to 81, January 1996.

[48] M. Mohaddas, A.M. Gole, and S. Elez. Steady state frequency response on statcom. *IEEE Transactions on Power Delivery*, 16(1):18–23, 2001.

[49] S. Todd and A.R. Wood. An s-domain model of an hvdc converter. *IEEE Transactions on Power Delivery*, 12(4):1723 to 1729. October 1997.

[50] H. Stemmler. Hvdc back to back interties on weak ac systems, second harmonic problems, analyses and solutions. *CIGRE Symposium*, 09-87(300-08):1 to 5, 1987.

[51] E. Mollerstedt and B. Bernhardsson. A harmonic transfer function model for a diode converter train. *IEEE Power engineering society winter meeting, 2000*, January 2000.

[52] H. Sandburg and E. Mollerstedt. Harmonic modelling of the moter side of an inverter locomotive. *Proceedings of the 2000 IEEE International conference on control applications, Alaska, USA*, pages 918–923, September 2000.

[53] J.C. Contreras-Sampayo, J. Usaola-Garcia, and A.R. Wood. Steady-state algorithm for switching power electronic devices. *IEE Proc.-Elect. Power Appl*, 148(2):245–250, March 2001.

[54] J. Arrillaga and C.P. Arnold. *Computer Analysis of Power Systems*. John Wiley and Sons Ltd, West Sussex, England, 1990.

[55] H. Sato and J. Arrillaga. Improved load-flow techniques for integrated ac/dc systems. *Proceedings of the IEE*, 116:525 to 532, 1969.

[56] B. Stott and ●. Alsac. Fast decoupled load flow. *IEEE Transactions on Power Apparatus and Systems*, PAS-93:859 to 869, 1974.

[57] G. Kron. *Tensor analysis of networks*. Macdonald and Co. (Publishers) Ltd, London, U.K., 1965.

[58] G. Kron. *Diakoptics – the piecewise solution of large scale systems*. Macdonald and Co. (Publishers) Ltd, London, U.K., 1963.

[59] G. Kron. *The application of tensors to the analysis of rotating electrical machinery*. General Electric Review, Schenectady, N.Y.. U.S.A., 1938.

[60] Wood A.R., Hume D.J., and Osauskas C.M. Linear analysis of waveform distortion for hvdc and facts devices. *9th International Conference on Harmonics and quality of power*, 3:967–972, October 2000.

[61] Osauskas C.M., Hume D.J., and Wood A.R. Small signal frequency domain model of an hvdc converter. *IEE Proceedings on Generation, Transmission and Distribution*, 148(6):573–578, November 2001.

[62] M Szechtman, T Weiss, and C V Thio. First benchmark model for HVDC control studies. *Electra*, 1(135):55 to 75, April 1991.

[63] E Acha. *Modelling of Power System Transformers in the Complex Conjugate Harmonic Space.* PhD thesis, University of Canterbury, Christchurch, New Zealand, 1988.

[64] A.R. Wood, D.J. Hume, and J. Arrillaga. Cross-modulation of harmonics in hvdc schemes. *CIGRE Working Group 14.25*, 1999.

[65] L. Hu and R. Yacamini. Calculation of harmonic interference in hvdc systems with unbalance. *International conference on AC and DC power transmission*, page 514 to 525, 1991.

[66] L. Hu and R.E. Morrison. The use of modulation theory to calculate the harmonic distortion in hvdc systems operating on an unbalance supply. *IEEE Transactions on Power Systems*, 12(2):973–980, May 1997.

[67] R Yacamini. How hvdc schemes can excite torsional oscillations in turbo-alternator stafts. *IEE Proceedings, Pt. C*, 133(6):301–307, September 1986.

[68] T.J. Hammons and J.J. Bremner. Stressing of turbine-generator-exciter shafts by variable-frequency currents superimposed on dc currents in asynchronous hvdc links and following disturbances at converter stations. *IEEE Transactions on Energy Conversion*, 9(3):503–513, September 1994.

[69] T.J. Hammons and J.J. Bremner. Analysis of variable-frequency currents superimposed on dc currents in asynchronous hvdc links in stressing turbine-generator-excitor shafts. *IEEE Transactions on Energy Conversion*, 10(1):95–104, March 1995.

[70] M. Schwartz, W. R. Bennett, and S. Stein. *Communication systems and techniques.* IEEE - Classic reissue, 1996.